

REPORT DOCUMENTATION PAGE			Form Approved OMB No. 0704-0188	
Public reporting burden for this collection of information is estimated to average 1 hour per response, including the time for reviewing instructions, searching existing data sources, gathering and maintaining the data needed, and completing and reviewing the collection of information. Send comments regarding this burden estimate or any other aspect of this collection of information, including suggestions for reducing this burden, to Washington Headquarters Services, Directorate for Information Operations and Reports, 1215 Jefferson Davis Highway, Suite 1204, Arlington, VA 22202-4302, and to the Office of Management and Budget, Paperwork Reduction Project (0704-0188), Washington, DC 20503.				
1. AGENCY USE ONLY (Leave blank)	2. REPORT DATE 22.Mar.01	3. REPORT TYPE AND DATES COVERED THESIS		
4. TITLE AND SUBTITLE CHARACTERIZING ACTINIDE TRANSPORT AND SPECIATION USING NUCLEAR MAGNETIC RESONANCE TRACER TECHNIQUES		5. FUNDING NUMBERS		
6. AUTHOR(S) MAJ CAPUTO DANIEL F				
7. PERFORMING ORGANIZATION NAME(S) AND ADDRESS(ES) MASSACHUSETTS INSTITUTE OF TECHNOLOGY		8. PERFORMING ORGANIZATION REPORT NUMBER CI01-63		
9. SPONSORING/MONITORING AGENCY NAME(S) AND ADDRESS(ES) THE DEPARTMENT OF THE AIR FORCE AFIT/CIA, BLDG 125 2950 P STREET WPAFB OH 45433		10. SPONSORING/MONITORING AGENCY REPORT NUMBER		
11. SUPPLEMENTARY NOTES				
12a. DISTRIBUTION AVAILABILITY STATEMENT Unlimited distribution In Accordance With AFI 35-205/AFIT Sup 1		12b. DISTRIBUTION CODE		
13. ABSTRACT (Maximum 200 words)				
14. SUBJECT TERMS			15. NUMBER OF PAGES 307	
			16. PRICE CODE	
17. SECURITY CLASSIFICATION OF REPORT	18. SECURITY CLASSIFICATION OF THIS PAGE	19. SECURITY CLASSIFICATION OF ABSTRACT	20. LIMITATION OF ABSTRACT	

**Characterizing Actinide Transport and Speciation
Using Nuclear Magnetic Resonance Tracer Techniques**

by

Daniel F. Caputo

B.S., Nuclear Engineering
Rensselaer Polytechnic Institute, 1988

M.Eng., Nuclear Engineering
Rensselaer Polytechnic Institute, 1989

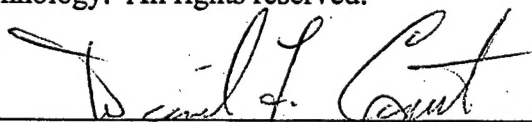
SUBMITTED TO THE DEPARTMENT OF NUCLEAR ENGINEERING IN PARTIAL
FULFILLMENT OF THE REQUIREMENTS FOR THE DEGREE OF

DOCTOR OF PHILOSOPHY IN NUCLEAR ENGINEERING
AT THE
MASSACHUSETTS INSTITUTE OF TECHNOLOGY

SEPTEMBER 2000

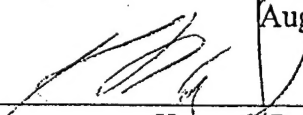
© 2000 Massachusetts Institute of Technology. All rights reserved.

Signature of Author _____



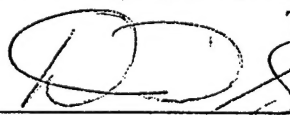
Department of Nuclear Engineering
August 8, 2000

Certified by _____



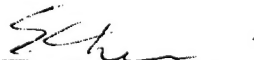
Kenneth R. Czerwinski
Assistant Professor of Nuclear Engineering
Thesis Supervisor

Certified by _____



David G. Cory
Professor of Nuclear Engineering
Thesis Reader

Accepted by _____



Sow-Hsin Chen
Professor of Nuclear Engineering
Chairman, Committee on Graduate Students

20010405 019

TABLE OF CONTENTS

TITLE PAGE	1
1. ABSTRACT	3
TABLE OF CONTENTS	5
2. THESIS SUMMARY	9
3. INTRODUCTION	29
3.1. Project Overview	
3.2. Thesis Overview	
4. BACKGROUND	39
4.1. Radioactive Waste Disposal in the U.S.	
4.2. Actinide Chemistry	
4.3. Nuclear Magnetic Resonance	
4.4. Ion-specific Resins	
5. EXPERIMENTAL TECHNIQUES	73
5.1. NMR Based Techniques	
5.2. ICP-AES	
6. NMR FLOW SYSTEM	107
6.1. Introduction	
6.2. NMR Susceptibility Effects	
6.3. Gas Transfer at the Air-Water Interface	
6.4. Experimental Setup	
6.5. Results	
6.6. Discussion and Conclusions	
7. MICROSCOPIC CHARACTERIZATION OF ION-SPECIFIC RESINS USING NMR	125
7.1. Introduction	
7.2. Three-Pool Resin Model	
7.3. Discussion and Results	
7.4. Conclusions	
8. NMR IMAGING OF ION-SPECIFIC RESINS	149
8.1. NMR Imaging Paper: Characterizing Transport and Separation In Ion-Specific Resin Columns using Nuclear Magnetic Resonance (NMR) Imaging	
8.2. NMR Imaging of Flow in PF Resin	
9. CONCLUSIONS	179
Appendix 1: RF and CF Resin Preparation	185
Appendix 2: Bruker Pulse Programs for the 3T and 12T Magnets	189
Appendix 3: Matlab Programs for Processing NMR Data	223
Appendix 4: NMR Spectroscopy and Relaxation Data	247
Appendix 5: NMR Imaging Data	287
Appendix 6: ICP-AES Data	295
Appendix 7: BET Surface Area Data	301

LIST OF FIGURES

1. ABSTRACT
2. THESIS SUMMARY
3. INTRODUCTION
4. BACKGROUND
 - 4.1. Ionic radii of the trivalent actinides and lanthanides
 - 4.2. Plot of T_1 relaxation rate versus Gd concentration
 - 4.3. Chemical structure of CF and RF resins
5. EXPERIMENTAL TECHNIQUES
 - 5.1. 3T 10 mm ID flow-through RF probe
 - 5.2. Typical single 90-degree excitation (zg) pulse sequence
 - 5.3. Inversion recovery pulse sequence
 - 5.4. CPMG pulse sequence
 - 5.5. PGSTE pulse sequence
 - 5.6. Goldman-Shen pulse sequence
 - 5.7. 3-D slice-selective spin echo imaging sequence
 - 5.8. Photo of a flow-through resin sample
 - 5.9. Photo of NMR flow-through sample tube
 - 5.10. ICP-AES system
 - 5.11. Plot of ICP-AES calibration data
6. NMR FLOW SYSTEM
 - 6.1. Schematic of the NMR Flow System
 - 6.2. Plot of normalized signal intensity versus axial position
 - 6.3. Plot showing O_2 bubble collapse
 - 6.4. The effect of deaerated water and over-pressurization
 - 6.5. A sample of 0.9-1.1 mm diameter glass beads filled with deaerated water
 - 6.6. The combined effect of over-pressurization and flow
7. MICROSCOPIC CHARACTERIZATION OF ION-SPECIFIC RESINS USING NMR
 - 7.1. Three-pool model of water saturated resins
 - 7.2. Three-pool model of water saturated CF resins
 - 7.3. Three-pool model of water saturated RF resins
 - 7.4. Deconvolution of CF clean resin and polybutadiene
 - 7.5. Evaluation of microscopic characteristics

8. NMR IMAGING OF RESINS

- 8.1. 2- and 3-D NMR images
- 8.2. RF sequence of 2-D NMR images
- 8.3. CF sequence of 2-D NMR images
- 8.4. CF and RF breakthrough curves
- 8.5. Plot of RF resin flow
- 8.6. Plot of CF resin flow
- 8.7. 3-D NMR image of a homogenized RF resin
- 8.8. 2-D image sequence of the Gd loading of PF resin
- 8.9. 2-D image sequence of the 0.1 M HNO₃ flow
- 8.10. Breakthrough curve for PF resin
- 8.11. Plot of the Gd balance through the PF resin column
- 8.12. 3-D images of PF resin loaded with Gd
- 8.13. 3-D images of PF resin showing 1.0 M and 6.0 M HNO₃ studies

9. CONCLUSIONS

LIST OF TABLES

1. ABSTRACT
2. THESIS SUMMARY
3. INTRODUCTION
4. BACKGROUND
 - 4.1. NRC classification criteria for long-lived radionuclides
 - 4.2. NRC classification criteria for short-lived radionuclides
 - 4.3. Listing of U.S. commercial radioactive waste disposal sites
 - 4.4. Metallic and ionic radii (\AA or m^{-10}) of select actinides and a few actinyl ions
 - 4.5. The actinides with known or suspected oxidation states
 - 4.6. Physical characteristic of CF and RF resins
5. EXPERIMENTAL TECHNIQUES
6. NMR FLOW SYSTEM
7. MICROSCOPIC CHARACTERIZATION OF ION-SPECIFIC RESINS USING NMR
 - 7.1. Clean CF Resin Data Table
 - 7.2. Clean CF Resin Reference Table
 - 7.3. Clean RF Resin Data Table
 - 7.4. Clean RF Resin Reference Table
 - 7.5. Deconvolution of CF Clean + Polybutadiene Spectrum
 - 7.6. Data from Gd-Loaded Experiments on CF and RF Resins
8. NMR IMAGING OF RESINS
9. CONCLUSIONS

[THIS PAGE INTENTIONALLY LEFT BLANK]

Characterizing Actinide Transport and Speciation Using Nuclear Magnetic Resonance Tracer Techniques

by

Daniel F. Caputo

Submitted to the Department of Nuclear Engineering
on 11 August, 2000 in Partial Fulfillment of the
Requirements for the Degree of Doctor of Philosophy in
Nuclear Engineering

ABSTRACT

There is a general lack of understanding of how actinides migrate in environmental systems. This lack of understanding stems from the fact that there is limited experience with many actinides in the environment, and due to the complex chemical reactivity of most actinide species. With a limited understanding of actinide environmental behavior, it is very difficult to predict and model environmental transport, which is necessary to determine the release of actinides to the biosphere from current and proposed radioactive waste disposal sites. To overcome the shortfall in the knowledge base of actinide environmental behavior, it is necessary to develop new tools and to take new approaches in increasing the awareness of actinide transport and chemical speciation. It is with this challenge that the application of nuclear magnetic resonance imaging (NMRI) to study actinide transport and speciation was employed.

Using the technique of NMRI coupled with a lanthanide tracer, actinide transport and chemical speciation can be studied non-invasively in a variety of porous flow environments. The NMRI tracer technique provides near real-time feedback on the reactive transport of an actinide analog, and transport properties such as degree of fingering, or channeling, can be determined. In addition, NMR techniques can be used to extract microscopic information from porous systems, such as bound water percentage and exchange rates between bound and interstitial water components. The NMR microscopic analysis of ion-exchange resins provided a direct measure of specific surface area (SSA) and a determination of the theoretical proton exchange capacity (PEC). The NMR techniques were shown to be the only direct analysis methods to measure the SSA and to provide a theoretical upper bound for the phenolic resins used in these studies. The study shows that NMR imaging and spectroscopic techniques provide a means to further understand actinide

Thesis Supervisor: Kenneth R. Czerwinski

Title: Assistant Professor of Nuclear Engineering

1. ABSTRACT

There is a general lack of understanding of how actinides migrate in environmental systems. This lack of understanding stems from the fact that there is limited experience with many actinides in the environment, and due to the complex chemical reactivity of most actinide species. With a limited understanding of actinide environmental behavior, it is very difficult to predict and model environmental transport, which is necessary to determine the release of actinides to the biosphere from current and proposed radioactive waste disposal sites. To overcome the shortfall in the knowledge base of actinide environmental behavior, it is necessary to develop new tools and to take new approaches in increasing the awareness of actinide transport and chemical speciation. It is with this challenge that the application of nuclear magnetic resonance imaging (NMRI) to study actinide transport and speciation was employed.

Using the technique of NMRI coupled with a lanthanide tracer, actinide transport and chemical speciation can be studied non-invasively in a variety of porous flow environments. The NMRI tracer technique provides near real-time feedback on the reactive transport of an actinide analog, and transport properties such as degree of fingering, or channeling, can be determined. In addition, NMR techniques can be used to extract microscopic information from porous systems, such as bound water percentage and exchange rates between bound and interstitial water components. The NMR microscopic analysis of ion-exchange resins provided a direct measure of specific surface area (SSA) and a determination of the theoretical proton exchange capacity (PEC). The NMR techniques were shown to be the only direct analysis methods to measure the SSA and to provide a theoretical upper bound for the phenolic resins used in these studies. The study shows that NMR imaging and spectroscopic techniques provide a means to further understand actinide speciation and transport in environmental and other complex systems.

[THIS PAGE INTENTIONALLY LEFT BLANK]

2. THESIS SUMMARY

This document is a summary of the thesis prepared by Daniel F. Caputo in partial fulfillment of requirements for a Doctor of Philosophy degree in Nuclear Engineering at the Massachusetts Institute of Technology. It consists of an overview of each section as it appears in the main thesis document.

2.1. Abstract

There is a general lack of understanding of how actinides migrate in environmental systems. This lack of understanding stems from the fact that there is limited experience with many actinides in the environment, and due to the complex chemical reactivity of most actinide species. With a limited understanding of actinide environmental behavior, it is very difficult to predict and model environmental transport, which is necessary to determine the release of actinides to the biosphere from current and proposed radioactive waste disposal sites. To overcome the shortfall in the knowledge base of actinide environmental behavior, it is necessary to develop new tools and to take new approaches in increasing the awareness of actinide transport and chemical speciation. It is with this challenge that the application of nuclear magnetic resonance imaging (NMRI) to study actinide transport and speciation was employed. Using the technique of NMRI coupled with a lanthanide tracer, actinide transport and chemical speciation can be studied non-invasively in a variety of porous flow environments. The NMRI tracer technique provides near real-time feedback on the reactive transport of an actinide analog, and transport properties such as degree of fingering, or channeling, can be determined. In addition, NMR techniques can be used to extract microscopic information from porous systems, such as bound water percentage and exchange rates between bound and interstitial water components. The NMR microscopic analysis of ion-exchange resins provided a direct measure of specific surface area (SSA) and a determination of the theoretical proton exchange capacity (PEC). The NMR techniques were shown to be the only direct analysis methods to measure the SSA and to provide a theoretical upper bound for the phenolic resins used in these studies. The study shows that NMR imaging and spectroscopic techniques provide a means to further understand actinide speciation and transport in environmental and other complex systems.

2.2. Introduction

The environmental behavior of actinides is not fully understood, and thus it is not possible to accurately predict their release and transport rates from current or proposed radioactive waste sites. The insufficient knowledge base of the actinides is due to the lack of natural analogs and thermodynamic data (particularly for transuranics), the limited duration of industrial use and study of these materials, and resultant complexity of modeling such systems.

In understanding environmental behavior, it is crucial to first determine the chemical and physical properties of the actinide at the source and under aqueous conditions, since groundwater movement is the primary release and transport route at most waste sites. Once the actinide's chemical and physical forms, or species, are known, we are able to determine the mobility of the actinide, which allows for prediction of the release and transport rates. Thus in order to understand the behavior of actinides in the environment, experimental tools and techniques need to be developed that provide a deeper understanding of actinide speciation and transport. One powerful tool to investigate the mechanisms that control speciation and transport is nuclear magnetic resonance (NMR) imaging. NMR imaging with appropriate experimental techniques can be used as a probe to provide temporal and spatial information of actinide speciation and transport in simulated aquatic environments. Information from the NMR studies will lead to a better understanding of actinide behavior in the environment, and in turn, it will lead to improved prediction of the fate of these contaminants in the biosphere and geosphere.

There are presently a large number of radioactive waste sites in the United States and throughout the world containing hazardous quantities of actinides and associated radioactive materials. Many of these sites either are in the process of environmental remediation or will be remediated at some time in the future in order to mitigate the public radiation dose. The actinide materials residing at these sites will either be left in place using some type of containment or encapsulation method, or they will be removed, packaged, transported, and disposed of at some other more suitable disposal site. In order to make informed decisions on how best to control the public radiation dose from these sites, it is critical to understand the chemical and physical processes that control the behavior of the actinides in their present and future environments. Thus, knowledge of the environmental behavior of actinides is critical to controlling the public radiation dose from actinide-containing radioactive waste sites.

This leads to the question of how best to understand the chemical and physical processes controlling the behavior of actinides in the environment. A typical approach to understand the behavior of metals in the environment includes the study of naturally occurring sources and a determination of the metal's chemical and physical properties, or species. Based on the environmental conditions (i.e. pH, alkalinity, temperature, pressure, ionic strength, REDOX potential, etc.) and the metal speciation under those conditions, a set of equilibrium constants for each species can be determined based only on thermodynamic properties. By verifying the thermodynamic data with experimental data from naturally occurring sites, a database of equilibrium constants can be assembled and applied to the speciation of that metal under any environmental conditions. However, this natural analog approach is highly restricted in the case of actinides, since there are very few naturally occurring sources of actinides with atomic numbers greater than uranium (atomic number 92). In addition, the industrial processing of actinides, mainly from commercial nuclear power and weapons production, is a relatively recent undertaking, and there is very little practical experience with the long-term performance of these materials in the environment. It is only recently that the United States and other actinide-producing countries have been motivated to gain a deeper understanding into the environmental behavior of the actinides. Therefore, to better understand the behavior of actinides in the environment, the limited historical record must be supplemented with empirical data obtained in the laboratory.

There are many traditional experimental methods for determining mass balance and equilibrium conditions of simulated environmental systems. These experimental methods include column and batch testing or acid-base titration, but it is often very difficult to interpret these results without some type of natural analog from which to reference. In addition, these traditional experimental techniques must often use homogenized media and idealized conditions to limited the degrees of freedom. In contrast, the proposed NMR imaging technique can be applied to heterogeneous flow systems using a wide range of flow conditions, and this will provide needed insight into the speciation of actinides under controlled conditions. The NMR technique is also inherently non-invasive and provides a means to investigate transport phenomena under precise environmental flow conditions with actual environmental media. The NMR tracer technique will contribute to a deeper understanding of actinide behavior in the natural environment.

2.3. Background

In general, radioactive waste can be described as solid, liquid, and gaseous materials from nuclear activities that are inherently radioactive or have been irradiated and have been declared waste products. In the U.S., waste is generally classified as high-level, low-level, or intermediate level. The primary regulatory authority for radioactive waste is the U.S. Nuclear Regulatory Commission (NRC), however the U.S. Environmental Protection Agency (EPA) has a role in setting public exposure criteria. Both the NRC and EPA have definitions for radioactive waste, and they both use the source of the waste as the criteria for categorization. This is contrary to most waste classification schemes, where the waste is defined in terms of its hazardous constituents or its risk to the biosphere.

It is apparent that the relatively poor performance of the U.S. commercial radioactive waste sites can be directly linked to a lack of understanding of the chemical and physical site characteristics. The regulatory and operational focus of radioactive waste disposal in the U.S. has been on the site hydrology and structural integrity. This type of approach requires little to no attention on controlling or understanding the near-field chemistry, which has proven to have a large impact on the long-term performance of U.S. waste sites. There is a need to re-address the regulatory framework of radioactive waste disposal (especially low-level waste) to include controls on waste forms and packaging with the intent of limiting highly reactive chemical environments. Without positive control and understanding of the chemical speciation at radioactive waste sites, there is no way to predict or model the release of the radionuclides to the biosphere.

The focus of this study is on actinide chemistry and its environmental behavior. Actinide chemistry is a complex area of study due to the lack of natural analogs for the higher actinides, the large variation in valence states, and the radioactive nature of these elements. The actinides are those elements with atomic numbers 89 (actinium) to 102 (nobelium), and they are distinguished from other elements by the filling of the 5f electronic subshells. Actinides with atomic numbers 92 (U) and below are naturally occurring, and those actinides with atomic number greater than U are called transuranic elements, and all are man-made. Since the transuranic elements are not readily found in natural settings, it is difficult to study these elements, since there is no environmental database from which extract empirical speciation

information. The lack of environmental data has lead researchers to resort to empirical chemistry studies and thermodynamic modeling to predict the speciation of the transuranic elements. These empirical studies and modeling efforts have been successful in predicting speciation under a small range of thermodynamic conditions, however the building of the actinide thermodynamic database is just beginning. Although vast improvements have been made in the field of thermodynamic modeling, the range of environmental conditions is so large that a complete thermodynamic database with the necessary kinetics information will not be available for quite some time. One other complication of the study of actinides is their radioactive nature. In a waste repository setting, the radiation emitted by actinides tends to have a major influence on the near-field chemistry. In an aquatic system, the radiation can cause local radiolysis leading to the formation of highly reactive free radical, subsequent peroxide formation, leading to pH adjustments, chemical bond disruption. Radiolysis is a complex local interaction and can have a large impact on the local chemical speciation of high concentrations of actinides. The approach used in this study to understand actinide chemistry is to describe the actinides in terms of their natural analogs, lanthanide analogs, and environmental behavior. Once this description is made, the analytical technique of NMR is applied to further study actinide interactions

Nuclear magnetic resonance (NMR) as a tool to study nuclear interactions was first discovered by Bloch and Purcell in 1946^[1,2]. This discovery has lead to widespread use of NMR as an analytical tool, and its applications to new and diverse areas of study are continuously expanding. The field of NMR can be split two separate areas, however there is much overlap between the two. These two areas of NMR study include spectroscopy and imaging. A third area of growing interest is the area of NMR relaxation, however this will be integrated into the discussion of spectroscopy and imaging for this presentation. The experimental applications of NMR are as varied and diverse as the number of measurable nuclear interactions, and new applications are constantly being created.

The ion-exchange resins used in these NMR studies were designed to separate similar metal ions from various waste streams in a nuclear fuel reprocessing operation. This separation of similar ions requires the use of an ion exchange media that preferentially sorbs to one metal type over another. Since the metals of interest are lanthanides and actinides that primarily exist in a trivalent form, separation through redox controls was not an option. The only other

mechanism was separation through physical mechanisms based on the interaction of the resin structure with the ion. In this way, the separation takes advantage of the variation in ionic radii of the metals, and thus various types of resins can be used to preferentially sorb certain metals.

The specific class of resins used in these experiments is organic ion exchangers that were first introduced in 1935^[3]. The first types of organic resins synthesized were phenol-formaldehyde polymers, and these are the types used in these studies. The phenolic resins used in these experiments are described and were prepared according to the procedures in ref. ^[4, 5, 6, 7], and in Appendix 1.0. The two primary phenolic resins used in these studies were resorcinol-formaldehyde (RF) and catechol-formaldehyde (CF). A third resin, phenol-formaldehyde (PF), was used for an imaging study, and its structure is the same as CF but with only one phenol (-OH) group.

2.4. Experimental Methods

Nuclear Magnetic Resonance (NMR) and Inductively-Coupled Plasma – Atomic Emission Spectroscopy (ICP-AES) techniques were used in performing the experiments. The NMR experiments included both traditional spectroscopic techniques as well as non-traditional NMR techniques such as imaging of fluid transport and magic-angle spinning (MAS) [⁸]. The traditional techniques will be discussed first with some MAS techniques integrated into the experiments. The NMR imaging experiments are discussed in second part of this section and in Section 7.0. All experiments were performed using Bruker spectrometers, and the Bruker experimental programs are provided in Appendix 2.0 for each type of experiment [⁹]. A description of the NMR equipment is provided in Section 4.3. Most data processing was done with Bruker spectrometer-based programs or using Matlab [¹⁰]. The Matlab processing codes and other data processing worksheets are provide in Appendix 3.0 for each type of processing used. The experimental data is available in Appendix 4.0. All NMR experiments in this study looked at proton resonance signal, and only square, or hard, radiofrequency (RF) pulses were used. Some deuterated water was used in the experiments, however only the signal from the trace protons was collected. The effluent from the gadolinium (Gd) flow experiments was analyzed using ICP-AES. The ICP-AES an analytical tool used to determine the Gd concentrations in solutions. A detailed description of ICP-AES and the procedures used are included.

2.5. NMR Flow System

NMR imaging is an emerging non-invasive tool to provide qualitative and quantitative information in the study of flow in granular media. Here, NMR imaging is applied to the investigation of contaminant transport in environmental groundwater systems. NMR can provide critical insight into both near real-time transport and chemical speciation parameters of environmental systems. However, the quality and utility of the data obtained is often degraded by the presence of air bubbles. These air bubbles are direct sources of NMR susceptibility effects that result in image distortions and signal attenuation. An experimental flow setup is described which minimizes the presence of air bubbles through water deaeration followed by over-pressurization. Experimental results show the degree of effectiveness for air bubble removal.

Susceptibility effects are an inherent problem in the NMR imaging of complex systems involving fluid flow through granular media. These susceptibility effects are often caused by air bubbles formed during sample preparation and under experimental flow conditions. The technique of deaeration followed by over-pressurization is highly effective in reducing air bubbles in granular media. The deaerated water provides a sink for the free air to be transferred into the aqueous phase, and the over-pressurization provides an added mechanism for this transfer to occur. The degree of deaeration is limited by the effectiveness of the deaeration system (i.e. mixing vessel and vacuum pump), and in these studies, deaeration to less than 0.6 ppm DO (20) was shown to be highly effective in incorporating free air. As for the degree of over-pressurization, the higher the pressure on the closed system, the more free air transfers into the aqueous phase. In these studies, pressurization to 620 kPa (90 psi) proved highly effective in driving the free air into solution.

For granular media with low porosity or dead end pathways, the diffusion time of the gas into the liquid may be excessively long to completely remove all of the free air. This problem can be mitigated by a flowing stream of deaerated liquid to provide a constant sink for the free air to be integrated. If advective flow is not possible for low porosity media, the deaeration times are purely diffusion dependent and gas exchange rates will be based only on molecular diffusion. In this case, it may be advantageous to impregnate the low porosity material with a gas that has higher water solubility, such as CO₂.

The experimental results of this section show the effectiveness of this deaeration technique at mitigating the unwanted susceptibility effects. The significant reduction and positive control over the effects of air/water susceptibility provides greater confidence in interpreting qualitative assessments of imaging media. The reduction in imaging artifacts may also provide the opportunity to develop quantitative evaluation methods for imaging techniques. NMR is also an effective means to evaluate the degree of deaeration in a sample. Experimental results in Figures 2 and 3 show how 1-D T_1 mapping of a sample can be used to evaluate the degree of deaeration and the rates at which the various deaeration mechanisms take place. Some limited deaeration time-scales can also be extracted from the 1-D data.

2.6. Microscopic Characterization of Ion-Specific Resins Using NMR

The use of NMR spectroscopy and relaxation techniques has proven very effective at probing the microscopic characteristic of a variety of materials. This study applies NMR techniques to probe the microscopic characteristic of phenolic-based ion-exchange resins. The study employs the use of a variety of the NMR experiments to extract information on the relaxation rates, spatial scales, and exchange rates of water molecules integrated into the resin microscopic structure. The study also uses two different magnetic fields, 3T and 12T, and magic-angle spinning (MAS) to separate dipolar from susceptibility induced interactions in the resins. Using a wide range of NMR techniques at two different magnetic field environments, the study showed there are three primary water environment, or spin pools, within the resin matrix. These pools were shown to belong to bound, interstitial or plasticizer, and free water components in relative populations of 40%, 40%, and 20%, respectively. The diffusion rates of the three pools were measured, and the results showed the fastest diffusion for the plasticizer pool and the slowest for the bound water. The exchange rate between the plasticizer and bound pools was measured to be 0.00396 ms^{-1} ($\tau_c=252.3 \text{ ms}$), and the exchange rate between the free and plasticizer pools was calculated to be 90 ms. The pore diameter for the bound water was measured to be $2.4 \text{ }\mu\text{m}$. NMR provides the only means to directly measure the pore volume of the bound water. The use of NMR spectroscopic and relaxation techniques has increased the understanding of the exchange mechanisms and spatial scales of these ion-specific resins.

Nuclear Magnetic Resonance (NMR) spectroscopic and relaxation techniques have proven very useful in the study of porous media [¹¹, ¹², ¹³]. These NMR techniques provide exceptional insight into water-saturated porous environments. This insight is gained through identification of various water pools within the porous matrix, and once these spin pools are identified, NMR provides a means to determine spatial and temporal scales for each pool [¹⁴, ¹⁵, ¹⁶].

This section provides a description of a series of NMR spectroscopic and relaxation experiments performed on phenolic ion-exchange resins. The specific phenolic resins used are Catechol-Formaldehyde (CF) and Resorcinol-Formaldehyde (RF), and these resins are further described in Section 4.4 and Appendix 1.0. The resins proved to be a particularly clean system with which to apply these NMR techniques. There were three easily distinguishable spin pools,

which were assigned to bound water, interstitial or plasticizer water, and free water components. With the use of NMR, relaxation times, diffusion rates, and relative populations were determined for each pool. In addition, the exchange rates between the various pools were determined, and finally, the pore volume of the bound water fraction was calculated. The bound water volume provided a means to calculate the effective surface area of the resin, which was otherwise impossible with the use of standard surface-area analysis techniques. This study also briefly looked at resins complexed, or loaded, with gadolinium (Gd) to see the effect of increased susceptibility. Thus, in this study, the resins are described as either Gd-loaded or clean, implying an unused Na^+ -form resin (described in Appendix 1.0).

The NMR techniques used in these studies are described in detail in Section 5.1, and the data is available in Appendix 4.0. These experiments made use of magic-angle spinning (MAS) techniques, as well as, the use of two different magnetic fields (3T and 12T) to evaluate the effects of dipolar and susceptibility related interactions. The experiments used in this section are described as follows.

- MAS spectral plots and deconvolution: these experiments were used to identify the various spin pools, and to measure the relative populations, dipolar line widths, and chemical shifts.
- Inversion recovery: these experiments were used to measure the spin-lattice (T_1) relaxation time.
- Carr-Purcell Meiboom-Gill (CPMG): these experiments were used to measure the spin-spin relaxation (T_2) times and spin pool populations.
- Pulsed Gradient Stimulated Echo (PGSTE): these experiments were used to find the diffusion constant for the various spin pools.
- Goldman-Shen Exchange Rate: these experiments were used to directly measure the exchange rate between the plasticizer and bound water pools.

Together, this array of experiments at two different magnetic fields provided deep insight into the microscopic nature of the RF and CF resins. Due to the expansion and contraction of the resins in the presence or absence of water, the resin proved a difficult material to study with standard physical chemistry techniques. With NMR, the resin analysis proved relatively straight forward, and this information can be applied to the evaluating the ultimate performance of these resins.

NMR methods have increased the understanding of the microscopic characteristics of CF and RF phenolic resins. The NMR spectral deconvolution first indicated the presence of three major components in the resin-water system. Further relaxation studies justified this initial assumption and gave effective lifetimes to the three components. Diffusion measurements helped describe the mobility of the three pools and led to a greater understanding of kinetic exchange between the pools. These exchange mechanisms are important in determining the ultimate performance of the ion-exchange resins. The differences in exchange rates could assist in the predicted performance of a resin. For example, the RF resins have a faster exchange rate than the CF resins between the free and plasticizer pools which could lead one to assume that the RF resin has a more ordered structure. This assumption is somewhat justified in that the empirically derived proton exchange capacity for the RF resins is 30% greater than for the CF resins.

The bound water volume is an important parameter extracted from these NMR studies. A bound water volume for these resins has proven difficult to measure using standard techniques. This is due to the gel-like nature of the resin with the water, and the swelling of the resins under saturated conditions. Standard surface area and volumetric techniques normally require the measured media to be in an unsaturated water state or of a known water bearing state. A completely dry resin is not possible without degrading the resin structure, and a partially saturated resin, does not allow the resin to reach its equilibrium state when in use as an ion exchanger. Therefore, for polymeric organic media like these phenolic resins, NMR techniques may be the best method for extracting accurate the bound water volume. In addition, the bound water volume allows for a direct determination of the specific surface area, which is a critical parameter for understanding ion exchange and other surface interactions.

The proton exchange capacity (PEC) is another critical parameter used in determining the effectiveness of ion-exchanging materials. A precise determination of the available functional sites is necessary in determining the theoretical PEC, however this is very difficult to determine with unstructured materials, such as organic resins. Most methods used to determine PEC rely on empirical measurements and assumptions, which could introduce large systematic error into a PEC determination. The NMR techniques used in this study allow for the determination of PEC from interactions at a microscopic level, thus reducing the likelihood of systematic discrepancies in the analysis. Although there may be error in estimating bond distances and functional site

densities, these NMR technique provide a direct evaluation of the theoretical PEC and can be used to place bounds on empirically derived values.

The three-pool model used to describe the microscopic interactions in the CF and RF ion-exchange resin has proven to be a good model. The model assists in the understanding of the exchange dynamics between the three pools, and provides a basis to extract spatial and temporal information from the system. This multi-faceted NMR approach to probing microscopic interactions in porous media holds great promise. These NMR methods provide information about certain types of porous systems that could not otherwise be measured.

2.7. NMR Imaging

The goal of this work is to characterize the physical transport properties of a lanthanide through an ion exchange resin while determining the separation properties of the resin. By coupling the physical transport with the chemical sorption, further insight can be gained into the behavior of the ion exchange resin. NMR imaging provides a powerful, non-destructive, means to extract spatial information from complex systems on a near real-time basis. An important example is fluid flow through granular media. With the use of a chemically reactive NMR contrast agent, the chemical speciation and separation can be traced along the physical flow path in the granular media. In this study, trivalent gadolinium (Gd^{3+}) was selected based on its chemical similarity to typical high-level waste components, ^{241}Am and ^{244}Cm , and it's a useful NMR contrast agent. NMR imaging results of flow experiments show characteristic flow phenomena and resin column loading profiles. A simple idealized flow model was developed to quantify the degree of preferential flow, or fingering, based on two-dimensional NMR images. ICP-AES analysis of the effluent gives resin ion exchange capacities (IECs) and breakthrough curves that can be coupled to the image loading profiles. The use of NMR imaging with the Gd^{3+} tracer leads to a better understanding of the transport and separation abilities of these ion-specific resins and can be useful in quantifying the degree of fingering in heterogeneous systems. NMR imaging provides the only real-time means to visualize metal loading in reactive, heterogeneous flow systems to extract true ion exchange capacity factors. There is no other non-invasive technique that can directly determine the volume of the reactive material exposed to the Gd solution, which is necessary to determine the ion exchange capacity of a heterogeneous flow system. This technique has direct application to other complex flow systems such as environmental transport of contaminants in geological media.

NMR imaging of Gd^{3+} flow is a useful technique to assist in the understanding of physical transport and chemical behavior of trivalent metal ions in a variety of granular media flow systems. It provides the only real-time means to visualize the Gd^{3+} loading onto chemically reactive surfaces which leads to true quantification of the ion exchange capacity factors in flow systems where fingering or other non-linear flow phenomena is encountered. It is only through the use of this NMR imaging tracer technique whereby the actual mass of complexed material can be assessed, based on an evaluation of the area (or volume) of material which has been

occupied by the Gd solution. Without knowing the actual flow area/volume probed by the Gd, it is impossible to determine the capacity of the granular flow system to sorb the Gd^{3+} ions. The NMR tracer technique provides a better understanding of chemical reactivity in heterogeneous flow systems, and this can then lead to a more accurate prediction of the fate of contaminants in more complex flow environments.

This section includes the results of a NMR imaging flow experiment using phenol-formaldehyde (PF) resin. The flow experiment was performed according to the procedures previously described in Sections 8.1, 5.1.2, 4.3 and 4.3. Therefore, only the experiment specific procedures will be described and the results will be presented. The raw data from the ICP-AES analyses is provided in Appendix 5.0, and the ICP-AES procedures are found in Section 5.2. The purpose of this flow experiment was to determine the proton exchange capacity of the PF resin under flow conditions, and to determine the stability of the PF-Gd complex under increasingly acidic conditions and with a competitive ligand. The competitive ligand was 1.0 mM EDTA (ethylenediaminetetraacetic acid, hexadentate).

The PF flow experiment performed in this experiment were design to first determine the flow and sorption characteristics of the resin. This was accomplished using the 2-D NMR sequences coupled with ICP-AES analysis of the effluent to determine the Gd concentrations. From this data, the proton exchange capacity (PEC) of 1.1 meq/g was measured. This value is reasonable based on previous measurements of a similar resin to PF, phenol-formaldehyde hydroxyquinolene (PQF). The experimental PEC for PQF was 1.5 meq/g that is very close to the 1.1 meq/g measured in this experiment.

The flow profile for the PF resin was highly irregular, and showed what appeared to be two parabolic fronts (Figure 8.8). This result could be a result of the packing method used in preparing the sample. There was also visible breakthrough of the Gd solution in the center of the resin pack, which showed up as a steady increase in the effluent Gd concentration. The PF resin during preparation proved the least permeable of all resins tested, and this low permeability could be the reason for sample packing anomalies in the images.

The breakthrough curves showed that resin had not reached full equilibrium loading prior to the stop of the Gd solution. This was exhibited by the steep rise of the Gd concentration but no plateau at the top of the curve equilibrating at the inlet concentration of 0.1 mM Gd. This non-equilibrium condition could have resulted in unequal loading, however this was not readily

apparent in the initial 2- and 3-D images. The second significant feature of the breakthrough curve is the large spike of Gd after the 0.1 M acid flush. This single spike removed approximately 10% of the Gd from the resin with little more Gd removed by subsequent higher acid concentrations. This would imply that there is a weakly bound Gd component, possibly belonging to single (mono-dentate) bonds. Further study could link this to one of the water components identified in the microscopic resin characterization of Section 7.0. A third interesting find in the breakthrough curves is the small spike of Gd eluted after a 20 hour equilibration time with 1.0 M acid. When the 1.0 M flush initially started, very little additional Gd was removed from the resin, but after a 20 hour equilibration time with the resin saturated with 1.0 M acid, a measurable portion of Gd was removed (about 1%). This implies that there are long time kinetics processes involved with sorption and de-sorption. It could also mean there are preferential flow pathways for the flush solution, and diffusive migration is necessary to probe other areas of the resin. These preferential pathways are seen in the 2- and 3-D images. This sorption/de-sorption mechanism needs greater study.

2.8. Conclusions

The conclusions for this work are provided in Section 9.0. Each of the major sections (6.0, 7.0 and 8.0) has its own discussion and conclusion sections, however a summary of the conclusions is presented here. In general, the NMR techniques used in these studies have proven very useful in characterizing the speciation and transport of trivalent actinides.

The NMR flow system developed for the imaging studies proved very successful in mitigating the susceptibility-induced artifacts from air bubbles in the porous media samples. The experimental results show the effectiveness of this deaeration technique at mitigating the unwanted susceptibility effects. The significant reduction and positive control over the effects of air/water susceptibility provides greater confidence in interpreting qualitative assessments of imaging media. The reduction in imaging artifacts may also provide the opportunity to develop quantitative evaluation methods for imaging techniques. NMR is also an effective means to evaluate the degree of deaeration in a sample. Experimental results in Figures 6.2 and 6.3 show how 1-D T_1 mapping of a sample can be used to evaluate the degree of deaeration and the rates at which the various deaeration mechanisms take place. Some limited deaeration time-scales can also be extracted from the 1-D data.

NMR spectroscopy and relaxation methods have increased the understanding of the microscopic characteristics of CF and RF phenolic resins. The NMR spectral deconvolution first indicated the presence of three major components in the resin-water system. Further relaxation studies justified this initial assumption and gave effective lifetimes to the three components. Diffusion measurements helped describe the mobility of the three pools and led to a greater understanding of kinetic exchange between the pools. These exchange mechanisms are important in determining the ultimate performance of the ion-exchange resins. The differences in exchange rates could assist in the predicted performance of a resin. The surface-to-volume and pore volume determinations are two important parameters extracted from these NMR studies. Therefore, for polymeric organic media like phenolic resins, NMR diffusion techniques may be the best method for extracting accurate surface-to-volume ratios and pore volume determinations. The proton exchange capacity (PEC) is another critical parameter used in determining the effectiveness of ion-exchanging materials. A precise determination of the available functional sites is necessary in determining the theoretical PEC, however this is very

difficult to determine with unstructured materials, such as organic resins. The NMR techniques used in this study allow for the determination of PEC from interactions at a microscopic level, thus reducing the likelihood of systematic discrepancies in the analysis. The three-pool model used to describe the microscopic interactions in the CF and RF ion-exchange resin has proven to be a good model. The model assists in the understanding of the exchange dynamics between the three pools, and provides a basis to extract spatial and temporal information from the system. This multi-faceted NMR approach to probing microscopic interactions in porous media holds great promise. These NMR spectroscopic and relaxation methods provide information about certain types of porous systems that could not otherwise be measured.

NMR imaging of Gd^{3+} flow is a useful technique to assist in the understanding of physical transport and chemical behavior of trivalent metal ions in a variety of granular media flow systems. It provides the only real-time means to visualize the Gd^{3+} loading onto chemically reactive surfaces which leads to true quantification of the ion exchange capacity factors in flow systems where fingering or other non-linear flow phenomena is encountered. It is only through the use of this NMR imaging tracer technique whereby the actual mass of complexed material can be assessed, based on an evaluation of the area (or volume) of material which has been occupied by the Gd solution. Without knowing the actual flow area/volume probed by the Gd, it is impossible to determine the capacity of the granular flow system to sorb the Gd^{3+} ions. The NMR tracer technique provides a better understanding of chemical reactivity in heterogeneous flow systems, and this can then lead to a more accurate prediction of the fate of contaminants in more complex flow environments. The NMR imaging techniques with the Gd tracer proved especially helpful in coupling the transport properties of the fluid with chemical reactivity data. These tracer studies allowed for the development of a model to determine the degree of channeling or non-linear (fingering) flow. This model can then be applied for prediction of increased transport rates and a more accurate determination of exchange capacities of the flow media. The distribution coefficients (K_d) used in current reactive transport models rely heavily on bulk flow parameters and exchange capacities of the flow media, and this NMR tracer technique can be used to help determine these parameters with greater certainty.

References for Thesis Summary

- ¹ F. Bloch, et.al., Phys. Rev. 69, 127, 1946.
- ² E.M. Purcell, et.al., Phys. Rev., 69, 37-38, 1946.
- ³ A.W. Adamson, Physical Chemistry of Surfaces, John Wiley and Sons, pp 418-9, 1976.
- ⁴ K.R. Czerwinski, M. Draye, J. Foos, and A. Guy: Ion Selective Resins: Development and Applications for Nuclear Waste Management. MRS Scientific Basis for Nuclear Waste Management XX. In press.
- ⁵ M. Draye, K.R. Czerwinski, A. Favre-Reguillon, J. Foos, A. Guy, and M. Lemaire, Sep. Sci. Tech., 35(8), pp. 1117-1132, 2000.
- ⁶ N.Dumont, A. Favre-Reguillon, B. Dunjic, and M. Lemaire, Sep. Sci. Tech., 31(7), pp. 1001-1010, 1996.
- ⁷ M. Draye, A. Favre-Reguillon, J. Foos, A. Guy, and K.R. Czerwinski, Proceedings of Waste Management '98 Conference, Tucson AZ, 1998.
- ⁸ E.R. Andrew, A. Bradbury, and R.G. Eades, Nature, 182, 1659, 1958.
- ⁹ Bruker Instruments, Inc.
- ¹⁰ Matlab by The Math Works, Inc., version 5.3.1.29215a(R11.1), 28 Sep 99.
- ¹¹ P.T. Callaghan, "Principles of Nuclear Magnetic Resonance Microscopy," Clarendon Press, Oxford (1991).
- ¹² B. Manz, P. Alexander, and L.F. Gladden, Correlations Between Dispersion and Structure in Porous Media Probed by Nuclear Magnetic Resonance, Physics of Fluids, 11 No. 2, 256-267 (February 1999).
- ¹³ W.E. Kenyon, Nucl. Geophys. 6, 153-71, 1992.
- ¹⁴ J. Pauli, G. Scheying, C. Mugge, A. Zschunke, and P. Lorentz, Determination of the Pore Widths of Highly Porous Materials with NMR Microscopy, Fresenius J Anal Chem, 357:508-513 (1997).
- ¹⁵ M.D. Hurlimann, K.G. Helmer, L.L. Latour, and C.H. Sotak, Restricted Diffusion in Sedimentary Rocks. Determination of Surface-to-Volume Ratio and Surface Relaxivity, J. Mag. Reson., Ser. A 111, 169 (1994).
- ¹⁶ R. Kimmich, NMR-Tomography, Diffusometry, Relaxometry, Springer, 1997.

[THIS PAGE INTENTIONALLY LEFT BLANK]

3. INTRODUCTION

The environmental behavior of actinides is not fully understood, and thus it is not possible to accurately predict their release and transport rates from current or proposed radioactive waste sites. The insufficient knowledge base of the actinides is due to the lack of natural analogs and thermodynamic data (particularly for transuranics), the limited duration of industrial use and study of these materials, and resultant complexity of modeling such systems.

In understanding environmental behavior, it is crucial to first determine the chemical and physical properties of the actinide at the source and under aqueous conditions, since groundwater movement is the primary release and transport route at most waste sites. Once the actinide's chemical and physical forms, or species, are known, we are able to determine the mobility of the actinide, which allows for prediction of the release and transport rates. Thus in order to understand the behavior of actinides in the environment, experimental tools and techniques need to be developed that provide a deeper understanding of actinide speciation and transport. One powerful tool to investigate the mechanisms that control speciation and transport is nuclear magnetic resonance (NMR) imaging. NMR imaging with appropriate experimental techniques can be used as a probe to provide temporal and spatial information of actinide speciation and transport in simulated aquatic environments. Information from the NMR studies will lead to a better understanding of actinide behavior in the environment, and in turn, it will lead to improved prediction of the fate of these contaminants in the biosphere and geosphere.

There are presently a large number of radioactive waste sites in the United States and throughout the world containing hazardous quantities of actinides and associated radioactive materials. Many of these sites either are in the process of environmental remediation or will be remediated at some time in the future in order to mitigate the public radiation dose. The actinide materials residing at these sites will either be left in place using some type of containment or encapsulation method, or they will be removed, packaged, transported, and disposed of at some other more suitable disposal site. In order to make informed decisions on how best to control the public radiation dose from these sites, it is critical to understand the chemical and physical processes that control the behavior of the actinides in their present and future environments. Thus, knowledge of the environmental behavior of actinides is critical to controlling the public radiation dose from actinide-containing radioactive waste sites.

This leads to the question of how best to understand the chemical and physical processes controlling the behavior of actinides in the environment. A typical approach to understand the behavior of metals in the environment includes the study of naturally occurring sources and a determination of the metal's chemical and physical properties, or species. Based on the environmental conditions (i.e. pH, alkalinity, temperature, pressure, ionic strength, REDOX potential, etc.) and the metal speciation under those conditions, a set of equilibrium constants for each species can be determined based only on thermodynamic properties. By verifying the thermodynamic data with experimental data from naturally occurring sites, a database of equilibrium constants can be assembled and applied to the speciation of that metal under any environmental conditions. However, this natural analog approach is highly restricted in the case of actinides, since there are very few naturally occurring sources of actinides with atomic numbers greater than uranium (atomic number 92). In addition, the industrial processing of actinides, mainly from commercial nuclear power and weapons production, is a relatively recent undertaking, and there is very little practical experience with the long-term performance of these materials in the environment. It is only recently that the United States and other actinide-producing countries have been motivated to gain a deeper understanding into the environmental behavior of the actinides. Therefore, to better understand the behavior of actinides in the environment, the limited historical record must be supplemented with empirical data obtained in the laboratory.

There are many traditional experimental methods for determining mass balance and equilibrium conditions of simulated environmental systems. These experimental methods include column and batch testing or acid-base titration, but it is often very difficult to interpret these results without some type of natural analog from which to reference. In addition, these traditional experimental techniques must often use homogenized media and idealized conditions to limited the degrees of freedom. In contrast, the proposed NMR imaging technique can be applied to heterogeneous flow systems using a wide range of flow conditions, and this will provide needed insight into the speciation of actinides under controlled conditions. The NMR technique is also inherently non-invasive and provides a means to investigate transport phenomena under precise environmental flow conditions with actual environmental media. The NMR tracer technique will contribute to a deeper understanding of actinide behavior in the natural environment.

3.1. Project Overview

This project overview summarizes the efforts completed in fulfillment of a doctoral thesis. Included in the overview is a description of the problem addressed in the thesis statement, research goals and objectives, and their significance, and a detailed description of each task with a timeline showing their completion dates.

3.1.1. Problem Description:

The environmental behavior of actinides is not sufficiently understood to accurately predict their release and transport rates from current or proposed radioactive waste sites. This insufficient knowledge is due to the lack natural analogs and empirical data (particularly for transuranics), the limited duration of industrial use and study, and resultant complexity of modeling such systems. In understanding environmental behavior, it is crucial to first determine the chemical and physical properties of the actinide at the source and under aqueous conditions, since groundwater movement is the primary release and transport route at most waste sites. Once we know the actinide's chemical and physical forms, or species, in an aquatic system, the mobility of the actinide can be determined, and this allows for accurate prediction of the release and transport rates. Thus, in order to understand the behavior of actinides in the environment, the development of experimental tools and techniques is need to provide a deeper understanding of actinide speciation and transport. One powerful tool to investigate the mechanisms that control speciation and transport is nuclear magnetic resonance (NMR) imaging. NMR imaging coupled with an appropriate lanthanide analog provides a method to extract temporal and spatial information of actinide speciation and transport in simulated aquatic environments. This information will lead to a better understanding of the behavior of actinides in the environment, which in turn leads to improved prediction of the fate of these contaminants in the biosphere.

3.1.2. Research Goals and Objectives

The primary goal of this work was to characterize the physical transport properties of a lanthanide tracer through an ion exchange resin while determining the separation properties of

the resin. By coupling the physical transport with the chemical sorption, further insight can be gained into the behavior of the ion exchange resin. NMR imaging provides a powerful, non-destructive, means to extract spatial information from complex systems on a near real-time basis. An important example is fluid flow through granular media. With the use of a chemically reactive NMR contrast agent, the chemical speciation and separation can be traced along the physical flow path in the granular media. In this study, trivalent gadolinium (Gd^{3+}) was selected based on its chemical similarity to typical high-level waste components, ^{241}Am and ^{244}Cm , and it's a useful NMR contrast agent. NMR imaging results of flow experiments show characteristic flow phenomena and resin column loading profiles. A simple idealized flow model was developed to quantify the degree of preferential flow, or fingering, based on two-dimensional NMR images. ICP-AES analysis of the effluent gives resin ion exchange capacities (IECs) and breakthrough curves that can be coupled to the image loading profiles. The use of NMR imaging with the Gd^{3+} tracer leads to a better understanding of the transport and separation abilities of these ion-specific resins and can be useful in quantifying the degree of fingering in heterogeneous systems. NMR imaging provides the only real-time means to visualize metal loading in reactive, heterogeneous flow systems to extract true ion exchange capacity factors. There are no other non-invasive techniques that can directly determine the volume of the reactive material exposed to the Gd solution, which is necessary to determine the ion exchange capacity of a heterogeneous flow system. This technique has direct application to other complex flow systems such as environmental transport of contaminants in geological media.

A secondary goal of this work was to use NMR spectroscopic techniques to understand the microscopic behavior of the ion-specific resins. The resorcinol- and catechol-formaldehyde (RF and CF) resins exhibited interesting behavior during various NMR spectroscopic experiments. The resins appeared to interact with the surrounding water, in a saturated system, to isolate certain percentages of water into various pools. The pools were assumed associate with a bound water fraction, and an interstitial or free water fraction. A series of NMR spectroscopic and relaxation experiments were run to investigate the characteristics of the resin-water interactions. The results of the techniques were used to extract exchange rates, diffusion constants, and the specific surface area of the resins. From this data, a theoretical upper bound for the proton exchange capacity was determined.

3.1.3. Research Task List

This research involves the use of various NMR techniques to investigate the macroscopic and microscopic behavior of ion exchange resins. The technique uses NMR imaging as a non-invasive probe to visualize spatial interactions. With the NMR probe, a relationship between radioactive contaminants and the environmental transport medium can be developed. This non-invasive characterization allows for the analysis of remediation techniques for containment and/or mitigation of environmental contamination. The development of these innovative techniques can be applied to assessing the behavior of radioactive waste in the environment. A listing of the research tasks used in development of the NMR tracer technique is provided below.

- Task 1 - Flow System Development: A NMR flow imaging system for investigating various radioactive analogs and environmental media was developed. This flow system is capable of ensuring air-bubble free samples to reduce the NMR susceptibility effects inherent in granular flow systems. The flow system employs the use of fluid deaeration followed by over-pressurization to accomplish this requirement. In addition, the flow system provides is capable of providing plug-type flow of a variety of fluids through complex granular samples with a high degree of reproducibility. A technical paper was prepared on the critical features and performance of the system.
- Task 2 – Homogeneous Sample Studies and NMR Tracer Technique Validation: The first approach in developing the NMR tracer technique was to validate the method using homogeneous media samples and known concentrations of a contrast fluid. The initial research activities focused on trivalent actinides ions (i.e. $^{241}\text{Am}^{3+}$, $^{244}\text{Cm}^{3+}$) using the chemical analog gadolinium (Gd^{3+}) as a NMR contrast fluid. The Gd^{3+} ion has the combined advantage of being chemically quite similar to ^{241}Am and ^{244}Cm and possessing the physical properties as an excellent NMR contrast agent. These combined properties of the Gd^{3+} ion make it an excellent NMR tracer to simulate and model environmental speciation and transport. The NMR tracer technique was first validated using homogeneous media (i.e. sand) and a Gd^{3+} solution. This validation compared the imaging data with inductively coupled plasma atomic emission spectroscopy (ICP-AES) analysis of the effluent to measure the sorption/desorption rates of the sand. The intensity of the NMR signal was then correlated to the amount of gadolinium sorbed to the sample media. The assumption was that

very little of the Gd^{3+} will remain sorbed in the sand sample. Next, a media with a higher and well-characterized proton exchange capacity (PEC) was investigated, and the imaging results was correlated with the effluent analysis data. Through the use this homogeneous media study, the NMR imaging data was correlated with sorption/desorption rates, and qualitative data was obtained on the speciation and flow profiles in the homogeneous media. A technical paper was prepared documenting the procedures used and the effectiveness of this approach to quantify speciation of the Gd in a media of known PEC. The paper shows the ability of the NMR tracer method to quantify non-linear transport phenomena (i.e. fingering) and couples this information to extract more accurate ion exchange capacities from non-uniform flow environments.

- Task 3 – Competitive Exchange Studies of Ion Exchange Resins: Once the homogeneous media studies and data analysis techniques were sufficiently documented and validated, the next studies focused on more advanced imaging studies of the resin samples. These studies served to further characterize the speciation and transport of the trivalent actinide analog under various reactive environments. Similar to the homogeneous media experiments, these studies characterized the speciation in heterogeneous media and correlated that data with effluent ICP-AES spectroscopy data. The heterogeneous flow studies used ion-specific resins to assess Gd^{3+} complexation and complex stability within the resin matrix. Additional research activities performed flow experiments with three different resin types and fluids of varying pH to characterize speciation and transport parameters from a variety of flow conditions. The data from this task is presented in this thesis showing the effectiveness of the NMR tracer technique to extract valuable speciation and transport parameters from varying flow environments that can then be applied to actual radioactive waste site conditions.
- Task 4 – Microscopic Characterization of the Resin Using NMR Techniques: These studies involved NMR and traditional laboratory techniques to evaluate the microscopic characteristics of the ion-specific resins. The NMR techniques included the use of two different magnetic field environments (3 and 12T) to separate the field dependent and independent interactions within the resin matrix. Magic Angle Spinning (MAS) was used on the 12T magnet to determine separate out the dipolar interactions to extract susceptibility information. Relaxation rate information was obtained using inversion recovery, progressive

saturation, and Carr-Purcell Mielboom-Gill sequences. Goldman-Shen experiments were used to extract correlation times and exchange rates between the various spin pools, and Pulsed-Gradient Stimulated Echo (PGSTE) experiments were run to determine diffusion rates. Using the NMR data and coupling this with surface area analysis and proton exchange capacities, the microscopic resin characteristics can be better understood with respect to chemical exchange on the functional sites and reaction kinetic information.

- Task 5 – Coupling NMR Data with Existing Analytical Techniques and Models to Develop an Integrated Approach to Further the Study of Speciation and Transport in Complex Systems: This task included an integrated approach to using the NMR tracer technique to increase the understanding of environmental transport and speciation. A description of what the NMR tracer technique brings to the study of environmental transport is described. Also described is how this information is coupled with chemical analysis to better understand the fate of the contaminants in environmental flow systems. The data gained from these studies provides necessary information to improve site-specific risk assessments and can ultimately be used to develop and employ much more effective waste remediation technologies. The results of these studies can be used to test the validity of geochemical models to assess the transport and speciation of trivalent actinides leaching from waste sites or future repositories into the environment.

3.2. Thesis Overview

This thesis contains the work undertaken by Daniel F. Caputo in fulfillment of a Doctor of Philosophy degree in Nuclear Engineering. The thesis topic is the use of NMR tracer techniques in characterizing actinide speciation and physical transport through porous media. The research involved in this thesis included NMR imaging and spectroscopic techniques, and standard chemical analysis techniques including ICP-AES and BET surface area analysis. In summary, NMR tracer techniques have proven useful in evaluating degrees of preferential flow and using this data to extract true ion exchange capacities in heterogeneous media. The use of NMR spectroscopy has proven useful in understanding the microscopic characteristics of ion-exchange resin, and this information can be applied to the evaluating the performance of resin in separating actinides and lanthanides from radioactive waste streams.

The thesis is broken down into 9 sections. Each section is listed below with a brief description of its contents.

- Section one is the thesis abstract with a short overview of the motivations and key findings from the thesis research.
- Section two is the thesis summary with a more detailed description of the main research activities, the results of those activities, and conclusions based on those findings.
- Section three is the introduction describing the thesis project from a performance standpoint, an overview of the thesis in terms of the document layout, and a justification for the importance of chemical speciation in radioactive waste management.
- Section four is the background section with information on the performance of radioactive waste disposal in the U.S., a description of actinide chemistry, an overview of NMR, and a definition of environmental transport as used in this document.
- Section five is a description of the experimental methods used, which include NMR spectroscopy, imaging, and ICP-AES analysis.
- Section six is a description of the NMR flow system used in performing the NMR imaging studies.
- Section seven contains the NMR spectroscopic experiments and results used in performing the microscopic evaluation of the resins.

- Section eight contains a description of the NMR imaging experiments and results.
- Section nine contains the thesis conclusions and future work related to the thesis research.

[THIS PAGE INTENTIONALLY LEFT BLANK]

4. BACKGROUND

The background for this work begins with an overview of radioactive waste issues in the United States (U.S.). This overview is not meant to be fully descriptive, however it gives the reader an understanding of how the U.S. regulatory agencies approach the management of radioactive waste. In addition, a qualitative performance analysis of the major commercial radioactive waste disposal sites shows the effect of those regulations and the problems created by a lack of appreciation of chemical speciation. The second background area describes actinide chemistry in terms of their natural analogs, lanthanide analogs, and the environmental behavior. This type of presentation for actinide chemistry allows the reader to understand the various approaches taken in understanding environmental actinide chemistry. It also shows the reader the difficulties and lack of information concerning the behavior of actinides in environmental systems. The third background section provides a general description of nuclear magnetic resonance (NMR) and its applications. An overview of experimental techniques, paramagnetism, and tracers is also provided. The final area presented as background is on ion-specific resins. The resins are used throughout the experimental studies, and it is necessary for the reader to understand some physical structure and chemical performance of the resins.

4.1. Radioactive Waste – A Brief U.S. Historical Perspective

Radioactive waste is a difficult subject to discuss and an even more difficult subject to define. The term radiation and radioactive waste stirs a variety of emotions in most people and their perceptions of what radioactive waste is and how it's been handle are greatly divergent. These perceptions are based on a relatively short history of the practice of waste disposal, and an even shorter history of the investigation of radioactive waste sites. With this in mind, the historical overview of radioactive waste in this document will be a performance-based perspective with emphasis on the root causes of any successes or failures in waste disposal practices. A discussion of the historical successes and failures of radioactive waste will lead towards a better understanding of the development of the industry and may provide more insight into what the future holds. Therefore, this section will briefly discuss a common approach to describing the radioactive waste from a time-based perspective, and then focus primarily on radioactive waste management practices and their performance from a performance-based perspective. The intent of this approach is to highlight some of the technical areas that have been and continue to be overlooked in the siting and licensing of waste disposal sites. A performance-based perspective will also be more likely to identify root causes for failure of some disposal practices. However, any start to a discussion of U.S. radioactive waste issue should begin with a description of radioactive waste.

4.1.1. Classification and Characteristics of Radioactive Waste

In general, radioactive waste can be described as solid, liquid, and gaseous materials from nuclear activities that are inherently radioactive or have been irradiated and have been declared waste products. In the U.S., waste is generally classified as high-level, low-level, or intermediate level. The primary regulatory authority for radioactive waste is the U.S. Nuclear Regulatory Commission (NRC), however the U.S. Environmental Protection Agency (EPA) has a role in setting public exposure criteria. Both the NRC and EPA have definitions for radioactive waste, and they both use the source of the waste as the criteria for categorization. This is contrary to most waste classification schemes, where the waste is defined in terms of its hazardous

constituents or its risk to the biosphere. The EPA generally defines five categories of radioactive waste [¹]:

- spent nuclear fuel from nuclear reactors and high-level waste from the reprocessing of spent nuclear fuel
- transuranic waste mainly from defense programs
- uranium mill tailings from the mining and milling of uranium ore
- low-level waste
- naturally-occurring and accelerator-produced radioactive materials.

The NRC generally classifies high-level waste (HLW) as having radiation content in the hundreds of thousands of curies per gallon or foot [²]. HLW consists of spent reactor fuel, liquid wastes from the fuel processing operations (front and back end), and solids that have formed in spent fuel processing. HLW is generated primarily from defense-related activities from the U.S. Department of Energy's (DOE) nuclear weapons program. These defense waste products are primarily generated from reprocessing operations during the extraction of weapons-grade materials. Low-level waste (LLW) is generally described as having radioactive content in the 1 microcurie per gallon or foot range [¹]. In 10 CFR Part 61, definitions [²] the NRC goes on to describe LLW as, "... those low-level radioactive wastes containing source, special nuclear, or byproduct material that are acceptable for disposal in a land disposal facility. For the purposes of this definition, low-level waste has the same meaning as in the Low-Level Waste Policy Act, that is, radioactive waste not classified as high-level radioactive waste, transuranic waste, spent nuclear fuel, or byproduct material as defined in section 11e.(2) of the Atomic Energy Act (uranium or thorium tailings and waste)." Intermediate level wastes fall between HLW and LLW descriptions, and this type of waste is often loosely classified as transuranic, or TRU, waste. TRU waste is usually described as defense waste material that is contaminated during reprocessing or fabrication activities.

Radioactive waste is categorized according to its origin and not necessarily according to its level of radioactivity. For example, some low-level waste has the same level of radioactivity as some high-level waste. This type of approach can cause some conflict when designing a waste disposal facility that includes both long and short lived radionuclides. A definition of radioactive waste can also be described by the characteristics or classifications of waste forms. This type of presentation can be very effective in defining the radioactive waste picture, however

it is often clouded by inconsistencies based on out-dated regulatory classifications. The NRC provides a classification and characterization scheme for wastes that are destined for near-surface burial, and this scheme is described in the following sections.

4.1.1.1. Waste Classification

The classification and regulatory characteristics of radioactive waste in the U.S. is set by the NRC in Title 10 of the U.S. Code of Federal Regulations Part 61 [3]. The NRC classification scheme defines the type of waste that can be disposed of in near-surface disposal facilities, and defines those waste types as Class A, B, and C. The waste class is based on concentration and half-life of the radionuclides in the waste form with the long-lived, high concentration wastes regulated more stringently. The NRC also considers in its classification scheme the concentration of shorter-lived radionuclides for which requirements on institutional controls, waste form, and disposal methods are effective.

The NRC classification lists the long-lived radionuclides in

Table 4.1 and the short-lived nuclides in Table 4.2. For the long-lived radionuclides in

Table 4.1, the Class A wastes are those that are less than 0.1 times the listed concentration, and Class C wastes are those greater than Class A but less than the listed concentration

Table 4.1: NRC classification criteria for long-lived radionuclides

Radionuclide	Concentration curies per cubic meter
C-14	8
C-14 in activated metal	80
Ni-59 in activated metal	220
Nb-94 in activated metal	0.2
Tc-99	3
I-129	0.08
Alpha emitting transuranic nuclides with half-life greater than 5 years	¹ 100 nCi/g
Pu-241	¹ 3,500 nCi/g
Cm-242	¹ 20,000 nCi/g

¹Units are nanocuries per gram.

The classification of short-lived radionuclides is established in Table 4.2. For the short-lived radionuclides, the waste is Class A if it does not exceed the value in Column 1. A typical Class A waste might include check sources used for performance checks of radiation detection instruments. If the concentration exceeds the value in Column 1, but does not exceed the value in Column 2, the waste is Class B. A typical Class B waste might include contaminated or slightly activated components from a nuclear power plant. If the concentration exceeds the value in Column 2, but does not exceed the value in Column 3, the waste is Class C. A typical Class C waste might include a used calibration source from a gamma irradiation facility. If the concentration exceeds the value in Column 3, the waste is not generally acceptable for near-surface disposal. Radioactive waste that does not contain any of the radionuclides listed in Table 4.1 or 4.2 is considered Class A. For wastes containing mixtures of the nuclides listed in Table 4.1 or 4.2, the total concentration shall be determined by the sum of fractions rule described in 10 CFR 61.55.

Table 4.2: NRC classification criteria for short-lived radionuclides

Radionuclide	Concentration, curies per cubic meter		
	Col. 1	Col. 2	Col. 3
Total of all nuclides with less than 5 year half-life	700	(¹)	(¹)
H-3	40	(¹)	(¹)
Co-60	700	(¹)	(¹)
Ni-63	3.5	70	700
Ni-63 in activated metal	35	700	7000
Sr-90	0.04	150	7000
Cs-137	1	44	4600

¹ There are no limits established for these radionuclides in Class B or C wastes. Practical considerations such as the effects of external radiation and internal heat generation on transportation, handling, and disposal will limit the concentrations for these wastes. These wastes shall be Class B unless the concentrations of other nuclides in Table 2 determine the waste to the Class C independent of these nuclides.

4.1.1.2. Waste Characteristics

Once the waste is classified, it must exhibit certain physical characteristics in order for the NRC to allow its disposal in shallow land burial. All classes of waste must exhibit the following minimum requirements. These requirements are intended to facilitate handling at the disposal site and provide protection of health and safety of personnel at the disposal site [⁴].

- Waste must not be packaged for disposal in cardboard or fiberboard boxes.
- Liquid waste must be solidified or packaged in sufficient absorbent material to absorb twice the volume of the liquid.
- Solid waste containing liquid shall contain as little free standing and non-corrosive liquid as is reasonably achievable, but in no case shall the liquid exceed 1% of the volume.
- Waste must not be readily capable of detonation or of explosive decomposition or reaction at normal pressures and temperatures, or of explosive reaction with water.
- Waste must not contain, or be capable of generating, quantities of toxic gases, vapors, or fumes harmful to persons transporting, handling, or disposing of the waste. This does not apply to radioactive gaseous waste packaged in accordance with paragraph (a)(7) of this section.

- Waste must not be pyrophoric. Pyrophoric materials contained in waste shall be treated, prepared, and packaged to be nonflammable.
- Waste in a gaseous form must be packaged at a pressure that does not exceed 1.5 atmospheres at 20°C. Total activity must not exceed 100 curies per container.
- Waste containing hazardous, biological, pathogenic, or infectious material must be treated to reduce to the maximum extent practicable the potential hazard from the non-radiological materials.

The NRC imposes additional requirements to provide for the stability of the waste form in the burial site. Stability is intended to ensure that the waste does not structurally degrade and affect overall stability of the site through slumping, collapse or other failure of the disposal unit and thereby lead to water infiltration. Stability is also a factor in limiting exposure to an inadvertent intruder, since it provides a recognizable and non-dispersible waste [5].

- Waste must have structural stability. A structurally stable waste form will generally maintain its physical dimensions and its form, under the expected disposal conditions such as weight of overburden and compaction equipment, the presence of moisture, and microbial activity, and internal factors such as radiation effects and chemical changes. Structural stability can be provided by the waste form itself, processing the waste to a stable form, or placing the waste in a disposal container or structure that provides stability after disposal.
- Notwithstanding the provisions in §61.56(a) (2) and (3), liquid wastes, or wastes containing liquid, must be converted into a form that contains as little free standing and non-corrosive liquid as is reasonably achievable, but in no case shall the liquid exceed 1% of the volume of the waste when the waste is in a disposal container designed to ensure stability, or 0.5% of the volume of the waste for waste processed to a stable form.
- Void spaces within the waste and between the waste and its package must be reduced to the extent practicable.

The NRC waste classification and characterization scheme is outdated and does not provide for adequate treatment of the various types of radioactive waste. The NRC approach does not take into account the effect of the waste form on the near-field chemistry, and does not segregate radionuclides based on their potential to migrate into the far-field environment. The NRC bases the classification criterion on the premise that the potential hazard from all long-lived

radionuclides is greater than shorter-lived nuclides due to their longer presence in the environment. Although this is normally a fair assumption, the NRC gives no further rationale for this regulatory basis, and leaves no room for a risk-based classification approach. The NRC's waste characterization is primarily concerned with limiting radiation exposure to the burial site workers and to maintaining the structural integrity of the burial site for hydrological purposes. The NRC waste form requirements do not imply or mandate consideration for the chemical form of the waste, which is an important consideration in limiting migration of the radioactive waste. Although the NRC waste classification and characterization scheme takes into account total activity and half-life of the waste constituents, it does not account for the long-term behavior of the waste in a geological setting. This waste classification scheme is outdated and is one of the root causes of problems occurring at current and possibly future waste disposal sites.

According to a EPA report on radioactive waste, it's stated that new LLW waste disposal facilities must be designed to avoid two kinds of failures: those caused by long-term processes such as subsidence and those caused by more unpredictable events such as human intrusion (either intentional or unintentional) and natural disaster [6]. Again, the U.S. regulatory agencies are focused on the structural integrity of the waste sites. Although waste site integrity is important from a hydrological standpoint, it is not the only factor governing off-site migration. The waste packages and site liner systems can never contain all of the radioactive materials from off-site migration. The focus of waste site management should be in limiting the waste migration to a point where the migration rate to the nearest critical exposure group is slower than the longest decay rate of the critical radionuclide (within regulatory limits). This type of analysis will shift the focus from containment to an understanding of the near and far-field geochemical interactions. Once the chemical speciation is understood, better decisions can be made as to the proper types of waste forms and packaging that are most compatible with the site's geochemistry.

4.1.2. Radioactive Waste from Time-Based Perspective

A description of the history of radioactive waste is often started with the beginning of the modern nuclear age, often defined as the start of the Manhattan Project at the University of Chicago. It is at this point where large fluxes of neutrons became readily available and

subsequently large quantities of activation and fission products were formed. From this so-called nuclear fuel cycle, natural fissionable radioactive materials were extracted, separated, converted, enriched, and placed in nuclear reactors where large quantities of high and low level radioactive wastes are generated. There are, of course, other sources of radioactive waste, but by volume and activity, the largest source of radioactive waste is from the fissioning process in nuclear reactors [7]. Although a time-based historical perspective is often an easy way to present the topic of radioactive waste, this method of presentation does not provide much insight into the performance of waste disposal practices. Therefore, the history of radioactive waste management in the U.S. will not be described in terms of event timelines and/or by their characteristics or classification, but rather through a performance-based approach of U.S. radioactive waste handling and disposal activities.

4.1.3. Radioactive Waste from a Performance-Based Perspective

The performance based historical perspective of radioactive waste defines radioactive waste management in terms of the successes and failures, and in the process of this description, a concept of a radioactive material cycle will be defined. Unlike the current "fuel cycle" definition, often referred to in nuclear fuel texts and documents, the radioactive material cycle is a true accounting of all radioactive material in and out of a system (i.e. fission reactor). The radioactive material cycle, proposed in this context, refers to a true closed-ended cycle with no loss of radioactive material as it progresses through the cycle. This radioactive material cycle concept is based on an energy balance, whereby all radiation emitted by a radioactive material or imparted to a fissile or fissionable material is accounted for. This implies a true "cradle-to-grave" approach whereby all radioactive materials whether waste or useful products are accounted for during every point in its handling. This cycle starts with an accurate accounting of all radioactive waste constituents with isotopic makeup, total isotopic activity, and chemical form. Then at each point in the handling process, the material inventory is updated and any changes accounted for. In the end, the entire material cycle will close with the fate of the radioactive material either transforming into another radioactive or non-radioactive species, or cycling into the geosphere as the material disperses through natural processes. This cycle will be discussed further in terms of its benefits in comparison with the once-through radioactive material

picture. The performance-based analysis will begin with a description and performance of the U.S. commercial disposal sites and a few DOE sites

4.1.4. Radioactive Waste Disposal Sites

In presenting the performance of radioactive waste in the U.S., each of the major commercial radioactive waste disposal sites will be addressed. The commercial waste sites are listed in Table 4.3 with a description of the site and current status. The performance assessment describes each waste site in terms of their projected performance, the actual performance, and the reasons for deviation from the engineered performance.

Table 4.3: Listing of U.S. commercial radioactive waste disposal sites

Disposal Site	Licensed Area (ha)	Volume of Waste Disposal (m ³)	Year Opened	Current Status	Reason for Closure
Envirocare, UT	14	ongoing	1988	operating	-
Barnwell, SC	121	488,700	1971	operating	-
Richland, WA	40	220,600	1965	operating	-
Beatty, NV	32	96,300	1962	closed 1992	Various technical, social, and political - off-site migration
Sheffield, IL	8	90,500	1967	closed 1978	filled to capacity, some limited off-site migration
Maxey Flats, KY	102	135,100	1963	closed 1978	off-site migration
West Valley, NY	9	66,800	1963	closed 1975	off-site migration

- Envirocare, Utah

The Envirocare site is a limited use low-level waste site. The site is licensed by the State of Utah and the NRC to accept primarily Class A wastes and naturally occurring waste materials. The site is located in a remote area of Utah in an arid region. The waste is placed in shallow trenches that are lined and covered with a barrier system. There is a group of radionuclides, identified as “mobile”, that are placed toward the center of the disposal site. A detailed waste characterization is required prior to shipment to the site. This characterization is required to

ensure compliance with the licenses and to reduce exposure to workers at the site. The site continues to operate and a license request to accept Class B and C waste is currently pending.

- Barnwell, South Carolina

The Barnwell site is licensed by the State of South Carolina under an U.S. Nuclear Regulatory Commission (NRC) agreement state arrangement to operate as a low-level waste facility. The state license specifically allows for the possession and disposal of source and by-product material with a separate NRC license allowing for the possession and disposal of special nuclear material. The Barnwell site was originally licensed as an above ground storage facility, but the licenses was amended in 1971 to allow for shallow land burial of low-level radioactive waste. The waste is placed in large trenches that are excavated from sandy soils that dominate the geology in the area. Compacted clay is used in the trenches to reduce lateral water infiltration and care is taken to reduce void space and water infiltration. A study by the U.S. Geological Survey (USGS) indicated that migration of radioactive material has migrated as much as 3 m from some of the older trenches [⁸]. The Barnwell site is currently operating and is accepting all forms of LLW from everywhere in the U.S. except North Carolina.

- Richland, Washington

The Richland site is licensed to possess and dispose of source and by-product material by the State of Washington. Some special nuclear material and transuranic waste was buried at the site prior to 1979. Most of the waste is disposed of in shallow trenches with an overburden of the previously excavated soil and cobblestones to prevent erosion/intrusion. Some high radiation exposure rate packages were places in caissons lined with steel and capped with concrete, and an evaporation pond was used for a short period. The Richland site is very arid and receives annual precipitation of approximately 6.3 in. There has been no detectable migration of radioactive materials from any of the waste trenches reported by the DOE, however an independent review article indicates some limited migration [⁹]. The Richland site continues to operate but only accepts waste from the those states in the Northwest and Rocky Mountain Compacts, as require by the Low Level Waste Policy Act of 1980.

- Beatty, Nevada

The Beatty waste site is located in Nye County, NV in the Amargosa Desert approximately 105 miles northwest of Las Vegas, Nevada. The site opened in September 1962 and received radioactive waste for burial until December 31, 1992. The Beatty low-level radioactive waste (LLW) disposal facility was the first commercially operated radioactive waste disposal facility, and it was originally licensed by the U.S. Atomic Energy Commission (predecessor to the US Nuclear Regulatory Commission). The State of Nevada gained licensing authority for regulation of this site in 1972. The Beatty site was closed due to various technical and political reasons. There was pressure by the state to close the site due to shipping violations and perceived problems with site maintenance. The U.S Geological Survey (USGS) reported in 1997 that some tritium contamination was found during off-site water testing, although the source of the contamination is inconclusive [¹⁰]. The site continues to operate as a hazardous waste facility, but no longer accepts radioactive waste.

- Sheffield, Illinois

The Sheffield site operated for 1967 to 1978. The State of Illinois originally granted a lease for the site and licensed the operators for possession and disposal of naturally occurring and accelerator-produced radioactive materials (NORM/NARM). The NRC licensed the operator for possession and disposal of by-product, source, and special nuclear materials. The site is operated as a shallow burial low-level waste site with 21 separate waste trenches. Each trench is capped with a clay layer and seeded to prevent erosion. In 1976, the USGS initiated a detailed study to correct some deficiencies in the hydrological cycle for the site, and in 1977, tritium contamination was found migrating from the one of the disposal trenches [¹¹]. Due to a number of factors including the tritium migration, the hydrological deficiencies, and a denial by the NRC to allow for increased disposal area, the site was closed in 1978.

- Maxey Flats, Kentucky

The Maxey Flats waste site operated from 1963 until 1977 under a State of Kentucky license. The site was licensed to accept both low and intermediate-level radioactive waste, which included some transuranic waste materials. The site employed shallow disposal techniques with 46 trenches and a number of hot wells and special pits. The hot wells were lined with concrete and used to dispose of high dose-rate packages. In the early 1970's, water

infiltration into the waste trenches generate public and regulatory concern, and an evaporation program and increased ground water monitoring were initiated. In 1976, the Kentucky legislature imposed a tax on waste receipts, in response to reports of off-site radioactive material migration. This legislative action and the growing water containment problem caused the eventual site closure in 1977 [2].

- West Valley, New York

The West Valley waste disposal site operated from 1963 until 1975. The site was licensed by the state of New York for low-level waste disposal and by the NRC for high-level waste disposal from an associate fuel reprocessing activity. The site consisted of 14 shallow burial trenches. In the early 1970's, water infiltration into some of the trenches became a cause of concern, and in 1975, the water had breached two of the trenches. The contaminated water leaching from the trenches caused the immediate cessation of waste burial and lead to the ultimate closure of the waste disposal operation.

It is apparent that the relatively poor performance of the U.S. commercial radioactive waste sites can be directly linked to a lack of understanding of the chemical and physical site characteristics. The regulatory and operational focus of radioactive waste disposal in the U.S. has been on the site hydrology and structural integrity. This type of approach requires little to no attention on controlling or understanding the near-field chemistry, which has proven to have a large impact on the long-term performance of U.S waste sites. There is a need to re-address the regulatory framework of radioactive waste disposal (especially low-level waste) to include controls on waste forms and packaging with the intent of limiting highly reactive chemical environments. Without positive control and understanding of the chemical speciation at radioactive waste sites, there is no way to predict or model the release of the radionuclides to the biosphere.

4.2. Actinide Chemistry

Actinide chemistry is a complex area of study due to the lack of natural analogs for the higher actinides, the large variation in valence states, and the radioactivity of these elements. The actinides are those elements with atomic numbers 89 (actinium) to 102 (nobelium), and they are distinguished from other elements by the filling of the 5f electronic subshells. Actinides with atomic numbers 92 and below are naturally occurring and are as follows.

- uranium (U, atomic number 92)
- protactinium (Pa, atomic number 91)
- thorium (Th, atomic number 90)
- actinium (Ac, atomic number 89).

The actinides with atomic number greater than U are called transuranic elements, and all are man-made. The transuranic elements are as follows.

- neptunium (Np, atomic number 93)
- plutonium (Pu, atomic number 94)
- americium (Am, atomic number 95)
- curium (Cm, atomic number 96)
- berkelium (Bk, atomic number 97)
- californium (Cf, atomic number 98)
- einsteinium (Es, atomic number 99)
- fermium (Fm, atomic number 100)
- mendelevium (Md, atomic number 101)
- nobelium (No, atomic number 102).

Since the transuranic elements are not readily found in natural settings, it is difficult to study these elements, since there is no environmental database from which extract empirical speciation information. The lack of environmental data has lead researchers to resort to empirical chemistry studies and thermodynamic modeling to predict the speciation of the transuranic elements. These empirical studies and modeling efforts have been successful in predicting speciation under a small range of thermodynamic conditions, however the building of the actinide thermodynamic database is just beginning. Although vast improvements have been made in the field of thermodynamic modeling, the range of environmental conditions is so large

that a complete thermodynamic database with the necessary kinetics information will not be available for quite some time.

One other complication of the study of actinides is that they are radioactive. In a waste repository setting, the radiation emitted by actinides tends to have a major influence on the near-field chemistry. In an aquatic system, the radiation can cause local radiolysis leading to the formation of highly reactive free radical, subsequent peroxide formation, leading to pH adjustments, chemical bond disruption. Radiolysis is a complex local interaction and can have a large impact on the local chemical speciation of high concentrations of actinides. The following sections will address actinide chemistry in terms of their natural analogs, lanthanide analogs, and environmental behavior.

4.2.1. Natural Analogs

Natural analog sites, as used in understanding actinide chemistry, are natural locations that have known thermodynamic conditions that are in equilibrium, and they are well characterized in terms of actinide species formed, local thermodynamic conditions, and major ligand concentrations. These natural analog sites are necessary in the understanding of actinide chemistry by providing a "reality check" on the complex thermodynamic modeling and empirical studies. Since any model or experimental approach is subject to bias and error, natural analog sites provide a validation to the techniques and assumptions used by the modeler and researchers. Although natural analogs are powerful tools for validation of theoretical and empirical data, they are very limited for the transuranic actinides. The natural analog sites for transuranics are limited to contaminated sites generated by fuel reprocessing and defense related activities.

However, there are plenty of natural analogs for actinides with atomic number 92 (uranium) and below, primarily Th and U. Since these elements are all relatively similar chemically, they tend to reside together in natural settings. Most of these lower actinides are also in the radioactive decay chains of each other, and thus this leads to the likelihood of finding these elements in proximity of each other. This natural abundance and close proximity allows for the study of actinides over a wide range of environmental conditions. The naturally occurring actinides, U and Th, have a much more detailed environmental record that allows for natural analog studies of these elements. The isotopes ^{232}Th , with a radioactive half-life ($t_{1/2}$) of 14

billion years, and ^{238}U , $t_{1/2}$ of 4.5 billion years, are in the greatest natural abundance with lesser natural quantities of ^{235}U ($t_{1/2}=7\text{E}8\text{y}$). Various isotopes of the elements Th, U, Pa, and Ac are also available in nature due to radioactive equilibrium with the uranium and thorium decay series. The natural abundance of U, Pa, Th, and Ac has made the study of these elements somewhat easier by having natural analogs to help validate thermodynamic models and empirical chemistry data. However, U can exist in at least four different valence states (3+, 4+, 5+, and 6+) which makes its study relatively more difficult. This is why it is important to validate empirical and theoretical studies with natural actinide deposits. Since uranium and thorium are found throughout the world in various concentrations and chemical environments, it is easy to correlate the actinide species formed with the local thermodynamic conditions.

Another property of some actinides (i.e. ^{239}Pu , ^{235}U) is their tendency to spontaneously fission. The spontaneous fission of such actinides leads to the formation of fission products and large amount of energy (the order of a few hundred MeV). Although this spontaneous fission is rare and only occurs with a few select actinides, the affects to the local chemical environment are drastic. When the environmental conditions are such that there are large concentrations of fissile and fissionable (i.e. ^{238}U) actinides and sufficient neutron moderation, there is a possibility for a self-sustaining nuclear reaction. These natural reactors are no longer possible due to radioactive decay of ^{235}U (the primary natural fissile material). However, at Oklo in Gabon, Africa, there was a natural nuclear reactor which fissioned for many thousands of years. This type of natural analog site provides an excellent opportunity to study the chemistry of actinides with their fission products and in the presence of relatively high natural radiation levels [¹²].

4.2.2. Lanthanide Analogs

The lanthanides are those elements with atomic numbers 57 to 70. The actinides are chemically very similar to lanthanide elements, since the lanthanides also have sufficiently energies to allow filling of the 4f subshells. The lanthanides and actinides are chemically very similar not only within their groups, but they are also quite similar between their groups. This chemical similarity arises from the ionic charge to volume ratios that are almost identical for the trivalent species. Almost all of the lanthanides have a trivalent (3+) oxidation state, and coupling this 3+ oxidation state with a similar ionic radii due to the 4f shell filling, the result is a relatively

similar charge to volume ratio. A partial listing of the actinide ionic radii are found in table 4.2.1.

Table 4.4: Metallic and ionic radii (Å or m⁻¹⁰) of select actinides and a few actinyl ions [13]

Element	Atomic Number	Metallic radii					Actinyl ions	
		M ⁰	M ³⁺	M ⁴⁺	M ⁵⁺	M ⁶⁺	M-O (V)	M-O (VI)
Actinium	89	1.88	1.076					
Thorium	90	1.80		0.984				
Protactinium	91	1.63		0.944	0.90			
Uranium	92	1.56	1.005	0.929	0.88	0.83		1.71
Neptunium	93	1.55	0.986	0.913	0.87	0.82	1.98	
Plutonium	94	1.60	0.974	0.896	0.87	0.81	1.94	
Americium	95	1.74	0.962	0.888	0.86	0.80	1.92	
Curium	96	1.75	0.946	0.886				
Berkelium	97		0.935	0.870				

Most actinides can be found in a trivalent state (except Pa and Th; U is rare), however the actinides also tend to have a wider range of oxidation states. When the actinides are found in their trivalent state and due to the 5f shell filling, the charge-to-volume ratios tend to be similar to the trivalent lanthanides (Figure 4.1). The differences in the trivalent actinide ionic radii values between Table 4.4 and Figure 4.1 are a result of variation in methodology used in determining this parameter, although the trend for contraction at higher f shell filling remains constant. The chemical similarity causes the actinides and lanthanides to often appear together in nature, and it makes them very difficult to separate from one another. This similarity also allowed for the early study of the actinides by reference to the abundant lanthanide properties. In 1944, Seaborg realized this relationship in his “actinide hypothesis” relating the properties of the lower oxidation state actinides with those of the lanthanide series [14]. The actinides are differentiated from the lanthanides in that the actinides are all radioactive, and the actinides have a larger range of oxidation states. This range of oxidation states for the actinides is due to the 5f and 6d electrons being bound less tightly than the 4f and 5d electrons of the lanthanides. Therefore, for the trivalent actinides, which are studied in this document, the lanthanides are very good chemical analogs.

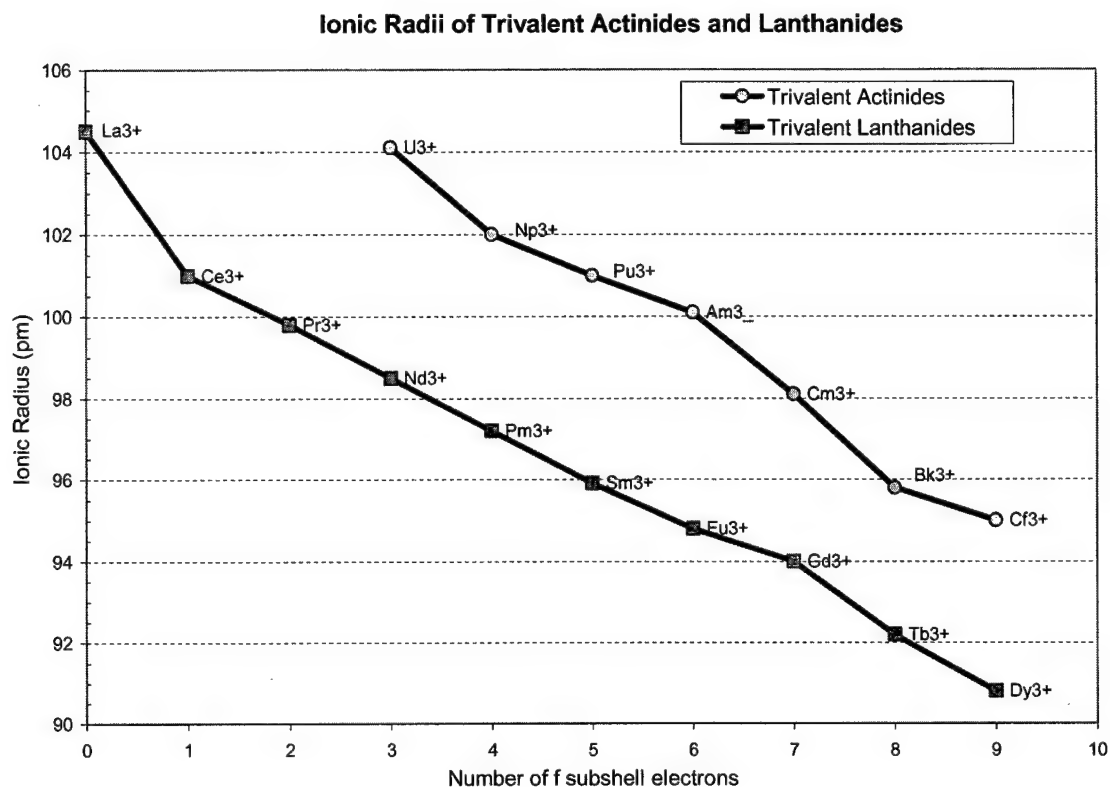


Figure 4.1: Ionic radii of the trivalent actinides and lanthanides. The range of charge-to-volume ratios is relatively small, which drives the use of lanthanides as actinide chemical analogs. The rate of ionic radii reduction for both series is about the same, and this contraction and subsequent increase in effective nuclear charge is due to the poor shielding of the 4f and 5f electrons [¹⁵].

4.2.3. Environmental Behavior

From an environmental perspective, actinide chemistry is dominated by aquatic interactions. The interactions that take place in aqueous environments are highly dependent on the solution equilibrium conditions, and the driver of the equilibrium conditions is thermodynamics. Therefore at the basic level of environmental actinide chemistry lies the study of thermodynamics, and in order to understand fully the state of any chemical system, it is necessary to determine the thermodynamics driving the systems. A second important factor in understanding aqueous chemistry is kinetics or the rate at which reactions take place. Although kinetics can have a great influence on short-term chemical interactions, on a geologic time scale,

most thermodynamically driven systems are in equilibrium and kinetics are normally not an issue.

Chemical thermodynamics for aquatic systems deals with changes in the chemical composition or species of the system. Those changes in the speciation are the result of chemical reactions and transfers of species between solid, aqueous and gaseous phases. Benes and von Gunten define speciation as the physico-chemical form of an element or isotope, and they go on to list the methods for the determination of speciation as thermodynamic (and kinetic) calculations, direct analysis of environmental samples (including in situ analysis), and model experiments (experimental simulation in the laboratory) [16]. In these studies, the general speciation methods are defined as thermodynamic or theoretical modeling, in situ and natural analog studies, and bench-top or empirical chemical analysis. Although it is theoretically possible to describe any environmental system in terms of its thermodynamic relationships, there is seldom a sufficient understanding of all interactions to adequately predict the behavior of a system based on thermodynamics alone. This is why in situ and natural analog studies coupled with empirical analysis are required to complement the thermodynamic modeling. In order to increase understanding of environmental actinide chemistry, it is necessary to increase the thermodynamic knowledge base through experimentation and observation. As the thermodynamics behind actinide speciation is further developed, there will be less reliance on site specific observation and improved prediction of environmental actinide behavior.

Chemical speciation can be described by the resultant physico-chemical form or by the process which creates that form. Silva and Nitsche define the four important processes that control speciation as precipitation, complexation, sorption, and colloid formation [17]. In order to determine what species are formed, it is necessary to have a good thermodynamic database of the system. This database must include equilibrium constants for all of the major reactions based on the available constituents and thermodynamic conditions.

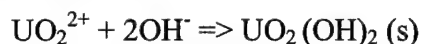
Any speciation analysis must first begin with an accounting of all major reactants. In actinide chemistry, the accounting normally includes the concentration of the free actinide metal ion by oxidation-state, the major ligands (anionic species), and any other cations that might compete with the actinides. Once the metals and ligands of interest are identified, it is necessary to determine the thermodynamic conditions of the aqueous environment. Besides the standard thermodynamic properties of temperature and pressure, there are two other important parameters

useful in defining the thermodynamic conditions of an aqueous solution. These parameters are pH and Eh.

The pH is measure of the free hydrogen ions in a system and is defined as follows, where $[H^+]$ is the concentration of hydrogen ions.

$$pH = -\log_{10} [H^+]$$

The pH is important since it is often considered a master variable in equilibrium calculations, and since water is the universal solvent for all aqueous interactions, hydrogen is an integral component [18]. With actinides in particular, reactions with water, or hydrolysis, is one of the most important aqueous reactions [19]. Hydrolysis is the displacement of a hydrogen ion from a water molecule, and with moderate to high pH, it can lead to precipitation as seen in the following reaction for hexavalent uranium.

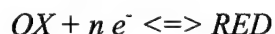


Precipitation of the tetravalent actinides is also facilitated by hydrolysis in high pH solutions.

The Eh, or redox potential, is measured in terms of volts and, similar to the definition of pH, it is a measure of the tendency of a solution to donate or accept electrons. The Eh is defined as follows,

$$E_H = \frac{2.3RT}{nF} \left[\ln K - \ln \frac{[RED]}{[OX]} \right]$$

where, R is the Gas constant ($8.314 \text{ J mol}^{-1} \text{ K}^{-1}$), T is temperature (K), n is the number of electrons transferred, F is the Faraday constant ($9.649E4 \text{ C mol}^{-1}$), K is the equilibrium constant for the reaction, and $[RED]$ and $[OX]$ are the free concentrations of the reduced and oxidized species as shown by the following reaction.



The Eh is especially important for actinide chemistry since it drives the oxidation-state of the metal and thus the ultimate speciation. The known oxidation states of the actinides are shown in Table 4.5. By coupling the Eh data with the pH and associated concentrations, an Eh/pH chart can be created to determine the major species over the entire range of environmental conditions. This type of chart is very helpful in scoping studies where experimental resources are limited.

Table 4.5: The actinides with known or suspected oxidation states ^[20]

Element	Symbol	Atomic Number	Oxidation State					
			M ²⁺	M ³⁺	M ⁴⁺	M ⁵⁺	M ⁶⁺	M ⁷⁺
Actinium	Ac	89		x*				
Thorium	Th	90		(x)	x*			
Protactinium	Pa	91		(x)	x	x*		
Uranium	U	92		x	x	x	x*	
Neptunium	Np	93		x	x	x*	x	x
Plutonium	Pu	94		x	x*	x	x	x
Americium	Am	95	(x)	x*	x	x	x	
Curium	Cm	96		x*	x			
Berkelium	Bk	97	(x)	x*	x			
Californium	Cf	98		x*				
Einsteinium	Es	99		x*				
Fermium	Fm	100		x*				
Mendelevium	Md	101	x	x*				
Nobelium	No	102	x	x				

x* - most stable oxidation state

x - other known oxidation states

(x) - unstable or suspected oxidation states

4.3. Nuclear Magnetic Resonance

Nuclear magnetic resonance (NMR) as a tool to study nuclear interactions was first discovered by Bloch and Purcell in 1946^[21, 22]. This discovery has lead to widespread use of NMR as an analytical tool, and its applications to new and diverse areas of study are continuously expanding. Bloch provides a semi-classical description of NMR spin dynamics, which is adequate to describe the experiments used in this study. For these studies, only proton NMR was used, and thus the description will be limited to spin ½ nuclei.

4.3.1. NMR Basics

Elements with non-zero spin angular momentum, I , and magnetic moment, μ , are related by the gyromagnetic ratio, γ , in the following relationship.

$$\mu = \gamma I$$

NMR experiments involve the interaction of an applied static magnetic field, B_0 , with the bulk magnetic moment, M , of a group of nuclear spins. This interaction is considered a Zeeman interaction with the energy related to the applied field as follows.

$$E = - M \cdot B_0$$

For a large number of nuclear spins, M is considered a superposition of the individual spins. For protons (spin = ½), the nuclear spin is a dipole with states that are either parallel or anti-parallel to the applied field. At equilibrium, the spins will populate the two states according to Boltzman statistics. With an applied magnetic field of between 1-20T (typical range of NMR magnets), this corresponds to increased population difference of approximately 10^{-6} . This implies that NMR is a relatively insensitive technique, which requires a large number of spins for a measurable signal (on the order of 10^{15} spins). The energy difference between the two states is related to the angular frequency, ω_0 , as follows.

$$\Delta E = \gamma \hbar |B_0| = \hbar \omega_0$$

This angular frequency is called the Larmor frequency, and it is described as a precession of the bulk magnetization about the applied field, B_0 (normally assigned to the z-direction). This precession is a result of torque created by the Zeeman energy, E , and originates from,

$$dM(t)/dt = \gamma M(t) \times B$$

Besides this precession, the bulk magnetization can undergo relaxation, which returns the magnetization to an equilibrium state. The relaxation process has components along the direction of the applied field (axial or z-direction), which relaxes back to the equilibrium magnetization (M_0), and in the transverse direction (x- and y-directions), which relaxes to zero. Since the bulk magnetization is composed of magnetic moments of many individual spins, the length of the magnetization vector has a maximum but no minimum, and therefore, the transverse component can relax faster than the axial component. Therefore, spin relaxation must be described using a relaxation time for the axial component (spin-lattice, T_1 time) and the transverse component (spin-spin, T_2 time).

Bloch described the complete spin dynamics in the rotating frame, with a rotating field along the x-direction, B_1 (RF field), as follows.

$$\begin{aligned}dM_x/dt &= \Delta\omega M_y - M_x/T_2 \\dM_y/dt &= -\Delta\omega M_x + \omega_1(t) M_z - M_y/T_2 \\dM_z/dt &= -\omega_1(t) M_y - (M_z - M_0)/T_1\end{aligned}$$

In the above equations, $\Delta\omega$ is the difference between the Larmor frequency and the rotating frame, and ω_1 is the RF field angular frequency ($\omega_1 = \gamma |B_1|$). For convenience, the NMR spin dynamics are normally reference to the rotating frame, since only the components that influence the spin dynamics are kept in this frame.

4.3.2. Experimental Techniques

A NMR experiment can be broken down into four primary components. The first component is to place a sample into a static magnetic field to create a population inversion of nuclear spins. The coherence is generated by the applied magnetic field through the Zeeman interaction with the nuclei, and the population inversion is a result of a Boltzman distribution. The second NMR experimental component involves a manipulation of the nuclear spins through the application of radiofrequency (RF) energy. This RF pulse creates an excitation of the nuclear spins. The third component in a NMR experiment is the relaxation and detection of the excited state. As the nuclear spins return to the equilibrium condition, they generate an oscillating signal, which can be detected and measured. The final stage in NMR experimentation is to process the detected signal, or free-induction decay (FID), to extract useful information about the

system. This processing of the FID normally involves the use of Fourier transformation (FT), which converts the time domain FID data into a frequency domain spectrum. Although this four component description of a NMR experiment is rather basic, almost all NMR experiments involve these four components. A more complete treatment of NMR experimentation can be found in Callaghan [23] or by Xia [24]. Many enhancements can be made to experimental techniques to extract certain types of information, and some of these are discussed in the following paragraphs. A further description of the experimental techniques used in this study are including in Section 5.0.

4.3.2.1. Spectroscopic Experiments

These experiments normally involve simple one-dimensional excitation experiments, however there are some experiments of this type, which are much more detailed 1- and 2-D experiments. The spectroscopy, or high-resolution spectroscopic, experiments are often used to determine molecular structure and interactions. The fundamental purpose behind most spectroscopy experiments is to determine the frequency spectrum emitted through relaxation of the sample spin environment. Due to a wide range of interactions and varying magnetic environments, the nuclear spins will not relax in the same manner. These variations can manifest themselves as chemical shifts ($\delta\nu$) from the center resonance frequency, and as dipolar line broadening (ω_d) measured as the full-width half-maximum (FWHM). There is much more information that can be extracted from spectral shape, but the primary parameters of interest for most spectroscopy experiments are $\delta\nu$ and ω_d .

4.3.2.2. Relaxation Experiments

Once an initial spectrum is collected, there are many other experiments provide further insight into interactions rates and lifetimes of the excitation. These types of experiments are often grouped into the relaxation experiment category. A few of these experiments and the parameters they measure are discussed. One of the most important parameters for any NMR experiment is the rate at which the equilibrium-state is re-populated after an excitation. The rate of this re-populations is called the spin-lattice, or T_1 , relaxation rate. The T_1 is a measure of the exchange of energy between the spin system and the surrounding thermal reservoir, or the lattice. The T_1 is most often measured using an inversion recovery experiment, however there are other

experiments used for special circumstances such as progressive saturation and saturation recovery experiments. A second characteristic parameter is the spin-spin, or T_2 , relaxation rate. The T_2 is the rate at which the spin system, in an excited condition, comes into thermal equilibrium with itself. These types of relaxation results in a phase de-coherence of the excited spins, thus resulting in loss of detected signal. The T_2 is most often measured with a Carr-Purcell (CP) or the advanced Carr-Purcell Meiboom-Gill (CPMG) experimental sequence. A relaxation parameter often measured is spin diffusion. Although this is not strictly a magnetic relaxation mechanism, it results in the attenuation signal, and thus it is usually grouped as a relaxation technique. The diffusion constant, D , is normally measured with a pulsed-gradient spin echo (PGSE) or stimulated echo (PGSTE) experiment.

4.3.2.3. Imaging Experiments

NMR imaging experiments are usually described in terms of the number of dimensions being imaged and the type of basic experiment being run. For example, there are 1-, 2-, and 3-dimensional versions of most imaging sequences, and the difference for each version is the application of spatial encoding in that dimension. Spatial encoding can be thought of as the tagging of spins in either a frequency or a phase domain. This tagging is accomplished through the manipulation spins in such a way to create a correlation between their spatial location and the tagged frequency or relative phase. This frequency or phase spin tagging is normally created with a magnetic gradient along one, two or three dimensions, and coupling the gradient with the normal spin evolution, a magnetization grating is created. A complete description of imaging principles and magnetization gratings is described by Cory [²⁵] and Callaghan [²⁶].

4.3.3. Paramagnetism and Susceptibility Variations

The interaction of a magnetic field with some material described by the magnetic induction or flux density, B (T or $\text{kg s}^{-2} \text{A}^{-1}$), in the material.

$$B = \mu H$$

Where, μ is the magnetic permeability (in $\text{m kg s}^{-2} \text{A}^{-2}$) and H is the magnetic field strength (A m^{-1}). The μ is defined as some deviation from a standard permeability of free space ($\mu_0 = 4\pi \times 10^{-7} \text{m kg s}^{-2} \text{A}^{-2}$) and this deviation is called the magnetic susceptibility, χ .

$$\mu = \mu_0 (1 + \chi)$$

Materials with negative values of χ are called diamagnetic and those with positive χ values are called paramagnetic. Ferromagnetic materials have positive χ values at two to three orders of magnitude greater than most paramagnetic materials. The paramagnetic nature of a material comes about due to unpaired electrons. The more unpaired electrons, the higher the degree of paramagnetism, and thus the greater the susceptibility.

In determining the susceptibility of a material, there are a few relationships that can be used for NMR studies. One important relationship is between the local field variations induced by susceptibility mismatch and the line-width,

$$\Delta\omega = \gamma \Delta B$$

where γ is the gyromagnetic ratio. This relationship shows how the line-width, or frequency range, is directly proportional to the local field variations, which can be expressed in terms of the susceptibility.

4.3.4. Gadolinium Tracers

This work uses the trivalent lanthanide gadolinium, Gd^{3+} , as a chemical analog for trivalent actinides. Lanthanides and actinides have long been used as chemical analogs for each other based primarily on the gradual filling of the 4f and 5f subshells by the lanthanides and actinides, respectively, which result in similar relative orbital energies. In particular, the trivalent lanthanides and actinides have similar ionic radii, which results in similar ligand-metal orbital interactions as seen in the resultant absorption spectra and stability constants. Based on these chemical similarities, Gd^{3+} ions can be used as a good analog in modeling the chemical reactivity of the trivalent actinide species, ^{241}Am and ^{244}Cm .

The Gd^{3+} ion has the additional physical property of being paramagnetic, due to its half-filled 4f subshell with seven unpaired electrons. This electron configuration creates localized fluctuating magnetic moments. The influence of the Gd^{3+} ion on the proton relaxation is highly localized and provides the ability of measuring Gd ion concentrations in solutions or Gd ions sorbed to surfaces. The effects of these fluctuating magnetic moments result in increased relaxation rates, which is proportional to Gd concentration. A good example of this relaxation enhancement can be seen in a plot of Gd solution concentration verses the spin-lattice (T_1)

relaxation rate. A series of experimentally measured T_1 times with varying Gd concentrations can be seen in Figure 4.2.

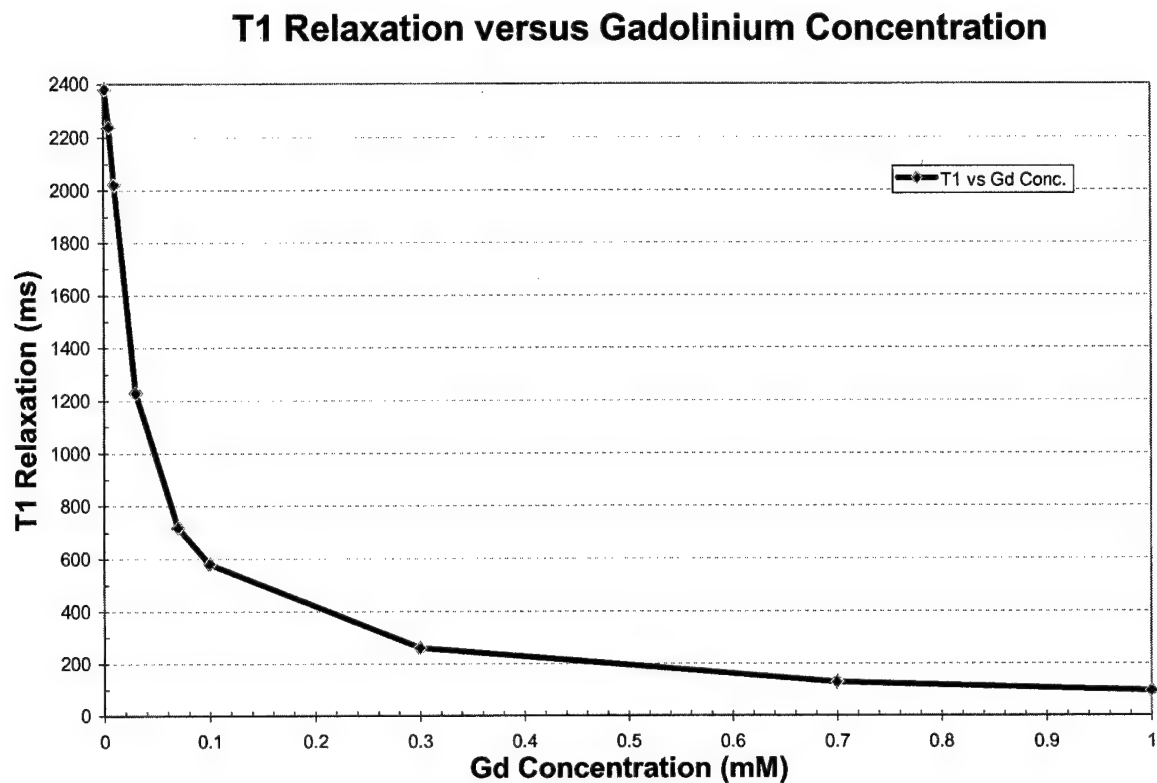


Figure 4.2: Plot of T_1 relaxation rate versus Gd concentration. It is clear how the T_1 decreases with increasing Gd concentration due to the increasing paramagnetic effects on local fluctuating magnetic fields.

4.4. Ion-Specific Exchange Resins

The ion-exchange resins used in this study were designed to separate similar metal ions from various waste streams in a nuclear fuel reprocessing operation. This separation of similar ions requires the use of an ion exchange media that preferentially sorbs to one metal type over another. Since the metals of interest are lanthanides and actinides that primarily exist in a trivalent form, separation through redox controls was not an option. The only other mechanism was separation through physical mechanisms based on the interaction of the resin structure with the ion. In this way, the separation takes advantage of the variation in ionic radii of the metals, and thus various types of resins can be used to preferentially sorb certain metals.

The specific class of resins used in these experiments is organic ion exchangers that were first introduced in 1935^[27]. The first types of organic resins synthesized were phenol-formaldehyde polymers, and these are the types used in these studies. The phenolic resins used in these experiments are described and were prepared according to the procedures in ref. ^[28, 29, 30, 31], and in Appendix 1.0. The two primary phenolic resins used in these studies were resorcinol-formaldehyde (RF) and catechol-formaldehyde (CF). A third resin, phenol-formaldehyde (PF), was used for an imaging study, and its structure is the same as CF but with only one phenol (-OH) group. The resin structures for the CF and RF resin are given in Figure 4.3.

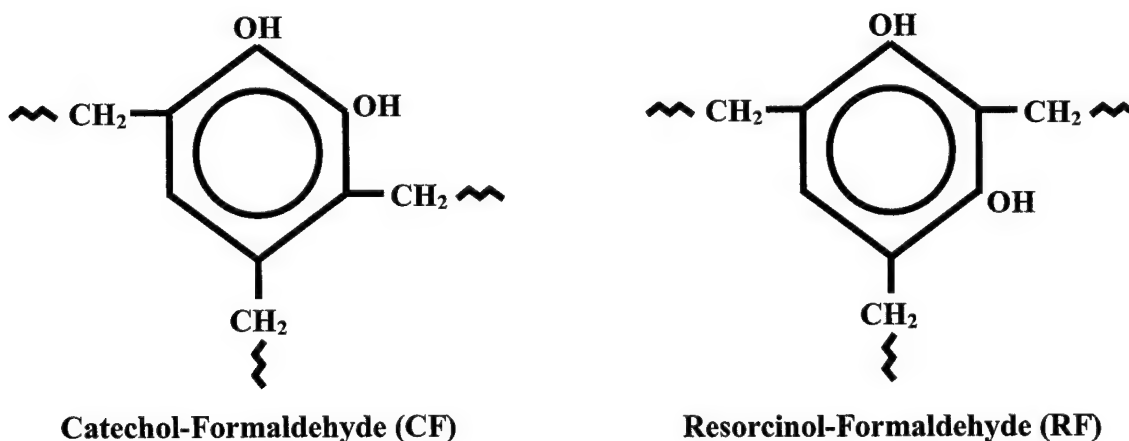


Figure 4.3: Chemical structure of CF and RF resins showing the ring structure, phenolic functional groups and formaldehyde synthesized cross-links.

4.4.1. CF and RF Physical Characteristics

The CF and RF resins used in these studies were synthesized by Draye and measurements of some important physical characteristics were made [32]. The chemical form of the resin is also given with the number of cross-links given as a variable (normally between 1-3). Each physical parameter is listed and referenced in Table 4.6.

Table 4.6: Physical characteristic of CF and RF resins

Resin Type	Chemical Form	Moisture Regain ($m_{\text{water}}/m_{\text{wet resin}}$) ¹	Proton Exchange Capacity (meq/g-dry) ¹	Trivalent Metal Loading Capacity [M(III)-Re]/[Re] ¹	Stability Constant $\log\beta(\text{L/mol})^2$	Thermal Decomposition $T_1 (\text{°C})^2$
CF	$\text{C}_6\text{H}_4(\text{OH})_2(\text{CH}_2)_n$	20%	8.6	0.622	3.2	148.84
RF	$\text{C}_6\text{H}_4(\text{OH})_2(\text{CH}_2)_n$	40%	11.5	0.54	3.2	152.19

note: n = # of cross links

- ref: 1. K.R. Czerwinski, M. Draye, J. Foos, and A. Guy: Ion Selective Resins: Development and Applications for Nuclear Waste Management.
MRS Scientific Basis for Nuclear Waste Management XX. In press.
2. M. Draye, K.R. Czerwinski, A. Favre-Reguillon, J. Foos, A. Guy, and M. Lemaire, Sep. Sci. Tech., 35(8), pp. 1117-1132, 2000.

4.4.2. Resin Experimental Preparation

The resins were crushed and sieved to 63-125 micron mesh (230-120 ASTM standard US mesh size). The resins were converted to the Na^+ form prior to use to limit hydrolysis during metal loading. The clean resin samples consisted of only the Na^+ form resin saturated with de-ionized water, and the gadolinium (Gd) – loaded samples consisted of the Na^+ form resin fully loaded with Gd ions in a water saturated condition. Each resin sample was prepared in a zirconium ceramic magic-angle-spinning (MAS) rotor with a total volume of approximately 100 μL . The resin samples were carefully prepared to ensure the complete water saturation with limited standing water remaining. The samples were stored in a water bath between uses to ensure a water-saturated condition.

4.4.3. Clean Resin Samples

The clean resin preparation consisted of a series of resin saturation steps. Dry resin exposed to ambient humidity levels was placed in each rotor and saturated in place to limit the standing water. The oven-dried resin mass is approximately 20-40% less than the ambient humidity resin mass due to its hygroscopic nature. Sufficient time was allowed between saturation steps to allow for resin expansion and complete saturation. The saturated resins were also stirred to ensure complete exposure to the free water and to prevent plugging due to rapid expansion. A final packing step was used to ensure there was limited standing water and to allow for good seating of the rotor cap. The clean resin samples were prepared as follows:

- CF Resin Sample: 27.8 mg of resin and 88 μ L of water for a total resin/water mass of 115.8 mg
 - 17.9 mg of ambient humidity resin was placed in Zr rotor #1797
 - 55 μ L of de-ionized water was injected into resin in 10 μ L increments
 - wet resin was mixed to ensure complete saturation with a wait time of approximately 5 minutes
 - 6.3 mg of resin was placed on top of saturated resin
 - 22 μ L of water was injected and allowed to saturate resin
 - 3.6 mg of resin was added
 - 11 μ L of water was added
 - saturated resin was allowed to equilibrate for 10 minutes and slightly packed to ensure a good fit of rotor cap
- RF Resin Sample: 32.3 mg of resin and 88 μ L of water for a total resin/water mass of 120.3 mg
 - 13.9 mg of ambient humidity resin was placed in Zr rotor #2109
 - 55 μ L of de-ionized water was injected into resin in 10 μ L increments
 - wet resin was mixed to ensure complete saturation with a wait time of approximately 5 minutes
 - 14.6 mg of resin was placed on top of saturated resin

- 33 μ L of water was injected and allowed to saturate resin
- 3.8 mg of resin was added
- saturated resin was allowed to equilibrate for 10 minutes and slightly packed to ensure a good fit of rotor cap

Note: the resins expand to approximately twice their volume when saturated with water; the dry resin mass is approximately 20-40% less than the ambient humidity resin mass; the resins sample had no visible standing water after final preparation

4.4.4. Gadolinium-Loaded Resin Samples

The Gd-loaded samples consisted of resin saturated with Gd ions. The Gd ions form very stable bonds with the phenolic functional groups on the resin. The surface complexation of the Gd increases the magnetic susceptibility of the resin matrix, thus allowing for further study of spatial characteristics. A fully loaded resin was ensured by exposing the resin to over 200% of the theoretical metal loading capacity and allowing sufficient time for equilibrium. The ion exchange capacity (IEC) and the loading capacity (LC) were used to determine the required Gd concentration and volume. A kinetics study of loading provided the required equilibrium time.^[33] The IECs for CF and RF resin are 2.9 and 3.8 milli-equivalents per gram-dry (meq/g), respectively. The LCs for CF and RF are 0.622 and 0.540, respectively. Combining the IEC and LC data, the total capacity for the CF and RF resin is 1.8 and 2.1 meq/g, respectively. The kinetics data shows that over 90% equilibrium is reached after 24 hours.

- CF and RF Gd-Loaded Samples:
 - 0.1 g of dry resin was placed in a 50 mL centrifuge vial
 - 50 mL of 10 mM GdCl_3 was added to the vial
 - vial was shaken for 24 hours
 - vial was then centrifuged for 15 minutes to ensure all resin was removed from suspension
 - resin/ GdCl_3 mixture was then placed in a vacuum-assisted filter vessel and filtered through a 25 μ m filter

- loaded resin was then washed with 250 mL of de-ionized water (neutral pH) to remove any free Gd
- resin was then allowed to air dry in filter assembly until all standing water was removed
- resin was placed in MAS rotor, slightly packed to remove voids, and stored in water prior to use

References for Section 4.0

- ¹ U.S. Environmental Protection Agency, Radioactive Waste Disposal: An Environmental Perspective, EPA 402-K-94-001, August 1994.
- ² From U.S. Nuclear Regulatory Commission internet web site, www.nrc.gov/NRC/EDUCATE/GLOSSARY/Waste.%20radioactive.html, 14 Jul 2000.
- ³ U.S. Code of Federal Regulation, Title 10, Part 61.
- ⁴ U.S. Code of Federal Regulation, Title 10, Part 61.56(a).
- ⁵ U.S. Code of Federal Regulation, Title 10, Part 61.56(b).
- ⁶ U.S. Environmental Protection Agency, Radioactive Waste Disposal: An Environmental Perspective, EPA 402-K-94-001, August 1994.
- ⁷ D. Savage, The Scientific and Regulatory Basis for the Geological Disposal of Radioactive Waste, John Wiley and Sons, New York, 1995.
- ⁸ J.M. Cahill, Hydrology of the Low-Level Radioactive Solid-Waste Burial Site and Vicinity Near Barnwell, South Carolina, U.S. Geological Survey Open-File Report 82-863, 1982.
- ⁹ H.G. Wilshire and I. Friedman, Contamination Migration at Two Low-level Radioactive Waste Sites in Arid Western United States – A Review, Environmental Geology, vol.37, no.1-2, p.111, 1999.
- ¹⁰ David E. Prudic, David A. Stonestrom, and Robert G. Striegl, Tritium, Deuterium, and Oxygen-18 in Water Collected From Unsaturated Sediments Near a Low-Level Radioactive Waste Burial Site South of Beatty, Nevada, U.S. Geological Survey Water-Resources Investigations Report 97-4062.
- ¹¹ K. Dragonnette, J. Blackburn, and K. Cartwright, Interagency Task Force Report on the Proposed Decommissioning of the Sheffield Nuclear Waste Disposal Site, U.S. Nuclear Regulatory Commission, Internal Report, September 1979.
- ¹² G.A. Cowan, A Natural Fission Reactor, Sci.Am. 235(1), 36, July 1976.
- ¹³ S. Ahrland, J.O. Liljenzin, and J. Rydberg, Solution Chemistry in Comprehensive Inorganic Chemistry, Vol. 5, Pergamon, Oxford, 1973.
- ¹⁴ G.T. Seaborg, Man-Made Transuranium Elements, Prentice-Hall Englewood Cliffs, NJ, 1963.
- ¹⁵ J.E. Huheey, Inorganic Chemistry-Principles of Structure and Reactivity, 3rd Ed., Harper and Row, NY, 1983.
- ¹⁶ H.R. von Gunten and P. Benes, Speciation of Radionuclides in the Environment, Radiochimica Acta 69, 1-29, 1995.
- ¹⁷ R.J. Silva and H. Nitsche, Actinide Environmental Chemistry, Radiochimica Acta 70/71, 377-396, 1995.
- ¹⁸ W. Stumm and J.J. Morgan, Aquatic Chemistry-Chemical Equilibria and Rates in Natural Waters, John Wiley and Sons, Inc., 1996.
- ¹⁹ M. Benedict, T.H. Pigford, and H.W. Levi, Nuclear Chemical Engineering, 2nd Ed., McGraw-Hill, 1981.
- ²⁰ S. Ahrland, J.O. Liljenzin, and J. Rydberg, Solution Chemistry in Comprehensive Inorganic Chemistry, Vol. 5, Pergamon, Oxford, pp465-635, 1973.
- ²¹ F. Bloch, et.al., Phys. Rev. 69, 127, 1946.
- ²² E.M. Purcell, et.al., Phys. Rev., 69, 37-38, 1946.
- ²³ P.T. Callaghan, Principles of Nuclear Magnetic Resonance Microscopy, Clarendon Press, Oxford (1991).
- ²⁴ Y. Xia, Introduction to Magnetic Resonance – section 65 of the compendium, Spatially Resolved Magnetic Resonance, Wiley-VCH, 1998.
- ²⁵ A. Sodickson and D.G. Cory, A Generalized k-space Formalism for Treating the Spatial Aspects of a Variety of NMR Experiments, Progress in Magnetic Resonance Spectroscopy 33, 77-108, 1998.
- ²⁶ P.T. Callaghan, Principles of Nuclear Magnetic Resonance Microscopy, Clarendon Press, Oxford (1991).
- ²⁷ A.W. Adamson, Physical Chemistry of Surfaces, John Wiley and Sons, pp 418-9, 1976.
- ²⁸ K.R. Czerwinski, M. Draye, J. Foos, and A. Guy: Ion Selective Resins: Development and Applications for Nuclear Waste Management. MRS Scientific Basis for Nuclear Waste Management XX. In press.
- ²⁹ M. Draye, K.R. Czerwinski, A. Favre-Reguillon, J. Foos, A. Guy, and M. Lemaire, Sep. Sci. Tech., 35(8), pp. 1117-1132, 2000.
- ³⁰ N.Dumont, A. Favre-Reguillon, B. Dunjic, and M. Lemaire, Sep. Sci. Tech., 31(7), pp. 1001-1010, 1996.
- ³¹ M. Draye, A. Favre-Reguillon, J. Foos, A. Guy, and K.R. Czerwinski, Proceedings of Waste Management '98 Conference, Tucson AZ, 1998.
- ³² M. Draye, et.al., Sep. Sci. Tech., 35(8), pp. 1117-1132, 2000.
- ³³ M. Draye, et.al, Sep. Sci. Tech., 35(8), pp. 1117-1132, 2000.

[THIS PAGE INTENTIONALLY LEFT BLANK]

5. EXPERIMENTAL TECHNIQUES

This section describes the experimental techniques used in this document. The first part of this section describes the NMR techniques, and it is broken up into NMR spectroscopic and imaging techniques. The second part describes the inductively coupled plasma - atomic emission spectroscopy (ICP-AES) analytical technique. Each description provides an overview of the technique, the purpose for using the technique, and the procedures to process and analyze the data. The results of these experiments are included in Sections 6.0 and 7.0, and the data is provided in Appendices 4.0 and 5.0.

5.1. NMR Experiments

The NMR experiments used in this study include spectroscopy, imaging of fluid transport, and magic-angle spinning (MAS) [¹]. The spectroscopic techniques will be discussed first with some MAS techniques integrated into the experiments. The NMR imaging experiments are discussed in second part of this section and in Section 7.0. All experiments were performed using Bruker spectrometers, and the Bruker experimental programs are provided in Section 5.1.1 for each type of experiment [²]. A description of the NMR equipment is provided in Section 4.3. Most data processing was done with Bruker spectrometer-based programs or using Matlab [³]. The Matlab processing codes and other data processing worksheets are provide in Appendix 3.0 for each type of processing used. The experimental data is available in Appendix 4.0. All NMR experiments in this study looked at proton resonance signal, and only square, or hard, radiofrequency (RF) pulses were used. Some deuterated water was used in the experiments, however only the signal from the trace protons was collected.

5.1.1. NMR System Descriptions

Two NMR systems were used in these experiments, and both will be described in this section. For the purposes of this discussion, the two NMR systems are given the names 3 tesla (3T) and 12T. The 3T system was used for both imaging and spectroscopy experiments, and the 12T was used only for spectroscopy experiments. Both the 3T and 12T have Magic-Angle

Spinning (MAS) capabilities, but only the 3T has flow through imaging capabilities. Since NMR is a rather complex analytical tool, the 3T and 12T systems will be described in terms of their many component systems and performance characteristics.

5.1.1.1. 3T NMR System

The 3T system is a horizontal bore magnet with Bruker spectrometer and gradient set. The major components of the system are the super-conducting magnet, the gradient set, the probes, and the spectrometer. The specifications for each of the system components are as follows.

- Magnet:
 - Manufacturer: Oxford
 - Magnetic Field: 3T or 122 MHz (protons)
 - Magnet Type: Superconducting
 - Orientation: Horizontal
 - Bore Diameter: 15 cm
- Gradient Set:
 - Maximum Output: 60 G/cm
 - Type: conducting coils
 - Inner Diameter: 4.5 cm
 - Axis: simultaneous in x, y, and z dimensions
 - Amplifiers: 3 at 2400 W max output
- Probe: a photo of the flow through probe is shown in Figure 5.1.
 - Manufacturer: M.I.T. – in-house built
 - Type: saddle coil, flow-through
 - Active Length: about 12 mm
 - Inner Diameter: 10 mm
 - Outer Diameter: 4.5 cm
 - Adjustments: 3 variable capacitors (2 match, 1 tune)

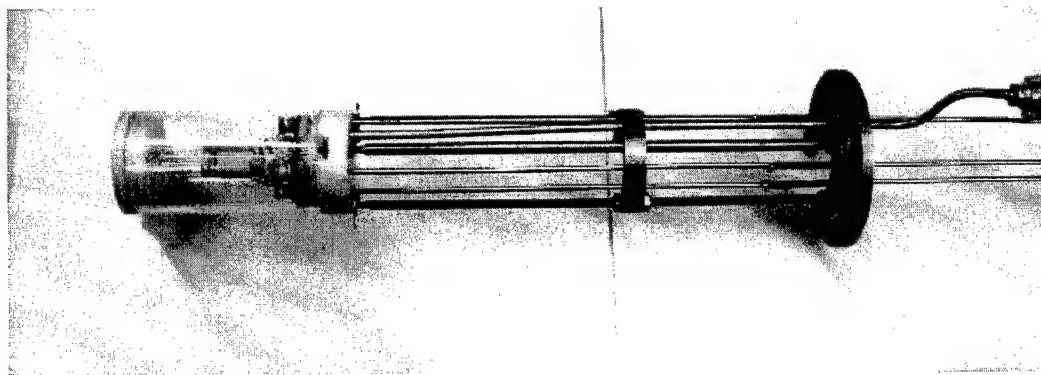


Figure 5.1: 3T 10 mm ID flow-through RF probe. The 3T flow-through probe was designed and built at M.I.T. The probe can handle up to 10 mm OD flow cells.

- Spectrometer

- Manufacturer: Bruker
- Model: AMX
- Software: UXNMR

5.1.1.2. 12T NMR System

The 12T NMR system is a vertical bore magnet with a Bruker spectrometer. The major components for the 12T are the super-conducting magnet, the probes, and the spectrometer. The specifications for each of the system components are as follows.

- Magnet:

- Manufacturer: Bruker
- Magnetic Field: 12T or 500 MHz (protons)
- Magnet Type: Superconducting
- Orientation: Vertical
- Bore Diameter: 5.2 cm

- Probes: two main types – MAS and high resolution

- Spectrometer:

- Manufacturer: Bruker
- Model: Avance DRX 500
- Software: XWIN-NMR version 2.6
- Add-on: MAS pneumatic controller H2620

5.1.2. NMR Spectroscopy

5.1.2.1. Spectral Collection and Deconvolution Experiments

The spectral deconvolution experiments involved simple one-dimensional, multi-scan, phase-cycled, proton excitation sequences. These experiments were performed on both the 3 tesla (T) and the 500 MHz, or 12 T magnets. The experiments were also performed using static and MAS techniques. All MAS experiments were run at 5 kHz rotor speed, since this was determined to be the point at which no further separation of the main peaks occurred. The purpose of this experiment was to determine how many separable components were in the resin samples and whether those components could be fit in such a way to extract spin population, chemical shift, and relaxation time data.

The spectral fit experiments were performed using the pulse sequences in Appendix 2.1. The variables used are included in each pulse sequence and on the spectral plots. The experimental setup started with the sample preparation that is fully described in section 4.3 and in Appendix 1.0. Each resin sample was then placed in the static or MAS probe and the following procedures were used to generate the spectral data. The single 90-degree excitation (zg) pulse sequence used in these experiments is shown in Figure 5.2.

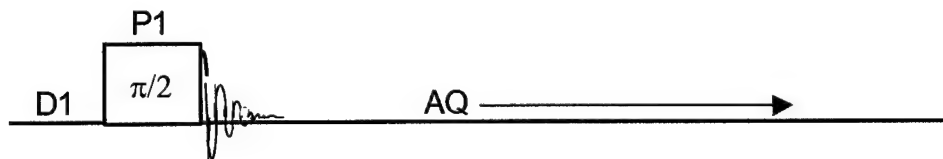


Figure 5.2: Typical single 90-degree excitation (zg) pulse sequence used for the spectral collection and deconvolution experiments. The figure shows the T_1 delay time (D1), the 90-degree pulse length (P1), and the acquisition time (AQ).

5.1.2.1.1. Initial Setup: The first procedure in any NMR experiment is to tune the probe. The tuning step is used to minimize the reflected radiofrequency (RF) signal, and thus to increase the overall efficiency of the transmitted RF energy. On the 12T, this tuning step is automated using the wobble sequence and pre-amplifier unit. On the 3T, this procedure is manual and performed as follows. The 3T tuning procedure is performed using an on-resonance

single excitation pulse sequence. A RF splitter is used and connected to an oscilloscope to view the transmitted and reflected RF signal. With the spectrometer pulsing in a continuous or "gs" mode, the NMR probe is tuned and matched to reduce the reflected signal as seen on the oscilloscope.

The next step in the setup is to determine the required parameters to run the pulse sequence. A low-power pulse (much less than a 90-degree excitation) is used to weakly excite the spins and the signal is collected as a free-induction decay (FID). The FID is Fourier transformed (FT) [4] to a frequency spectrum. The real part of the spectrum is phase corrected (using pk, ph0 and ph1 adjustments) to produce a completely absorptive line shape. From this FT and PK process, the absorptive line shape is set on resonance using the offset frequency (O1). Once the proper O1 is set, the low-power sequence is repeated to ensure proper phasing and O1 selection. It is at this time that the proper dwell time (DW) and time domain (TD) points are selected. The DW times the TD determine the acquisition time (AQ), so this combination must be large enough to ensure acquisition of the entire FID. In addition, the DW sets the spectral width (SWH) for the acquisition, so it's important to ensure the spectral width is large enough to acquire the entire frequency range (important for samples with broad line width). Once the TD and DW are selected, the processing parameter SI was selected to be at least twice the TD value.

5.1.2.1.2. Parameter Determination: Now that the spectrometer is on resonance and the proper acquisition and processing parameters are selected, the maximum excitation or 90 degree ($\pi/2$) pulse is selected. This was performed by increasing the pulse time (P1) in small increments (1-2 μsec) while keeping pulse attenuation constant (TL0=10dB or PL1=-6dB). Once a maximum signal was reached, the pulse time was noted and the small time steps were continued until the on-resonance part of the spectrum reached a zero net signal. This first zero point is the 180 degree, or π pulse. The $\pi/2$ pulse was then set as exactly one half of the π pulse. This technique of determining the π pulse to find the $\pi/2$ is more accurate than finding the $\pi/2$ pulse directly, since the maximum signal is often difficult to determine. By convention, the $\pi/2$ pulse was assigned the P1 time, and the π pulse assigned the P2 time. The P1 time was entered into the pulse sequence and, a series of 4-8 scans with CYCLOPS phase cycling [5] was used to generate a representative excitation. The phase-cycled signal was then processed and re-phased, if necessary. At this point, a decision was made to if shimming is required. If shimming was deemed necessary, the gradient offsets (3T) or the shim controller was used to minimize the line

width and improve the overall line shape by reducing magnetic field inhomogeneities. Once the magnet is shimmed, the receiver gain (RG) was set to the optimal setting. This was done either using the Bruker “rga” macro or by increasing the RG until just before the FID begins to show clipping (peak truncation of the signal) in the acquisition window. If the RG changed, the spectrum was re-phased. At this point, it was appropriate to run the complete 4-8 scan sequence, and the dipolar line width (ω_d), or full-width at half-maximum (FWHM), was recorded. This information was useful to get qualitative information on the complexity of the spin pools, and the overall transverse relaxation rate ($T_2 = 1/(\pi \cdot \omega_d)$). Now that we have the P1 and P2 times, the spin-lattice, T_1 , relaxation time can be determined in order to set the pulse sequence delay time (D1). The D1 time should be at least 5 times the T_1 time in order to ensure the spins have reached full equilibrium prior to the start of the next sequence. The T_1 was determined by performing an inversion-recovery sequence, which is described in section 5.1.2.2.

5.1.2.1.3. Data Collection and Processing: Now that all of the acquisition and processing parameters are set, a single excitation, or Bruker “zg”, pulse sequence is run. The collected FID is then processed with a Fourier Transform and phase correction. The spectra now reside in a processed form as a Bruker 1r or 1i file. The resultant spectra is further processed with the Bruker XWIN Plot (12T), or transferred to a personal computer (PC) for processing with Bruker XWIN NMR or Matlab. A deconvolution of the spectra is performed using one of the processing packages, and the resultant spectral fits are summarized in Table 7.1.

5.1.2.2. Inversion Recovery T_1 Measurements

The inversion recovery (IR) sequence consists of a 180-degree pulse followed by a delay time (D2) and then a 90-degree pulse. The purpose of the IR experiments is to determine the spin-lattice, T_1 , relaxation time for the sample. When the IR sequence is performed with MAS and there is sufficient chemical shift between the spin pools, the T_1 time of each spin pool can be determined. Both the 3 and 12T magnets were used for these measurements and static and MAS experiments were run on the 12T. The results of the IR measurements are provided in Section 7.0 and the procedures used to generate the results are included below. The inversion recovery pulse sequence is shown in Figure 5.3.

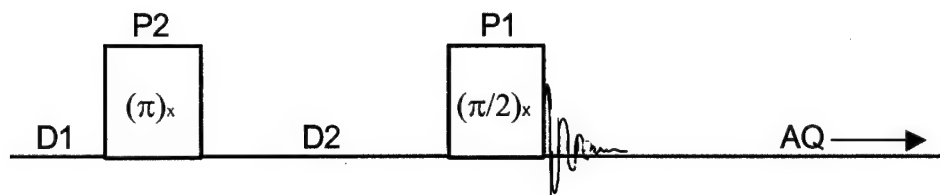


Figure 5.3: Inversion recovery pulse sequence used for the T_1 spin-lattice relaxation experiments. The figure shows the T_1 delay time (D1), the 180-degree pulse time (P2), the storage time (D2), the 90-degree pulse length (P1), and the acquisition time (AQ). The x-subscripts for the two RF pulses indicate that the pulses are given at the same phase.

5.1.2.2.1. Initial Setup: The resin samples were placed in MAS rotors put into the appropriate probe for each magnet. The 3 and 12T were tuned and acquisition parameters set according to the procedures in section 5.1.2.1.1.

5.1.2.2.2. Parameter Determination: The D1 time was set according to the procedures in section 5.1.2.1.2. However, since the inversion recovery experiment is so sensitive to the T_1 relaxation time, the D1 was set to 10 times the T_1 value (normally 5 times). The 90- and 180-degree pulse times (P1 and P2) were also set according to the section 5.1.2.1.2 procedures.

5.1.2.2.3. Data Collection and Processing: The data for the inversion recovery sequences were run using the Bruker parameter optimization or “paropt” macro. The paropt sequence generates a series of transformed spectra in a 1r file. Prior to the start of the paropt, a single, inversion recovery spectrum with a very long storage-time (D2) is collected, Fourier transformed (FT), and phase corrected (PK). This manual phase correction is stored, and all subsequent phase corrections use these stored values. The paropt sequence is started by selecting the variable parameter (D2 in our case), the starting value (0.1ms), and the number of increments (32). Once a FID is collected, the paropt macro performs a FT and PK, which results in a processed spectrum. The series of 32 processed FIDs are stored in the processed data set number 999 of the current experiment number. The 1r file is then processed using the Matlab. The Matlab program takes the 1r file and splits it into as many increments as were programmed. The resultant spectra can then be integrated or the peak height determined. The integral or peak

height is then plotted versus the storage time, D2, and the data is fit using a Levy three parameter model [6]. The fit model defines the signal intensity at storage time τ , $S(\tau)$, as follows.

$$S(\tau) = A + B \cdot \exp(-\tau/T_1)$$

The model is not overly sensitive to the inversion or equilibrium magnetization values, and thus provides a very good fit even if the 180-degree pulse is not accurate or the relaxation time is not long enough.

5.1.2.3. Carr-Purcell-Meiboom-Gill (CPMG) T_2 Measurements

The CPMG experiments were performed using the pulse sequence suggested by Carr and Purcell in 1954 [7] and modified by Meiboom and Gill [8]. The sequence consists of a 90-degree excitation pulse followed by a series of 180-degree pulses to refocus phase incoherences. The signal is collected at even or odd number of 180 pulses in order to ensure all data points are in the same phase. The method for incrementing the transverse storage time is to use a "vc" list, which is used to cycle through the refocusing loop. After a set number of loops, half an echo is collected and the experiment is repeated until a series of half-echoes are collected. The result of the CPMG experiment is a measure of the T_2 relaxation in a single experiment. The basic sequence is described in more detail by Callaghan [9] and shown in Figure 5.4.

For these studies, the delay time between 180-degree pulses was varied to determine whether there was mobility of the spins between various magnetic environments in the sample. Multiple and exponential least-square fitting was used to determine the T_2 times from the experimental data. By coupling the exponential fitting to the T_2 decay curves along with the effects from spin migration, the data provided a determination of the relative populations in each spin pools and a measure of the T_2 times for each pool. In addition, the shift of the curve at different echo times provided information as to the degree of diffusion and exchange between pools. The experiments were also run in the 3T and 12T magnets to determine the effects of dipolar and susceptibility induced local magnetic field variations. MAS CPMG experiments were run on the 12T magnet to measure the T_2 decay of each spin pool due to the chemical shift variations. The results of the CPMG experiments are provide in Section 7.0.

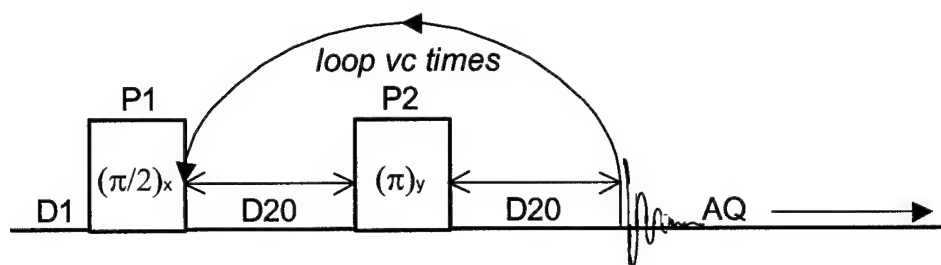


Figure 5.4: CPMG pulse sequence used for the T_2 spin-spin relaxation experiments. The figure shows the T_1 delay time (D1), the 90-degree pulse length (P1), the refocusing times (D20), the 180-degree pulse time (P2), and the acquisition time (AQ). The x- and y-subscripts for the two RF pulses indicate that the pulses are 90 degrees out of phase. The loop after the second D20 shows the “vc” loop that is incremented through a series of steps to acquire a range of half-echoes.

5.1.2.3.1. Initial Setup: The CPMG setup and initial parameter selections were performed using the same methods as in the previous two experiments. The CPMG is run in a 2-D acquisition mode in order to collect a series of half-echoes in one data set. Therefore, in addition to the 1-D setup for the previous two experiments, there are additional values for the second dimension. This second dimension corresponds to the Bruker f1 direction, and the time domain points in this dimension are given by 1 TD, which is the number of half-echoes collected. In the CPMG sequence, another parameter that must be set is the l4 value or the number of times through the sequence. The l4 value corresponds to the number of half-echoes collected (1 TD) or the number of values in the “vc” list. From the processing standpoint, the 2-D acquisition requires a second signal processing value (1 SI) be set, although a FT is not performed in this dimension. In order to maintain consistency, the 1 SI value is set to the 1 TD value. The phase cycling for this experiment is a combination of CYCLOPS and EXORCYCLE [10].

5.1.2.3.2. Parameter Determination: The important parameters for the CPMG experiment are the D20, or half-echo time, and the increments for the “vc” list. For a single run through the CPMG experiment, there are no loops (vc=0) and the echo time, τ_e , is equal to 2 times D20. This is the time (τ_e) for phase de-coherence to occur with the resultant attenuation of the measure signal. Based on the rate of de-coherence, or T_2 decay, the D20 is set to ensure a

good range of signal attenuation values while limiting the effects of longer time domain interactions. Therefore, to get good T_2 values for fast decaying components, it is necessary to make D20 as short as possible. However, there is a lower limit on D20 associated with the pulse time (P1). This lower limit is based on the potential for spin locking when the D20 is less than 50 times the P1 value. For these experiments, the P1 is on the order of 5-10 μ s, so the lowest D20 should be approximately 250 μ s. The upper limit on D20 is on the order of the T_1 relaxation time, however, the longer D20 is the more long-time interactions can influence the T_2 measurement. These long-time interactions can include diffusion and exchange. The second parameter which must be determined is the delay time between half-echoes. This delay time is governed by the number of cycles through the refocusing loop, and the number of cycles are contained in the "vc" list. This "vc" list begins with a very low (or zero) number of cycles and slowly increments the number of cycles to produce a good range of signal attenuation. The lower limit on the vc list should be zero in order to get the maximum (or near maximum) magnetization value. The final number of cycles should correspond to a number whereby the signal-to-noise ratio is in the range of 2-3. Whatever values for the "vc" list are selected, they must either all be even or odd to ensure the signal is collected in the same phase orientation each time. This will provide a good dynamic range and ensure all spin pools in the sample are accounted for in the decay curve.

5.1.2.3.3. Data Collection and Data Processing: The data was processed on the spectrometer using a one-dimensional FT in the f2 direction (XF2). The transformed 2-D spectra were phase corrected using a 2-D phase correction routine. The Bruker 2-D phase correction allows for simultaneous phase correction on three spectra across the range of echo times. The final phase correction on the spectrometer was an automatic baseline correction. Now that the data is in a series of phase and baseline corrected spectra in a Bruker 2rr (2ii) file, the next processing step depends on the type of data and preference from fitting the data. With static (non-MAS) data, the spectra are broad, so it is best to integrate each peak to evaluate the total magnetization. This integration is done on the spectrometer using the following procedure.

- The range of the integration (f2 direction) is set.
- The interval in the f1 direction is set manually in the automatically generate "roi" file. To do this, the f1 and f2 directions are selected as described in the manual integration menu.

Although this procedure works fine for the f2 direction, the f1 direction (since it wasn't

transformed) is not correct. Based on the known number of ser files (1 TD values), the f1 range is set manually as the first integral corresponding to the first ser set (i.e. f1 for integral 1 is 1 1, integral2 is 2 2, etc; entering the ppm or Hz values is not necessary).

- Now that the regions are set in the f1 and f2 directions (f2 automatically set), an automatic integration is performed.
- The integration places the integrals in an int file (pdata/# directory), and the values are given for each spectra.
- The integral data from the "int" file can be extracted using MS Excel, Matlab, or manually.

A second type of data processed from the CPMG experiments is MAS data. This data (especially from the 12T) can be processed in two ways. The easy way is to read 2rr data directly into a Matlab program and find the maximum for each spectrum. The peak heights are then fit using a Matlab least squares fitting method. This is the peak height method of processing and produces relatively good results. The better and much more time consuming method is to deconvolute the multiple peak spectra using the Bruker XWIN NMR processing tools. From the deconvolution, the peak heights of each peak and their integrals are available for Matlab processing. Although this is the proper method, the deconvolution can enter significant error into the data, and in the case of poorly defined peaks (as with the 3T data), the deconvolution can give multiple results.

Once the integral or peak heights are determined, the values are imported into a Matlab program, and a least squares fit is performed to a variety of functions. The type of function used is determined by the type and number of spin pools in the sample. In these studies, three primary spin pools were determined to exist, and thus a three exponential fit was used. A stretched bi-exponential function was also fit to determine the distribution of spins. The data reported from the fits included T_2 bounding times and spin population percentages.

5.1.2.4. Pulsed-Gradient Stimulated Echo Diffusion Experiments (PGSTE)

The PGSTE diffusion experiments were performed using a stimulated echo sequence (90° - τ - 90° - Δ - 90°) with a pair of pulsed gradients. The purpose of the PGSTE experiments was to measure the diffusion coefficients of the various spin pools in the resin samples. The stimulated echo sequence was initially described by Hahn in 1950 [11] and further explained by Callaghan [12]. The use of the PGSTE for diffusion experiments is also described by Callaghan [13], and

also by Sodickson and Cory [¹⁴]. The diffusion experiments were all run using MAS on the 12T magnet. There were three sets of PGSTE experiments run with the resin samples. In the first set of experiments, only the echo time (τ_e) was varied to determine the effect on diffusion by removing a spin pool with short T_2 decay time. The second set of experiments kept the diffusive attenuation coefficient constant and varied the diffusion time, Δ . The third set of experiments used a precursor CPMG experiment (defined above) to allow long T_2 decay in order to isolate the diffusion coefficient of a long-lived component. The PGSTE experiment used in these studies is shown in Figure 5.5.

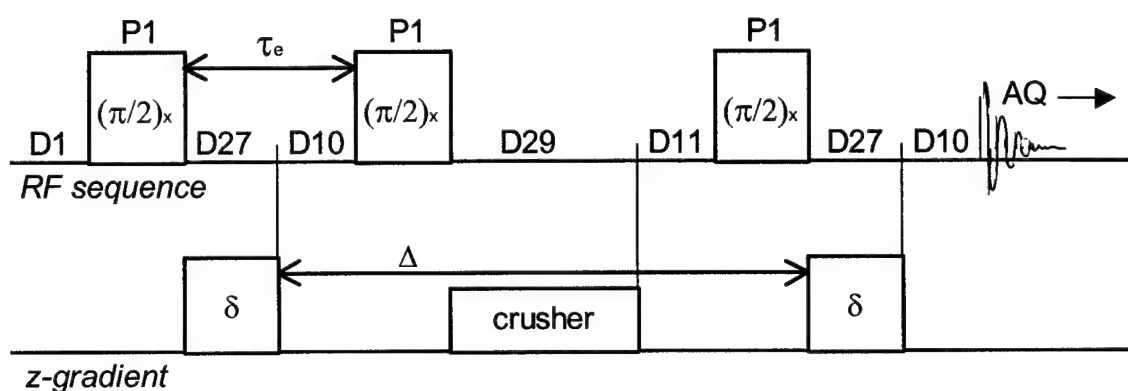


Figure 5.5: PGSTE pulse sequence used for the diffusion experiments. The figure shows the T_1 delay time (D1), the 90-degree pulse lengths (P1), the pulsed gradient times ($d27=\delta$), the crusher gradient time (D29), the echo time (τ_e), the storage time (Δ), and the acquisition time (AQ). The storage time is varied in some experiments and the gradient strength is varied in others. The echo time can be manipulated to eliminate faster decaying components.

5.1.2.4.1. Initial Setup: All diffusion measurements were performed on the 12T magnet with MAS. The initial setup was the same as the CPMG experiments except there was no variable cycle list, however, gradients were used in these experiments. The gradient strength was incremented from zero to some percentage of the maximum gradient value. This was accomplished by using a 2D gradient loop that incremented the gradient for each experiment for 1 TD times. Therefore, 1 TD is set to the number of experiments or gradient steps from 0 to some maximum.

5.1.2.4.2. Parameter Determination: The value of D1 and P1 were determined as stated in section 5.1.1.1. In the PGSTE experiment, two important parameters must be determined first in order to establish the sequence delay times are the echo time, τ_e , and the storage, or diffusion time, Δ . The two parameters are defined below in terms of the sequence pulse and delay times.

$$\tau_e = D27 + D10 + 2*(P1/2) + 6\mu s$$

$$\Delta = D29 + D11 + D10 + 2*P1 + 9\mu s$$

The echo time, τ_e , is normally set to be less or more than some minimum T_2 time. Once τ_e is determined, the gradient on-time, D27 or δ , must be set to be long enough relative to the eddy current time (on the order of a few hundred microseconds), but small enough to protect the gradient amplifiers and coils. The diffusion time, Δ , is often varied over some range to determine the type of diffusion in a sample (i.e. bounded or unrestricted, long or short).

The ideal goal of a well-formed PGSTE experiment is to cover all of the diffusion regimes while getting the maximum dynamic range of diffusive attenuation. In order to compare the results of diffusion experiments with varying storage (Δ) or echo times (τ_e), the maximum gradient strength was changed in order to keep the value, q , constant as seen in the following equation for diffusive attenuation (A).

$$A = e^{-q} = e^{-D\gamma^2 g^2 \delta^2 \left(\Delta + \frac{2\delta}{3} \right)}$$

Therefore, since δ is set by the echo time (τ_e), γ (the gyromagnetic ratio) is constant, and D (the diffusion coefficient is bounded), the maximum gradient strength (g) and the diffusion time (Δ) can be balanced to keep the attenuation A relatively constant (usually calculated for $A(q)/A(0) = 0.1$). By determining the parameters in this manner, the diffusion coefficient, D , can be isolated and measured directly.

5.1.2.4.3. Data Collection and Processing: The PGSTE experiment is run in a 2-D acquisition mode. The resultant “ser” data is processed on the spectrometer as described in section 5.1.1.3. The 2rr files are then brought into Matlab and least squares fit to single or double exponential functions. The resultant data produces an effective diffusion coefficient for each storage/diffusion time and for the varying echo times.

5.1.2.5. Goldman-Shen Exchange Experiments

In these studies, the Goldman-Shen experiments [¹⁵] measure the transfer of water molecules from some bound pool into a second spin pool (either free or interstitial space). This transfer process is the result of molecular diffusion and/or chemical exchange of the protons between adjacent water molecules. The purpose of the Goldman-Shen experiment is to determine the exchange rate and subsequent correlation time of water transfer from some bound spin pool into a free and/or interstitial water volume.

The Goldman-Shen experiment is designed to eliminate a fast T_2 decaying component and allow a slower decaying component time to re-populate the fast decaying spin volume. In these experiments, the fast decaying volume is associated with the bound water fraction, and the slower decaying fraction is in the free and interstitial volumes. Once the fast decaying component is eliminated, the only way to re-populate this spin pool is through exchange processes. MAS techniques are used to measure the various spin pools. The bound water peak is shifted (approximately 50 Hz on the 12T), so it is easy to measure the decay and growth of the bound component. The resultant data is only the peak height data from the bound water spectra. The Goldman-Shen experiment is shown in Figure 5.6.

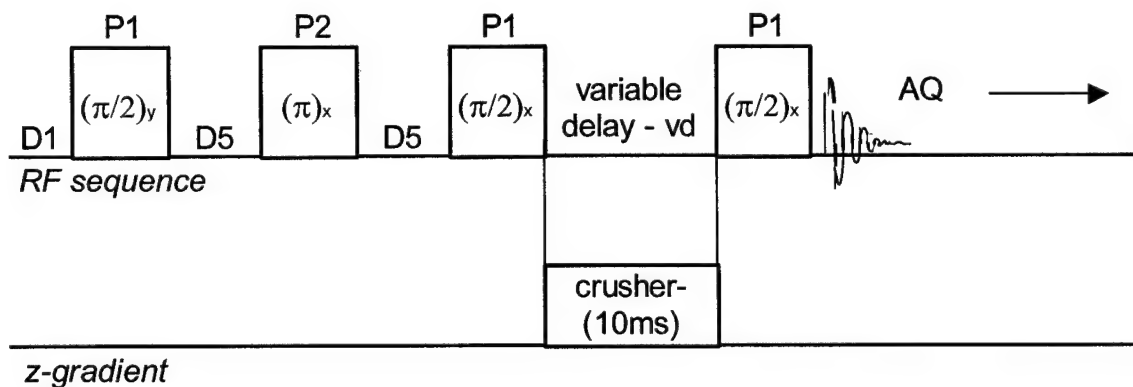


Figure 5.6: Goldman-Shen pulse sequence used for the exchange experiments. The figure shows the T_1 delay time (D1), the 90-degree pulse lengths (P1), the 180-degree pulse length (P2), the fast T_2 decay time (D5), the crusher gradient with fixed time (10ms), the storage time with variable delay (vd), and the acquisition time (AQ). The D5 decay time was set to 5 ms to allow the fast T_2 decaying component (bound water, $T_2 < 5\text{ms}$) to be eliminated. The storage time is varied to allow time for the bound water volume to be re-populated. The 180-degree pulse is used to refocus the slower decaying components.

5.1.2.5.1. Initial Setup: All Goldman-Shen experiments were performed on the 12T magnet using MAS techniques. The initial setup was same as the diffusion and CPMG experiments, with the additional need of determining the required number of experiments ($1/TD = L4$), which is the number of storage times in the variable delay, or "vd", list. The number of experiments is determined by the interval and range of storage times necessary to re-populate the bound water volume.

5.1.2.5.2. Parameter Determination: The first parameters that need to be found were the T_2 times for the bound and free/interstitial water. These times came from the CPMG experiments, and it was determined that the bound water decays on the order of a few milliseconds while the free/interstitial water decays at times greater than 100 ms. The CPMG data allowed the D5 decay time to be set at 5 ms. The next parameter that needed to be known was the interval and range of the storage times. The interval for the vd list is based on the exchange correlation time, so that the re-population of the bound fraction can be measured prior to T_1 decay. The correlation time was roughly determined by a series of 1-D Goldman-Shen experiments. These 1-D studies indicated the crossover point between exchange and pure T_1 decay. From this information, the initial storage time was set to 100 ms and the time interval set to 20 ms. The number of experiments, or vd list delay times, was determined from the inversion recovery data. The T_1 for the resin samples was determined to be approximately 1.2 seconds, so this allowed for the collection of 64 spectra at 20ms intervals (1340ms max storage time).

5.1.2.5.3. Data Collection and Processing: The data was acquired and collected in a 2-D mode, where the data is stored in a ser files as a series of FIDs. The ser data was then processed on the spectrometer the same as the CPMG and PGSTE data. The peak heights from the bound water peaks were measured, imported into a Matlab program, and plotted versus the storage time. The Matlab program was used to perform a least squares single exponential fit of the initial part (positive exponential portion) of the plot to determine the exchange rate and subsequent correlation time. The decaying portion of the data was also fit to verify the T_1 decay time.

5.1.3. NMR Imaging Experiments

The NMR imaging experiments consisted of a series of 2-D and 3-D image sequences. All imaging experiments were performed using the 3T magnet and the flow system described in section 6.0. The 2-D and 3-D image sequences are fundamentally the same experiments, with the 3-D images having a second encoded direction. Since the 3-D imaging techniques can be considered an extension of the 2-D techniques, this section will present the procedures for 3-D imaging in terms of a series of 1- and 2-D experiments.

The purpose of the 2-D imaging was to observe flow behavior through the resin materials and attempt to quantify non-linear flow phenomena. One parameter that was of interest was channeling and preferential flow pathways. The 2-D images provided thin cross-sections of the resin, which allowed for visualization and quantification of the areas occupied by the fluid. The 2-D images were also useful to determine where the sorption of the Gd occurred. The purpose of the 3-D images was qualitative by providing a visualization of the heterogeneous flow pathways and sorption sites in a relatively homogeneous matrix.

5.1.3.1. 3-D Slice-Selective Spin Echo Sequence

The primary imaging sequence used is the 3-D slice-selective spin echo sequence and is shown in **Figure 5.7**. The simple spin echo [¹⁶] sequence is a 90-degree RF excitation pulse followed by an echo delay time and a 180-degree pulse, or [90-τ-180-acquire]. The result of this sequence is an echo with an amplitude relatively the same as the initial excitation. This slice-selective spin echo sequence uses an initial soft, or shaped, pulse as the primary excitation. The purpose of the soft pulse is to limit the bandwidth of the excitation, thus resulting in a smaller spatially excited region or otherwise called a slice (Δz = slice thickness in cm). With proper refocusing of the soft pulse using a gradient echo, the excited bandwidth (Δf) is as follows, where γ is the gyromagnetic ratio (Hz/G), G is the gradient amplitude (G/cm), and τ is the half of the primary soft pulse length (s).

$$\Delta f = 2/\tau = (1/2\pi) * \gamma * G * \Delta z$$

Using this relationship, it is possible to get slice selection in the sub-millimeter range, however it should be noted that there is significant loss of signal as slice thickness decreases. The 3-D imaging sequence uses gradient spatial encoding in the x-, y-, and z- directions to

reconstruct images in three dimensions. The gradient along the z-direction is often used for slice-selection and phasing encoding. The y-gradient is typically a second incremented phase encoding gradient, and the x-gradient is the read or frequency-encoding gradient. The 2-D sequence is similar to the 3-D sequence with the slice-selective gradient typically in the y-direction, the read gradient on the z-direction, and the incremented phase gradient along the x-direction.

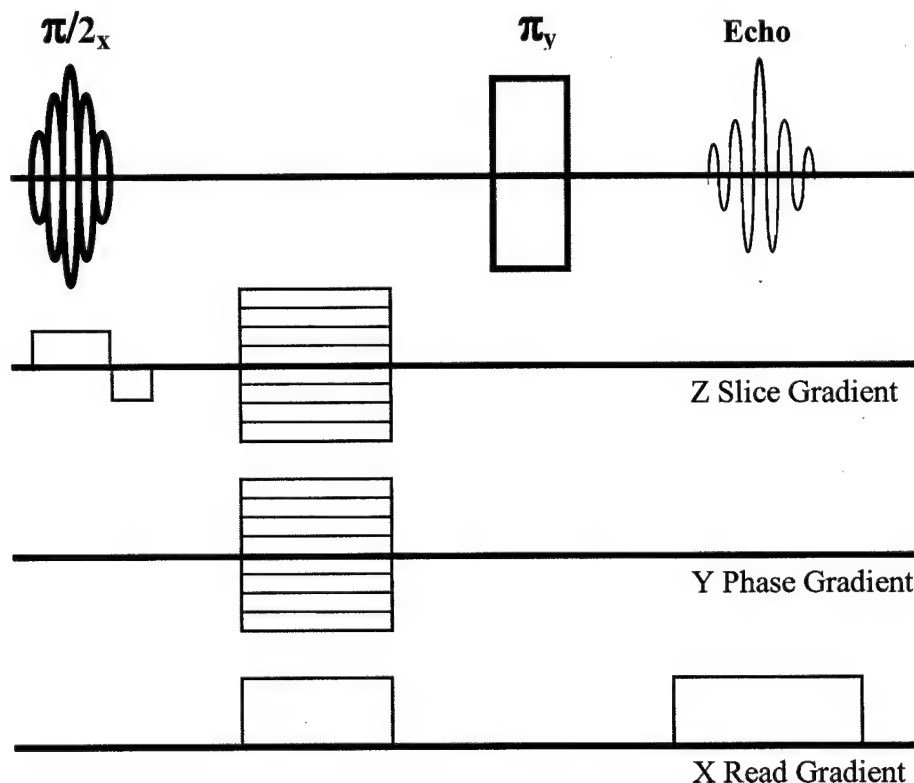


Figure 5.7: 3-D slice-selective spin echo imaging sequence for use in the resin imaging experiments. The first line of the figure shows the RF pulse sequence, where the first pulse is a 90-degree shaped pulse, the second pulse a 180-degree refocusing pulse, and the resultant echo. The second line shows the z-gradient sequences showing the slice-selective gradient and the incremented phasing encoding gradient. The third line is the y-gradient with a second increment phase encoding gradient, and the final line belongs to the x-gradient with a frequency encoding read gradient. The 2-D sequence is identical with the slice-selective gradient on the y-direction, the read on the z-direction, and the phase along the x-direction.

5.1.3.2. Sample Preparation and Flow System Setup

The first step in the resin imaging experiments was to construct the sample and prepare the flow system for imaging. The resin samples were all made in 10 mm outer diameter (OD) NMR flow-through tubes. The inner diameter (ID) of the medium wall tubes was approximately 8 mm, and the tube length was 18 cm. An image of a flow-through resin sample can be seen in Figure 5.8. It is important to note that since the resin sample must be placed in a high magnet field, none of the sample materials can have ferromagnetic properties, or otherwise perturb the magnetic field. The samples were prepared as follows:

- The resin (RF, CF, or PF) was prepared according to the procedures in Appendix 1.0.
- The tube was acid washed and dried prior to use.
- A 4 cm long flow-through spacer, double screened at the inner end, was placed in one end of the tube. The screen material is 50 μm mesh that was sized to hold the resin and glass diffuser beads. The screen material was made of 316 stainless steel.
- The NMR tube was placed in a vertical position, and the bottom end (with the spacer) was capped. This allows for the filling of the tube with sample materials.
- The tube was filled with de-ionized water, and approximately 2.0 g of 100 μm diameter high purity (biological grade) glass beads were dropped into the tube and allowed to settle. The tube was placed in an ultrasonic bath to ensure the diffuser beads were fully seated. The 2.4 g of glass beads displaces approximately 2.4 cm of the tube length. The diffuser beads act to hold the resin in place while allowing unrestricted fluid flow.
- With the tube filled with de-ionized water and in a vertical position, the resin was slowly dropped into the tube and allowed to settle. Most samples used approximately 0.2 g of dry resin that displaces about 1.2 cm of tube length. It was important to allow time for the resin to slowly settle since the resin swells with water. This is also the reason the tube can not be prepared dry. The tube with the resin and lower diffuser beads was again placed in the ultrasonic bath to ensure proper packing. The resin was given approximately 30 minutes to stabilize prior to the next step.
- At this point, the water in the tube is slowly drained to a point just below the top of the resin. This is necessary to prevent the top diffuser layer from mixing with the top end of the resin layer.

- With the top of the tube dry, approximately 1.0 g (1.2cm) of 100 μ m glass diffuser beads are placed on top of the resin layer. The tube is refilled with de-ionized water and placed in the ultrasonic bath to allow time for settling.
- The final step is to prepare a spacer segment (with double screening) that is the proper size to fill the remaining length of the tube. This step is very important to prevent movement of the resin and glass beads while under flow conditions. It is best to make the final spacer extend out of the tube approximately 1-2 mm, since the connections will seat against this spacer and provide constant compression on the sample volume.
- Now that the sample is prepared, the water is topped off in the tube and sealed to ensure the sample is fully saturated until the time of use.

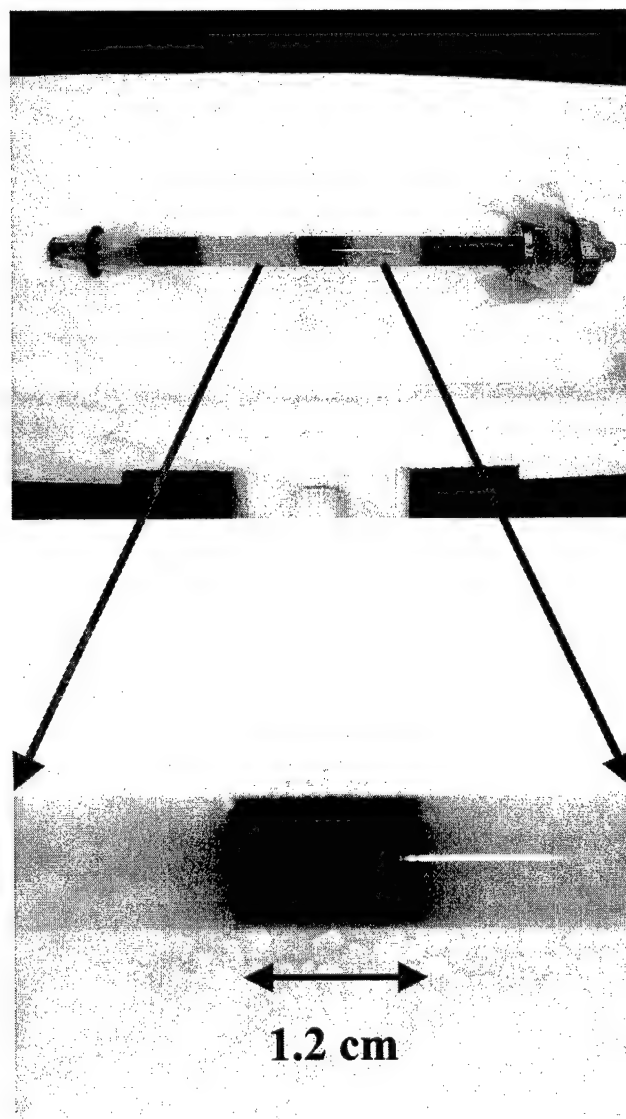


Figure 5.8: Photo of a flow-through resin sample. The image clearly shows the resin material (dark material in center-1.2 cm long), the glass bead diffusers bordering each end of the resin (white material), the spacers with double screening and each end, and one of the tube-to-tubing connectors (right side). It is clear from the bottom image the fine degree of separation between the resin and glass bead diffusers.

With the sample tube prepared, the next step is to place the tube in the flow system and de-aerate the sample according to the procedures in Section 6. The sample tube is mated to the flow system with the use of in-house designed connections. The connections are needed to mate the 1/8 in OD teflon tubing with the 10 mm OD glass NMR tube. Since the flow system can operate under negative and positive pressure (up to 1.0 MPa), the connections must be able to

hold a seal under tension and compression. In addition, there was the added constraints of limiting the compression on the glass tube (due to breakage), making the connections reusable (cost and sample recovery), and ensuring no ferromagnetic components were used. These limitations were overcome by using standard Swagelok♦ 1/8 to 3/4 inch connections. The stainless steel Swagelok♦ adapter was fitted with special sleeves to allow for the placement of a double o-ring compressive seal. In this NMR tube-to-flow tubing connection, as the Swagelok♦ fitting is tightened, the o-rings are compressed axially which then provides a radial seal with the inner housing of the Swagelok♦ adapter. The sample tube-to-tubing connections are shown Figure 5.9.

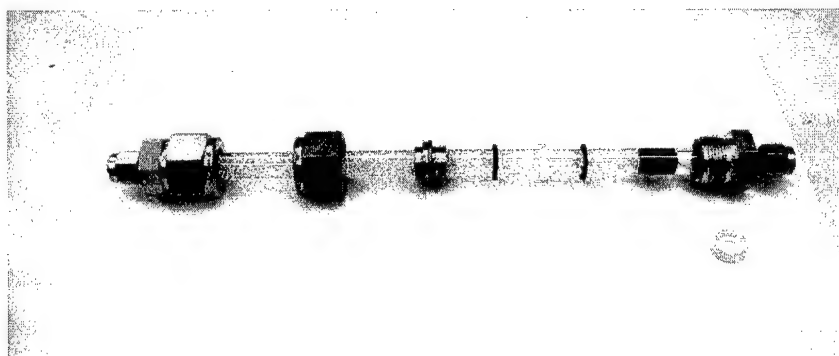


Figure 5.9: Photo of NMR flow-through sample tube showing the tube-to-tubing connections. An assembled fitting is on the left side of the image and an exploded view of the fitting is on the right end. From the right, the exploded view shows the 1/8 in to 3/4 in Swagelok♦ adapter (male end), the 1st o-ring, teflon spacer, 2nd o-ring, brass spacer fitting, the female Swagelok♦ nut, and teflon seating piece which placed in the bottom of the male Swagelok♦ piece.

5.1.3.3. Imaging Experiment Analysis

With the sample tube connected to the flow system and properly de-aerated according the procedures in Section 6.0, the imaging setup procedures can begin. The initial setup for an imaging experiment begins with a general understanding of the sample to define the imaging protocols that must be used. For the resin samples, the grain size was on the order of 80-125 μm mesh, so the desired spatial resolution is about 100 μm . The resin samples also sorbs the Gd quite readily, and once bound, the T_2 for the surrounding protons becomes very short. This allows for the use of T_2 contrast to differentiate the bulk water signal from that of the water near the Gd. Based on this information, it was determined that the simple spin echo sequence with an echo time of a few milliseconds was enough to eliminate the Gd solution signal while

maintaining the bulk water signal. In this mode, the water-saturated resin was the baseline intensity and as the Gd solution entered the resin, the clean water was displaced and the NMR signal was reduced accordingly.

For imaging experiments, the acquisition time (AQ) along with the number of time domain points (TD) and dwell time (DW) are critical parameters that need to meet some strict criteria. One such criteria is the Nyquist condition which drives the sampling frequency, or dwell time, based on the desired spatial resolution (Δx), and acquisition time (AQ) and strength (G). The Nyquist condition requires that at least two data points must be collected for each periodic cycle in order to define the frequency. In spin echo imaging experiments, the AQ is set to twice the gradient on time to maintain a constant gradient amplitude, and thus, the minimum DW and TD combination can be set. The Nyquist condition for spin echo imaging is given by the following equation, where γ is the gyromagnetic ratio.

$$\text{Nyquist Condition, } \Delta x = 2\pi / k_{\max}$$

$$\text{where, } k_{\max} = \gamma * G * AQ = \gamma * G * TD * DW$$

Additionally, the criteria for meeting the spatial resolution in the final image must be determined to set the TD. For a Fourier transformation (FT) with zero filling, the SI, or number of pixels, can be set to twice the TD. Therefore, if the field of view is 8 mm and the desired spatial resolution is 80 μm , the number of pixels must be 100 corresponding to a TD of 50. Another criterion to factor into the setup is the range of spectral frequencies in the sample line shape. The broadness of the line shape (FWHM) and the number of pixels desired is related to the total spectral width ($[SWH = 1/2 * DW]$) as follows.

$$SWH = (2 * DW)^{-1} = FWHM * (\# \text{ of pixels})$$

With a FWHM for a resin sample of 500 Hz and the desired number of pixels as 128 (best to maintain a factor of 2), the SWH is 64 kHz corresponding to a minimum DW of about 8 μs .

However, now the practicality of the imaging system must be factored into the imaging setup. The 3T spectrometer in its current configuration is limited to a maximum gradient strength of 60 G/cm. Using this maximum G value and the 80 μm resolution, the maximum AQ must be about 6 ms. Additionally, due to the unshielded configuration of the gradient coil, the eddy currents can interfere with signal collection for up to 200 μs after the start and stop of a gradient pulse. This eddy current factor coupled with empirical evidence drives the minimum

gradient on time to approximately 1 ms, corresponding to an AQ of 2ms. With these constraints of the AQ ranging from 2-6 ms and the minimum DW of 8 μ s, the minimum TD is calculated to be 250 which is perfectly acceptable. Some tweaking of the setup parameters may be necessary, but with this setup approach, the experiment should be based on a sound evaluation.

5.1.3.4. Acquisition Parameter Determination

Now that the general system performance is understood and the governing criteria are established, it is necessary to determine the acquisition parameters and determine the NMR characteristics of the sample. In order to perform any NMR experiments, the water-saturated sample must first be tuned according to the procedures outlined in Section 5.1.2.1. Once tuned, some of the required acquisition parameters are determined using the procedures in 5.1.2.1. These parameters include the resonance frequency ($SFO1=BF1+O1$), and the 90- and 180-degree pulse times (P1 and P2). However, since this imaging sequence uses a soft pulse, the soft pulse time (P3) and attenuation (TP1) must be determined.

The P3 is determined from the required slice thickness. Once the slice thickness (Δx) and shape of the soft pulse (the three cycle sinc is used in these studies) is established, the parameters are plugged into the excitation bandwidth (Δf) equation, of Section 5.1.3.1, and the half pulse length, τ , is calculated. With the three cycle sinc pulse used in these studies, the full soft pulse time, P3, is $6*\tau$. Unlike the method for determining the 90-degree hard pulse time (P1), the soft pulse 90 is determined by adjusting the attenuation, TP1, and keeping P3 constant. The “dan.soft” pulse sequence, as seen in Appendix 2.0, is used to cycle through a series of TP1 values until a maximum peak height is established. The procedure for setting P3 is as follows.

- Set the P3 to the desired pulse length.
- Set to the TP1 to a large attenuation value. Usually 60 dB is sufficient.
- Reduce TP1 in 2 dB increments until a measurable signal is detected.
- Transform the FID with a FT and phase correct it with a PK.
- Continue lowering the TP1 in 1 dB increments until a maximum spectra is achieved. Note this value as the possible 90-degree attenuation value.
- Continue lowering TP1 to ensure the signal intensity decreases as the spins rotate past the 90-degree point. The 180-degree point is difficult to determine with a soft pulse, but effort

should be made to correlate the smallest signal with the 90-degree TP1 value. The TP1 is RF power attenuation so the doubling value should be at 6 dB increments.

The next step in establishing a soft pulse for use in the spin echo imaging sequence is to use a gradient echo to refocus the soft pulse excitation. This is performed using the "dan.softgrad" program from Appendix 2.0 and the following procedures. The goal of this procedure is to set the length, or time, of the refocusing gradient. Optimally this value should be exactly equal to $P3/2$, but due to many variables, this is not always the case.

- With the proper P3 and TP1 entered into the program and the gradient amplitude determined by the required spatial slice thickness, the length of the refocusing gradient (inverse portion of the encoding gradient) must be optimized.
- Set the refocusing gradient time to $P3/2$ and collect a spectrum.
- Cycle through the refocusing gradient time in 0.1 ms steps (plus and minus $P3/2$) until a maximum spectral intensity is obtained. This value should be close to $P3/2$ without leading to line broadening, which indicates more than half the echo is collected.
- Enter this time value in as the refocusing time.

Now that the required parameters are known, some basic experiments will be run to define some NMR characteristics of the sample. The first experiment is an inversion recovery experiment (Section 5.1.1.2) to determine the T_1 of the sample. Once this is known, the relaxation delay time (D1) is set to 5 times the T_1 . If the D1 time proves to be too long for the imaging experiments, a shorter time may be used if there is a sufficient signal-to-noise (S/N) ratio and the imaging sequence is started with a proper series of dummy scans. The next basic NMR parameter to know is the T_2 relaxation time. This value is determined using a CPMG experiment (Section 5.1.2.3). The T_2 is necessary to determine the range of echo times that can be used in the imaging experiments.

5.1.3.5. Final Setup and Sequence Development

With the selective pulse properly configured and the T_1 and T_2 relaxation times in hand, the next step is to determine the actual gradient strengths and delay times for the final imaging sequences. This step can be considered a fine-tuning or optimization of the basic sequence development. The methods used to optimize the imaging sequences are normally difficult to define since there are many non-linear variables inherent in complex imaging sequences. Some

of these non-linearities include eddy currents, switching times, and sample dependent factors. It is also important to learn more about the sample behavior under the image sequence conditions to determine the degree of signal averaging that must take place to improve the signal-to-noise ratio. Remember that a 3-D image sequence can take hours to days to complete, and thus it is imperative that the image sequence is proven prior to performing a lengthy experiment. Therefore, to optimize and validate the sequence, it is best to run through a series of 1-D image sequences with all of the parameters previously established. This technique is used to determine the best combination of gradient times/amplitudes, delay times, and acquisition parameters. The 1-D sequences discussed below are all found in Appendix 2.0. Although the ranges of some of the acquisition parameters are set by the criteria established in previous sections, the precise values must be established to produce a well-formed imaging experiment. Any significant changes to the parameters previously established should be checked against the experimental criteria to ensure the Nyquist condition continues to be met and the spatial resolution is sufficient.

The first 1-D imaging sequence is "dan.se1d". This sequence is a hard 90-degree pulse and is used to determine the proper read gradient times and eddy current delay times to center the echo in the acquisition window. The gradients should be checked in all three dimensions, and the optimal times documented. In this sequence, the centered echo should be transformed (FT) and a magnitude calculation (MC) performed to visualize the cross-section of the sample for each dimension. Assuming the sample is uniformly distributed in the sample tube, the three image cross-sections should all appear relatively centered and well formed. Any deviation from a half-circle for the x- and y-directions or a top-hat for the z-direction could indicate problems with timing or initial setup. The spectral widths of the 1-D cross-sections should also be checked and verified with the values previously calculated. These optimized cross-sections should be stored for comparison with the next slice-selection sequence. The delay time after the 180-degree pulse can also be optimized in this "se1d" sequence.

The next 1-D sequence to evaluate is "dan.imsess", which is the slice-selective version of the "se1d" sequence. The sequence should be run in all three dimensions, as above, and the resultant slices compared against the full-width cross-sections. The slices should be centered (or properly offset by $tpoffs1$) with the full-width images. The spectral width of the slices should

also be measured and compared with the calculated values. The gain (RG) should also be set in the “imsess” sequence, since the S/N has dropped due to the application of the selective slice.

The next step is to run a 2-D sequence with a hard, 90-degree sequence (dan.se2d) in order to ensure the phase gradient is properly configured. Once processed, the image should appear symmetric in the viewing window and relatively centered. This is also a good time to look for artifacts, such as ghosting or repeating hot spots, which could be caused by improper phase cycling, processing errors, or timing problems. Once the “se2d” images look good, the “dan.imsess2d” sequence should be run using the phase gradients on both the transverse (x and y) and axial (z) directions. This is to optimize the gradients for the 3-D imaging. The 3-D setup is now complete, and the “dan.imsess3d” sequence is ready to run.

5.1.3.6. Processing the 2-D and 3-D Data

Once the data is collected in by either the 2-D or 3-D imaging sequences, the raw NMR data must be processed and converted into a usable format. Both sets of data are initially processed on the spectrometer. The 2-D data is processed using a 2-D Fourier transform with automatic baseline correction and magnitude calculation (XFB). This 2-D processed data is stored as a 2rr file that can be imported into Matlab for direct viewing. The 3-D data must first be configured into the proper format using an “r23m” command, which stores the data as a series of slices. The data is then Fourier transformed, magnitude calculated, and baseline corrected using the “imft3d” Bruker AU macro. The resultant data can then be imported into Matlab or some other multi-image manipulation package for assembly into one complete three-dimensional image.

5.2. Inductively Coupled Plasma – Atomic Emission Spectroscopy (ICP-AES) Analysis

The effluent from the gadolinium (Gd) flow experiments was analyzed using Inductively Coupled Plasma - Atomic Emission Spectroscopy (ICP-AES). The ICP-AES an analytical tool used to determine the Gd concentrations in solutions. This section includes a brief description of the ICP-AES technique and the procedures used in analyzing the samples.

5.2.1. Overview of the ICP-AES Technique

In general, the ICP-AES is part of a broad range of chromatographic spectroscopy used to analyze various elements through atomic excitation and subsequent emission of photons. The rate and wavelength(s) of the emitted photons can be correlated with known emission spectra for elemental identification and quantification. More information on the ICP-AES technique can be found in Castellan [¹⁷].

The ICP-AES works on the principle of plasma generation to excite and transfer energy to a continuous stream of sample. This is accomplished by first ionizing argon (Ar) atoms with an ignition device. The ionized argon ions are then sent through a radiofrequency (RF) coil that generates a rapidly oscillating electromagnetic (EM) field. The EM field couples with the Ar ions transferring energy to other atoms producing a continuous excitation until a steady state is reached. This steady state of ionized atoms defines the plasma, which maintains a continuous population of ionized atoms in the induction region. At this point, a liquid sample can be introduced at a continuous rate into a nebulizer module. The nebulizer creates a fine mist or aerosol that is injected into the induction region. In the induction region, the sample atoms go through collisional excitation with the carrier Ar atoms, which results in an increase in the atomic energy state. Upon de-excitation, the sample ions relax to some lower energy state(s) with the emission of photons. The photon wavelengths are directly related to the difference in energy levels, and thus the emission spectrum is element specific. A photon spectrometer measures the photon energy and emission rate, and produces a photon count rate based on the wavelength(s) selected. This count rate is directly proportional to the number of atoms in the detection volume, and thus the spectrometer output can be directly related to an atomic density or concentration.

5.2.2. ICP-AES Description

The specific ICP-AES system used for this work is the Spectroflame ICP-D model Inductively Coupled Plasma - Atomic Emission Spectroscopy system. The unit is user maintained and calibrated with biannual service and inspection performed by Spectro Analytical. The system and operating procedures are further described in the operating manual [18]. The specifications for the system are as follows and a photo is shown in Figure 5.10.

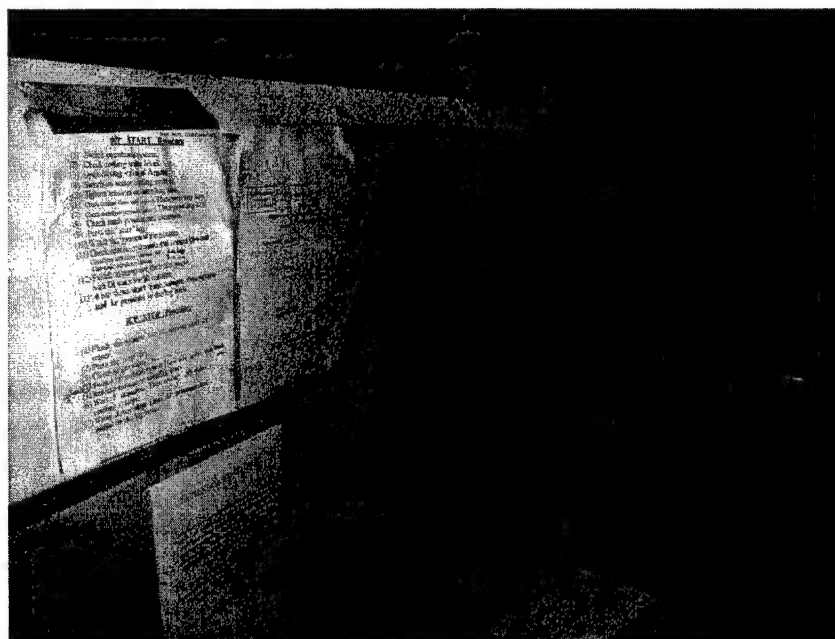


Figure 5.10: ICP-AES system used to measure the concentration of metals and other elements with fluorescence spectra. This unit was used in these studies to measure Gd solution concentration in the range of 1 μM to 2 mM using a standard nebulizer. Lower-limits of detection can be decreased by one to two orders of magnitude with an ultra-sonic nebulizer.

- Spectrometer: direct wavelength drive, fixed grating, Pashen-Runge mount, focal length 750 mm, holographic grating on Zerodur blank, temperature stabilized construction, and four entrance slits
- Monochromator #1: grating 2400 lines/mm, dispersion 0.55 nm/mm, wavelength coverage 190 - 460 nm (165 - 460 nm, w/ N_2 purge), flushed direct optical path for low wavelength
- Monochromator #2: grating 1200 lines/mm, dispersion 1.1 nm/mm, wavelength coverage 240 - 790 nm
- Sample Introduction: integrated peristaltic pump, pneumatic nebulizer w/ conical spray chamber, fixed torch, argon humidifier, temperature controlled sample compartment
- RF Generator: 2.5 kW maximum output power, 27.12 MHz operating frequency, power and frequency stabilized, microprocessor controlled, auto-start, integrated water cooling system

5.2.3. ICP-AES Sample Preparation

Since the nebulizer produces a very fine aerosol, it is necessary to filter all samples that may contain particles in excess of few microns. Therefore to prevent clogging, the samples were filtered a 0.45 μm filter prior to analysis. Another factor to consider is preparing samples for analysis is the range of concentrations. There is minimum and maximum count rate that the spectrometer can measure without poor signal-to-noise ratio or saturation. For the Gd samples and the normal nebulizer (non-ultrasonic), the measurement range was approximately 1 to 2000 μM . Therefore, any concentrations above 2 mM should be diluted to between 1 μM and 2mM. Measurements below 1 μM are considered inconclusive. A third factor to consider when dilution is necessary is to maintain continuity among sample solution chemistry. All samples and standard solutions should be prepared with the same dilution solution (i.e. same de-ionized water source and/or low concentration acid). This is necessary to avoid interferences with measurements (i.e. changes in background at the wavelength of interest), or hold-up and release problems due to changes in fluid chemistry (i.e. pH variations releasing sorbed metals). The incorporation of 0.1 M nitric acid into the standards and solutions is beneficial to reduce sorption on sample container walls or in sample analysis.

5.2.4. Calibration and Background Determination

In order to correlate the photon count rate output with a concentration, it is necessary to perform a calibration using a traceable standard solution. For these studies, the only element of interest was Gd, so calibration curves for Gd were the only ones produced. The calibration starts with the production of a range of Gd standards. Normally three to five concentrations were used, and these standards ranges from 0.01 $\mu\text{mol/L}$ (μM) to 10 mM. Once the typical measurement range was determined, the standards were normally in the range of 1 to 1000 μM . The standards were made using a certified stock solution of 6.39 mM Gd from Aldrich Chemicals (Gadolinium are ICP/DCP standard solution, $[\text{Gd}] = 1005 \mu\text{g/mL}$). Once the standards were prepared, they were analyzed using the measurement procedure in the following section. Before, during, and after the standard analysis, a blank flush solution (0.1 M HNO_3) was analyzed to produce a lower

level of detection for the system. The resulting photon count rate data (counts per second – cps) was then plotted versus the known concentration, and a linear, least-squares fit to the data was made to determine the calibration factor ($\mu\text{M}/\text{cps}$). The background or blank data was also plotted to determine a lower level of detection. An example of a calibration and background determination plot is shown in Figure 5.11.

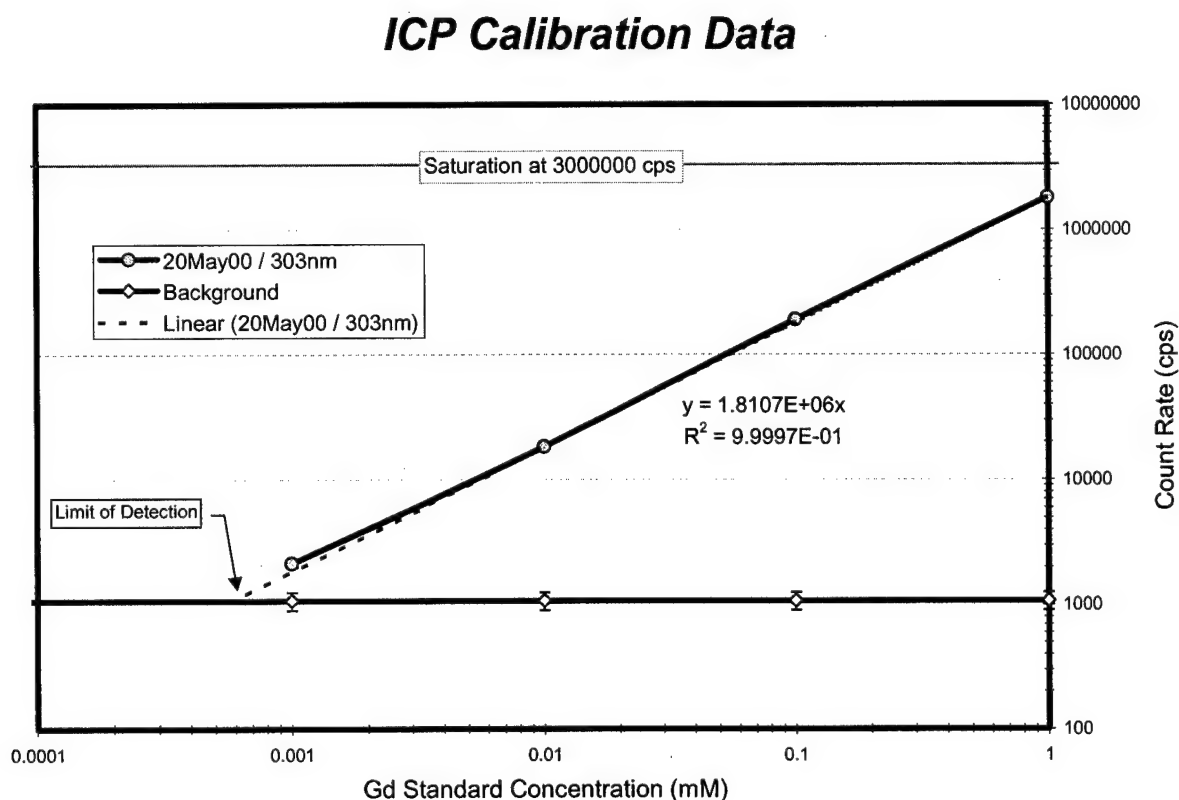


Figure 5.11: Plot of ICP-AES calibration data showing the Gd standard solution concentration (mM) versus the measured count rate (cps). The calibration factor is $1.8107E6$ cps/mM. The lower limit of detection is approximately $0.6 \mu\text{M}$. The background count rates taken at various points between the calibration intervals are also plotted. The one standard deviation error bars plotted for all data points. The errors are too small on the Gd standard data to be seen.

5.2.5. Initial Setup

Prior to running any samples, a method to introduce and analyze the samples needed to be developed. This was accomplished using the method development procedure. The method created was called "Gd Counts", referring to only raw count rate data. The important method parameters are as follows.

- Measurement Line: 303.284 nm
- Coolant Temperature: 15 °C
- Argon Pressure: 100 psig
- Coolant Flow Setting: 40
- Nebulizer Pressure: 3.3 bar
- Pre-Flush Time: 45 s
- High Flush Time: 15 s
- Pump Speed Setting: 2 (high flush), 1 (low flush and measurement)
- Measurement Time: 100 % (100% = 2 seconds)
- # of Measurements: 3 per sample

5.2.6. ICP-AES Measurement Procedure

The following procedure was used to measure all samples including standards and blanks.

- 1) Turn on exhaust vent, water coolant supply, and argon gas.
- 2) Inspect ICP tubing and nebulizer prior to use.
- 3) Transfer the waste outlet tube to the appropriate waste collection container.
- 4) Start the ICP system following the standard operating procedures. The plasma is ignited.
- 5) Allow the system to flush for at least 15 minutes with de-ionized (DI) water or 0.1M HNO₃ (flushing fluid).
- 6) Load "Gd Counts" method.
- 7) Re-profile ICP optics using the re-profile command in the <F3> menu.
- 8) Run a series of blanks and check counting rates and statistic for consistency.
- 9) Wipe sample inlet tubing with a clean Kimwipe between each sample introduction.
- 10) Run standards. The standards should be run from lowest to highest concentration. Run a blank between each standard to ensure there is no hold up.
- 11) Press <F4> to start new sample.
- 12) Enter a brief sample description.
- 13) Insert sample inlet tube into sample and ensure it stays submerged in sample during flush and sampling periods.
- 14) Press <F12> to begin measurement.
- 15) The ICP will measure the sample 3 times, printing out the observed intensity after each measurement.
- 16) After the third measurement, press the <F7> key to get the average and standard deviation in the measurement.

- 17) Remove the sample inlet tube from sample. Wipe with Kimwipe. Return it to flush fluid container.
- 18) Repeat the procedure from step 11) with the next sample. After measuring 6 to 8 samples, the system should be re-profiled (step 7). After re-profiling, a standard should be run. If the results from the standard are in agreement with the results obtained previously, it will not be necessary to repeat all of the standards.
- 19) After all of the samples have been measured, re-measure all of the standards and blanks in the same order as initially done.
- 20) Once the standards have been run again, the shutdown procedures can be started. Follow the standard operating procedures listed on the machine (and in the users manual).
- 21) After the ICP is shutdown, return the waste outlet tube to the default waste storage container. Return waste container to satellite accumulation point.

5.2.7. Data Collection and Processing

With the count rate, calibration and background data in hand, it is necessary to convert the data into Gd concentrations. All of the data is imported into a Microsoft (MS) Excel spreadsheet. Assuming the background data was relatively consistent (within one standard deviation) over the measurement interval, the background measurements are averaged to get a single background count rate. This average background rate is then subtracted from all sample and standard measurements to get the net count rate. The Gd standards net count rates are then plotted versus the known Gd concentration, and the data is fit to linear extrapolation through the zero concentration-zero counts point. This type of fit proved very successful, and resulted in a single calibration factor to convert count rate data directly to Gd concentration.

References for Section 5.0

- ¹ E.R. Andrew, A. Bradbury, and R.G. Eades, *Nature*, 182, 1659, 1958.
- ² Bruker Instruments, Inc.
- ³ Matlab by The Math Works, Inc., version 5.3.1.29215a(R11.1), 28 Sep 99.
- ⁴ T.C. Farrar and E.D. Becker, *Pulse and Fourier transform NMR*, Academic Press, New York, 1971.
- ⁵ D.I. Hoult and R.E. Richards, *Proc. Roy. Soc. (London)*, A344, 311, 1975.
- ⁶ J. Kowalewski, G.C. Levi, L.F. Johnson, and L. Palmer, *Journal of Magnetic Resonance* 26, 533-536, 1977.
- ⁷ H.Y. Carr and E.M. Purcell, *Phys. Rev.*, 94, 630, 1954.
- ⁸ S. Meiboom and D. Gill, *Rev. Sci. Instr.*, 29, 688, 1959.
- ⁹ P.T. Callaghan, *Principles of Nuclear Magnetic Resonance Microscopy*, Oxford Press, New York, pp74-5, 1991.
- ¹⁰ G. Bodenhausen, R. Freeman, and D.L. Turner, *J. Magn. Reson.* 27, 511, 1977.
- ¹¹ E.L. Hahn, *Phys. Rev.* 80, 580, 1950.
- ¹² P.T. Callaghan, *Principles of Nuclear Magnetic Resonance Microscopy*, Oxford Press, New York, pp75-6, 1991.
- ¹³ P.T. Callaghan, *Principles of Nuclear Magnetic Resonance Microscopy*, Oxford Press, New York, p166, 1991.
- ¹⁴ A. Sodickson and D.G. Cory, *Progress in Nuclear Magnetic Resonance Spectroscopy* 33, 77-108, 1998.
- ¹⁵ M. Goldman and L. Shen, *Phys. Rev.* 144, 321, 1966.
- ¹⁶ E.L. Hahn, *Phys. Rev.* 80, 4, 580-594, 1950.
- ¹⁷ G.W. Castellan, *Physical Chemistry*. 3rd Ed., Benjamin/Cummings Publishing Co. Menlo Park, CA., 1983.
- ¹⁸ SPECTRO ANALYTICAL INSTRUMENTS GMBH. Spectroflame Modula; Spectroflame EOP Operation Manual. Kleve, Germany.

[THIS PAGE INTENTIONALLY LEFT BLANK]

6. NMR FLOW SYSTEM

This section describes a flow system built and used for the imaging experiments in Section 8. A complete description of the flow system and its performance characteristics are provided in the format of a technical report. The enclosed technical report has been submitted to the journal *Measurement Science and Technology* and is currently in the review process.

ABSTRACT

NMR imaging is an emerging non-invasive tool to provide qualitative and quantitative information in the study of flow in granular media. Here, NMR imaging is applied to the investigation of contaminant transport in environmental groundwater systems. NMR can provide critical insight into both near real-time transport and chemical speciation parameters of environmental systems. However, the quality and utility of the data obtained is often degraded by the presence of air bubbles. These air bubbles are direct sources of NMR susceptibility effects that result in image distortions and signal attenuation. An experimental flow setup is described which minimizes the presence of air bubbles through water deaeration followed by over-pressurization. Experimental results show the degree of effectiveness for air bubble removal.

6.1. Introduction

Nuclear Magnetic Resonance (NMR) imaging is a powerful means for exploring the structure and dynamics of fluids in granular media [¹⁻⁹]. Some properties which are readily measurable using NMR include the porosity of heterogeneous systems, mobile and immobile pore zones, complexation sites, and the overall flow structure of the system [¹⁰⁻¹⁴].

One of the greatest challenges in NMR imaging of granular media is the seemingly trivial but, in practice, persistent complications that arise from the local susceptibility distortions from air pockets [¹⁵]. In most heterogeneous granular systems, complete saturation of all void spaces is very difficult, and in some systems, total saturation is not possible.

A technique described below that can be used to reduce the presence of air in water-saturated granular media samples is efficient deaeration followed by high pressure. The deaeration technique varies for each sample type, but typically involves exposing the sample to high vacuum followed by imbibition with a de-aired liquid. The high-pressure, or over-pressurization, technique is the pressurization of the system up to 0.6 MPa (~6 atm). The degree of pressurization and required diffusion time is sample and experiment dependent.

6.2. NMR Susceptibility Effects

In heterogeneous samples, local magnetic fields are created by spatially varying magnetic susceptibility. On a macroscopic scale, these susceptibility effects generally result in complex field distortions and signal attenuation from molecular diffusion through large internal magnetic field gradients. Whenever spatial discontinuities exist within a sample, a macroscopic influence is created from the local magnetic field distortions associated with variations in the bulk susceptibility. This local variation results in a new mean magnetic field in the sample, $B_o(r)$ which is shifted from the applied free-space magnetic field, B_o^{free} , by the spatial diamagnetic susceptibility, $X_m(r)$. In granular media samples, the largest such disturbances are the small regions of inhomogeneity created by air bubbles within the water-saturated media. The susceptibility artifacts from air bubbles are much more pronounced than the granular media artifacts since the susceptibility mismatch between the air and water is much greater than that between the media and the water. For example, the molar susceptibility for air is approximately $+8.98\text{E-}9 \text{ m}^3/\text{mol}$, the susceptibility for sand (SiO_2) is $-3.72\text{E-}10 \text{ m}^3/\text{mol}$, and the susceptibility for water is $-1.63\text{E-}10 \text{ m}^3/\text{mol}$ [16]. In the region surrounding the air bubble, $\Delta B_o(r)$ is the local magnetic field offset from the average field, $X_m^o B_o^{free}$, or,

$$\Delta B_o(r) = [X_m^o - X_m(r)] B_o^{free} \quad [1]$$

where X_m^o is the average or background susceptibility near the spatial inhomogeneity. The offset, $\Delta B_o(r)$, introduces image distortions that are dependent on the shape of the air bubbles within the water-filled media.

Magnetic field distortions that vary slowly through the sample lead to frequency shifts, but strong magnetic field gradients are common and lead to a local reduction in the apparent transverse (spin-spin) relaxation, T_2 . As the molecules containing the spins of interest diffuse across regions of variable susceptibility, they experience fluctuating magnetic fields. Two controlling parameters for diffusive attenuation are the fluctuation due to local field variations, $\overline{\Delta\omega_o^2}$, and the correlation time, τ_c . In the fast motion limit, $\overline{\Delta\omega_o^2} \tau_c^2 \ll 1$, the line broadening is homogeneous, whereas in the slow motion case, $\overline{\Delta\omega_o^2} \tau_c^2 \gg 1$, it is heterogeneous. For field fluctuations resulting from air bubbles in a water-saturated medium, the cutoff point between the fast and slow motion cases occurs when the radius of curvature of the bubble exceeds

approximately $2\text{ }\mu\text{m}$ [¹⁷]. This delineation for an air/water system is derived from the diffusion coefficient of free water and a typical susceptibility induced frequency spread, $\gamma\Delta X_m B_0$.

6.3. Gas Transfer at the Air-Water Interface

The reduction in susceptibility artifacts by pressurization can be explained through an understanding of gas transfer at the air-water interface. The equilibrium distribution and kinetics of this transfer are well known functions of the concentrations, system pressure, and transport due to diffusion. From Fick's first law, the flux through the boundary layer at the gas-liquid interface, F ($\text{mol cm}^{-2} \text{s}^{-1}$), of thickness Z (cm), is described by the differential relationship,

$$F = D \frac{dC}{dZ}, \quad [2]$$

where D ($\text{cm}^2 \text{s}^{-1}$) is the diffusion coefficient and C (mol L^{-1}) is the concentration. From Fick's second law, the changes in the concentration with time and distance are related by,

$$\frac{\partial C}{\partial t} = D \frac{\partial^2 C}{\partial Z^2}. \quad [3]$$

By the Einstein-Smoluchowski equation, the distance, z , that a single molecule travels in time, t , by diffusion is then given as,

$$(z^2)^{1/2} = (2Dt)^{1/2}. \quad [4]$$

This shows the temporal component of the gas and liquid mixing due to diffusion. At steady state, the flux through both boundary layers is given as,

$$F = J_g = J_l, \quad [5]$$

where J_g and J_l are the flux of the gas species out of and into the liquid sink, respectively.

The general expression for exchange of a nonreactive volatile species between a gaseous and liquid phase is thus given by,

$$J_l = k_g (C_g^s - C_g^l), \quad [6]$$

where J_l is the rate of transfer of the gas per unit area ($\text{mol cm}^{-2} \text{s}^{-1}$) or flux into the liquid, k_g is the rate transfer coefficient (cm s^{-1}), C_g^s is the dissolved concentration of the gas (mol L^{-1}) at equilibrium with the partial pressure, p_g , in the gas phase, and C_g^l is the dissolved gas concentration in the liquid phase (mol L^{-1}).⁽¹⁸⁾

The rate law is empirically derived and can be described in terms of various physical models of the gas exchange process to define the rate transfer coefficient, k_g . The rate transfer coefficient is a function of the properties of the volatile species (primarily molecular diffusion) and the characteristics of fluid motion. For granular media systems, the *surface film model* is

appropriate, since it describes a system in which gas exchange is controlled by molecular diffusion through the surface film membrane at the gas-liquid interface.⁽¹⁹⁾ The transfer coefficient, k_g , is then defined as the ratio of the molecular diffusion coefficient, D_g ($\text{cm}^2 \text{s}^{-1}$), and the thickness of the boundary layer, Z (cm),

$$k_g = \frac{D_g}{Z}. \quad [7]$$

Assuming the gas exchange in our system is controlled by molecular diffusion across a laminar sub-layer and that the system is at steady state, the rate of gas transfer can be described by,

$$J_l = \frac{D_g}{Z} (C_g^s - C_g^l). \quad [8]$$

The tendency of a volatile species to partition between the liquid and gas phase is controlled by its vapor pressure. Species with high vapor pressures tend to accumulate in the gas phase, and those with low vapor pressures tend to reside in the liquid phase. This partitioning of gas and liquid phases at the interface is described by Henry's law,

$$K_H = \frac{C_g^l}{P_g}, \quad [9]$$

where K_H ($\text{mol L}^{-1} \text{Pa}^{-1}$) is Henry's law constant and P_g (Pa) is the partial pressure of the gas at equilibrium with the pure liquid. Since K_H is relatively constant for most conditions of interest, an increase in the pressure will demand an increase in the aqueous gas concentration, C_g^l . In a system with a fixed gas volume (closed system), an increase in C_g^l will result in a decrease in the gas phase concentration, C_g^s . With the pressurization system presented in this paper and an oxygen K_H of $10^{-7.9}$, the dissolved oxygen concentration is increased from 8.5 parts per million (ppm), at atmospheric pressure (O_2 partial pressure - 21.28 kPa), to 507.6 ppm, at an over-pressure of 6 MPa. In a closed system, the increase in dissolved oxygen concentration, C_g^l , must result in a decrease in gaseous oxygen content, C_g^s , and this is the principle of over-pressurization to reduce the free air concentration in a closed system.

The transfer coefficient, D_g/Z , may now be expressed as a total mass-transfer velocity, V_{total} , which is analogous to the inverse of the resistance to gas exchange across the interface, Ω .

$$\text{Resistance } (\Omega) \equiv \frac{1}{V_{\text{total}}} = \frac{1}{V_l} + \frac{K_H RT}{V_g}, \quad \left(\text{where } V_l = \frac{D_l}{Z_l} \text{ and } V_g = \frac{D_g}{Z_g} \right) \quad [10]$$

The following relationship shows the dependence of the flux into the aqueous state on the concentration of the species in the gaseous and liquid phases,

$$J_l = V_{total} \left(C_g^s K_H RT - C_g^l \right) = \frac{1}{\Omega} \left(C_g^s K_H RT - C_g^l \right). \quad [11]$$

Since Ω and $K_H RT$ are held relatively constant, a decrease in C_g^l will cause an increase J_l until new equilibrium concentrations are reached. In a closed system, the transfer from the gaseous to the aqueous phase will cause a reduction in the C_g^s . With the deaeration system presented in this paper, the initial dissolved oxygen concentration is decreased from an ambient 8.5 ppm (2.64×10^{-4} mol/L) to less than 0.6 ppm (1.88×10^{-5} mol/L). In a closed system, this reduction in the dissolved oxygen concentration, C_g^l , will cause a decrease in the gaseous oxygen concentration, C_g^s , and this is the principle of deaeration to reduce the free air concentration in a closed system.

6.4. Experimental Setup

The NMR system consists of an Oxford horizontal (15cm bore) 3T magnet equipped with an integrated gradient set coupled to a Bruker AMX spectrometer for gradient control, pulse application, and data acquisition. The flow system (Figure 6.1) consists of an Edwards high-vacuum pump, a Nold 6L Water De-aerator [²⁰], a Varian stepper motor/piston pump, a source of compressed air, and a set of pressure reservoirs with associated tubing, valves, gauges, and NMR sample tube.

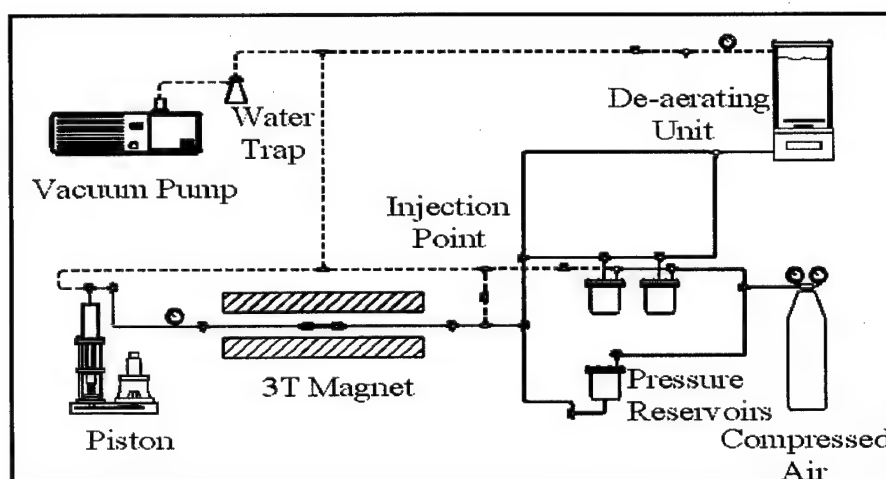


Figure 6.1: Schematic of the NMR Flow System showing the high-vacuum pump, water deaerator, stepper motor/piston pump, source of compressed air, and a set of pressure reservoirs with associated tubing, valves, gauges, and NMR sample tube. The porous sample in the NMR magnet is initially placed under vacuum. The de-aired fluid is then injected into the sample and the entire system is pressurized. The fluid can then be moved through the sample by piston control at the front end of the sample.

The flow system is able to evacuate the test specimen and tubing, fill the sample media with deaerated water (or another liquid), and then apply a positive pressure to assure saturation, thus eliminating air bubbles and subsequent susceptibility effects. All of these components are linked in a closed loop flow system that permits complete control of fluid movement through the test specimen. The vacuum pump is used to draw air out of solution in the water deaerating unit and to evacuate the piston chamber, specimen tube, flow tubing, and pressure reservoirs down to a vacuum of 0.1 MPa (~30" of Hg). The water deaerating unit is operated in a batch mode and

can produce up to 6 L of water with an air content of less than 0.6 ppm dissolved oxygen, DO (9 ppm DO ambient level) [²¹]. The deaerated water is then used to saturate the test specimen via the piston pump or the pressure reservoirs. The piston pump is used to control the flow rate and pressurization of the system. This system is capable of displacing up to 375 ml of fluid per stroke at a rate of up to 5 ml/sec at pressures in excess of 6.0 MPa (~60 atm). By overpressuring the liquid in the reservoirs at the inlet end and displacing the piston at the outlet end of the sample tube, the liquid can be moved through the system in plug-flow fashion.

6.5. Results

6.5.1. 1-D T_1 Mapping Experiments

The spin-lattice relaxation rate is a convenient measure of the efficiency of deaeration. A particularly clean example is the study of residual protons in an aged sample of D_2O . This sample is convenient since the normally dominant relaxation mechanism of inter-nuclear dipole-dipole coupling between water molecules is greatly reduced. The T_1 of residual protons in D_2O increased to 12.3s from 8.4s following deaeration of the normally aerated heavy water. An experimental example of the effect of air on the T_1 reduction can be seen in Figure 6.2. The experiment is an inversion recovery sequence with frequency encoding along the axial plane of the sample. The experimental approach was to inject a small bubble of oxygen (approximately 50 μ L of O_2) into a de-aired sample of D_2O , then increase the pressure on the sample to 0.2 MPa (30psi), and gather data as the O_2 bubble collapses and diffuses into the D_2O . A baseline T_1 distribution of a de-aired D_2O sample is provided for comparison and normalization of the data. Figure 6.2 shows how the O_2 bubble initially reduces signal by displacing the proton signal in the D_2O , however as the bubble collapses, the reduction in T_1 occurs as a function of the O_2 diffusion rate. The baseline (no O_2) shows the full scale T_1 intensity, and the pressure steps of 0, 15 and 30 psi show bubble compression, thus reducing signal. The time steps from 0 to 615 min show bubble collapse, while the 975 to 1635 min time steps show pure O_2 diffusion.

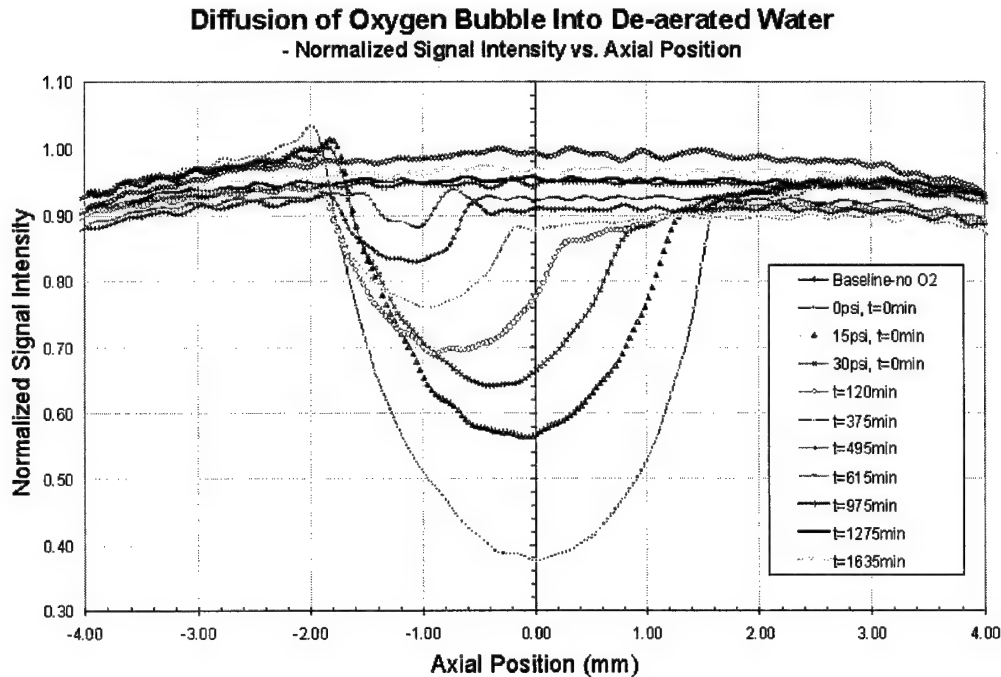


Figure 6.2: Plot of normalized signal intensity versus axial position shows the axial T_1 distribution in the presence of a collapsing and diffusing O_2 bubble. As expected, the O_2 bubble initially reduces signal by displacing the proton signal in the D_2O , however as the bubble collapses, the reduction in T_1 occurs as a function of the O_2 diffusion rate. The baseline (no O_2) shows the full scale T_1 intensity, and the pressure steps of 0, 15 and 30 psi show bubble compression. The time steps from 0 to 615 min show bubble collapse, while the 975 to 1635 min time steps show pure O_2 diffusion.

The plot in Figure 6.3 also shows O_2 bubble collapse, or reduction, and subsequent diffusion. During the O_2 bubble reduction phase, the signal intensity is dependent primarily on bubble volume, and the plot yields a volume reduction rate of $0.01 \text{ mm}^3/\text{min}$. The volume reduction rate is based on the known initial bubble volume of approximately 50 mm^3 collapsing over the extrapolated time of approximately 480 min, from Figure 6.3. Once the bubble collapses, the signal variation in the relaxation study is based on pure O_2 diffusion, and the diffusion rate of the O_2 into the de-aired water is approximately $0.0066 \text{ mm}^2/\text{min}$. The diffusion rate was calculated using the Einstein-Smoluchowski relationship [Eq. 4] and extrapolating the Figure 6.3 curve from a fully saturated O_2 concentration to the de-aired concentration of 0.6 ppm dissolved oxygen.

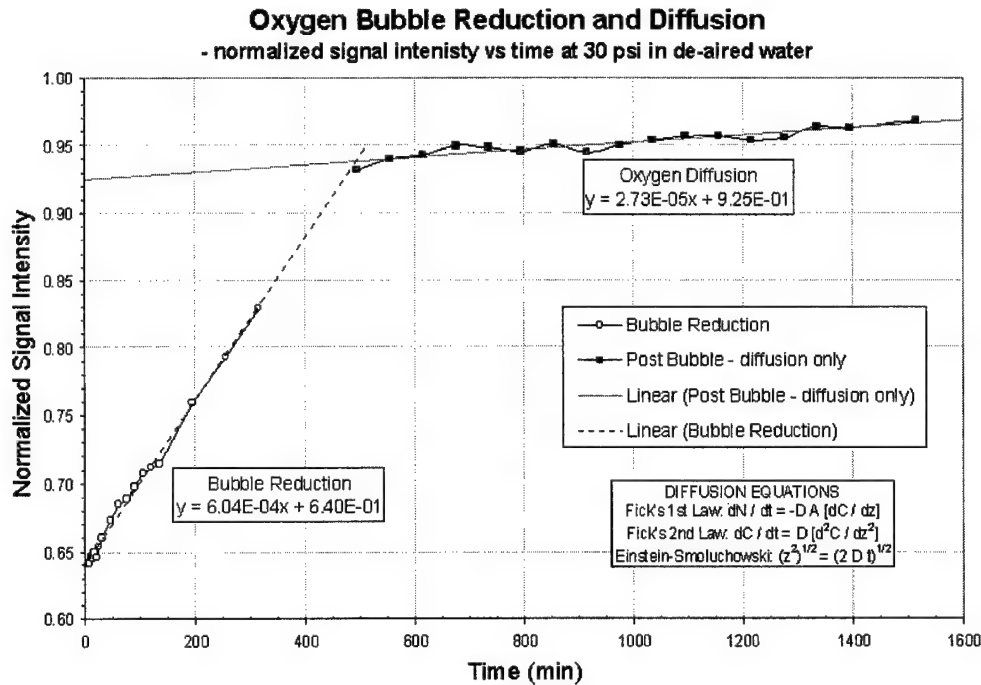


Figure 6.3: Plot showing O₂ bubble collapse, or reduction, and pure diffusion. During the O₂ bubble reduction phase, the signal intensity is dependent primarily on bubble volume, and the plot yields a volume reduction rate of 0.084 mm³/min. Once the bubble collapses, the signal intensity is based on pure O₂ diffusion, and the diffusion rate of the O₂ into the de-aired water is approximately 0.0066 mm²/min.

6.5.2. 2-D Imaging Experiments

A series of NMR images were made to demonstrate the efficiency of deaeration and over-pressurization to reduce air bubbles. These images were recorded by a 2-D slice-selective spin echo sequence. Each image sequence shows the effect of deaeration and over-pressurization on the image quality and shows the ability of the system to eliminate air bubbles from a NMR specimen containing several small air pockets (up to 1 mm³ in volume).

Figure 6.4 displays a foam specimen that was filled with deaerated water and over-pressurized in discrete stages of 68.9 kPa (10 psi), 413.7 kPa (60 psi), and 620.5 kPa (90 psi). The first frame of the sequence (10 psi) shows the significant influence of susceptibility effects surrounding air bubbles trapped in the foam. As the pressure is increased to 60 and 90 psi, the number of artifacts in the image decreases and the image becomes uniform. This shows that the

majority of the air bubbles, and their susceptibility effects, have been eliminated from the specimen. This reduction of the free air concentration, C_g^s , is shown by Eq. [10] and Eq. [12].

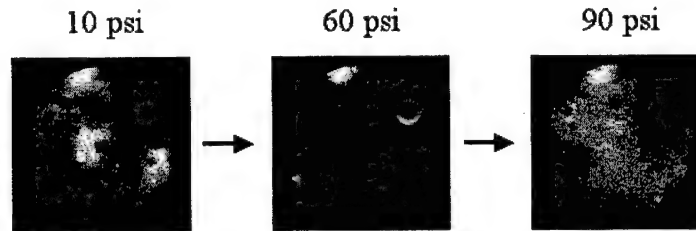


Figure 6.4: The effect of deaerated water and over-pressurization on a foam specimen containing trapped air bubbles. As shown by Eqs. [9] and [11], and displayed in the figure, an increase in the deaerated fluid pressure surrounding the foam forces the air bubbles back into solution. The feature in the top right is a glass rod intentionally placed for reference.

Figure 6.5 displays a sequence of images using a sample of 0.9-1.1 mm glass beads. The sample with trapped air bubbles was over-pressured to 68.9 Pa (10 psi) and 413.7 kPa (60 psi) for a one minute, and then to 413.7 kPa (60 psi) for a 100 minutes. These images show the effect of over-pressurization of deaerated water and the effect of time on diffusion. The reduction in C_g^s by over-pressurization is shown in Eq. [11], and the temporal dependence on diffusion is shown in Eq. [3] and Eq. [4].

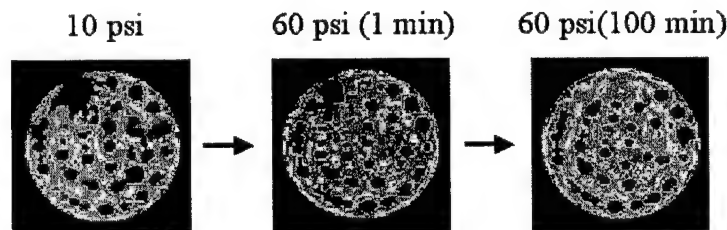


Figure 6.5: A sample of 0.9-1.1 mm diameter glass beads filled with deaerated water and over-pressured to 10 psi and 60 psi for a one minute duration, and 60 psi for a 100 minute duration. Air bubbles are readily apparent in the first image (10 psi), and the subsequent images show a consistent reduction in gaseous air volume with increased pressure and time. As shown in Eqs. [3], [4], and [9] and displayed by this sequence, the benefits of over-pressurization coupled with molecular diffusion is an effective means of deaeration.

Figure 6.6 is a sequence of images that show the positive effect of over-pressurization and flow of deaerated fluid on the removal of air from a specimen consisting of a set of 1.2 mm diameter glass capillary tubes. An increase in pressure to 413.7 kPa (60 psi) eliminates all but one small air pocket. The third frame of the sequence shows the effect of flow through the system, which removes all remaining air. Again, the reduction in C_g^s by over-pressurization is shown in Eq. [10], and the effect of flow is described by advection.

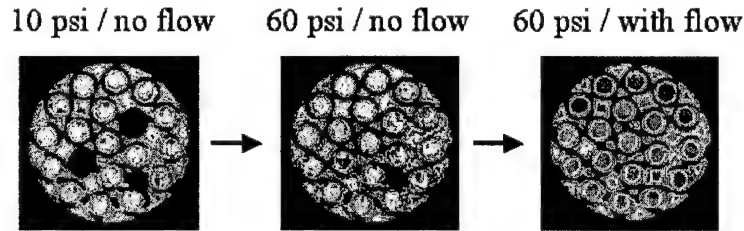


Figure 6.6: The combined effect of over-pressurization and flow of deaerated fluid on the saturation of 1.2 mm glass capillary tubes. Air is initially contained in three of the tubes, the tubes are over-pressurized to 413.7 kPa (60 psi) and then advective flow is initiated to enhance gas exchange. By Eq.[9] and as displayed in the figure, all air pockets are eliminated.

6.6. Discussion and Conclusions

Susceptibility effects are an inherent problem in the NMR imaging of complex systems involving fluid flow through granular media. These susceptibility effects are often caused by air bubbles formed during sample preparation and under experimental flow conditions. The technique of deaeration followed by over-pressurization is highly effective in reducing air bubbles in granular media. The deaerated water provides a sink for the free air to be transferred into the aqueous phase, and the over-pressurization provides an added mechanism for this transfer to occur. The degree of deaeration is limited by the effectiveness of the deaeration system (i.e. mixing vessel and vacuum pump), and in these studies, deaeration to less than 0.6 ppm DO (20) was shown to be highly effective in incorporating free air. As for the degree of over-pressurization, the higher the pressure on the closed system, the more free air transfers into the aqueous phase. In these studies, pressurization to 620 kPa (90 psi) proved highly effective in driving the free air into solution.

For granular media with low porosity or dead end pathways, the diffusion time of the gas into the liquid may be excessively long to completely remove all of the free air. This problem can be mitigated by a flowing stream of deaerated liquid to provide a constant sink for the free air to be integrated. If advective flow is not possible for low porosity media, the deaeration times are purely diffusion dependent and gas exchange rates will be based only on molecular diffusion. In this case, it may be advantageous to impregnate the low porosity material with a gas that has higher water solubility, such as CO₂.

The experimental results show the effectiveness of this deaeration technique at mitigating the unwanted susceptibility effects. The significant reduction and positive control over the effects of air/water susceptibility provides greater confidence in interpreting qualitative assessments of imaging media. The reduction in imaging artifacts may also provide the opportunity to develop quantitative evaluation methods for imaging techniques. NMR is also an effective means to evaluate the degree of deaeration in a sample. Experimental results in Figures 6.2 and 6.3 show how 1-D T₁ mapping of a sample can be used to evaluate the degree of deaeration and the rates at which the various deaeration mechanisms take place. Some limited deaeration time-scales can also be extracted from the 1-D data.

References for Section 6.0

1. E. Fukushima, Nuclear Magnetic Resonance as a Tool to Study Flow, *Annual Review of Fluid Mechanics*, 31:95-123, 1999.
2. J.D. Seymour and P.T. Callaghan, Generalized Approach to NMR Analysis of Flow and Dispersion in Porous Media, *AIChE Journal*, **43 No.8**, 2096-2111 (August 1997).
3. A. Caprihan and E. Fukushima, Flow Measurements by NMR, *Physics Reports*, **198 No. 4**, 198-235 (1990).
4. S. Chen, F. Qin, K. Kim, and A.T. Watson, NMR Imaging of Multiphase Flow in Porous Media, *AIChE Journal*, **39 No. 6**, 925-934 (June 1993).
5. A. Feinaur, S.A. Altobelli, and E. Fukushima, NMR Measurements of Flow Profiles in a Course Bed of Packed Spheres, *Magnetic Resonance Imaging*, **15 No. 4**, 479 (1997).
6. S. Stapf, K.J. Packer, S. Bekri, and P.M. Adler, Two-Dimensional Nuclear Magnetic Resonance Measurements and Numerical Simulations of Fluid Transport in Porous Rocks, *Physics of Fluids*, **15 No. 3**, 566-580 (March 2000).
7. B. Manz, P. Alexander, and L.F. Gladden, Correlations Between Dispersion and Structure in Porous Media Probed by Nuclear Magnetic Resonance, *Physics of Fluids*, **11 No. 2**, 256-267 (February 1999).
8. J. Williams, G. Maddinelli, D.G. Taylor, P. Enwere, and J.S. Archer, Contribution of NMR Imaging Technique in the Study of the Polyphasic Flow in Porous Media, *Magnetic Resonance Imaging*, **9 No. 5**, 869-874, (1991).
9. A.J. Sederman, M.L. Johns, A.S. Bramley, P. Alexander, and L.F. Gladden, Magnetic Resonance Imaging of Liquid Flow and Pore Structure in Packed Beds, *Chem. Eng. Sci.* **52**, 2239 (1997).
10. J. Pauli, G. Scheying, C. Mugge, A. Zschunke, and P. Lorentz, Determination of the Pore Widths of Highly Porous Materials with NMR Microscopy, *Fresenius J Anal Chem*, **357**:508-513 (1997).
11. M.D. Hurlimann, K.G. Helmer, L.L. Latour, and C.H. Sotak, Restricted Diffusion in Sedimentary Rocks. Determination of Surface-to-Volume Ratio and Surface Relaxivity, *J. Mag. Reson., Ser. A* **111**, 169 (1994).
12. C.A. Baldwin, A.J. Sederman, M.D. Mantle, P. Alexander, and L.F. Gladden, Determination and Characterization of the Structure of a Pore Space from 3D Volume Images, *J. Colloid Interface Sci.* **181**, 79 (1996).
13. S. Chen, F. Qin, K. Kim, and A.T. Watson, Determining Fluid Saturations during Multiphase Flow Experiments by NMR Imaging Techniques, *AIChE Journal*, **40 No. 7**, 1238-1245 (June 1994).
14. L.F. Gladden and M.P. Hollewand, Characterization of Structural Inhomogeneities in Porous Media, *AIChE Journal*, **41 No. 4**, 894-906 (April 1995).
15. P.D. Majors, J.L. Smith, F.S. Kovarik, and E. Fukushima, NMR Spectroscopic Imaging of Oil Displacement in Dolomite, *Journal of Magnetic Resonance*, **89**, 470-478 (1990).
16. D.R. Lide, "CRC Handbook of Chemistry and Physics, 80th Edition, 1999-2000," CRC Press, (2000).
17. P.T. Callaghan, "Principles of Nuclear Magnetic Resonance Microscopy," Clarendon Press, Oxford (1991).
18. W. Stumm and J.J. Morgan, "Aquatic Chemistry: Chemical Equilibria and Rates in Natural Waters, Third Edition," John Wiley and Sons Inc. (1996).
19. F.M. Morel and J.G. Herring, *Principles and Applications of Aquatic Chemistry*, John Wiley, Inc. 1993.
20. W. Nold, "The Nold DeAerator Manual," Revision 18, Walter Nold Company, Natick, MA.
21. W. Nold, The Nold DeAerator, *Design News*, 68, (17 Aug 81).

[THIS PAGE INTENTIONALLY LEFT BLANK]

7. MICROSCOPIC CHARACTERIZATION OF ION-SPECIFIC RESINS USING NMR

Abstract

The use of NMR spectroscopy and relaxation techniques has proven very effective at probing the microscopic characteristic of a variety of materials. This study applies NMR techniques to probe the microscopic characteristic of phenolic-based ion-exchange resins, catechol-formaldehyde (CF) and resorcinol-formaldehyde (RF). The study employs the use of a variety of the NMR experiments to extract information on the relaxation rates, spatial scales, and exchange rates of water molecules integrated into the resin microscopic structure. The study also uses two different magnetic fields, 3T and 12T, and magic-angle spinning (MAS) to separate dipolar from susceptibility-induced interactions in the resins.

Using a wide range of NMR techniques at two different magnetic field environments, the study showed there are three primary water environments, or spin pools, within the resin matrix for both the CF and RF. These pools were shown to belong to bound, interstitial or plasticizer, and free water components in relative populations of 40%, 40%, and 20%, respectively. The diffusion rates of the three pools were measured, and the results showed the fastest diffusion for the free water pool and the slowest for the bound water. The exchange rates between the free and bound pools were measured to be 0.00396 ms^{-1} ($\tau_c=252.3 \text{ ms}$) and 0.00362 ms^{-1} ($\tau_c=276.2 \text{ ms}$) and the exchange rates between the bound and plasticizer pools was calculated to be 185.8 ms^{-1} ($\tau_c=5.4 \text{ ms}$) and 218.8 ms^{-1} ($\tau_c=4.6 \text{ ms}$) for the CF and RF resins, respectively. The bound water volume for the CF resin was measured to be $3.6 \text{ }\mu\text{L}$. NMR provides the only means to directly measure the bound water volume due to the gel-like nature of the resins. Based on the bound water volume per mass of resin and the intermolecular water distance, the specific surface area of the CF resin was determined to be $2370 \text{ m}^2/\text{g}$. From this value and an estimate of the number of functional sites per unit area, the theoretical proton exchange capacity was calculated as 63.0 meq/g . The use of NMR spectroscopic and relaxation techniques has increased the understanding of the exchange mechanisms and spatial scales of these ion-specific resins and provides the only means to directly determine bound water volume and specific surface area.

7.1. Introduction

Nuclear Magnetic Resonance (NMR) spectroscopic and relaxation techniques have proven very useful in the study of porous media [^{1,2,3}]. These NMR techniques provide exceptional insight into water-saturated porous environments. This insight is gained through identification of various water pools within the porous matrix, and once these spin pools are identified, NMR provides a means to determine spatial and temporal scales for each pool [^{4,5,6}].

This section provides a description of a series of NMR spectroscopic and relaxation experiments performed on phenolic ion-exchange resins. The specific phenolic resins used are Catechol-Formaldehyde (CF) and Resorcinol-Formaldehyde (RF), and these resins are further described in Section 4.4 and Appendix 1.0. The resins proved to be a particularly clean system with which to apply these NMR techniques. There were three easily distinguishable spin pools, which were assigned to bound water, interstitial or plasticizer water, and free water components. With the use of NMR, relaxation times, diffusion rates, and relative populations were determined for each pool. In addition, the exchange rates between the various pools were determined, and finally, the pore volume of the bound water fraction was calculated. The bound water volume provided a means to calculate the effective surface area of the resin, which was otherwise impossible with the use of standard surface-area analysis techniques. This study also briefly looked at resins complexed, or loaded, with gadolinium (Gd) to see the effect of increased susceptibility. Thus, in this study, the resins are described as either Gd-loaded or clean, implying an unused Na⁺-form resin (described in Appendix 1.0).

The NMR techniques used in these studies are described in detail in Section 5.1, and the data is available in Appendix 4.0. These experiments made use of magic-angle spinning (MAS) techniques, as well as, the use of two different magnetic fields (3T and 12T) to evaluate the effects of dipolar and susceptibility related interactions. The experiments used in this section are described as follows.

- MAS spectral plots and deconvolution: these experiments were used to identify the various spin pools, and to measure the relative populations, dipolar line widths, and chemical shifts.
- Inversion recovery: these experiments were used to measure the spin-lattice (T₁) relaxation time.

- Carr-Purcell Meiboom-Gill (CPMG): these experiments were used to measure the spin-spin relaxation (T_2) times and spin pool populations.
- Pulsed Gradient Stimulated Echo (PGSTE): these experiments were used to find the diffusion constant for the various spin pools.
- Goldman-Shen Exchange Rate: these experiments were used to directly measure the exchange rate between the plasticizer and bound water pools.

Together, this array of experiments at two different magnetic fields provided deep insight into the microscopic nature of the RF and CF resins. Due to the expansion and contraction of the resins in the presence or absence of water, the resin proved a difficult material to study with standard physical chemistry techniques. With NMR, the resin analysis proved relatively straight forward, and this information can be applied to the evaluating the ultimate performance of other types of unstructured porous materials.

7.2. Three-Pool Resin Model

A three-pool model was developed to describe the interactions of the water with the resins. This model was developed based primarily on NMR data from MAS spectral plots and CPMG experiments. The MAS spectra clearly showed two peaks, associated with the plasticizer and bound water components, and a third broad component belonging to the free water. The CPMG data supported this three-pool model in that a three-exponential fit provided good agreement with the data. In addition, MAS CPMG stacked plots clearly showed one short-lived pool shifted to the right of the main peak (bound water), one on-resonance pool decaying at an intermediate rate (plasticizer pool), and one long-lived pool belonging to the free water. One complication to the model arose in that the long-lived free water component has a rather broad line-width, which implies a short T_2 time (by $T_2 = 1/(\pi \cdot \omega_d)$) [7]. However, this assignment was justified using PGSTE diffusion measurements showing fast diffusion of the free water component thus allowing for increased susceptibility-induced broadening. The three-pool model is shown in Figure 7.1.

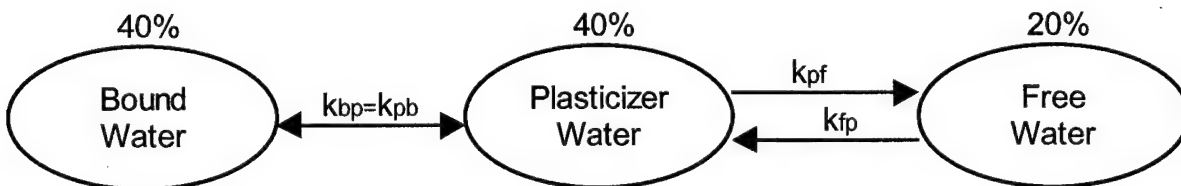


Figure 7.1: Three-pool model of water saturated resins with relative populations for the clean CF resin. The relative populations were determined by spectral deconvolution of the MAS data and three-exponential fitting to the MAS CPMG data. Based on the population data, the exchange rates are the same for the bound and plasticizer pool.

In developing the model, a few assumptions needed to be made and verified. These assumptions were as follows.

- Spin-Lattice Relaxation Times, T_1 :
 - all T_1 values should be approximately the same
 - T_1 values should be longer than the short T_2 components and exchange correlation times
- Spin-Spin Relaxation Times, T_2 :
 - the T_2 value for the bound water should be the smallest
 - the T_2 value for free water should be the upper bound
 - the T_2 value for the plasticizer pool should have an intermediate value
- Diffusion Coefficient, D :
 - the diffusion rate for free water should approach that of free, unrestricted water ($2.5E-5 \text{ cm}^2/\text{s}$)
 - the diffusion rate for bound water should be the slowest due to restricted diffusion
- Exchange Rates, k :
 - there is no exchange between the free and bound pools
 - the exchange rate between the bound-plasticizer water is slow relative to the plasticizer-free water
 - the exchange from the plasticizer to the bound water can be measured directly with Goldman-Shen
 - based on relative populations, $k_{bp}=k_{pb}$ and $k_{fp}=2*k_{pf}$

7.3. Discussion and Results

The results for the microscopic characterization of the resins include those results from direct experimental data, and those results calculated from the data based on a physical model and knowledge of coupled processes. The directly measured results include spin populations, line widths, chemical shifts, and the exchange rate between the plasticizer and bound components. Those results, which must be calculated, include the T_2 relaxation rates, the diffusion constants, the susceptibility, and the exchange rate between the free and plasticizer components.

7.3.1. Experimental Results

The experimental results of these studies are summarized in Table 7.1 and 7.3, for the CF and RF resins, respectively. The experimental data used in evaluating these results are found in Appendix 4.0. Tables 7.1 and 7.3 are referenced to the relevant sections of Appendix 4.0 through cross-reference with Tables 7.2 and 7.4. A description of the experimental techniques is provided in Section 5.0.

The interpreted data of Tables 7.1 and 7.3 is not always an exact measurement of the physical parameter displayed. Some of the results listed in Tables 7.1 and 7.3 have greater than or less than signs indicating a lower or upper bound. This is necessary due to coupled processes, which may increase or decrease the measured effective value. The actual values for such parameters as the T_2 and the diffusion constant, D , must be calculated from known relationships and interactions. These calculations are described and the results presented after Table 7.2 for the CF resins and after Table 7.4 for the RF resins. The susceptibility numbers in the data tables are easily derived from the relationships defined in Section 4.3.

Table 7.1: Clean CF Resin Data Table (with data source reference in Table 7.2)

CF Clean Resin

	Bound Water	Free Water	Plasticizer Water	Ref:
<u>Population (% of total)</u>				
P(3T-MAS Spectra)	21%	24%	55%	1
P(3T-Static CPMG)	33%	32%	36%	2
P(12T-MAS Spectra)	41%	39%	20%	3
P(12T-Static CPMG)	26%	43%	29%	4
<u>Chemical Shift (Hz)</u>				
δ (3T-MAS Spectra)	-12.1	19.9 / 8.5	0.0	5
δ (12T-MAS Spectra)	-57.8	-6.5 / -8	0.0	6
<u>Spin-Lattice Relaxation (ms)</u>				
T_1 (3T-Static IR)	1084.4	>1084.4	1084.4	7
T_1 (12T-Static IR)	1378.4	>1378.4	1378.4	8
T_1 (12T-MAS IR)	1170.0	>1360	1360.0	9
<u>Spin-Spin Relaxation (ms)</u>				
T_2 (3T-MAS Spectra)	≤ 14.1	>65.2	>26.7	10
T_2 (3T-Static CPMG)	≤ 10.3	>166.04	>52.9	11
T_2 (12T-MAS Spectra)	≤ 6.7	>6.7	>38.4	12
T_2 (12T-Static CPMG)	≤ 5.9	>100.9	>22.21	13
T_2 (12T-MAS CPMG)	<9.2	≥ 333.8	≥ 87.4	14
<u>Diffusion Coefficient (cm²/s)</u>				
D(PGSTE- $\tau=0.5$ ms, $\Delta=152$ ms)	8.7E-06	1.6E-05	1.6E-05	15
D(PGSTE- $\tau=15$ ms, $\Delta=165$ ms)		1.2E-05	1.2E-05	16
D(PGSTE- $\tau=3.2$ ms, $\Delta=100$ ms)		1.5E-05	1.5E-05	17
D(PGSTE- $\tau=4.2$ ms, $\Delta=100$ ms)	1.1E-05	1.6E-05	1.6E-05	18
D(PGSTE- $\tau=3.2$ ms, $\Delta=20$ ms)		2.9E-05	2.9E-05	19
D(PGSTE- $\tau=4.2$ ms, $\Delta=20$ ms)	2.5E-05	3.9E-05	3.9E-05	20
D(CPMG[550ms]+PGSTE)		2.6E-04	1.2E-03	21
<u>Dipolar Line-Width (Hz)</u>				
ω_d (3T-MAS Spectra)	22.5	12.7	12.0	22
ω_d (12T-MAS Spectra)	47.2	47.1	8.3	23
<u>Exchange Rates (ms⁻¹)</u>				
k (a \leftrightarrow b)			0.00396	24
correlation time (ms)			252.3	25
<u>Susceptibility</u>				
ΔX (3T-cs)	3.0			26
ΔX (3T-line width)	6.5			27
ΔX (12T-cs)	3.8			28
ΔX (12T-line width)	3.0			29

Table 7.2: Clean CF Resin Reference Table (referenced sections in Appendix 4.0)

Ref:	Data Source	Section
1	MAS spectral fit on 3T data	A.4.1.1
2	Static CPMG on 3T magnet, 250us echo time	A.4.3.1
3	MAS spectral fit on 12T data	A.4.1.2
4	Static CPMG on 12T magnet, 250us echo time	A.4.3.2
5	MAS spectral fit on 3T data	A.4.1.1
6	MAS spectral fit on 12T data	A.4.1.2
7	Static IR on 3T magnet	A.4.2.1
8	Static IR on 12T magnet	A.4.2.2
9	MAS IR on 12T magnet	A.4.2.4/5
10	MAS spectral fit on 3T data	A.4.1.1
11	Static CPMG on 3T magnet, 250us echo time	A.4.3.1
12	MAS spectral fit on 12T data	A.4.1.2
13	Static CPMG on 12T magnet, 250us echo time	A.4.3.2
14	Static CPMG on 12T magnet, 200us echo time	A.4.3.5
15	MAS PGSTE with 0.5ms pre-filter, $\Delta=152\text{ms}$	A.4.4.1
16	MAS PGSTE with 15ms pre-filter, $\Delta=165\text{ms}$	A.4.4.2
17	MAS PGSTE, $\Delta=100\text{ms}$, $\tau=3.2\text{ms}$	A.4.4.7
18	MAS PGSTE, $\Delta=100\text{ms}$, $\tau=4.2\text{ms}$	A.4.4.8/9
19	MAS PGSTE, $\Delta=20\text{ms}$, $\tau=3.2\text{ms}$	A.4.4.7
20	MAS PGSTE, $\Delta=20\text{ms}$, $\tau=4.2\text{ms}$	A.4.4.8/9
21	MAS CPMG(550ms)+PGSTE, $\Delta=20\text{ms}$, $\tau=3.2\text{ms}$	A.4.4.11
22	MAS spectral fit on 3T data	A.4.1.1
23	MAS spectral fit on 12T data	A.4.1.2
24	Goldman-Shen on 12T MAS	A.4.5.1
25	Goldman-Shen on 12T MAS	A.4.5.1
26	MAS spectral fit on 3T data	A.4.1.1
27	MAS spectral fit on 3T data	A.4.1.1
28	MAS spectral fit on 12T data	A.4.1.2
29	MAS spectral fit on 12T data	A.4.1.2

Table 7.3: Clean RF Resin Data Table (with data source reference in Table 7.4)

RF Clean Resin

	Bound Water	Free Water	Plasticizer Water	Ref:
<u>Population (% of total)</u>				
P(3T-MAS Spectra)	27%	34%	39%	1
P(3T-Static CPMG)	39%	33%	26%	2
P(12T-MAS Spectra)	44%	38%	18%	3
P(12T-Static CPMG)	40%	36%	21%	4
<u>Chemical Shift (Hz)</u>				
δ (3T-MAS Spectra)	-21.0	11.5 / -2.55	0.0	5
δ (12T-MAS Spectra)	-80.6	7.5 / -2.5	0.0	6
<u>Spin-Lattice Relaxation (ms)</u>				
T_1 (3T-Static IR)	1241.3	>1241.3	1241.3	7
T_1 (12T-Static IR)	1278.1	>1278.1	1278.1	8
<u>Spin-Spin Relaxation (ms)</u>				
T_2 (3T-MAS Spectra)	≤ 6.4	>11.2	>31.5	9
T_2 (3T-Static CPMG)	≤ 5.9	>158.7	>46.5	10
T_2 (12T-MAS Spectra)	≤ 4.0	>12.1	>57.8	11
T_2 (12T-Static CPMG)	≤ 5.6	>137.2	>42.2	12
T_2 (12T-MAS CPMG)	<5.7	>178.8	>70.2	13
<u>Diffusion Coefficient (cm²/s)</u>				
D(PGSTE- $\tau=0.5$ ms, $\Delta=152$ ms)	4.7E-06	1.9E-05	1.9E-05	14
D(PGSTE- $\tau=15$ ms, $\Delta=165$ ms)		1.5E-05	1.5E-05	15
<u>Dipolar Line-Width (Hz)</u>				
ω_d (3T-MAS Spectra)	50.2	28.5	10.1	16
ω_d (12T-MAS Spectra)	79.1	26.2	5.5	17
<u>Exchange Rates (ms⁻¹)</u>				
k (a \leftrightarrow b)			0.00362	18
correlation time (ms)			276.2	19
<u>Susceptibility ()</u>				
ΔX (3T-cs)	6.0			26
ΔX (3T-line width)	15.7			27
ΔX (12T-cs)	5.7			28
ΔX (12T-line width)	5.6			29

Table 7.4: Clean RF Resin Reference Table (referenced sections in Appendix 4.0)

Ref:	Data Source	Section
1	Spectral fit on 3T MAS data	A.4.1.3
2	Static CPMG on 3T magnet, 250us echo time	A.4.3.9
3	Spectral fit on 12T MAS data	A.4.1.4
4	Static CPMG on 12T magnet, 250us echo time	A.4.3.12
5	Spectral fit on 3T MAS data	A.4.1.3
6	Spectral fit on 12T MAS data	A.4.1.4
7	IR on 3T magnet	A.4.2.6
8	IR on 12T magnet	A.4.2.7
9	Spectral fit on 3T MAS data	A.4.1.3
10	Static CPMG on 3T magnet, 250us echo time	A.4.3.6
11	Spectral fit on 12T MAS data	A.4.1.4
12	Static CPMG on 12T magnet, 250us echo time	A.4.3.7
13	MAS CPMG on 12T magnet, 200us echo time	A.4.3.9
14	MAS PGSTE with 0.5ms pre-filter, $\Delta=152\text{ms}$	A.4.4.12
15	MAS PGSTE with 15ms pre-filter, $\Delta=165\text{ms}$	A.4.4.13
16	Spectral fit on 3T MAS data	A.4.1.3
17	Spectral fit on 12T MAS data	A.4.1.4
18	Goldman-Shen on 12T MAS	A.4.5.2
19	Goldman-Shen on 12T MAS	A.4.5.2
26	MAS spectral fit on 3T data	A.4.1.3
27	MAS spectral fit on 3T data	A.4.1.3
28	MAS spectral fit on 12T data	A.4.1.4
29	MAS spectral fit on 12T data	A.4.1.4

7.3.2. Calculated Exchange Rates for the CF and RF resins

Although Table 7.1 and 7.3 contain all of the directly measured results, these are not all strictly defined for the three pools due to coupled processes affecting the relaxation times. One such couple process is the exchange between the plasticizer pool and the bound and free pools. Although the relaxation processes can be considered coupled, the exchange between the pools can be considered uncoupled since there is no assumed exchange between the bound and free pools. Only the plasticizer pool exchanges with the other two pools, and the rates of exchange are assumed vary greatly. As described by Sandstrom [⁸] and derived by McConnell [⁹], the general equation for an uncoupled two-site exchange process is as follows:

$$dM_{\text{bound}}/dt = -M_{\text{bound}}(k_{\text{bp}} + 1/T_{2\text{bound}}) + M_{\text{plasticizer}}k_{\text{pb}}$$

and

$$dM_{\text{plasticizer}}/dt = -M_{\text{plasticizer}}(k_{\text{pb}} + 1/T_{2\text{plasticizer}}) + M_{\text{bound}}k_{\text{bp}}$$

However, since the populations of the bound (P_b) and plasticizer pools (P_p) are approximately equal, the exchange rates must also be equal (assuming no coupling with the free and bound water) by the following relationships.

$$P_b + P_p = 1, P_b k_{\text{bp}} = P_p k_{\text{pb}}, \text{ and if } P_b = P_p \text{ then,}$$

$$k_{\text{bp}} = k_{\text{pb}}$$

Using the Goldman-Shen experiment, the exchange rate from the free to the bound pool for the CF resin was measured to be 0.00396 ms^{-1} ($\tau_{\text{fb}}=252.3 \text{ ms}$), and since the k_{pb} are k_{bp} assumed to be fast (τ less than 10 ms) and equivalent, then k_{fp} is approximately 0.00396 ms^{-1} or $\tau_{\text{fp}}=252.3 \text{ ms}$. For the RF resin, k_{fb} was measured as 0.00367 ms^{-1} ($\tau_{\text{p}}=272.5 \text{ ms}$), and thus $\tau_{\text{fp}}=272.5 \text{ ms}$. From this measurement and using the population ratios of one to four (free to plasticizer and bound), the k_{pf} is 0.00099 ms^{-1} ($\tau_{\text{pf}}=1009.2 \text{ ms}$) for the CF resin. The k_{pf} for the RF is then 0.00092 ms^{-1} ($\tau_{\text{pf}}=1090.0 \text{ ms}$).

Slow Exchange: Since this measured exchange rate is considered a slow exchange ($\tau > 150\text{-}500\text{ms}$) [¹⁰], and with $T_{2, \text{plasticizer-effective}}$ and k_{fp} known, the following relationship can be used to find the true T_2 for the bound and plasticizer pools.

$$T_{2, \text{effective}} = [T_2 / (1 + kT_2)]$$

Using this relationship, the $T_{2, \text{plasticizer}}$ for the CF plasticizer is 95.7 ms, and the $T_{2, \text{plasticizer}}$ for the RF plasticizer is 75.0 ms. A summary of the calculated results for the T_2 times for the clean CF resin is provided in Figure 7.2, and in Figure 7.3 for the RF resins.

Fast Exchange: In the case of fast exchange with unequal populations as in the plasticizer-bound water exchange process, the solution for the exchange rate is as follows.

- General Equations for Uncoupled 2-site Exchange

$$dM_{\text{free}}/dt = -M_{\text{free}}(k_{\text{fp}} + 1/T_{2\text{free}}) + M_{\text{plasticizer}}k_{\text{pf}}$$

$$dM_{\text{plasticizer}}/dt = -M_{\text{plasticizer}}(k_{\text{pf}} + 1/T_{2\text{plasticizer}}) + M_{\text{free}}k_{\text{fp}}$$

- Assumptions concerning populations and exchange rates include the following,

$$P_b + P_p = 1,$$

$$P_b k_{\text{bp}} = P_p k_{\text{pb}},$$

$$\text{but if } P_f = P_p \text{ then,}$$

$$k_{\text{bp}} = k_{\text{pb}}$$

- In the case of fast exchange (correlation time, $\tau < 150\text{ms}$)^[11], the exchange time becomes,

$$k_b = 4 \pi P_b P_p^2 (\delta\nu)^2 [\omega - (P_b T_{2b} + P_p T_{2p}) / (\pi T_{2b} T_{2p})]^{-1}$$

where $\delta\nu$ is the chemical shift between the plasticizer and free spectra, and ω is the line-width of the free component.

Using this equation and the measured values from Table 7.1, the CF exchange rate for the bound to the plasticizer water, $k_{\text{bp}} = 185.8 \text{ s}^{-1}$ (τ_{bp} is 5.4 ms), and thus the τ_{pb} is also 5.4 ms, since the populations are equal. This assumes a T_{2b} of 9.2 ms, which may be slightly high. An iterative approach to solving the exchange and T_2 rate may improve the accuracy. The RF exchange rates are calculated as, $k_{\text{bp}} = 218.8 \text{ s}^{-1}$ (τ_{bp} is 4.6 ms), and thus the τ_{pb} is also 4.6 ms. This assumes a T_{2b} of 5.7 ms, which may be slightly high. A summary of the calculated results for the exchange rates with the clean CF resin is provided in Figure 7.2, and in Figure 7.3 for the RF resins.

CF Resins

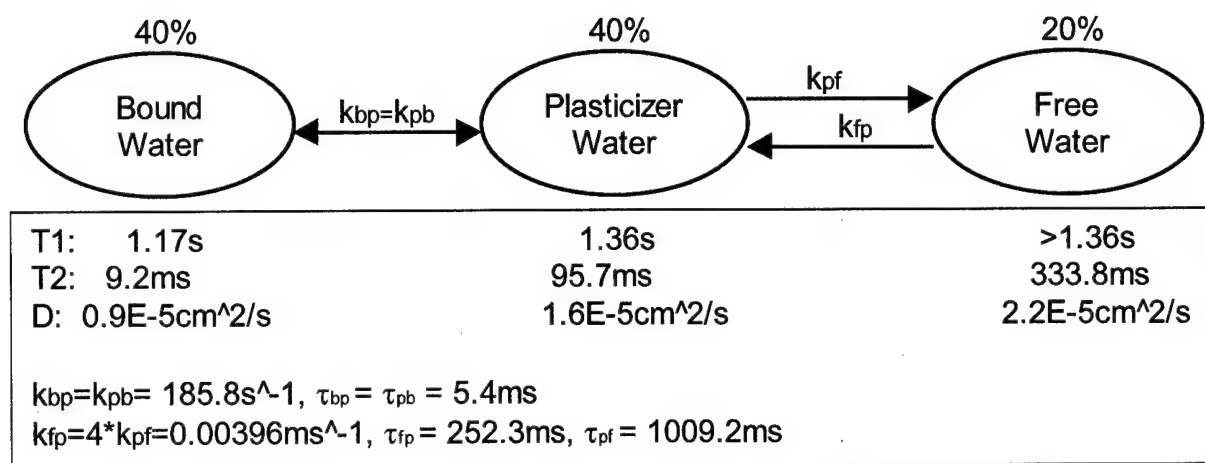


Figure 7.2: Three-pool model of water saturated resins with measured physical characteristic of clean CF resin. The bound water has the shortest lifetime and a moderate diffusion coefficient. The plasticizer has an intermediate lifetime and a large diffusion coefficient, and the free water has the longest lifetime and small diffusion coefficient. Due to exchange between the three pools, the measured relaxation times are coupled, and thus, they are only bounds on the actual values.

RF Resins

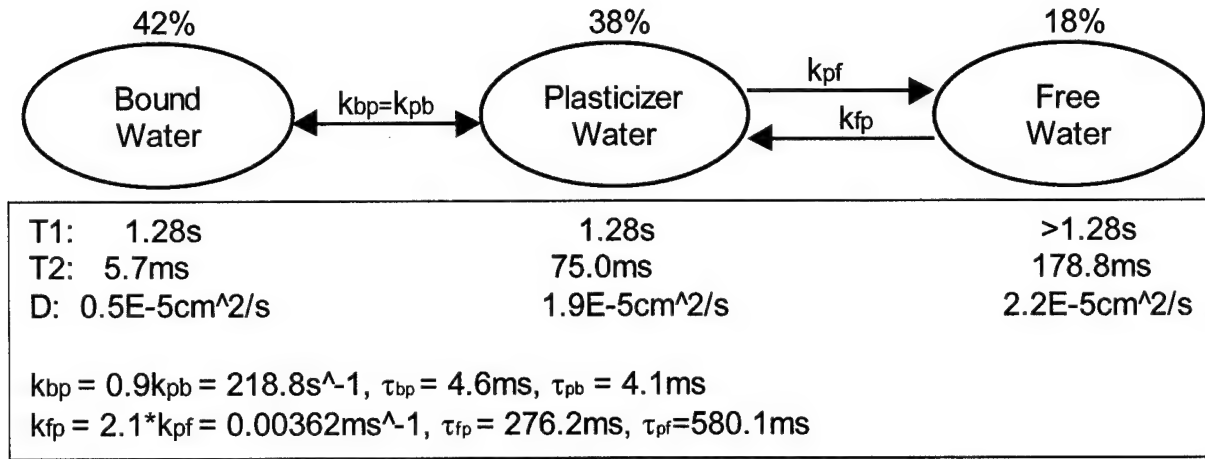


Figure 7.3: Three-pool model of water saturated resins with measured physical characteristic of clean RF resin. The bound water has the shortest lifetime and a moderate diffusion coefficient. The plasticizer has an intermediate lifetime and a large diffusion coefficient, and the free water has the longest lifetime and small diffusion coefficient. Due to exchange between the three pools, the measured relaxation times are coupled, and thus, they are only bounds on the actual values.

7.3.3. Specific Surface Area Determination

The bound, pore water volume is an important parameter to measure since this component is assumed to be in direct contact with the functional exchange sites on the resin. Once the bound, pore water volume is known, it is possible to determine the specific surface area, or surface area of resin per unit mass of resin. Based on the available surface area and the known number of functional groups (phenols) unit area, the theoretical proton exchange capacity can be calculated. Therefore, it is of great interest to determine the specific surface area of any chemically reactive solid matrix. However, due to the gel-like structure of the phenolic resins and their large swelling capacity under water-saturated conditions (150-300% volume increase with saturation), it was not possible to get accurate surface area measurements using standard surface area analysis techniques (i.e. N₂ BET) [12].

The results of numerous surface area analyses on both the CF and RF resin gave specific surface areas of between 0.2 to 1.5 m²/g, which is far below the range of most polymeric species. The results of the nitrogen BET surface area analyses are provided in Appendix 7.0. This deviation from expected surface area values is most likely due to the presence of bound water that is integrated into the resin structure to stabilize the matrix. This hypothesis is justified by the results of thermogravimetric analyses (TGA) [13]. The TGA indicates the presence of bound water on the resins at temperatures greater than 150 °C, and after this point, the resins begin to degrade (see Section 4.4.). Therefore, it is reasonable to assume that functional surface area of the resins is occupied by water molecules, thus leaving a standard surface-area analysis to measure far below the actual surface area available for ion exchange. Another type of surface area analysis for RF gels used a freeze-drying technique and determined a surface area of less than or equal to 300 m²/g [14]. Although this method provides a more realistic specific surface area as compared with the standard BET measurement, the authors acknowledge that the resin structure is most likely altered in the analysis process.

7.3.3.1. Experimental Description

This section describes the experimental method to determine the specific surface area for the CF resin. The method uses the bound, pore water volume per mass of resin and the

intermolecular distance for water to determine the specific surface area. Using a simple model for the resin structure, it can be assumed that the bound water is the only water component in direct contact with the exchanging resin surfaces. This bound water fraction is assumed to be one monolayer thick and uniformly covers the resin surfaces. With these assumptions, the following relationship between the resin surface area, S_{CF} , and the bound water volume, V_{bw} , can be made, which is related by some intermolecular distance for water, d_w .

$$S_{CF} = V_{bw} / d_w$$

The intermolecular distance for water, d_w , is 2.76 \AA (0.276 nm) [15]. Using this relationship and an experiment relating the volume of bound water to the resin mass, it is possible to calculate a specific surface area for the resin. The volume of bound water per gram of CF resin is determined by the polybutadiene (poly-b) experiment described below.

The poly-b experiment involved the use of a known amount of polybutadiene ($[-CH_2-CH=CH-CH_2-]_n$) used as a standard to evaluate the volume of bound water in a known quantity of resin. This was accomplished by placing a known mass of polybutadiene in the center of a sample, and based on the integrated signal and known proton density, it's possible to determine the relative signal per proton. With this signal to proton ratio, the number of protons belonging to the water signal can be determined. With the total number of water protons, it's possible to determine the volume of water based on the known proton density for water.

The experiment involved a simple excitation and spectral deconvolution to get relative signal for each component. The polybutadiene was used since it has clearly distinguishable peaks shifted to the right and left of the water peak. A special magic-angle-spinning rotor was used to ensure the entire sample was within the active area of the RF coil to ensure even excitation and signal collection. The experiment was performed on the 12T magnet using a high-resolution non-spinning probe. Details of the experiment and the resultant spectra are included in Figure 7.4, Table 7.5, and the following section.

7.3.3.2. Experimental Results

The results of the poly-b experiment and a calculation of the specific surface area for the CF resin are provided as follows.

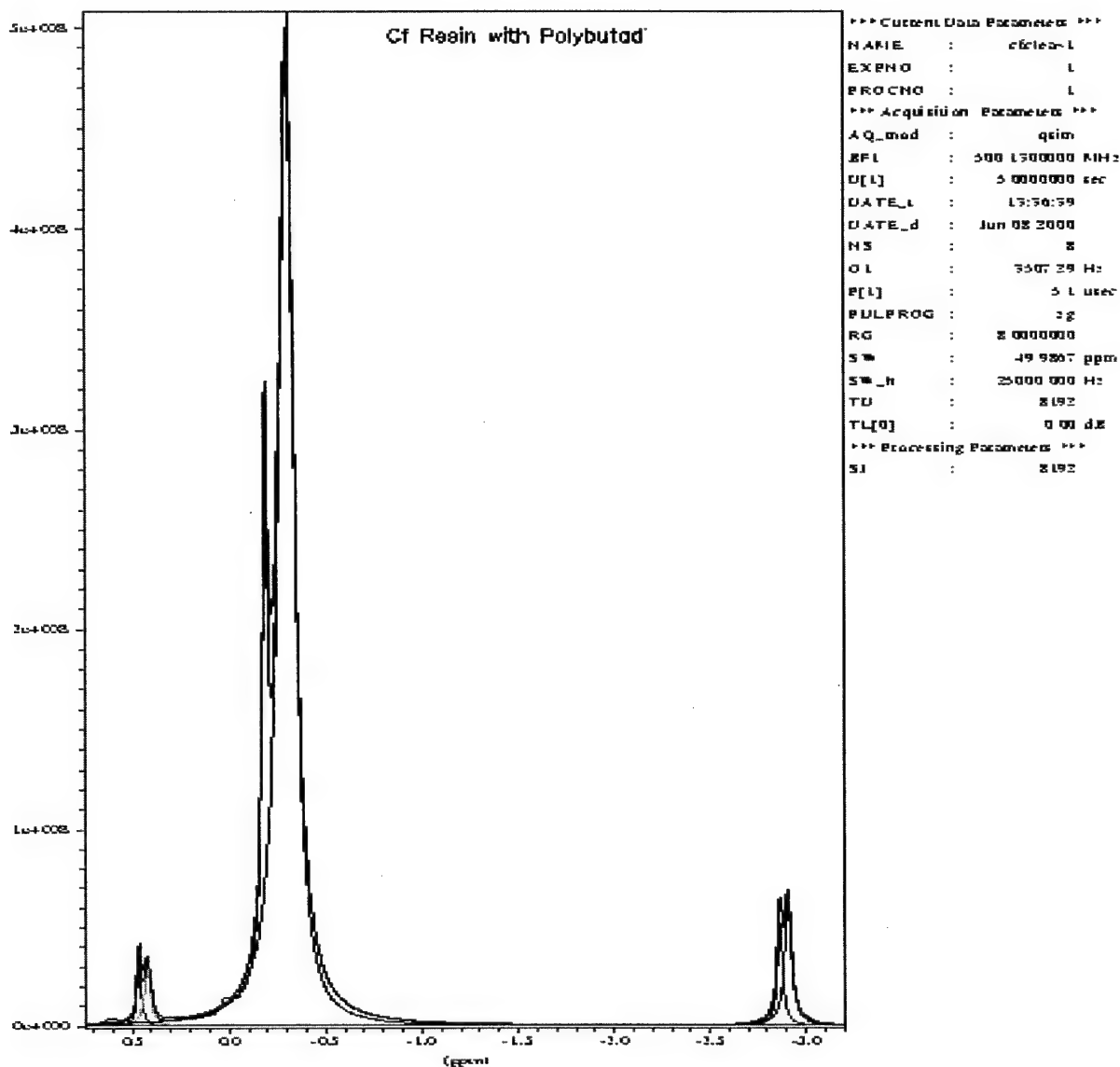


Figure 7.4: Deconvolution of CF clean resin and polybutadiene to determine the mass of water belonging to the bound water pool. This is accomplished by using a known quantity of polybutadiene and using its integrated signal to determine the water signal.

Table 7.5: Deconvolution of CF Clean + Polybutadiene Spectrum

No.	Position [ppm/Hz]	Intensity [abs.]	Width [Hz]	G/L	Integral (abs.)	Population[%]
1	0.4621/231.1	32819028	15.16	0.50	2.302112e+008	1.5-polyb
2	0.4219/211.0	31074588	22.74	0.20	3.490161e+008	2.4-polyb
3	-0.3054/-152.7	497193408	44.31	0.10	1.111039e+010	74.3-water
4	-0.1900/-95.0	247766688	17.49	0.20	2.140338e+009	14.3-water
5	-2.8664/-1433.2	49501992	16.91	0.10	4.221516e+008	2.8-polyb
6	-2.9072/-1453.6	62367232	22.15	0.00	7.110498e+008	4.7-polyb

Based on the deconvolution, 88.6% of the signal is associate with the water and 11.4% belongs to the polybutadiene. Since the initial sample was composed of 5.6 mg of CF resin and 1.17 mg of polybutadiene, the following proton densities and water volumes can be calculated.

- Polybutadiene:
 - $(-\text{CH}_2-\text{CH}=\text{CH}-\text{CH}_2-)_n$
 - mw: 54 g/n or 4.2E5g/mol ($n=7778/\text{mol}$)
 - 6-protons/n or 6.7E22 protons/g
 - molecular density: 0.9 g/cm³
 - proton density: 6.02E22 protons/cm³
 - quantity in sample: 1.17 mg or 2.8E-9mol or 1.3E-3cm³
 - protons in polyb sample: 7.83E19 protons
 - relative signal: 11.4% / 7.83E19 protons = 1.46E-19 % signal/proton
 - signal density: 8.8E3 % sig/cm³
- Water:
 - H₂O
 - mw=18.02 g/mol
 - 2-protons/molecule or 1.2E24 protons/mol
 - molecular density: 1 g/cm³
 - proton density: 6.7E22 protons/cm³
 - relative signal: 88.6%
 - protons related to signal: 6.1E20 protons
 - volume of water in sample: 9.1E-3 cm³ or 9.1E-3 mL
 - **Bound water volume: $V_{bw} = 3.6\text{E-}3 \text{ mL } (3.6\text{E-}9 \text{ m}^3)$**
 - (assume 40% bound water by volume – ref. Figure 4.1)
- CF Resin:
 - Mass: 5.6 mg
 - **Volume of bound water per g resin: $V_{bw} / m_{cf} = 0.65\text{E-}4 \text{ L/g } (6.54\text{E-}7 \text{ m}^3/\text{g})$**

With the volume of bound water per gram of resin, V_{bw} / m_{cf} , of 6.54E-7 m³/g and the intermolecular distance of water, d_w , of 2.76E-10 m, the specific surface area of the CF resin (SSA_{CF}) is,

$$\text{SSA}_{CF} = (V_{bw} / m_{cf}) / d_w = 2370 \text{ m}^2/\text{g}$$

7.3.4. Theoretical Proton Exchange Capacity Determination

Based on SSA, an estimate of theoretical proton exchange capacity can be made. In general, the proton exchange capacity refers to the number of protons per gram of material that exchanges with another monovalent cationic species. For these resins, the theoretical proton exchange capacity (PEC) is a measure of the number of phenolic function groups per gram of resin, which assumes all hydrogen ions on the phenolic group are available for exchange. However, due to a number of physical and chemical interferences, the experimentally measured exchange capacity is usually less than the theoretical PEC. The ratio of the measured PEC to the theoretical PEC is termed the loading capacity. Now that the terms are defined, it is possible to describe the rationale of the NMR method to calculating the PEC.

First, the functional sites per mass of resin must be determined. For the CF resin, there are two neighboring functional groups on the ring structure, and assuming one CH₂ cross-link per ring. With a carbon-carbon bond length of approximately 0.154 nm and a carbon-oxygen bond length of 0.143 nm, an estimate of the average phenolic functional group distance per ring structure is about 0.5 nm. This estimate is based on both function groups being accessible on the wetted surface, and the phenolic groups coming off the ring structure at 60-degrees from each other. In addition, the CH₂ cross-links add another 0.5 nm (minimum) to the spacing between phenolic groups on adjacent ring structures.

With these assumptions, it is reasonable to assume that the average distance between phenolic groups on the CF polymer is at least 0.5nm, and could be two to three times this value. Thus in 1 g of resin, we could have as many as four functional sites per 2.5E-19 m², or 1.6E19 - OH groups/m². With a SSA of 2370 m²/g, the number of functional sites (-OH groups) per gram could be as high as 3.8E22 functional sites/g-resin. The PEC is defined in terms of the number of moles of protons exchanged per mass of resin with units of equivalents per gram. Therefore, the theoretical proton exchange capacity for the CF resin is 6.3E-2 equivalents/g or 63.0 meq/g.

$$\text{Theoretical PEC}_{\text{NMR}} = 63.0 \text{ meq/g}$$

The measured, empirically derived PEC is 8.6 meq/g with a loading capacity of 0.622 (ref. Section 4.4). This measured PEC and loading capacity can be back calculated to determine a theoretical PEC of 13.8 meq/g.

$$\text{Theoretical PEC}_{\text{measured}} = 13.8 \text{ meq/g}$$

Comparing the NMR derived PEC of 63.0 meq/g with the empirically derived PEC of 13.8 meq/g, it is apparent that the NMR method generates a rather high estimate. The greatest error in the NMR measurement is most likely in the assumption of phenolic group distances. It is likely that the distances between phenolic groups is greater than 0.5nm (on average), and thus, an increase in average –OH group distance may correct the discrepancy. Another area for improvement of the method would be to perform a magic-angle-spinning experiment on the poly-b sample. This would allow for direct determination of the bound water fraction and more accurate relative populations.

7.3.5. Gadolinium Loaded Resin Experiments

A series of experiments were performed on CF and RF resin which were saturated with gadolinium (Gd), as described in Section 4.4. The purpose of the experiments was to determine the effect of the increased susceptibility variation and attempt to quantify the loading capacity. Although some results are presented for this study, there is much more work to be done with Gd-loaded resins. The data presented includes spectral and relaxation data. The experiments used are described in Section 5.1. The experiments include spectral collection and deconvolution, inversion recovery, progressive saturation, and CPMG. The results are provided in Table 7.6.

Table 7. 6: Data from Gd-Loaded Experiments on CF and RF Resins

	CF Clean	CF Loaded	RF Clean	RF Loaded
Dipolar Line-Width				
ω_d -Static (Hz)	232	22070	220	24000
ω_d -MAS 5kHz (Hz)	9	390	18	500
Spin-Lattice Relaxation				
$T_{1\text{-Static}}$ (ms)	1378	123	1340	170
Spin-Spin Relaxation				
Bound Water $T_{2\text{-Static}}$ (ms)	8.9	4.1	13.2	1.8

The results of the Gd-loaded experiments show the effect of the paramagnetic Gd species on the relaxation rates and the spectral line-width. From this data, the relative susceptibility for the Gd-loaded CF and RF resins are calculated from the relationships in Section 4.3. The susceptibilities for the Gd-loaded resins are as follows:

$$\chi_{\text{CF}} = 43$$

$$\chi_{\text{RF}} = 28$$

7.4. Conclusions

NMR methods have increased the understanding of the microscopic characteristics of CF and RF phenolic resins. The NMR spectral deconvolution first indicated the presence of three major components in the resin-water system. Further relaxation studies justified this initial assumption and gave effective lifetimes to the three components. Diffusion measurements helped describe the mobility of the three pools and led to a greater understanding of kinetic exchange between the pools. These exchange mechanisms are important in determining the ultimate performance of the ion-exchange resins. The differences in exchange rates could assist in the predicted performance of a resin. For example, the RF resins have a faster exchange rate than the CF resins between the free and plasticizer pools which could lead one to assume that the RF resin has a more ordered structure. This assumption is somewhat justified in that the empirically derived proton exchange capacity for the RF resins is 30% greater than for the CF resins.

The bound water volume is an important parameter extracted from these NMR studies. A bound water volume for these resins has proven difficult to measure using standard techniques. This is due to the gel-like nature of the resin with the water, and the swelling of the resins under saturated conditions. Standard surface area and volumetric techniques normally require the measured media to be in an unsaturated water state or of a known water bearing state. A completely dry resin is not possible without degrading the resin structure, and a partially saturated resin, does not allow the resin to reach its equilibrium state when in use as an ion exchanger. Therefore, for polymeric organic media like these phenolic resins, NMR techniques may be the best method for extracting accurate the bound water volume. In addition, the bound water volume allows for a direct determination of the specific surface area, which is a critical parameter for understanding ion exchange and other surface interactions.

The proton exchange capacity (PEC) is another critical parameter used in determining the effectiveness of ion-exchanging materials. A precise determination of the available functional sites is necessary in determining the theoretical PEC, however this is very difficult to determine with unstructured materials, such as organic resins. Most methods used to determine PEC rely on empirical measurements and assumptions, which could introduce large systematic error into a PEC determination. The NMR techniques used in this study allow for the determination of PEC

from interactions at a microscopic level, thus reducing the likelihood of systematic discrepancies in the analysis. Although there may be error in estimating bond distances and functional site densities, these NMR techniques provide a direct evaluation of the theoretical PEC and can be used to place bounds on empirically derived values.

The three-pool model used to describe the microscopic interactions in the CF and RF ion-exchange resin has proven to be a good model. The model assists in the understanding of the exchange dynamics between the three pools, and provides a basis to extract spatial and temporal information from the system. This multi-faceted NMR approach to probing microscopic interactions in porous media holds great promise. These NMR methods provide information about certain types of porous systems that could not otherwise be measured.

References for Section 7.0

- ¹ P.T. Callaghan, "Principles of Nuclear Magnetic Resonance Microscopy," Clarendon Press, Oxford (1991).
- ² B. Manz, P. Alexander, and L.F. Gladden, Correlations Between Dispersion and Structure in Porous Media Probed by Nuclear Magnetic Resonance, *Physics of Fluids*, 11 No. 2, 256-267 (February 1999).
- ³ W.E. Kenyon, *Nucl. Geophys.* 6, 153-71, 1992.
- ⁴ J. Pauli, G. Scheying, C. Mugge, A. Zschunke, and P. Lorentz, Determination of the Pore Widths of Highly Porous Materials with NMR Microscopy, *Fresenius J Anal Chem*, 357:508-513 (1997).
- ⁵ M.D. Hurlimann, K.G. Helmer, L.L. Latour, and C.H. Sotak, Restricted Diffusion in Sedimentary Rocks. Determination of Surface-to-Volume Ratio and Surface Relaxivity, *J. Mag. Reson., Ser. A* 111, 169 (1994).
- ⁶ R. Kimmich, *NMR-Tomography, Diffusometry, Relaxometry*, Springer, 1997.
- ⁷ D.Kost, E.H. Carlson, and M. Raban, *Chem. Commun.* 656, 1971.
- ⁸ J. Sandstrom, *Dynamic NMR Spectroscopy*, Academic Press, pp 12-29, 1982.
- ⁹ H.M. McConnell, *J. Chem. Phys.* 28,430, 1958.
- ¹⁰ J. Sandstrom, *Dynamic NMR Spectroscopy*, Academic Press, p. 17, 1982.
- ¹¹ L.H. Anderson and W.A. Anderson, *J. Chem. Phys.* 30, 899, 1959.
- ¹² S. Brunauer, P.H. Emmett, and E. Teller, *J. Amer. Chem. Soc.* 60, 309, 1938.
- ¹³ M. Draye, K.R. Czerwinski, A. Favre-Reguillon, J. Foos, A. Guy, and M. Lemaire, *Sep. Sci. Tech.*, 35(8), pp. 1117-1132, 2000.
- ¹⁴ B. Mathieu, B. Michaux, O. Van Cantfort, F. Noville, R. Pirard, and J.P. Pirard, *Ann. Chim. (Paris)* 22(1), 19-29, 1997.
- ¹⁵ R.A. Horne, *Marine Chemistry*, Wiley Interscience, 1969.

8. NMR IMAGING OF ION-SPECIFIC RESINS

This section is broken into two sub sections. The first section (8.1) contains a technical paper that has been submitted to the journal, Separation Science and Technology. The paper is currently in review. The content of the paper includes a general description of NMR flow measurements, 2- and 3-dimensional images of Gd sorption to CF and RF resins, and the presentation of a flow model to quantify fingering of the flow front. The second section (8.2) contains a flow study on PF resins with varying flow chemistry. The purpose of the experiments were to visualize desorption of Gd under various flow conditions and to measure the proton exchange capacity of the PF resin.

8.1. NMR Imaging Paper:

Characterizing Transport and Separation In Ion-Specific Resin Columns using Nuclear Magnetic Resonance (NMR) Imaging

(Submitted to Separation Science and Technology, Jun 00 – currently in review)

ABSTRACT

The goal of this work is to characterize the physical transport properties of a lanthanide through an ion exchange resin while determining the separation properties of the resin. By coupling the physical transport with the chemical sorption, further insight can be gained into the behavior of the ion exchange resin. NMR imaging provides a powerful, non-destructive, means to extract spatial information from complex systems on a near real-time basis. An important example is fluid flow through granular media. With the use of a chemically reactive NMR contrast agent, the chemical speciation and separation can be traced along the physical flow path in the granular media. In this study, trivalent gadolinium (Gd^{3+}) was selected based on its chemical similarity to typical high-level waste components, ^{241}Am and ^{244}Cm , and it's a useful NMR contrast agent. NMR imaging results of flow experiments show characteristic flow phenomena and resin column loading profiles. A simple idealized flow model was developed to quantify the degree of preferential flow, or fingering, based on two-dimensional NMR images. ICP-AES analysis of the effluent gives resin ion exchange capacities (IECs) and breakthrough curves which can be coupled to the image loading profiles. The use of NMR imaging with the Gd^{3+} tracer leads to a better understanding of the transport and separation abilities of these ion-specific resins and can be useful in quantifying the degree of fingering in heterogeneous systems. NMR imaging provides the only real-time means to visualize metal loading in reactive, heterogeneous flow systems to extract true ion exchange capacity factors. There is no other non-invasive technique that can directly determine the volume of the reactive material exposed to the Gd solution, which is necessary to determine the ion exchange capacity of a heterogeneous flow system. This technique has direct application to other complex flow systems such as environmental transport of contaminants in geological media.

8.1.1. Introduction

Ion-specific resins have been developed to partition similar inorganic chemical species, such as Cs from Na, from waste streams in radioactive waste reprocessing operations. The resins used in these studies are synthetic organic structures with phenol functional groups. The resins are made selective by incorporation of a chelating compound within the resin structure. These types of resins have been shown to form stable complexes with a variety of radionuclides [1].

Due to the recent development of these synthetic resins, there is a general lack of information on the behavior of the resins under operational conditions. Many analytical methods exist to provide information on the bulk characteristics of a packed resin column, however, few methods exist to extract real-time spatial information from the columns under operational conditions. The method chosen in this study is nuclear magnetic resonance (NMR) imaging with the use of a lanthanide tracer to examine new ion-specific resins for the separation of trivalent metal ions.

NMR imaging is a non-invasive technique to probe the spatial structure of a variety of complex systems [²⁻⁵]. By using a paramagnetic ion in a water-based solution, the behavior of that ion can be traced as it moves through the NMR sampling volume, since the paramagnetic ion reduces the NMR relaxation times of neighboring water spins [⁶]. The ability to use an ion as a NMR tracer provides a means to assess the physical structure of porous media while identifying the chemical behavior along the flow path [⁷]. Specifically, the chemical speciation (sorption, complexation, colloid formation, and precipitation) can be traced along a flow path, which leads to a greater understanding of the ultimate fate of the ion. This NMR tracer method can be applied to a variety of systems where chemical behavior must be coupled to physical transport in order to predict the change in ion concentration along a flow path.

8.1.2. Experimental Setup

This work uses the trivalent lanthanide, Gd^{3+} , as a chemical analog for trivalent actinides. Lanthanides and actinides have long been used as chemical analogs for each other based primarily on the gradual filling of the 4f and 5f subshells by the lanthanides and actinides, respectively, which result in similar relative orbital energies [8-9]. In particular, the trivalent lanthanides and actinides have similar ionic radii, which results in similar ligand-metal orbital interactions as seen in the resultant absorption spectra and stability constants [10-11]. Based on these chemical similarities, Gd^{3+} ions can be used as a good analog in modeling the chemical reactivity of the trivalent actinide species, ^{241}Am and ^{244}Cm .

The Gd^{3+} ion has the additional physical property of being paramagnetic, due to its half-filled 4f subshell with seven unpaired electrons [12]. This electron configuration creates localized fluctuating magnetic moments. The influence of the Gd^{3+} ion on the proton relaxation is highly localized and provides the ability of measuring Gd ion concentrations in solutions or Gd ions

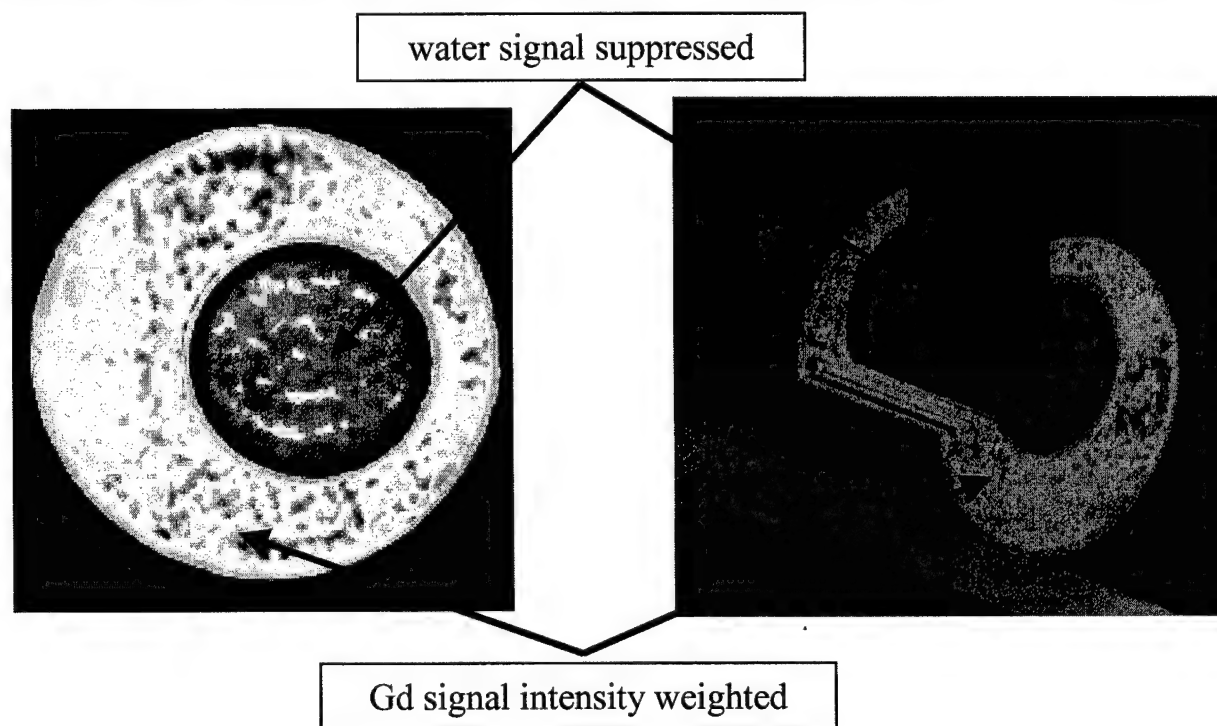


Figure 8.1: 2- and 3-D NMR images showing an inner 5.0 mm diameter tube of water surrounded by a 0.1mM Gd solution in sand (10.0 mm OD). Using a T_1 weighted inversion recovery sequence, the protons in the Gd solution exhibit an increased signal intensity with respect to the bulk water signal.

sorbed to surfaces. The NMR experiments in this paper make use of the increased spin-lattice relaxation rate of water protons near the Gd^{3+} ion to track the physical and chemical behavior of the Gd^{3+} ions as they flow through granular media. An example of this weighting is shown in Figure 8.1, where the NMR signal of water in the outer annulus is enhanced by the presence of the contrast agent. The NMR sequence used in Figure 8.1 was preceded by an inversion recovery sequence so that the normal water resonance was partially saturated.

8.1.2.1. NMR Flow System

The NMR components consist of an Oxford horizontal (15cm bore) 3T magnet equipped with an integrated gradient set coupled to a Bruker AMX spectrometer for gradient control, pulse programming, and data acquisition. The NMR programs used were 2- and 3-D slice selective, spin echo imaging sequences with an initial inversion-recovery step to separate the fast and slow relaxing components.

The flow system consists of an Edwards high-vacuum pump, a Nold 6L Water De-aerator [¹³], a Varian stepper motor/piston pump, a source of compressed air, and a set of pressure reservoirs with associated tubing, valves, gauges, and NMR sample tube. The flow system is able to evacuate the test specimen and tubing, fill the sample media with deaerated water (or another liquid), and then apply a positive pressure to assure saturation, thus eliminating air bubbles and subsequent susceptibility effects. All of these components are linked in a closed loop flow system that permits complete control of fluid movement through the test specimen. The vacuum pump is used to draw air out of solution in the water deaerating unit and to evacuate the piston chamber, specimen tube, flow tubing, and pressure reservoirs down to a vacuum of 0.1 MPa. The water deaerating unit is operated in a batch mode and can produce up to 6 L of water with an air content of less than 0.6 ppm dissolved oxygen, DO (9 ppm DO ambient level) [¹⁴]. The deaerated water is then used to saturate the test specimen via the piston pump or the pressure reservoirs. The piston pump is used to control the flow rate and pressurization of the system. This system is capable of displacing up to 375 mL of fluid per stroke at a rate of up to 5 mL/sec at pressures more than 6.0 MPa. By over-pressuring the liquid in the reservoirs at the inlet end and displacing the piston at the outlet end of the sample tube, the liquid can be moved through the system in plug-flow fashion. In this experiment, the system was under 0.42 MPa of pressure

during the entire flow experiment. The flow rate was held constant at 0.1 mL/sec or approximately 0.5 cm/sec through the 10.0 cm long sand and resin filled column.

8.1.2.2. Phenolic Resins

The phenolic resins used in these experiments are described and were prepared according to the procedures in ref. [15-16]. The NMR sample contained 0.2 g (dry) of the resorcinol-formaldehyde (RF) resin. The resin was converted to the Na^+ form through a wash and neutralization cycle with 1N NaOH and de-ionized water. The resin was then sieved with sand (high purity, ignited) into a 0.8 cm inner diameter NMR sample tube to produce a homogenous resin/sand layer approximately 2.0 cm long. This homogenized mixture allowed for good flow pathways through the sample and provided maximum available resin surface area for ion exchange. Pure sand was placed on each end of the resin/sand mixture to ensure good dispersion and flow development of the inlet solution. The inlet solution was 1.0 mM GdCl_3 at pH 5.4, and thus, the Gd ion was not hydrolyzed under experimental conditions.

8.1.2.3. ICP-AES

The ICP-AES system used for this work is the Spectroflame ICP-D model Inductively Coupled Plasma - Atomic Emission Spectroscopy. The samples were extracted from the column in a batch process of between 10 and 50 mL. The samples were then filtered through 0.45 μm filters to remove any particulates which could clog the ICP-AES system. Three measurements were taken for all samples, and the average and standard deviations were calculated. A six point calibration curve was generated using Aldrich ICP Gd Calibration solution diluted over the range of expected concentrations. The count rate data from the batch samples was converted to Gd concentration using the six point calibration curve ranging from 0.1 μM to 6.4 mM. A lower limit of detection of 0.7 μM was established at two standard deviations above background level for the de-ionized flush water.

8.1.3. Results

8.1.3.1. 2-D Flow Series

The series of 2-D NMR images in Figures 8.2 and 8.33 show the ingress of a 1.0 mM Gd solution into a 0.8 cm diameter flow columns containing RF and CF resin, respectively. The column in Figure 2 is packed with a homogenous mixture of 2.0 g sand and 0.4 g-wet (0.2 g dry) resorcinol-formaldehyde (RF) ion-specific resin, and the column in Figure 8.3 is packed with pure 0.1 g-dry catechol-formaldehyde (CF) resin. Both resin samples were saturated with de-ionized water before Gd ingress in order to establish a fully saturated condition for image analysis. The images were generated using a two-dimensional, slice-selective, spin echo imaging sequence with spin-lattice relaxation, or T_1 , weighting. The paramagnetic nature of the Gd^{3+} ion causes a decrease in the T_1 of neighboring protons thus allowing for a separation of the NMR signal from the protons in free/bulk water and to those in the Gd solution. The T_1 of the pure water in resin is approximately 0.5 s for both resins, whereas, the T_1 for the Gd loaded resin is on the order of 50 ms. The T_1 measurements were performed using a combination of inversion recovery and progressive saturation NMR sequences. Due to the short T_1 of the Gd, and thus shortened spin-spin (T_2) relaxation rates of a few milliseconds, the spin echo delay (2-4 ms) resulted in a complete loss of the Gd signal. The RF resin image size is 150 by 255 pixels corresponding to 0.8 cm in height and 1.2 cm in width, and the slice thickness is approximately 0.1 cm. This provides an effective resolution of 50 μm in the imaging plane. The CF resin image size is 75 by 90 pixels corresponding to 0.8 cm in height and 1.2 cm in width, and the slice thickness is also approximately 0.1 cm. This provides an effective resolution of about 100 μm in the imaging plane, which although double the RF resin resolution is still more than adequate for these studies.

The RF image sequence in Figure 8.2 clearly shows the development of a characteristic parabolic flow, which eventually leads to preferential, or fingering, flow (Fig. 8.2, Image #5). The fingering flow phenomena is characteristic in heterogeneous flow environments with varying hydraulic conductivity and/or varying flow conditions. The CF image sequence of Figure 8.3 shows the development of a square flow profile which is indicative of plug flow behavior. Plug flow is characteristic in homogeneous flow environments where the hydraulic conductivity and flow conditions are constant. Some fingering can be seen in front of the square

flow profile (Fig. 8.3, Image #5), however the fingering is limited and does not appear to be growing as the flow progresses.

During the 2-D imaging sequences of Figures 8.2 and 8.3, the effluent was collected and the Gd concentration analyzed using ICP-AES. The results of the effluent analyses are provided in Figures 8.4 for pure sand, RF resin, and CF resin column experiments. The pure sand data was added as a baseline showing a non-reactive, idealized flow environment. All sample concentrations were normalized to an initial 1.0 mM Gd concentration from the flow reservoir. Figure 4 shows the typical breakthrough curves showing the normalized Gd effluent concentration versus the total volume of fluid through the column. All flow experiments started with an initial flush of 50 mL of de-ionized water. From the breakthrough curves, the volume of Gd solution necessary to saturate the resin ion-exchange, or functional, sites with the Gd^{3+} ions can be determined, and thus, the ion exchange capacity can be calculated. With an initial Gd concentration of 1.0 mM, the 0.2 g-dry RF resin reaches saturation after an influx of approximately 775 mL and the 0.1 g-dry CF resin reaches saturation after 425 mL. This corresponds to an ion exchange capacity (IEC) of 3.9 milli-equivalents per gram of dry RF resin (meq/g-dry) and an IEC of 4.25 meq/g-dry of CF resin. Both IECs were calculated at the experimental pH of 5.4. Since the Na^+ form of the resin was used and the exchange ion was trivalent Gd, the corresponding proton exchange capacity is 11.7 meq/g for the RF resin and 12.8 meq/g for the CF resin, assuming three functional sites per Gd^{3+} ion. This value correlates well with the literature value for the RF resin of 11.5 meq/g but deviates from the literature value of 8.6 meq/g for the CF resin [16]. This deviation from the published laboratory data is most likely due to the variation in flow parameters for the two systems. The Figure 8.4 plot also shows the high affinity of the RF and CF resins for Gd^{3+} ion. This high stability of the resin/Gd complex is shown by the immediate reduction and stabilization of the Gd effluent concentration to below background ($<0.7 \mu\text{M}$) after up to a 1.0 L water flush.

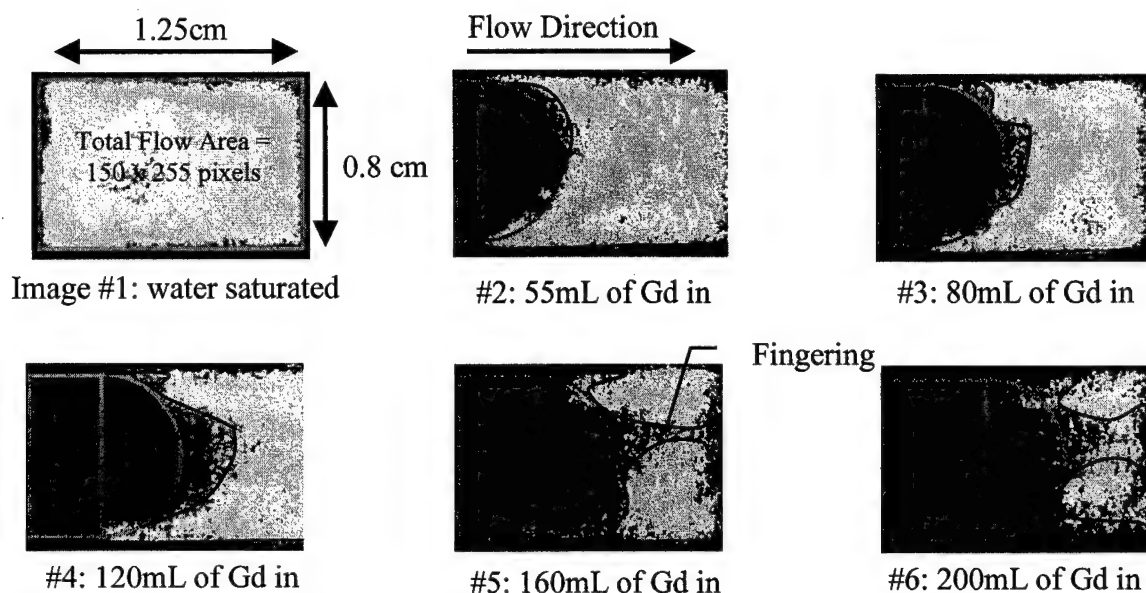


Figure 8.2: Sequence of 2-D NMR images (0.8cm x 1.2cm) showing the flow profile of a 1.0 mM Gd solution entering a RF ion exchange resin column with increasing fingering as the flow progresses. Image #1 is the total flow area of 150 by 255 pixels which corresponds to a completely water saturated resin bed. A parabolic flow front is seen developing in images #2-4 which is indicative of laminar flow. Image #5 clearly shows fingering flow phenomena which can be coupled to effluent data as shown in the breakthrough curve (Figure 8.4). Each image in the sequence shows the idealized flow area, calculated from the amount of fluid into the resin, and the increasing degree of fingering as the Gd flow deviates from the idealized flow path.

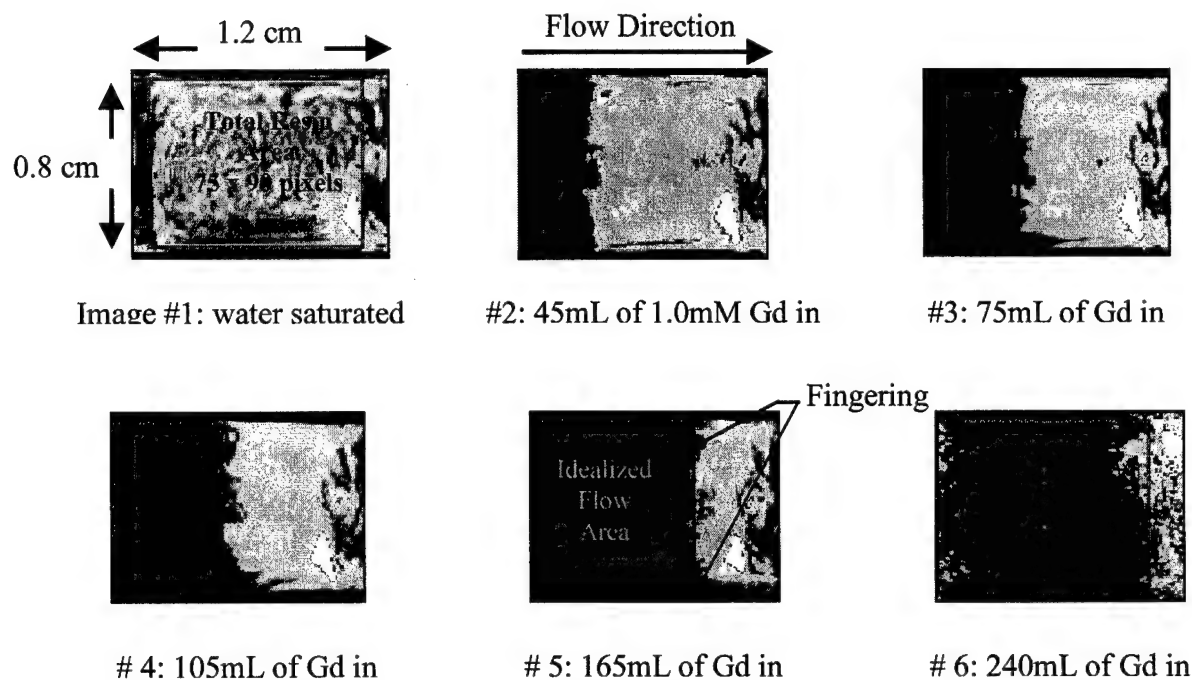


Figure 8.3: Second sequence of 2-D NMR images (0.8cm x 1.2cm) showing the flow profile of a 1.0 mM Gd solution entering a CF ion exchange resin column. This sequence shows a typical square, or plug, flow profile indicative turbulent flow with constant permeability and back-pressure across the sample. A limited and constant degree of fingering is seen throughout the images. The image #1 is the total imaged flow area of 75 by 90 pixels which corresponds to a completely water saturated resin bed. The remaining images show the idealized flow area, calculated from the amount of fluid into the resin.

8.1.3.2. 2-D Quantification of Fingering

From the image sequences in Figure 8.2 and 8.3, the amount of Gd solution flowing in front of an idealized flow profile can be quantified using an idealized flow model. This model defines the degree of fingering as the amount of Gd penetration in front of an idealized flow front (i.e. parabolic or square), and this fingering flow is visualized in Figures 8.2 and 8.3 (image #5) as the Gd occupied regions out in front of the parabolic or square flow fronts. The first image in sequence of both Figures 8.2 and 8.3 is the total area of the resin bed being imaged: 150 by 255 pixels for the RF resin, and 75 by 90 pixels for the CF resin. This area corresponds to a fully saturated/loaded resin bed with 100% of the pixels in the viewing area occupied. The remaining images in the sequence show a steady breakdown of the idealized flow front with increased penetration of the Gd solution as the fluid probes varying pathways in the resin. The idealized flow front and fingering are outlined in the Figure 8.2 and 8.3 images.

Figures 8.5 and 8.6 show the degree of fingering and percent of area occupied by the Gd for both the predicted, idealized, case and for the actual, idealized with fingering, case. The percent or degree of fingering is the Gd occupied area in front of the idealized flow profile divided by the total area in front of the profile. The shape and position of the flow front was determined from the known flow conditions, and the fingering area was extracted from the images by setting an intensity threshold. The degree of fingering is not very sensitive to the chosen intensity threshold since the interface for the Gd is very sharp. The images in Figures 8.2 and 8.3 show this sharp contrast between Gd occupied space and pure water saturated areas.

The idealized flow model was validated through an assessment of the known capacity of the resin in the imaging area and the volume of Gd solution necessary to load that resin. In the RF resin experiments, the quantity of resin in the imaging area (half the total resin area) was 0.1 g (dry) which corresponds to a theoretical loading capacity of 0.39 mmol of Gd^{3+} ions. The imaging area contained approximately half of the total RF resin in the column (0.2 g-dry total). With a Gd solution concentration of 1.0 mM, the volume of solution which would fully load the resin in the imaging window is 390 mL. By extending the idealized flow line in Figure 8.5 to the 100% loaded, or area occupied, point, the model predicts that the required volume of Gd is 386 mL, which is very close to the calculated fully loaded volume of 390 mL. This shows that it is only through a visualization of the actual loading with fingering behavior that a correct accounting of the capacity factor can be given.

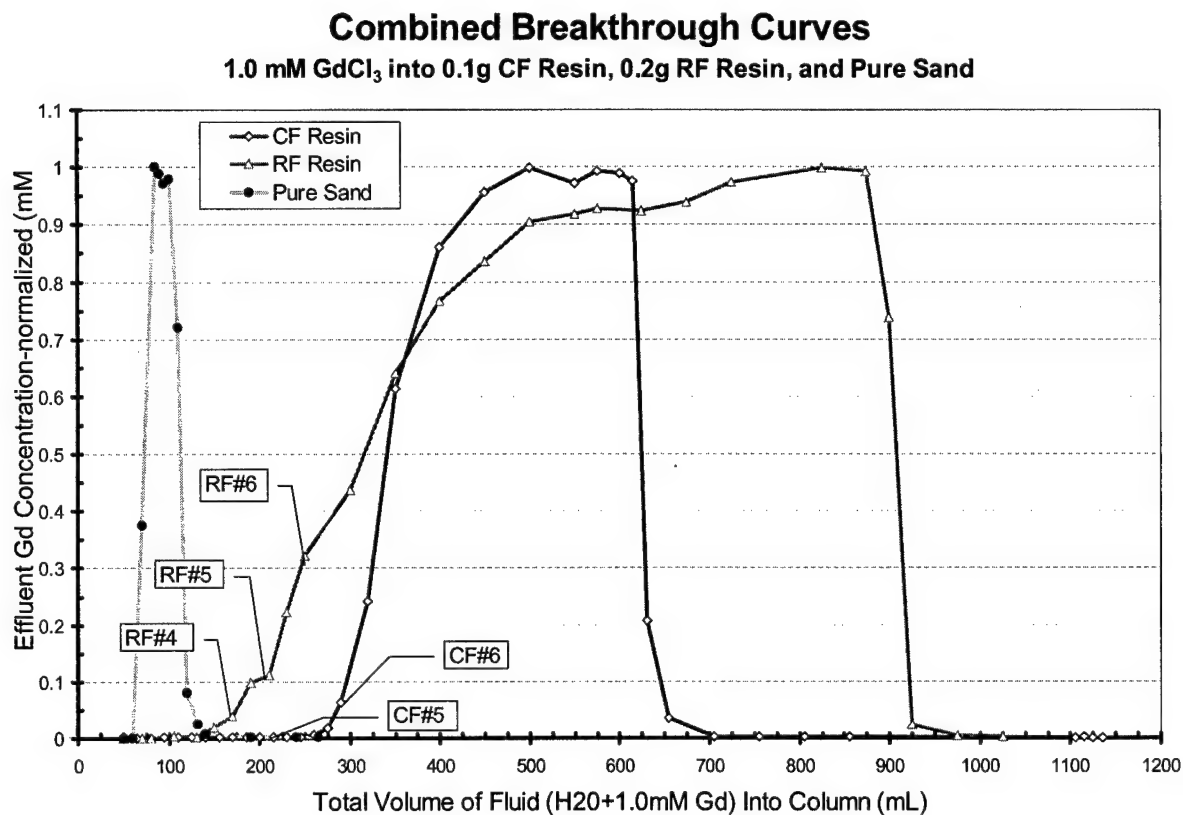


Figure 8.4: Breakthrough curves showing the normalized effluent Gd versus the total volume of fluid through the column for pure sand, and for RF and CF resins. The differences in reactivity and flow conditions of the Gd solution are readily apparent in the shapes of the three curves. The numbers on the plot represent selected NMR images from Figures 8.2 and 8.3 which shows how the imaging can be used to predict breakthrough.

Degree of Fingering in RF Resin

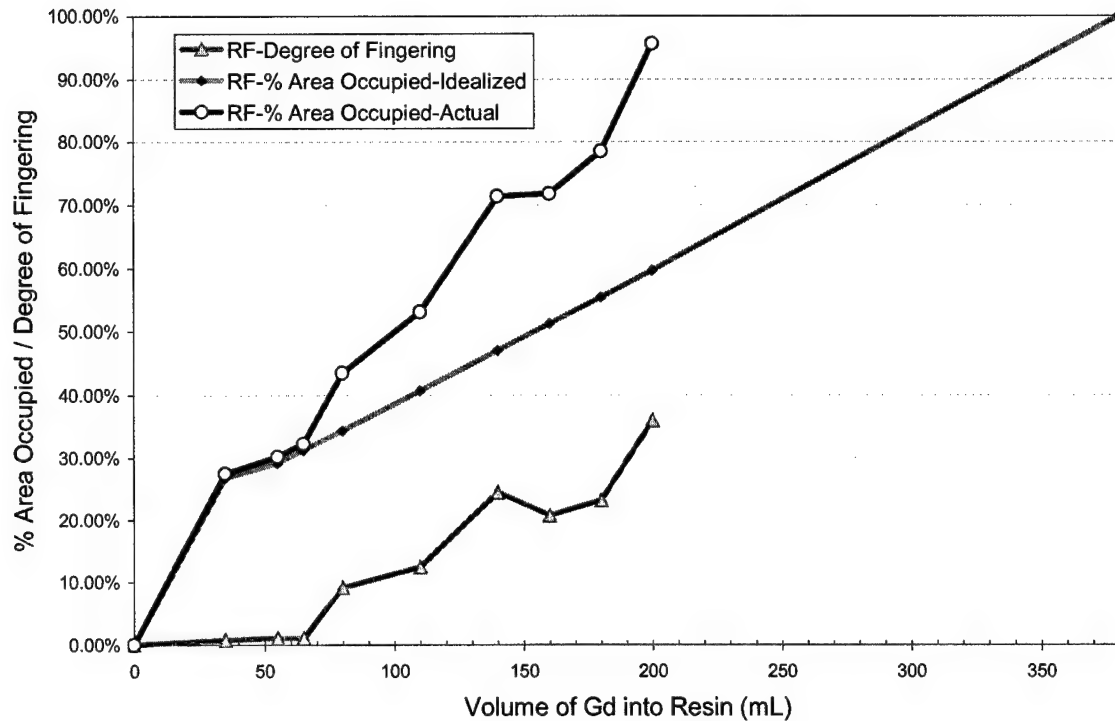


Figure 8.5: Plot of RF resin flow showing the percent of the total flow area predicted by the idealized flow model and the actual flow area (idealized plus fingering) extracted from the 2-D image analysis. The degree of fingering is given as the flow area occupied in front of the idealized flow profile. The increase in fingering as the parabolic flow front breaks down is due to variations in packing, or permeability, of the resin bed.

Degree of Fingering in CF Resin

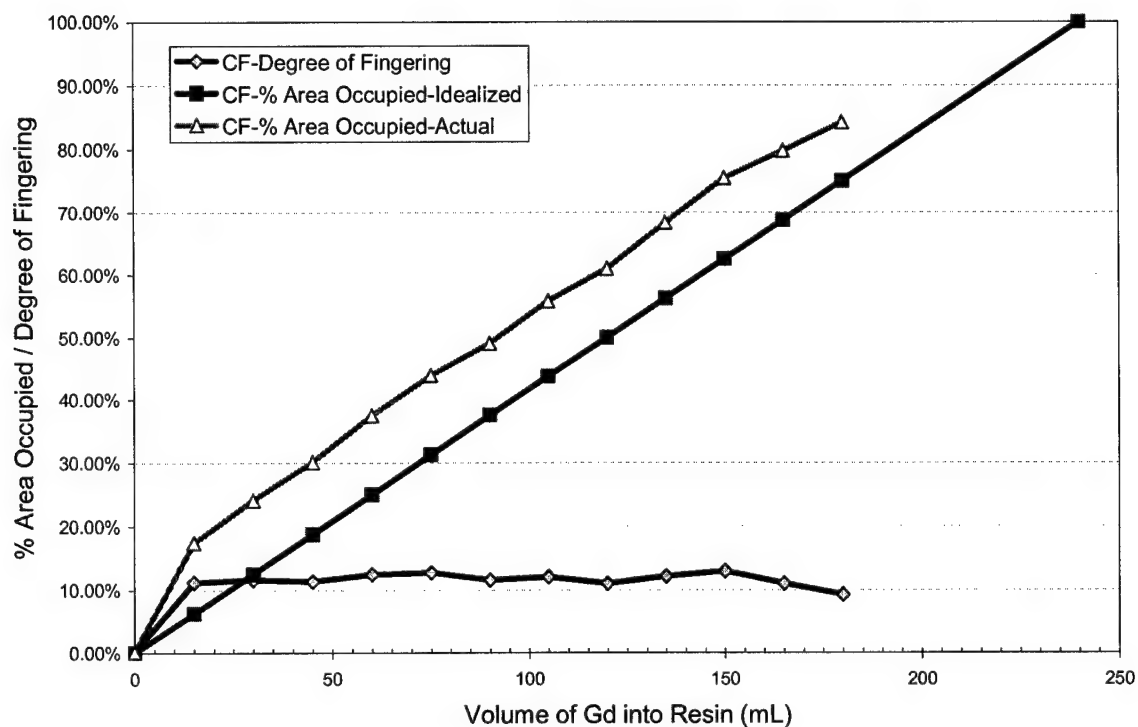


Figure 8.6: Plot of CF resin flow showing the percent of the total flow area predicted by the idealized flow model and the actual flow area (idealized plus fingering) extracted from the 2-D image analysis. The degree of fingering is given as the area occupied in front of the idealized flow profile. In this sequence, the plug-type flow seen in Figure 8.3 leads to a relatively constant and small degree of fingering.

8.1.3.3. 3-D Qualitative Imaging Analysis

The 3-D NMR image in Figure 8.7 shows the physical structure of the sand/resin column and the sorption behavior of the Gd^{3+} ions. The image size is 0.8 cm in diameter by 1.0 cm long with a minimum spatial resolution of approximately 150 μm (128 x 128 x 64 pixels). The resin is completely loaded with Gd^{3+} ions, and the higher loading capacities are visible in the dark areas to the rear of the image. The white areas in the bulk of the image show uniform loading with the exception of a few voids spaces, that are visible at the near end of the image. The heterogeneous voids are due to areas of low sorption, which is a result of sand layering or resins with low Gd loading capacity. The homogenous (spherical) voids are most likely the result of large sand grain sizes or agglomerated resins, since care was taken to exclude all air from the sample. The 3-D image clearly shows the heterogeneous nature of ion exchange in granular resin columns.

The parabolic and square flow profiles of Figures 8.2 and 8.3, respectively, are indicative of the type of flow present in each resin column. The parabolic flow front is characteristic of laminar flow where the pressure drop is proportional to the volume rate of flow, and the Reynolds number, $Re = D\langle v_z \rangle \rho / \mu$, for circular tubes is less than 2100. The square, or plug, flow front is characteristic of turbulent flow where the pressure drop is approximately proportional to the volume rate of flow to the 7/4 power, and Re is greater than 4000. The only difference between the two resin columns is the presence of sand in the RF (Figure 8.2) column that increases the porosity, and thus the volumetric flow area of the column. With all other flow parameters being constant, the sand will have the effect of decreasing the average flow rate in the RF resin due to the increase in cross-sectional flow area. This variation in average flow rate through the two resins accounts for the laminar and turbulent flow profiles.

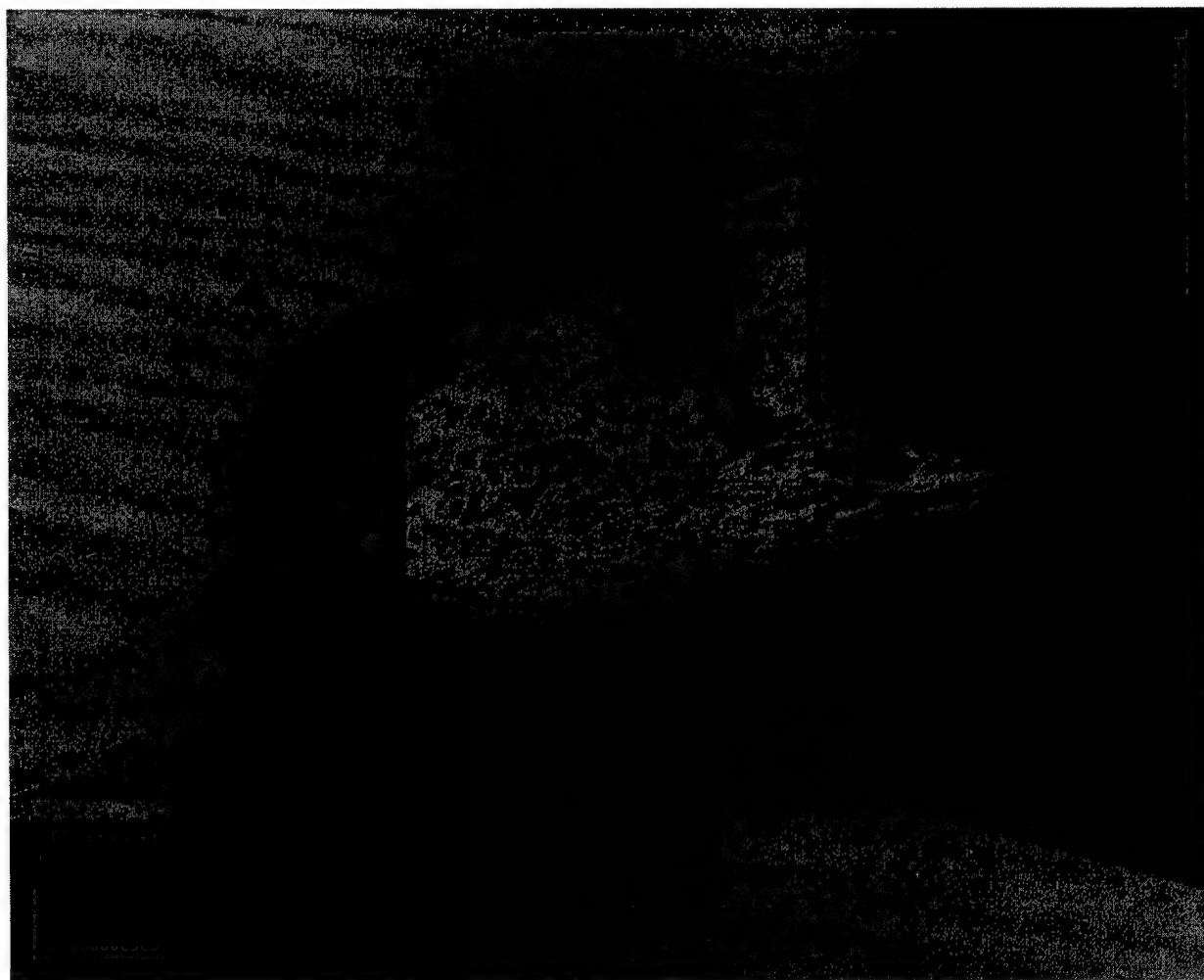


Figure 8.7: 3-D NMR image of a homogenized RF resin and sand sample, 0.8 cm in diameter by 1.0 cm in length. The resin is completely loaded with Gd^{3+} ions, and the heterogeneous nature of the loading is easily visualized. Voids in the sample are also readily apparent.

8.1.4. Conclusions

NMR imaging of Gd^{3+} flow is a useful technique to assist in the understanding of physical transport and chemical behavior of trivalent metal ions in a variety of granular media flow systems. It provides the only real-time means to visualize the Gd^{3+} loading onto chemically reactive surfaces which leads to true quantification of the ion exchange capacity factors in flow systems where fingering or other non-linear flow phenomena is encountered. It is only through the use of this NMR imaging tracer technique whereby the actual mass of complexed material can be assessed, based on an evaluation of the area (or volume) of material which has been occupied by the Gd solution. Without knowing the actual flow area/volume probed by the Gd, it is impossible to determine the capacity of the granular flow system to sorb the Gd^{3+} ions. The NMR tracer technique provides a better understanding of chemical reactivity in heterogeneous flow systems, and this can then lead to a more accurate prediction of the fate of contaminants in more complex flow environments.

8.2. NMR Imaging of Flow in PF Resin

This section includes the results of a NMR imaging flow experiment using phenol-formaldehyde (PF) resin. The flow experiment was performed according to the procedures previously described in Sections 8.1, 5.1.2, 4.3 and 4.3. Therefore, only the experiment specific procedures will be described and the results will be presented. The raw data from the ICP-AES analyses is provided in Appendix 5.0, and the ICP-AES procedures are found in Section 5.2. The purpose of this flow experiment was to determine the proton exchange capacity of the PF resin under flow conditions, and to determine the stability of the PF-Gd complex under increasingly acidic conditions and with a competitive ligand. The competitive ligand was 1.0 mM EDTA (ethylenediaminetetraacetic acid, hexadentate).

8.2.1. Experimental Description and Results

The sample consisted of 0.22 g(dry) PF resin and was prepared according to the procedures in Section 5.1.3.2. The fluids used for the flow experiment consisted of 0.1 mM GdCl_3 solution, 0.1 M HNO_3 , 1.0 M HNO_3 , 6.0 M HNO_3 , and 1.0 mM EDTA. The experiment began with the loading of the PF resin with Gd. The loading was based on a proton exchange capacity of 5.0 meq/g-dry and a loading capacity of 0.2 (interpreted from ref 16 data). Using these values, the 100% loading for trivalent Gd(III) is 0.073 mmol or 730 mL of 0.1 mM GdCl_3 solution. Once the resin was fully loaded using 900 mL of 0.1 mM GdCl_3 solution, the remaining GdCl_3 solution was flushed from the resin with a 220 mL de-ionized water flush. This left the resin fully loaded with Gd with clean water in the interstitial spaces. The 2-D image sequence showing the loading of the resin can be seen in Figure 8.8.

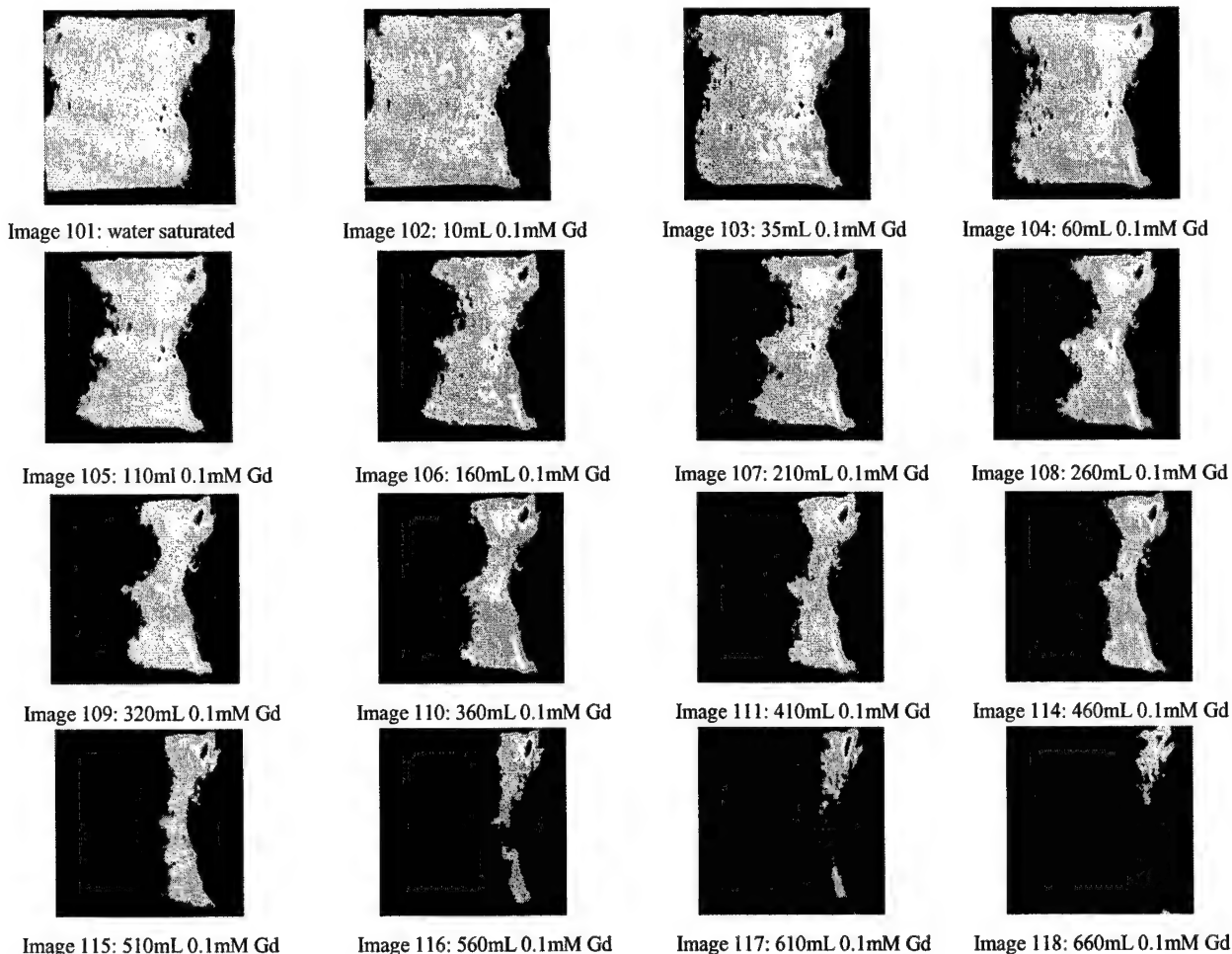


Figure 8.8: 2-D image sequence of the Gd loading of PF resin. The first image (#101) shows the PF resin fully saturated with water. As the sequence progress, the 0.1 mM Gd enters the resin and displaced the clean water. The null signal belongs to the Gd solution and resin sorbed with Gd. The image dimensions are 0.8 cm high by 0.7 cm in length. The spatial resolution for the image sequence is 100 μm by 100 μm (128 by 128 pixels) with a 1000 μm thick slice.

The next part of the experiment was to flow 0.1 M HNO_3 through the Gd-loaded resin to determine the stability of the resin and the effect on the imaging. The imaging sequence in Figure 8.9 shows how the loosely bound Gd is removed and resin is clearly seen again. This would imply that the loosely bound resin has a more dramatic effect on relaxation rate decrease than does the more strongly bound Gd. This could be the result of electronic shielding of the water by the resin for the more strongly bound Gd ions.

Figure 8.9 also shows the effect of the 1.0 M and 6.0 M HNO_3 . The 1.0 M acid doesn't appear to have any effect on the resin, but the 6.0 M acid appears to have a dramatic effect. However, the post 6.0 M acid water flush returns the resin image back to pre-6.0 M flush conditions. This indicates that the 6.0 M flush did not remove Gd from the resin, but rather interfered with the image due to other processes (i.e. increased pH). There were two additional stages to this experiment. One was a kinetic study, where the 1.0M acid was allowed to remain in the resin for 20 hours. This allowed the acid to diffuse into areas of the resin that were otherwise outside the normal flow path. Image #137 in Figure 8.9 shows how the more of the Gd is removed, thus improving the contrast of the image. The final stage of the experiment was to flush the resin with 1.0 mM EDTA. Due to the high stability of a Gd-EDTA complex, the EDTA flush is a way to measure the stability of the Gd-resin complex.

During the flow experiments, the effluent was collected for analysis of the Gd concentration. This allowed the imaging results to be coupled with the effluent Gd concentration to better understand the Gd interaction with the resin. The effluent analysis also allowed for the calculation of the proton exchange capacity (PEC). The PEC was measured to be 1.1 meq/g. A plot of the breakthrough curve with Gd concentration versus fluid volume is shown in Figure 8.10. A plot of the Gd balance through the PF resin showing total Gd into resin and total Gd out is provided in Figure 8.11.

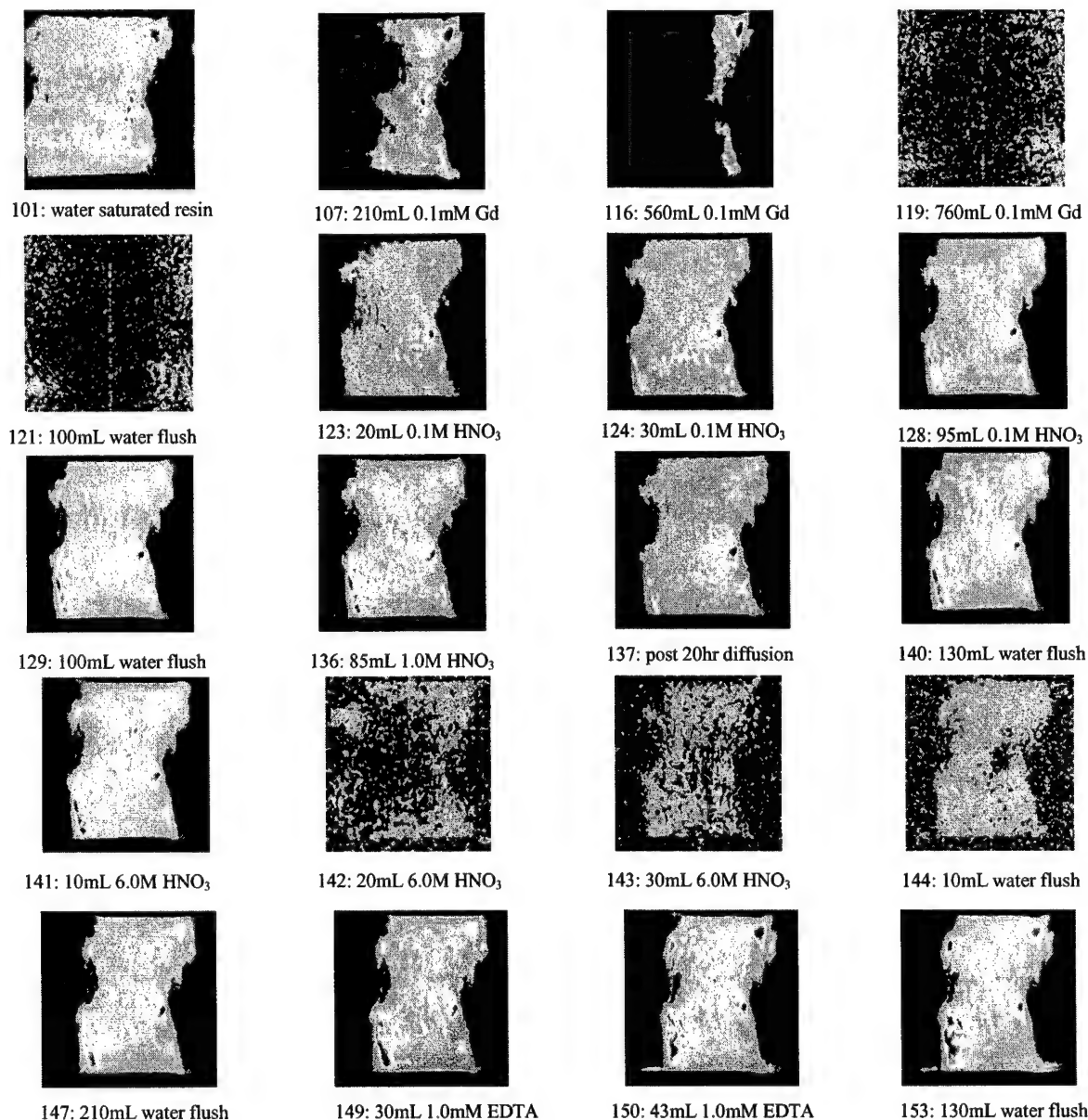


Figure 8.9: 2-D image sequence of the 0.1 M HNO_3 flow into Gd-loaded PF resin. The first image (#101) shows the PF resin fully saturated with water. The first line is the Gd-loading. The second line is flush of the 0.1 M HNO_3 . The third line is flush of the 1.0 M HNO_3 , and the fourth line is flush of the 6.0 M HNO_3 . The sequence shows the dramatic effect of the 0.1 M acid, but, very little effect from the 1.0 M acid. The 6.0 M acid appears to have some influence on Gd binding, but the resulting water flush returns to the pre-6.0 m flush. Image #137 shows the effect of a 20 hour diffusion time. The image dimensions are 0.8 cm high by 0.7 cm in length. The spatial resolution for the image sequence is 100 μm by 100 μm (128 by 128 pixels) with a 1000 μm thick slice.

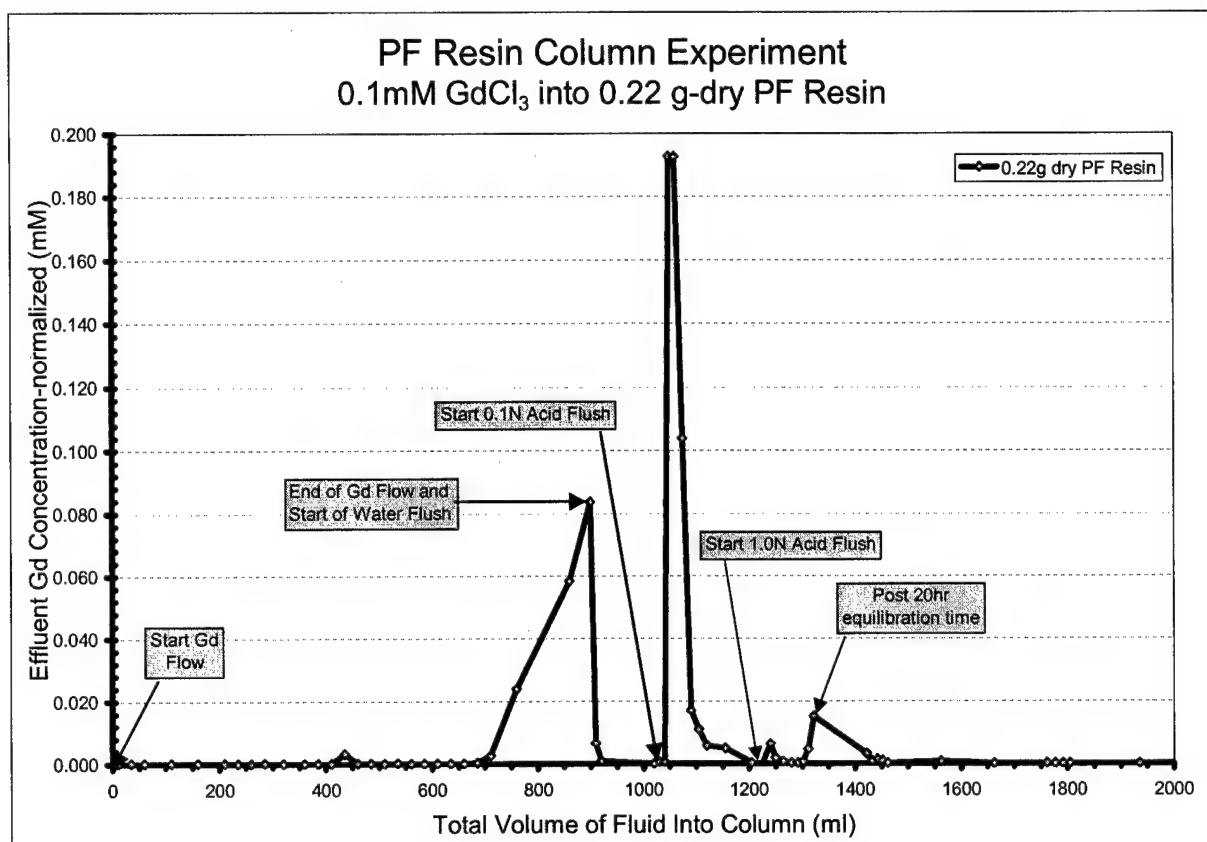


Figure 8.10: Breakthrough curve for PF resin showing the effluent Gd concentration versus the fluid volume into the resin column. It is clear to see that a large amount of Gd comes off the resin after the initial flow of 0.1 M acid, but not much more Gd de-sorbs after that point. The 20 hour kinetics study clearly shows a small spike in the Gd concentration. The 6.0 M acid at 1420 mL and the 1.0 mM EDTA at 1760 mL flushing shows no further Gd de-sorption.

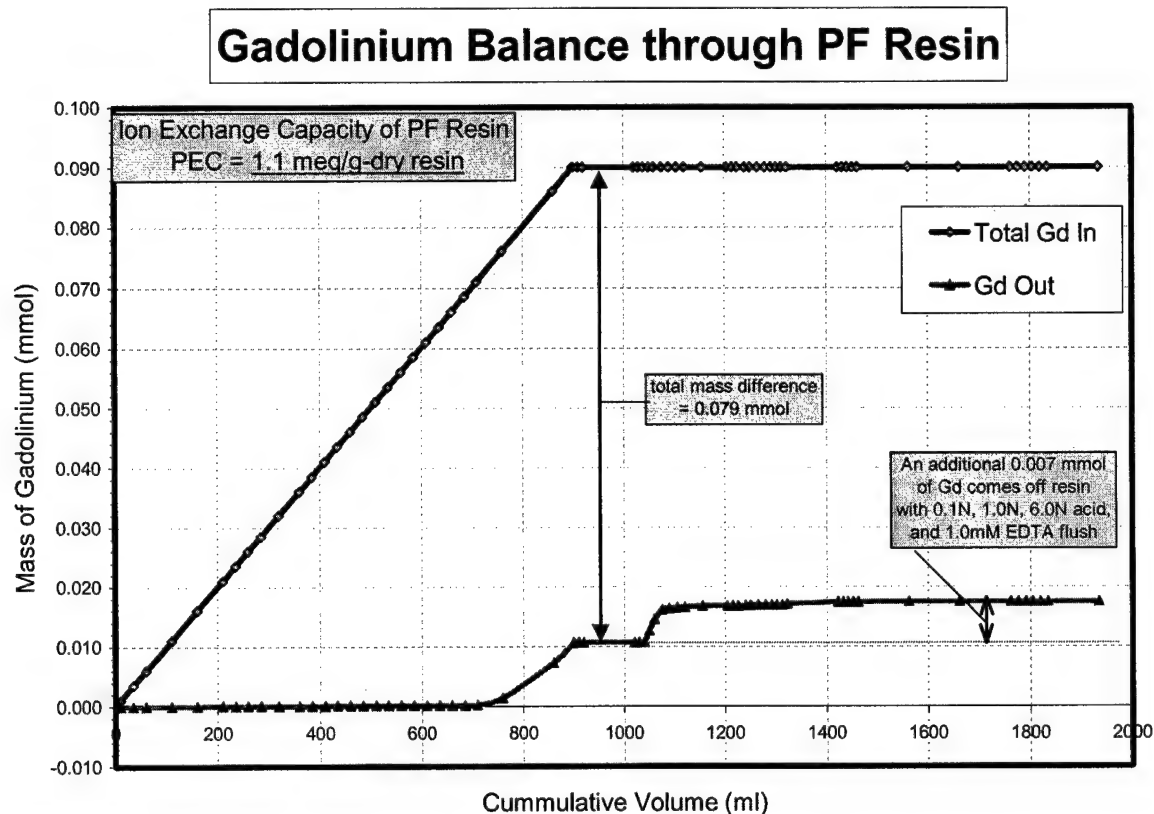


Figure 8.11: Plot of the Gd balance through the PF resin column. The plot is a measure of the total quantity of Gd put into the column and the total quantity out of the column. The difference between the two is the Gd sorbed to the resin, and this allows for a measure of the proton exchange capacity. The measured proton exchange capacity for the PF resin is 1.1 meq/g.

The PF resin column was also imaged in 3-D to view the spatial distribution of the Gd throughout the sample. The images in Figures 8.12 and 8.13 show the distribution of Gd loading in the PF resin. The first image (#22) of Figure 8.12 shows a fully loaded resin with reduced signal due to the high concentration of Gd. The Gd acts to reduce the relaxation rate thus decreasing the collected signal. The second image of Figure 8.12 shows the same sample location after a 0.1 M HNO_3 and water flush. This image shows increased signal from the resin that indicates a decreased in the amount of sorbed Gd. This assumption is verified by the ICP-AES results in Figures 8.10 and 8.11. The images of Figure 8.13 clearly show the tortuous pathways that the 1.0 M and 6.0 M HNO_3 follow through the resin. The inhomogeneous removal of Gd from the resin indicates that there are preferential flow paths through the resin. The ICP-AES results verify this indication by the Gd spike generated after a 20 hour equilibration time.

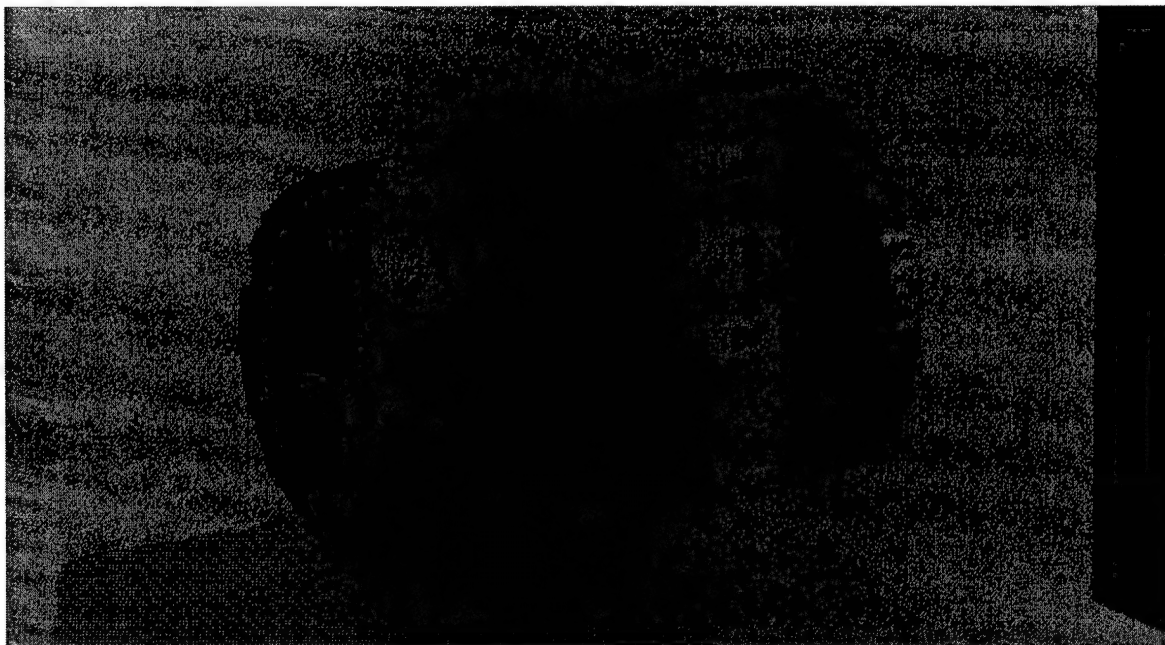


Image # 22: Half-cutout of a PF resin 3-D image. The image shows a 1.5 cm long by 0.8 cm in diameter sample loaded with Gd. The reduced signal in the center area is the Gd-loaded PF resin with water saturated 100 micron glass beads on each end. The Gd causes a reduction in the relaxation rate of the water protons resulting in reduced signal.

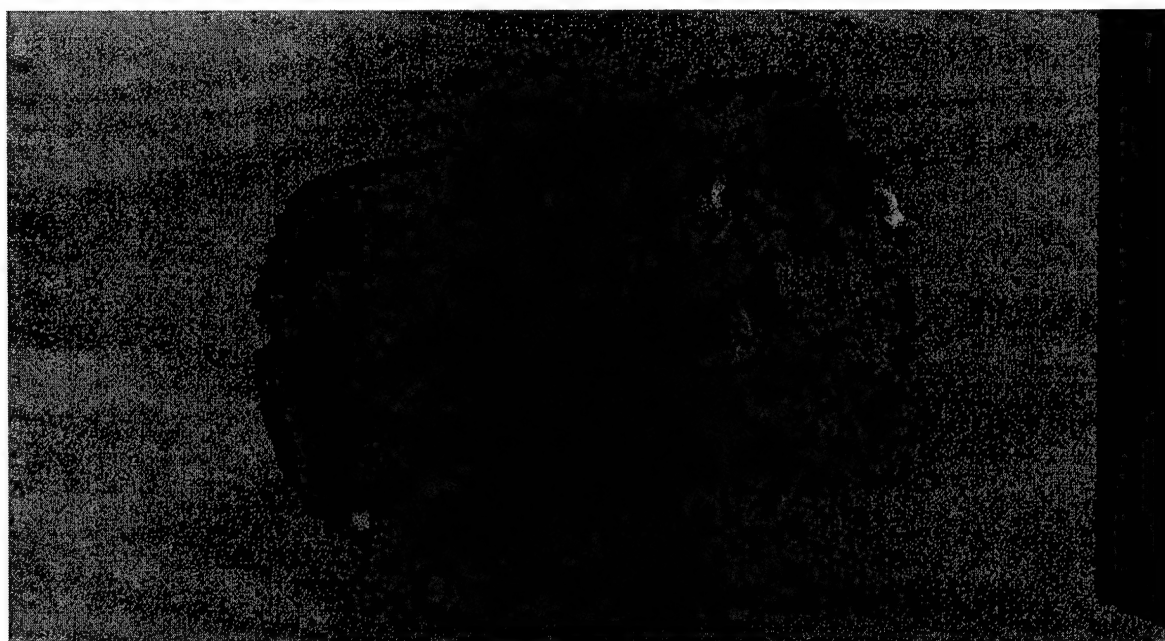


Image # 212: Half-cutout of a PF resin 3-D image after Gd loading and a 95 mL 0.1 M HNO_3 flush. The 0.1 M acid removed the loosely bound Gd and resulted in decreased relaxation rates. The areas of reduced signal (dark areas) throughout the image is Gd-loaded PF resin where the acid did not penetrate. The image is 1.5 cm long by 0.8 cm in diameter.

Figure 8.12: 3-D images of PF resin loaded with Gd and flushed with 0.1 M HNO_3 .

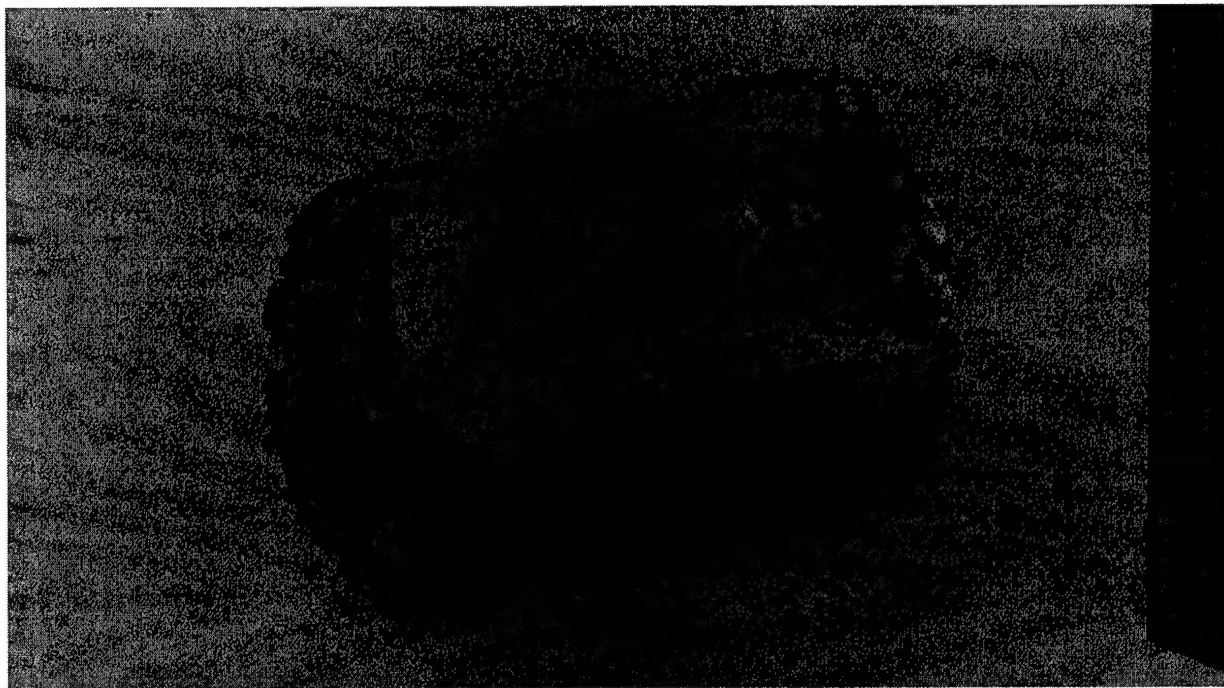


Image # 222: Quarter-cutout of a PF resin 3-D image after a flush with 1.0 M HNO_3 and water sample loaded with Gd. The reduced signal areas (dark spots) are where Gd-loaded PF resin remains, and the white areas are areas with reduced Gd sorption. There are clear preferential pathways through the resin. The image is 1.5 cm long by 0.8 cm in diameter.

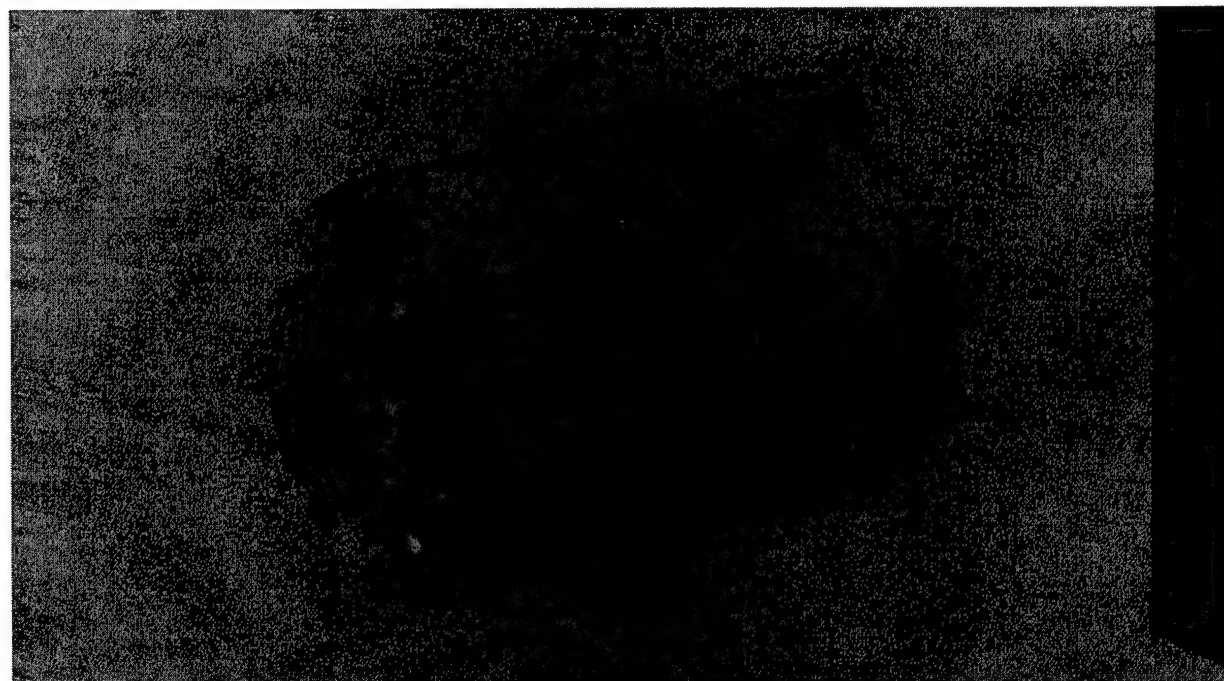


Image # 232: Quarter-cutout of a PF resin 3-D image after Gd loading and a 6.0 M HNO_3 flush. The image clearly shows the heterogeneous sorption and removal from the acid flush. The dark spots are areas of increased Gd sorption and the white areas have reduced Gd content. The dark areas are spatial locations where the acid was unable to remove the Gd, most likely due to preferential flow around these locations. The image size is 1.5 cm long by 0.8 cm in diameter.

Figure 8.13: 3-D images of PF resin showing 1.0 M and 6.0 M HNO_3 flushes.

8.3. Discussion and Conclusions

The PF flow experiments performed in this section were designed to first determine the flow and sorption characteristics of the resin. This was accomplished using the 2-D NMR sequences coupled with ICP-AES analysis of the effluent to determine the Gd concentrations. From this data, the proton exchange capacity (PEC) of 1.1 meq/g was measured. This value is reasonable based on previous measurements of a similar resin to PF, phenol-formaldehyde hydroxyquinolene (PQF). The experimental PEC for PQF was 1.5 meq/g that is very close to the 1.1 meq/g measured in this experiment.

The flow profile for the PF resin was highly irregular, and showed what appeared to be two parabolic fronts (Figure 8.8). This result could be a result of the packing method used in preparing the sample. There was also visible breakthrough of the Gd solution in the center of the resin pack, which showed up as a steady increase in the effluent Gd concentration. The PF resin during preparation proved the least permeable of all resins tested, and this low permeability could be the reason for sample packing anomalies in the images.

The breakthrough curves showed that resin had not reached full equilibrium loading prior to the stop of the Gd solution. This was exhibited by the steep rise of the Gd concentration but no plateau at the top of the curve equilibrating at the inlet concentration of 0.1 mM Gd. This non-equilibrium condition could have resulted in unequal loading, however this was not readily apparent in the initial 2- and 3-D images. The second significant feature of the breakthrough curve is the large spike of Gd after the 0.1 M acid flush. This single spike removed approximately 10% of the Gd from the resin with little more Gd removed by subsequent higher acid concentrations. This would imply that there is a weakly bound Gd component, possibly belonging to single (mono-dentate) bonds. Further study could link this to one of the water components identified in the microscopic resin characterization of Section 7.0. A third interesting find in the breakthrough curves is the small spike of Gd eluted after a 20 hour equilibration time with 1.0 M acid. When the 1.0 M flush initially started, very little additional Gd was removed from the resin, but after a 20 hour equilibration time with the resin saturated with 1.0 M acid, a measurable portion of Gd was removed (about 1%). This implies that there are some long time kinetics involved with the sorption/de-sorption process. It could also mean there are preferential flow pathways for the flush solution, and it requires diffusive migration to

sample normally inaccessible areas of the resin. These preferential pathways are seen in the 2- and 3-D images. This sorption/de-sorption mechanism requires further study.

References for Section 8.0

1. N. Dumont, A. Favre-Reguillon, B. Dunjic, M. Lemaire, *Sep. Sci. Tech.*, **31**(7), 1001-1010 (1996).
2. J.D. Seymour and P.T. Callaghan, *AIChE Journal*, **43** No.8, 2096-2111 (August 1997).
3. A. Caprihan and E. Fukushima, *Physics Reports*, **198** No. 4, 198-235 (1990).
4. S. Chen, F. Qin, K. Kim, and A.T. Watson, **39** No. 6, 925-934 (June 1993).
5. A. Feinaur, S.A. Altobelli, and E. Fukushima, *Mag. Res. Imaging*, **15** No. 4, 479 (1997).
6. A. Greiner, W. Schreiber, G. Brix, W. Kinzelbach, *Water Resour. Res.*, **33**(6), 1461-1473 (1997).
7. A.E. Fischer, B.J. Balcom, E.J. Fordham, T.A. Carpenter, L.D. Hall, *J.Phys. D: Appl. Phys.* **28**(2), 384-97 (1995).
8. G.T. Seaborg, *Actinides Rev.*, **1**, 3 (1967).
9. J.E. Huheey, *Inorganic Chemistry*, 3rd ed. (Harper Row Publishers, New York, 1983), p.803.
10. P.R. Fields and T. Moeller, *Advances in Chemistry Series*, No. 71, American Chemical Society, Washington, DC, (1967).
11. W. Stumm and J.J. Morgan, *Aquatic Chemistry: Chemical Equilibria and Rates in Natural Waters*, 3rd ed. (John Wiley and Sons Inc., New York, 1996).
12. P.T. Callaghan, "Principles of Nuclear Magnetic Resonance Microscopy," Clarendon Press, Oxford (1991).
13. W. Nold, "The Nold DeAerator Manual," Revision 18, Walter Nold Company, Natick, MA.
14. W. Nold, *The Nold DeAerator*, *Design News*, **68**, (17 Aug 81).
15. K.R. Czerwinski, M. Draye, J. Foos, and A. Guy: *Ion Selective Resins: Development and Applications for Nuclear Waste Management. MRS Scientific Basis for Nuclear Waste Management XX*. In press.
16. M. Draye, K.R. Czerwinski, A. Favre-Reguillon, J. Foos, A. Guy, and M. Lemaire, *Sep. Sci. Tech.*, **35**(8), pp. 1117-1132, 2000.

[THIS PAGE INTENTIONALLY LEFT BLANK]

9. CONCLUSIONS

The conclusions for this work are provided in this section. Each of the major sections (6.0, 7.0 and 8.0) has its own discussion and conclusion sections, however all conclusions are presented here to facilitate their review. The conclusions for each section are included in the following sub-sections.

In general, the NMR techniques used in these studies have proven very useful in characterizing the speciation and transport of trivalent actinides. This work provides an integrated approach to characterizing both the macroscopic and microscopic transport and speciation in porous media. The NMR integrated approach will help couple these two length scales, which will lead to a better understanding of the migration of actinides in porous systems.

9.1. NMR Flow System

Susceptibility effects are an inherent problem in the NMR imaging of complex systems involving fluid flow through granular media. These susceptibility effects are often caused by air bubbles formed during sample preparation and under experimental flow conditions. The technique of deaeration followed by over-pressurization is highly effective in reducing air bubbles in granular media. The deaerated water provides a sink for the free air to be transferred into the aqueous phase, and the over-pressurization provides an added mechanism for this transfer to occur. The degree of deaeration is limited by the effectiveness of the deaeration system (i.e. mixing vessel and vacuum pump), and in these studies, deaeration to less than 0.6 ppm DO (20) was shown to be highly effective in incorporating free air. As for the degree of over-pressurization, the higher the pressure on the closed system, the more free air transfers into the aqueous phase. In these studies, pressurization to 620 kPa (90 psi) proved highly effective in driving the free air into solution.

For granular media with low porosity or dead end pathways, the diffusion time of the gas into the liquid may be excessively long to completely remove all of the free air. This problem can be mitigated by a flowing stream of deaerated liquid to provide a constant sink for the free air to be integrated. If advective flow is not possible for low porosity media, the deaeration times are purely diffusion dependent and gas exchange rates will be based only on molecular diffusion. In this case, it may be advantageous to impregnate the low porosity material with a gas that has higher water solubility, such as CO₂.

The experimental results show the effectiveness of this deaeration technique at mitigating the unwanted susceptibility effects. The significant reduction and positive control over the effects of air/water susceptibility provides greater confidence in interpreting qualitative assessments of imaging media. The reduction in imaging artifacts may also provide the opportunity to develop quantitative evaluation methods for imaging techniques. NMR is also an effective means to evaluate the degree of deaeration in a sample. Experimental results in Figures 6.2 and 6.3 show how 1-D T₁ mapping of a sample can be used to evaluate the degree of deaeration and the rates at which the various deaeration mechanisms take place. Some limited deaeration time-scales can also be extracted from the 1-D data.

9.2. Microscopic Evaluation of Ion-Specific Resins Using NMR

NMR methods have increased the understanding of the microscopic characteristics of CF and RF phenolic resins. The NMR spectral deconvolution first indicated the presence of three major components in the resin-water system. Further relaxation studies justified this initial assumption and gave effective lifetimes to the three components. Diffusion measurements helped describe the mobility of the three pools and led to a greater understanding of kinetic exchange between the pools. These exchange mechanisms are important in determining the ultimate performance of the ion-exchange resins. The differences in exchange rates could assist in the predicted performance of a resin. For example, the RF resins have a faster exchange rate than the CF resins between the free and plasticizer pools which could lead one to assume that the RF resin has a more ordered structure. This assumption is somewhat justified in that the empirically derived proton exchange capacity for the RF resins is 30% greater than for the CF resins.

The bound water volume is an important parameter extracted from these NMR studies. A bound water volume for these resins has proven difficult to measure using standard techniques. This is due to the gel-like nature of the resin with the water, and the swelling of the resins under saturated conditions. Standard surface area and volumetric techniques normally require the measured media to be in an unsaturated water state or of a known water bearing state. A completely dry resin is not possible without degrading the resin structure, and a partially saturated resin, does not allow the resin to reach its equilibrium state when in use as an ion exchanger. Therefore, for polymeric organic media like these phenolic resins, NMR techniques may be the best method for extracting accurate the bound water volume. In addition, the bound water volume allows for a direct determination of the specific surface area, which is a critical parameter for understanding ion exchange and other surface interactions.

The proton exchange capacity (PEC) is another critical parameter used in determining the effectiveness of ion-exchanging materials. A precise determination of the available functional sites is necessary in determining the theoretical PEC, however this is very difficult to determine with unstructured materials, such as organic resins. Most methods used to determine PEC rely on empirical measurements and assumptions, which could introduce large systematic error into a PEC determination. The NMR techniques used in this study allow for the determination of PEC from interactions at a microscopic level, thus reducing the likelihood of systematic discrepancies

in the analysis. Although there may be error in estimating bond distances and functional site densities, these NMR techniques provide a direct evaluation of the theoretical PEC and can be used to place bounds on empirically derived values.

The three-pool model used to describe the microscopic interactions in the CF and RF ion-exchange resin has proven to be a good model. The model assists in the understanding of the exchange dynamics between the three pools, and provides a basis to extract spatial and temporal information from the system. This multi-faceted NMR approach to probing microscopic interactions in porous media holds great promise. These NMR methods provide information about certain types of porous systems that could not otherwise be measured.

9.3. NMR Imaging

NMR imaging of Gd^{3+} flow is a useful technique to assist in the understanding of physical transport and chemical behavior of trivalent metal ions in a variety of granular media flow systems. It provides the only real-time means to visualize the Gd^{3+} loading onto chemically reactive surfaces which leads to true quantification of the ion exchange capacity factors in flow systems where fingering or other non-linear flow phenomena is encountered. It is only through the use of this NMR imaging tracer technique whereby the actual mass of complexed material can be assessed, based on an evaluation of the area (or volume) of material which has been occupied by the Gd solution. Without knowing the actual flow area/volume probed by the Gd, it is impossible to determine the capacity of the granular flow system to sorb the Gd^{3+} ions. The NMR tracer technique provides a better understanding of chemical reactivity in heterogeneous flow systems, and this can then lead to a more accurate prediction of the fate of contaminants in more complex flow environments.

The NMR imaging techniques with the Gd tracer proved especially helpful in coupling the transport properties of the fluid with chemical reactivity data. These tracer studies allowed for the development of a model to determine the degree of channeling or non-linear (fingering) flow. This model can then be applied for prediction of increased transport rates and a more accurate determination of exchange capacities of the flow media. The distribution coefficients (K_d) used in current reactive transport models rely heavily on bulk flow parameters and exchange capacities of the flow media, and this NMR tracer technique can be used to help determine these parameters with greater certainty.

The PF flow experiments performed in Section 8.2 were designed to first determine the flow and sorption characteristics of the resin. This was accomplished using the 2-D NMR sequences coupled with ICP-AES analysis of the effluent to determine the Gd concentrations. From this data, the proton exchange capacity (PEC) of 1.1 meq/g was measured. This value is reasonable based on previous measurements of a similar resin to PF, phenol-formaldehyde hydroxyquinolene (PQF). The experimental PEC for PQF was 1.5 meq/g that is very close to the 1.1 meq/g measured in this experiment.

The flow profile for the PF resin was highly irregular, and showed what appeared to be two parabolic fronts (Figure 8.8). This result could be a result of the packing method used in

preparing the sample. There was also visible breakthrough of the Gd solution in the center of the resin pack, which showed up as a steady increase in the effluent Gd concentration. The PF resin during preparation proved the least permeable of all resins tested, and this low permeability could be the reason for sample packing anomalies in the images.

The breakthrough curves showed that resin had not reached full equilibrium loading prior to the stop of the Gd solution. This was exhibited by the steep rise of the Gd concentration but no plateau at the top of the curve equilibrating at the inlet concentration of 0.1 mM Gd. This non-equilibrium condition could have resulted in unequal loading, however this was not readily apparent in the initial 2- and 3-D images. The second significant feature of the breakthrough curve is the large spike of Gd after the 0.1 M acid flush. This single spike removed approximately 10% of the Gd from the resin with little more Gd removed by subsequent higher acid concentrations. This would imply that there is a weakly bound Gd component, possibly belonging to single (mono-dentate) bonds. Further study could link this to one of the water components identified in the microscopic resin characterization of Section 7.0. A third interesting find in the breakthrough curves is the small spike of Gd eluted after a 20 hour equilibration time with 1.0 M acid. When the 1.0 M flush initially started, very little additional Gd was removed from the resin, but after a 20 hour equilibration time with the resin saturated with 1.0 M acid, a measurable portion of Gd was removed (about 1%). This implies that there are some long time kinetics involved with the sorption/de-sorption process. It could also mean there are preferential flow pathways for the flush solution, and it requires diffusive migration to sample normally inaccessible areas of the resin. These preferential pathways are seen in the 2- and 3-D images. This sorption/de-sorption mechanism requires further study.

APPENDIX 1.0

PROCEDURE FOR PREPARING PHENOLIC RESINS

PROCEDURE FOR PREPARING PHENOLIC RESINS

The following procedure is used to prepare the ion-selective phenol-formaldehyde based resins into a proton or sodium form for use in exchange studies. This procedure will take the resins through a series of physical and chemical processes to properly size, regenerate, and convert the resins into reproducible forms.^[1,2] The procedure assumes the resin material has been fully synthesized ^[3,4], and it is in an unprocessed form.

1. Sizing:

- Crush the resin in a porcelain mortar or other non-metallic crushing device.
- Sieve the resin to 230-120 ASTM standard U.S. mesh ($63 < \varnothing < 125 \mu\text{m}$).

2. Regeneration

- Place 0.5 g of resin into 100 mL of 1.0 M NaOH solution. Resin quantity may increase but resin/NaOH ratio must remain constant.
- Shake resin/NaOH mixture for 4 hours.
- Place resin/NaOH mixture into vacuum-assisted filtration vessel with filter size less than $63 \mu\text{m}$.
- Rinse with de-ionized (DI) water until neutral pH ($< \text{pH } 8$).
- Place resin into 100 mL of 1.0 M HCl solution.
- Stir resin/HCl mixture for 15 minutes.
- Rinse with DI water until equilibrated with DI wash water pH.
- This is the end of the first regeneration cycle.
- Repeat entire regeneration procedure a second time for two complete cycles.
- The resin is now in an H^+ form.

3. Drying

- After the second regeneration cycle, place the resin (H^+ form) into a shallow wide-mouthed vessel for drying.
- Place resin in oven at 60°C for 24 hours (minimum) or until resin appears dry (i.e. no standing water).

- Place resin in sealed vacuum vessel with P₂O₅, and place container back into 100°C oven for an additional 24 hours.
- Mass resin and document as “dry resin mass”.
- Place resin in unsealed storage vessel and let resin equilibrate to ambient humidity levels.
- Mass resin and document as “wet resin mass”.
- Moisture regain is determined by the ratio of the water mass (wet - dry mass) to the wet resin mass.

$$\text{Moisture Regain} = \frac{\text{wetmass} - \text{drymass}}{\text{wetmass}}$$

4. Conversion to Na⁺ Form

- Place 0.5 g of H⁺ form resin into 100 mL of 1M NaOH.
- Shake resin/NaOH mix for 2 hours
- Place resin/NaOH mixture into vacuum-assisted filtration vessel with filter size less than 63 µm.
- Rinse with de-ionized (DI) water until neutral pH (<pH 8).
- The resins are now in the Na⁺ form.

¹ K.R. Czerwinski, M. Draye, J. Foos, and A. Guy: Ion Selective Resins: Development and Applications for Nuclear Waste Management. MRS Scientific Basis for Nuclear Waste Management XX, 1998.

² M. Draye, K.R. Czerwinski, A. Favre-Reguillon, J. Foos, A. Guy, and M. Lemaire, Sep. Sci. Tech., 35(8), pp. 1117-1132, 2000.

³ N.Dumont, A. Favre-Reguillon, B. Dunjic, and M. Lemaire, Sep. Sci. Tech., 31(7), pp. 1001-1010, 1996.

⁴ M. Draye, A. Favre-Reguillon, J. Foos, A. Guy, and K.R. Czerwinski, Proceedings of Waste Management '98 Conference, Tucson AZ, 1998.

[THIS PAGE INTENTIONALLY LEFT BLANK]

APPENDIX 2.0

BRUKER PULSE PROGRAMS FOR THE 3T AND 12T MAGNETS

3T Pulse Programs for Spectroscopy

```
;dan.zg - low power  
;amx-version modified for use on the 3T  
;1D sequence  
d2=10u
```

```
1 ze  
2 d1 tlo  
3u tlo  
p1 ph1  
;d2  
5u ph0 adc  
aq  
rcyc=2 ph31  
wr #0  
exit
```

```
ph0=0  
ph1=0 1 2 3  
ph31=0 1 2 3
```

```
;hl1: ecoupler high power level  
;p1 : 90 degree transmitter high power pulse  
;d1 : relaxation delay; 1-5 * T1
```

```
;dan.ir - low power inversion recovery sequence for measuring  $T_1$ 
;amx-version modified by dan for use on the 3T
;1D sequence
;d1=10s
```

```
1 ze
2 d1 tlo
3u tl0
p2 ph1
d2
p1 ph2
3u ph0 adc
aq
rcyc=2 ph31
wr #0
exit
```

```
ph0=0
ph1=0 1 2 3
ph2=0 1 2 3
ph31=0 1 2 3
```

```
;tl0: ecoupler low power level
;p1 : 90 degree transmitter pulse
;p2 : 180 degree transmitter pulse
;d1 : relaxation delay; 1-5 *  $T_1$ 
;d2 : inversion recovery time
```

```
;dan.cpmg
;amx-version for the 3T
;T2 measurement using Carr-Purcell-Meiboom-Gill sequence
```

```
;;p2=p1*2
;d11=30m
;d1=5s
;d20=0.5m
```

```
1 ze
2 d1 tlo
  p1 ph1
3 d20
  p2 ph2
  d20
  lo to 3 times c
  go=2 ph31
  30m wr #0 if #0 vc
  lo to 1 times l4
exit
```

```
ph1=0 0 2 2 1 1 3 3
ph2=1 3 1 3 0 2 0 2
ph31=0 0 2 2 1 1 3 3
```

```
;hl1: ecoupler high power level
;p1 : 90 degree transmitter high power pulse
;p2 : 180 degree transmitter high power pulse
;d1 : relaxation delay; 1-5 * T1
;d11: delay for disk I/O [30 msec]
;d20: fixed echo time to allow elimination of diffusion
; and J-mod. effects
;vc : variable loop counter, taken from vc-list
;L4: 14 = number of experiments = number of values in vc-list
;NS: 8 * n
;DS: 2 or 4
;td1: number of experiments
;define VCLIST
;this pulse program produces a ser-file (PARMOD = 2D)
;d20: d20 should be << 1/J ,but > (50 * P2)
;vc : vc should contain even numbers to provide
; for cancellation of 180 degree pulse errors
```

```
;goldshen
;amx-version for the 3T
;Goldman-Shen experiment for the measurement of exchange rates
```

```
;d11=30m
;d1=5s
;d5=5m
```

```
1 ze
2 d1
  p1 ph1
  d5
  p2 ph2
  d5
  p1 ph3
  300u gron2
  10m
  100u groff
  vd
  p1 ph4
  go=2 ph31
  30m wr #0 if #0 ivd
  lo to 1 times l4
exit
```

```
ph1=0 0 0 0 2 2 2 2 1 1 1 1 3 3 3 3
ph2=1 3 1 3 1 3 1 3 0 2 0 2 0 2 0 2
ph3=1 3 0 2
ph4=1 3 0 2
ph31=0 0 2 2 2 2 0 0 3 3 1 1 1 1 3 3
```

```
;p1 : 90 degree transmitter high power pulse
;p2 : 180 degree transmitter high power pulse
;d1 : relaxation delay; 1-5 * T1
;vc : variable loop counter, taken from vc-list
;L4: l4 = number of experiments = number of values in vc-list
;NS: 8 * n
;DS: 2 or 4
;td1: number of experiments
;define VCLIST
;this pulse program produces a ser-file (PARMOD = 2D)
;d20: d20 should be << 1/J ,but > (50 * P2)
;vc should contain even numbers to provide for cancellation of 180 degree pulse errors
```


3T Pulse Programs for Imaging

;dan.se: spin echo - low power, for use on the 3T
;written by dan - 21 Oct 99
;1D sequence

d2=aq/2.0
d3=1u

1 ze
2 d1 tlo ;relaxation delay
3u tl0
p1 ph1 ;excitation pulse
d2
d3
p2 ph2 ;PI pulse
d3
d2
5u ph0 adc
aq
rcyc=2 ph31
wr #0
exit

ph0=0
ph1=0 1 2 3 0 1 2 3 0 1 2 3 0 1 2 3
ph2=1 2 1 2 ;0 1 2 3 1 2 3 0 2 3 0 1 3 0 1 2
ph31=0 1 2 3 2 3 0 1 0 1 2 3 2 3 0 1

;p1 : 90 degree transmitter high power pulse
;d1 : relaxation delay; 1-5 * T1

```
;dan.imse: spin echo w/ gradients – 1d imaging module
;low power for use on the 3T
;written by dan - 21 Oct 99
;gradient program: dan.imse.r
```

```
d2=aq/2.0
d3=50u
```

```
1 ze
2 d1 tlo ;relaxation delay
3u tl0 ;low power transmitter attenuation
p1 ph1 ;PI/2 excitation
5u :ngrad ; gradient on
d2
5u:ngrad
d3
p2 ph2 ;PI pulse to invert spins
d3
5u:ngrad ; read gradient on
5u ph0
5u adc
aq ; acquire
5u:ngrad
rcyc=2 ph31
wr #0 ; write to disk
exit
```

```
ph0=0
ph1=0 1 2 3
ph2=1 2 1 2
ph31=0 1 2 3
```

```
;p1 : 90 degree transmitter high power pulse
;d1 : relaxation delay; 1-5 * T1
```

; Gradient program for dan.imse

{(2.0) (0.00)	(0.0)}
{(0.0) (0.0)	(0.0)}
{(2.0) (0.00)	(0.0)}
{(0.0) (0.0)	(0.0)}

```
;dan.imse2d: 2-D spin echo w/ gradients - low power
;written by dan, 24 Jan 00
;2D sequence for use on the 3T
;gradient program: dan.imse2d.r
```

```
d1=1.0s
d3=50u
d2=aq/2.0
```

```
1 ze
2 d1 tlo ;relaxation delay, low power
3u tl0
p1 ph1 ;excitation pulse
5u:ngrad ;gradient on
d2 ;gradient on time
5u:ngrad ;gradient off
d3 ;short delay to allow eddy currents to subside
p2 ph2 ;PI pulse
d3 ;used to re-phase previous d3
5u:ngrad ;gradient on
5u ph0
5u adc
aq
5u:ngrad
rcyc=2 ph31
400m wr #0 if #0 ze ;write to disk
lo to 2 times td1 ;td1=number of points in k-space
20m ip1 ;phase cycling
20m ip2
20m ip31
20m rf #0
lo to 2 times 2
20m ip1
20m dp2
20m ip31
20m rf #0
lo to 2 times 2
exit
```

```
ph0=0
ph1=0
ph2=0
ph31=0
```

```
;d1 : relaxation delay; 1-5 * T1
```

;Gradient program for dan.imse2d

loop td1 <2D>

```
{  
  {(2.0)      | (0.0)      | (0.0)}  
  {(0.0)      | (0.0)      | (0.0)}  
  {(2.0),r2d(0.0) |( 0.0),r2d(2.00)| (0.0)}  
  {(0.0)      | (0.0)      | (0.0)}  
}
```

```
; dan.imse3d2 for 3D spin echo
; 3d program for imaging on the 3T, modified 3-10-00 by Rich and Dan
; use gradient program dan.imse3d
```

```
d1=1.5s ;at least 5*T1
d2=aq/2.3 ;centers the acquisition
d3=200u ;kills PI fid
```

```
1s ze
5m st0
1 d1 tlo
3u tl0
10 d1
p1 ph1 ; 90 deg hard pulse, Gd spins into xy
5u:ngrad ; phase encode, read gradients on
d2 ; phase encode time
5u:ngrad ; phase encode, read gradients off
d3 ;
p2 ph2 ; PI pulse
d3 ; kills PI fid
5u:ngrad ; gradient on
5u ph0 ; acquire
5u adc
aq ;
5u:ngrad ; gradient off
rcyc=10 ph31 ; acquire fid
20m st ; switch memory block
lo to 10 times nbl ; phase encode increment loop
400m wr #0 if #0 ze ; store FIDs in ser file
400m igrad ; increment gradient
20m st0 ; reset address to beginning of buffer
lo to 10 times td1 ; number of slices
20m ip1 ; increment receiver and transmitter
20m ip2
20m ip31
20m rf #0 ; reset memory block pointer
lo to 10 times 2 ; phase cycling loop
20m ip1
20m dp2
20m ip31
lo to 10 times 2 ; # of averages
exit
ph0=0
ph1=0
ph2=1
ph31=0
```

;Gradient program for dan.imse3d

```
loop td1 <3D>
{
  loop nbl <2D>
  {
    {(2.0) | (0.0),r2d(2.0) | (0.0),,r3d(1.5)}
      {(0.0) | (0.0)      | (0.0)      }
      {(2.0) | (0.0)      | (0.0)      }
      {(0.0) | (0.0)      | (0.0)      }
    }
  }
}
```



```
;dan.soft: soft zg –  
;low power, for use on the 3T  
;1D sequence, created by dan on 10 Nov 99  
;used to determine soft pulse length, p3,the attenuation,tp1,and shape
```

```
1 ze  
2 d1 tlo  
  3u tl0  
p3:tp1 ph1  
  2u ph0 adc  
  aq  
  rcyc=2 ph31  
  wr #0  
exit
```

```
ph0=0  
ph1=0 1 2 3  
ph31=0 1 2 3
```

```
;d1 : relaxation delay; 1-5 * T1
```

;dan.softgrad: soft zg with selective gradient
;low power, for use on the 3T
;1D sequence, created by dan on 10 Nov 99
;used to determine the refocusing time and gradient strength for a soft pulse

d3=p3/1.9
d4=aq/2.4

1 ze
2 d1 tlo
3u tl0
5u:ngrad
500u
p3:tp1 ph1
5u:ngrad
d3
5u:ngrad
5u ph0 adc
aq
rcyc=2 ph31
wr #0
exit

ph0=0
ph1=0 1 2 3
ph2=1 2 1 2
ph31=0 1 2 3

;d1 : relaxation delay; 1-5 * T1

;Gradient Program for use with dan.softgrad

$$\begin{aligned} & \{ (0.0) \mid (0.0) \mid (2.5) \} \\ & \{ (-0.0) \mid (-0.0) \mid (-2.5) \} \\ & \{ (0.0) \mid (0.0) \mid (0.0) \} \end{aligned}$$

```
;dan.imsess: spin echo w/ gradients, slice selective
;low power, 1-D imaging module for use on the 3T
;written by dan - 14 Nov 99
;gradient program: dan.imsess.r
```

```
d2=aq/2.3
d3=200u
d4=p3/2
```

```
1 ze
2 d1 tlo ;relaxation delay
3u tl0
5u:ngrad ;gradient to precede selective pulse
200u
p3:tp1 ph1 ;selective PI/2 pulse
5u:ngrad ;inverse gradient to refocus selective pulse
d4
5u :ngrad ;selective gradient off, read gradient on
d2
5u:ngrad
d3
p2 ph2 ;PI pulse
d3
5u:ngrad
5u ph0
5u adc
aq ; acquisition
5u:ngrad
rcyc=2 ph31
wr #0 ; write to disk
exit
```

```
ph0=0
ph1=0 1 2 3
ph2=1 2 1 2
ph31=0 1 2 3
```

```
;p1 : 90 degree transmitter high power pulse
;d1 : relaxation delay; 1-5 * T1
```

;Gradient Program for use with pulse program dan.imsess

{ (1.5)	(0.0)	(0.0)}
{(-1.5)	(-0.0)	(-0.0)}
{ (2.0)	(0.0)	(0.0)}
{ (0.0)	(0.0)	(0.0)}
{ (2.0)	(0.0)	(0.0)}
{ (0.0)	(0.0)	(0.0)}

```
;dan.imsess2d: 2-D slice selected spin echo w/ gradients
;low power, 2-D imaging module for use on the 3T, written by dan - 10 Dec 99
;2D sequence generates 2rr file by processing with xfb, gradient program: dan.imsess2d.r
```

```
d1=1s
d3=200u
d2=aq/2.2
d4=p3/2
```

```
1 ze
2 d1 tlo ;relaxation delay
3u tl0
5u:ngrad ;start of gradient echo to refocus selective pulse
500u
p3:tp1 ph1 ; selective excitation
5u:ngrad
d4
5u:ngrad ;selective gradient off, phase and read gradients on
d2
5u:ngrad ; phase and read gradients off
d3
p2 ph2 ;PI pulse
d3
5u:ngrad ; read gradient on
5u ph0
5u adc ; acquire
aq
5u:ngrad ; phase and read gradients off
rcyc=2 ph31
400m wr #0 if #0 ze
lo to 2 times td1 ;td1=number of points in k-space
20m ip1 ;phase cycling loops
20m ip2
20m ip31
20m rf #0
lo to 2 times 2
20m ip1
20m dp2
20m ip31
lo to 2 times 2 ;l1=number of scans/4
exit
ph0=0
ph1=0
ph2=0
ph3=0
ph31=0
```

;Gradient program for use with dan.imsess2d

loop td1 <2D>

```
{
  {(1.5) | (0.0)      | (0.0)}
  {(-1.5) | (0.0)     | (-0.0)}
  {(0.0) | (0.0),r2d(2.5) | (2.0)}
  {(0.0) | (0.0)      | (0.0)}
  {(0.0) | (0.0),r2d(0.00) | (2.0)}
  {(0.0) | (0.0)      | (0.0)}
}
```

12T Pulse Programs


```
;zg pulse sequence for 12T
;avance-version
;1D sequence
```

```
#include <Avance.incl>
```

```
1 ze
2 d1
  p1 ph1
  go=2 ph31
  wr #0
exit
```

```
ph1=0 2 2 0 1 3 3 1
ph31=0 2 2 0 1 3 3 1
```

```
;p11 : f1 channel - power level for pulse (default)
;p1 : f1 channel - high power pulse
;d1 : relaxation delay; 1-5 * T1
```

```
;tlir1d
;avance-version
;T1 measurement using inversion recovery for the 12T
;ONLY to be used by au-program ("invrec_au")
```

```
#include <Avance.incl>
```

```
::"p2=p1*2"
```

```
1 ze
2 d1
  p2 ph1
  d7
  p1 ph2
  go=2 ph31
  wr #0
exit
```

```
ph1=0 2
ph2=0 0 2 2 1 1 3 3
ph31=0 0 2 2 1 1 3 3
```

```
;p11 : f1 channel - power level for pulse (default)
;p1 : f1 channel - 90 degree high power pulse
;p2 : f1 channel - 180 degree high power pulse
;d1 :relaxation delay; 1-5 * T1
;d7 : delay for inversion recovery
;NS :8 * n
;DS :4
```

```
;cpmg pulse sequence for 12T
;avance-version
;T2 measurement using Carr-Purcell-Meiboom-Gill sequence
```

```
#include <Avance.incl>
```

```
"d11=30m"
```

```
1 ze
2 d1
  p1 ph1
3 d20
  p2 ph2
  d20
  lo to 3 times c
  go=2 ph31
  d11 wr #0 if #0 ivc
  lo to 1 times l4
exit
```

```
ph1=0 0 2 2 1 1 3 3
ph2=1 3 1 3 0 2 0 2
ph31=0 0 2 2 1 1 3 3
```

```
;p1 : f1 channel - power level for pulse (default)
;p1 : f1 channel - 90 degree high power pulse
;p2 : f1 channel - 180 degree high power pulse
;d1 : relaxation delay; 1-5 * T1
;d11: delay for disk I/O [30 msec]
;d20: fixed echo time to allow elimination of diffusion
; and J-mod. effects
;vc : variable loop counter, taken from vc-list
;l4: l4 = number of experiments = number of values in vc-list
;NS: 8 * n
;DS: 16
;td1: number of experiments
;define VCLIST
;this pulse program produces a ser-file (PARMOD = 2D)

;d20: d20 should be << 1/J ,but > (50 * P2)
;vc : vc should contain even numbers to provide
; for cancellation of 180 degree pulse errors
```

0	360	; cpmg vc list for 250u experiments
2	376	
4	396	
6	408	
8	500	
10	600	
12	700	
14	800	
16	900	
18	1000	
20	1100	
22	1200	
24	1300	
26	1400	
28	1600	
30	1800	
32	2000	
40	2200	
48	2400	
56	2560	
64	(above values continued from 1 st column)	
72		
80		
88		
96		
104		
112		
120		
128		
136		
144		
152		
168		
184		
200		
216		
232		
248		
264		
280		
296		
312		
328		
344		

0	104	; cpmg vc list for 1ms experiments
2	112	
4	120	
6	128	
8	160	
10	192	
12	224	
14	256	
16	288	
18	320	
20	352	
22	384	
24	416	
26	448	
28	480	
30	512	
32	544	
34	640	
36	(above values continued from 1 st column)	
38		
40		
42		
44		
46		
48		
50		
52		
54		
56		
58		
60		
62		
64		
66		
68		
70		
72		
74		
76		
78		
80		
82		
84		
86		
88		
96		

;cpmg vc list for 10ms experiments

0
2
4
6
8
10
12
14
16
18
20
22
24
26
28
30
32
34
36
38
40
42
44
46
48
50
52
54
56
58
60
64

```

;Pulsed Gradient Stimulated Echo Sequence (PGSTE)
;for diffusion experiment on 12T
#include <Avance.incl>
#include <Grad.incl>
1 ze
2 d1
3 p1 ph1
   3u:ngrad
   d27      ;δ= d27
   3u:ngrad
   d10      ; echo time = d27 + d10 + 2*(p1/2) + 6u
p1 ph2
3u
   3u:ngrad
   d29
   3u:ngrad
d11      ; storage time = Δ= d29 + d11 + d10 + 9u + (2*p1)
p1 ph3
   3u:ngrad
   d27
   3u:ngrad
d10
3.6u      ; refocusing time = d27 + d10 + 9.6u + (p1/2)
go=2 ph31 ;NS=1 !!!!
d1 wr #0 if #0 zd
lo to 2 times td1
3m rf #0
3m ip1
3m ip1
3m ip31
3m ip31
lo to 2 times l1
      exit
ph1=0
ph2=0
ph3=0
ph31=0

;p11 : f1 channel - power level for pulse (default)
;p1 : f1 channel - 90 degree high power pulse
;d1 : relaxation delay; 1-5 * T1
;in0: 1/(2 * SW) = DW
;NS: 8 * n
;DS: 16
;td1: number of experiments
;MC2: TPPI

```

; gradient file for use by PGSTE diffusion experiment - pgste

```
loop td1 <2D>
{
{ (0) | (0) | (48.5) ,r2d(48.5)}
{ (0) | (0) | (0) }
{ (0) | (0) | (50) }
{ (0) | (0) | (0) }
{ (0) | (0) | (48.5) ,r2d(48.5)}
{ (0) | (0) | (0) }
}
```



```
;goldshen
;12T-version
;Goldman-Shen Experiment for measurement of exchange times
```

```
;d1=5s
;d5=5m
```

```
1 ze
2 d1
  p1 ph1
  d5
  p2 ph2
  d5
  p1 ph3
  300u gron2
  10m
  100u groff
  vd
  p1 ph4
  go=2 ph31
  30m wr #0 if #0 ivd
  lo to 1 times l4
exit
```

```
ph1=0 0 0 0 2 2 2 2 1 1 1 1 3 3 3 3
ph2=1 3 1 3 1 3 1 3 0 2 0 2 0 2 0 2
ph3=1 3 0 2
ph4=1 3 0 2
ph31=0 0 2 2 2 2 0 0 3 3 1 1 1 1 3 3
```

```
;hl1: ecoupler high power level
;p1 : 90 degree transmitter high power pulse
;p2 : 180 degree transmitter high power pulse
;d1 : relaxation delay; 1-5 * T1
;vd : variable delay list taken from vd-list
;L4: l4 = number of experiments = number of values in vd-list
;NS: 8 * n
;DS: 2 or 4
;td1: number of experiments
;define VCLIST
;this pulse program produces a ser-file (PARMOD = 2D)
;d20: d20 should be << 1/J ,but > (50 * P2)
```

0	980m	;vd list for use by the goldman-shen programs
100m	1000m	
120m	1020m	
140m	1040m	
160m	1060m	
180m	1080m	
200m	1100m	
220m	1120m	
240m	1140m	
260m	1160m	
280m	1180m	
300m	1200m	
320m	1220m	
340m	1240m	
360m	1260m	
380m	1280m	
400m	1300m	
420m	1320m	
440m	1340m	
460m	(continuation of column 1)	
480m		
500m		
520m		
540m		
560m		
580m		
600m		
620m		
640m		
660m		
680m		
700m		
720m		
740m		
760m		
780m		
800m		
820m		
840m		
860m		
880m		
900m		
920m		
940m		
960m		

```
;zgpr – magnetization transfer experiment on 12T
;avance-version
;1D sequence with f1 pre-saturation
```

```
#include <Avance.incl>
```

```
"d12=1u"
"d13=3u"
```

```
1 ze
2 d13 fq1:f1
3 d12 pl9:f1
  d1 cw:f1
  d13 do:f1
  d12 pl1:f1
  d13 fq1:f1
  p1 ph1
  go=2 ph31
  wr #0
exit
```

```
ph1=0 1 2 3
ph31=0 1 2 3
```

```
;pl1 : f1 channel - power level for pulse (default)
;pl9 : f1 channel - power level for presaturation
;p1 : f1 channel - 90 degree high power pulse
;d1 : relaxation delay; 1-5 * T1
;d12: delay for power switching [20 usec]
;d13: short delay [3 usec]
```

; gradient file for use by magnetization transfer experiment - zgpr

```
loop td1 <2D>
{
{ (0) | (0) | (48.5) ,r2d(48.5)}
{ (0) | (0) | (0) }
{ (0) | (0) | (50) }
{ (0) | (0) | (0) }
{ (0) | (0) | (48.5) ,r2d(48.5)}
{ (0) | (0) | (0) }
}
```

APPENDIX 3.0

MATLAB PROGRAMS TO PROCESS NMR DATA


```

% *** build the obtained fit curve:
A=x1(1);
B=x1(2);
C=x1(3);
D=x1(4);
E=x1(5);
F=x1(6);
Y_new=(A*B)/((X-C).^2+B)+(D*E)/((X-F).^2+E);

% *** plot fit solution:
plot(X,Y_new,'b-')

YL1=(A*B)/((X-C).^2+B);
YL2=(D*E)/((X-F).^2+E);
plot(X,YL1,'g-',X,YL2,'g-')

legend('exp','initial guess','L1 g','L2 g','lsq fit w/2L','L1 fit','L2 fit')

% *** calculate the area under the fit ***
figure(3)

% *** define the limits for integration ***
a1=1;
b1=900;
y1=YL1_g(a1:b1);
plot(y1)
sum1=0;
for i=1:(b1-a1-1);
sum1=sum1+y1(i)+y1(i+1);
end;
area1=sum1/2
FWHM1=2*sqrt(X01(2))
FWHM1_Hz=(1/2/dw)*FWHM1/td
hold on
%figure(4)
a2=1;
b2=900;
y2=YL2_g(a2:b2);
plot(y2)
sum2=0;
for i=1:(b2-a2-1);
sum2=sum2+y2(i)+y2(i+1);
end;
area2=sum2/2
FWHM2=2*sqrt(X01(5))
FWHM2_Hz=(1/2/dw)*FWHM2/td

```

```

%%%%%%%%%%%%%%%%%%%%%%%%%%%%%%%%%%%%%%%%%%%%%%%%%%%%%%%%%%%%%%%%%%%%%%%%
%%%%%%%%%%%%%%%%%%%%%%%%%%%%%%%%%%%%%%%%%%%%%%%%%%%%%%%%%%%%%%%%%%%%%%%% Define Function fit_simp_2, %%%%%%%%%
%%%%%%%%%%%%%%%%%%%%%%%%%%%%%%%%%%%%%%%%%%%%%%%%%%%%%%%%%%%%%%%%%%%%%%%% for use in previous 2-Lorenzian fit program %%%%%%%%%
%%%%%%%%%%%%%%%%%%%%%%%%%%%%%%%%%%%%%%%%%%%%%%%%%%%%%%%%%%%%%%%%%%%%%%%%

```

```

function FF = fit_simp2(x,X)

```

```

A=x(1);
B=x(2);
C=x(3);
D=x(4);
E=x(5);
F=x(6);

```

```

FF = (A*B)./((X-C).^2+B)+(D*E)./((X-F).^2+E);

```



```

[dsermin(j),xdsermin(j)]=min(dser(xmin:xmax));
xdsermin(j)=xdsermin(j)+(j-1)*dx; xdsermax(j)=xdsermax(j)+(j-1)*dx;
xextrem(j)=round((xdsermax(j)+xdsermin(j))/2); yextrem(j)=ser(xextrem(j),1);
end;
plot(xextrem, yextrem,'ro')
plot(xextrem, yextrem,'r-')
plot(xdsermin,dser(xdsermin),'yo')
plot(xdsermax,dser(xdsermax),'go')
pause
hold off
% *** plot the extreme values vs time: ***
xtime=fsttime+(xextrem-xextrem(1))*dtime/(xextrem(2)-xextrem(1));
X=[xtime(1) xtime(2) xtime(3) xtime(4) xtime(5) xtime(6) xtime(7) xtime(11) xtime(12)
xtime(13) xtime(14) xtime(15) xtime(16) xtime(17) xtime(18) xtime(19) xtime(20) xtime(21)
xtime(22) xtime(23) xtime(24) xtime(25) xtime(26) xtime(27) xtime(28) xtime(29) xtime(30)
xtime(31) xtime(32)] ;
Y=[yextrem(1) yextrem(2) yextrem(3) yextrem(4) yextrem(5) yextrem(6) yextrem(7)
yextrem(11) yextrem(12) yextrem(13) yextrem(14) yextrem(15) yextrem(16) yextrem(17)
yextrem(18) yextrem(19) yextrem(20) yextrem(21) yextrem(22) yextrem(23) yextrem(24)
yextrem(25) yextrem(26) yextrem(27) yextrem(28) yextrem(29) yextrem(30) yextrem(31)
yextrem(32)];
Y=Y./1E8;
% *** build the IC's guess vector ***
X01=[3.4 -6.4 1.3];
% *** call the fitting function - the parameters are returned in x1: ***
[x1,r1,r2,e3,o4]=lsqcurvefit('fit_simp_levy',X01,X,Y);
% *** build the obtained fit curve ***
Y_new=x1(1)+x1(2)*exp(-X./x1(3));
% *** plot the data and the fit ***
plot(X,Y,'ro',X,Y_new,'r')
pause
% *** plot the experimental data and the fit on semilog scale ***
A=x1(1);
B=x1(2);
Yexp=log((Y-A)./B);
Yfit=log((Y_new-A)./B);
plot(X,Yexp,'ro',X,Yfit,'r-')
title('T1')
xlabel('time(s)')
ylabel('ln((M(t)-A)/B)')
gtext('M(t)=A+B*exp(-t/T1)')
text=['T1=',num2str(x1(3)), 's']
text1=['A=',num2str(x1(1))]
text2=['B=',num2str(x1(2))]
gtext(text) gtext(text1) gtext(text2)

```

```

%%%%%%%%%%%%%%%%%%%%%%%%%%%%%%%%%%%%%%%%%%%%%%%%%%%%%%%%%%%%%%%%%%%%%%%%
%% Define Function fit_simp_levy, %%%%%%%%%
%% for use in previous Inversion recovery program %%
%%%%%%%%%%%%%%%%%%%%%%%%%%%%%%%%%%%%%%%%%%%%%%%%%%%%%%%%%%%%%%%%%%%%%%%%

```

```

function diff = fit_simp_levy(x,X,Y);

```

```

A=x(1);

```

```

B=x(2);

```

```

C=x(3);

```

```

diff = A+B*exp(-X./C) - Y;

```

```

%%%%%%%%%%%%%%%%%%%%%%%%%%%%%%%%%%%%%%%%%%%%%%%%%%%%%%%%%%%%%%%%%%%%%%%%
%%%%%%%%%%%%%%%%%%%%%%%%%%%%%%%%%%%%%%%%%%%%%%%%%%%%%%%%%%%%%%%%%%%%%%%% Matlab Program for a 3 Exponential Fit to CPMG Data %%%%%%%%%%
%%%%%%%%%%%%%%%%%%%%%%%%%%%%%%%%%%%%%%%%%%%%%%%%%%%%%%%%%%%%%%%%%%%%%%%%
close all
clear all

%%%%%%%%%%%%%%%%%%%%%%%%%%%%%%%%%%%%%%%%%%%%%%%%%%%%%%%%%%%%%%%%%%%%%%%%250us data%%%%%%%%%%%%%%%%%%%%%%%%%%%%%%%%%%%%%%%%%%%%%%%%%%%%%%%%%%%%%%%%%%%%%%%%
t1=[1 2 4 6 8 10 12 14 16 18 20 22 24 26 28 30 32 40 48 56 64 72 80 88 96 104 112 120 128 136
144 152 168 184 200 216 232 248 264 280 296 312 328 344 360 376 396 408 500 600 700 800
900 1000 1100 1200 1300 1400 1600 1800 2000 2200 2400 2560];
t1=0.25*t1; %time data 250us per echo
load cf_250u_12t.txt -ascii %read integral data from text file
Y=cf_250u_12t;
Y=Y';
inty1=Y./Y(1); %normalization
m0=2000;
X=t1(2:64);
Y=inty1(2:64);

%%%%%%%%%%%%%%%%%%%%%%%%%%%%%%%%%%%%%%%%%%%%%%%%%%%%%%%%%%%%%%%%%%%%%%%%Begin Fit%%%%%%%%%%%%%%%%%%%%%%%%%%%%%%%%%%%%%%%%%%%%%%%%%%%%%%%%%%%%%%%%%%%%%%%%
X01=[0.3254 10.2753 0.3556 52.7678 0.3158 166.0420]; %best guess for fit
x1=leastsq('fit_simp3',X01,[],[],X,Y); %access fit program
Y_new=x1(1)*exp(-X./x1(2))+ x1(3)*exp(-X./x1(4))+ x1(5)*exp(-X./x1(6));
plot(X,log(Y),'ro',X,log(Y_new),'r')
hold on

%%%%%%%%%%%%%%%%%%%%%%%%%%%%%%%%%%%%%%%%%%%%%%%%%%%%%%%%%%%%%%%%%%%%%%%%1ms data%%%%%%%%%%%%%%%%%%%%%%%%%%%%%%%%%%%%%%%%%%%%%%%%%%%%%%%%%%%%%%%%%%%%%%%%
t2=[1 2 4 6 8 10 12 14 16 18 20 22 24 26 28 30 32 34 36 38 40 42 44 46 48 50 52 54 56 58 60 62
64 66 68 70 72 74 76 78 80 82 84 86 88 96 104 112 120 128 160 192 224 256 288 320 352 384
416 448 480 512 544 640];
t2=1*t2;

load cf_1m_12t.txt -ascii
Y=cf_1m_12t;
Y=Y';
inty2=Y./(Y(1)+50); %normalization
X=t2(2:64);
Y=inty2(2:64);
X01=[0.2903 11.6617 0.3263 62.0267 0.2659 177.9543];
x2=leastsq('fit_simp3',X01,[],[],X,Y);
Y_new=x2(1)*exp(-X./x2(2))+x2(3)*exp(-X./x2(4))+x2(5)*exp(-X./x2(6));
plot(X,log(Y),'b+',X,log(Y_new),'b')
hold on

```

```

%%%%%%%%%%10ms data%%%%%%%%%%
t3=2:2:64;
t3=10*t3;
load cf_10m_12t.txt -ascii
Y=cf_10m_12t;
Y=Y';
inty3=Y./3500;
X=t3(2:30);
    Y=inty3(2:30);
    X01=[0.2400  0.5267  0.2537  29.9704  0.1330  131.1862];
x3=leastsq('fit_simp3',X01,[],[],X,Y);
    Y_new=x3(1)*exp(-X./x3(2))+x3(3)*exp(-X./x3(4))+x3(5)*exp(-X./x3(6));
    plot(X,log(Y),'g^',X,log(Y_new),'g')
hold on

%%%%%%%%%Output data to plot%%%%%%%%%

title('Clean CF(new)CPMG 12T FFT/pk/integral/3exp - 06/20/00')
ylabel('ln(I/Io)')
legend('250us','1ms','10ms','')
xlabel('time (ms)')
axis([0 700 -8 0.00])
gtext('M(t)=A*exp(-t/B)+ C*exp(-t/D)+ E*exp(-t/F)')
t2_1=['T2(250u)=',num2str(x1(2),4),',',num2str(x1(4),4),',',num2str(x1(6),5),',ms;A=',num2str(x1(1),2),',C=',num2str(x1(3),2),',E=',num2str(x1(5),2),'(pts1-64)'];
t2_2=['T2(1m)=',num2str(x2(2),4),',',num2str(x2(4),4),',',num2str(x2(6),5),',ms;A=',num2str(x2(1),2),',C=',num2str(x2(3),2),',E=',num2str(x2(5),2),'(pts2-64)'];
t2_3=['T2(10m)=',num2str(x3(2),4),',',num2str(x3(4),4),',',num2str(x3(6),5),',ms;A=',num2str(x3(1),2),',C=',num2str(x3(3),2),',E=',num2str(x3(5),2),'(pts2-30)'] ;

gtext(t2_1)
gtext(t2_2)
gtext(t2_3)

```

```

%%%%%%%%%%%%%%%%%%%%%%%%%%%%%%%%%%%%%%%%%%%%%%%%%%%%%%%%%%%%%%%%%%%%%%%%
%% Define Function fit_simp3 - 3 exp, for use in previous CPMG program %%
%%%%%%%%%%%%%%%%%%%%%%%%%%%%%%%%%%%%%%%%%%%%%%%%%%%%%%%%%%%%%%%%%%%%%%%%

```

```

function diff = fit_simp3(x,X,Y)

```

```

A=x(1);

```

```

B=x(2);

```

```

C=x(3);

```

```

D=x(4);

```

```

E=x(5);

```

```

F=x(6);

```

```

diff = A*exp(-X./B)+ C*exp(-X./D)+E*exp(-X./F)-Y; %.^E) - Y;

```



```

load cf_10m_12t.txt -ascii
Y=cf_10m_12t;
Y=Y';
inty3=Y./1500;
X=t3(3:31);
Y=inty3(3:31);
X01=[2.7756 10.2400 0.8223 49.7115 0.661];
x3=leastsq('fit_simp2',X01,[],[],X,Y);
Y_new=x3(1)*exp(-X./x3(2))+ x3(3)*exp(-((X/x3(4)).^x3(5)));
plot(X,log(Y),'g^',X,log(Y_new),'g')
hold on

%%%%% Output Data to Plot %%%%%%%%%%

title('Clean CF(new)CPMG 12t fp/integral/stretched exp. fit - 06/19/00')
ylabel('ln(I/Io)')
legend('250us','1ms','10ms','')
xlabel('time (ms)')
axis([0 700 -6 0.00])
gtext('Y=A*exp(-X/B)+C*exp(-((X/D)^E)')
gtext('T2(250u)=11.76/63.4ms; A=0.22,C=0.80,E=0.57(pts1-56)')
gtext('T2(1ms)=10.4/31.6ms; A=0.05,C=1.03,E=0.44(pts3-60)')
gtext('T2(10ms)=10.2/49.7ms; A=2.8,C=82,E=0.66(pts3-31)')

```



```

%%%%%%%%%%%%%%%%%%%%%%%%%%%%%%%%%%%%%%%%%%%%%%%%%%%%%%%%%%%%%%%%%%%%%%%%
%% Define Function fit_simp2 – stretched bi-exp for use in previous program %%
%%%%%%%%%%%%%%%%%%%%%%%%%%%%%%%%%%%%%%%%%%%%%%%%%%%%%%%%%%%%%%%%%%%%%%%%

```

```

function diff = fit_simp2(x,X,Y)

A=x(1);
B=x(2);
C=x(3);
D=x(4);
E=x(5);
diff = A*exp(-X./B)+ C*exp(-((X/D).^E)) - Y;

```

```

%%%%%%%%%%%%%%%%%%%%%%%%%%%%%%%%%%%%%%%%%%%%%%%%%%%%%%%%%%%%%%%%%%%%%%%%
%%%%%%%%%%%%%%%%%%%%%%%%%%%%%%%%%%%%%%%%%%%%%%%%%%%%%%%%%%%%%%%%%%%%%%%%
Matlab Program for Fit of Peak Height Diffusion Data %%%%%%%%%%
%%%%%%%%%%%%%%%%%%%%%%%%%%%%%%%%%%%%%%%%%%%%%%%%%%%%%%%%%%%%%%%%%%%%%%%%
%%%%%%%%%%%%%%%%%%%%%%%%%%%%%%%%%%%%%%%%%%%%%%%%%%%%%%%%%%%%%%%%%%%%%%%%

```

```

close all
clear all

```

```

%% peak height data for free and bound peaks
y=[30.6 9.31 3.90 2.68 1.66 1.06 0.67 0.41 0.24 0.14 0.08 0.05 0.03 0.02 0.015 0.01]*1E7;
yb1=[1.22 0.78 0.64 0.55 0.41 0.30 0.20 0.14 0.087 0.053 0.03 0.02 0.013 0.01 0.009
0.007]*1E7;
y=log(y./y(1));
y=y';

```

```

%%loop to assign gradient strengths
a=zeros(16,1);
for i=1:15
    a(i+1)=a(i)+60/15;
end
b=a./100;
c=zeros(16,1);
for i=1:16
    c(i)=b(i)*b(i);
end

```

```

%% smalldelta and bigdelta in values in seconds
sd=2.5E-3;
bd=167E-3;

```

```

%% max gradient (G/cm)
G=47;
const=7.143E8*sd*sd*(bd+(2/3)*sd)*G*G;
x=c.*const;
xb=x(1:12);
yb=log(yb1(1:12)/yb1(1));
yb=yb';
x0=x(3:10);           %define ranges for fits
y0=y(3:10);
x1=x(5:10);
y1=y(5:10);
x2=x(11:16);
y2=y(11:16);

```

```

pb=polyfit(xb,yb,1);           %fit bound data
fb = polyval(pb,xb);
plot(xb,yb,'b+',xb,fb,'-')

```

hold on

p0=polyfit(x0,y0,1); %fit free data

p1=polyfit(x1,y1,1);

p2=polyfit(x2,y2,1);

f0 = polyval(p0,x0);

f1 = polyval(p1,x1);

f2 = polyval(p2,x2);

plot(x0,y0,'ro',x0,f0,'r-')

hold on

Db=['Db=',num2str(-pb(1)),'cm^2/s'];

Df=['Df=',num2str(-p0(1)),'cm^2/s'];

hold on

plot(x,y,'ro')

plot(x(1:16),log(yb1(1:16)./yb1(1)),'b+')

%%Output data to plot%%

title('CF clean 12T Stimulated Echo Diffusion (peak plot) - echo time=15ms')

xlabel('\gamma^2 g^2 \delta^2 (\Delta + 2/3 \delta) (s/cm2)')

ylabel('ln(I/Io)')

legend('Bound Water',' ','Free Water','')

gtext(Db)

gtext(Df)

```

%%%%%%%%%%%%%%%%%%%%%%%%%%%%%%%%%%%%%%%%%%%%%%%%%%%%%%%%%%%%%%%%%%%%%%%%
%%%%%%%%%%%%%%%%%%%%%%%%%%%%%%%%%%%%%%%%%%%%%%%%%%%%%%%%%%%%%%%%%%%%%%%% Matlab Program for Fit of Peak Height Diffusion Data %%%%%%%%%
%%%%%%%%%%%%%%%%%%%%%%%%%%%%%%%%%%%%%%%%%%%%%%%%%%%%%%%%%%%%%%%%%%%%%%%%
% four different storage times, 20ms, 100ms, 300ms, and 1s; constant echo time of 3.2ms
close all
clear all
td2=65536;
N=16;
td=1:td2;
dw=40E-6;
    %varying gradient percentages to keep q2 constant with changing delta
grad_percent20=92.09;grad_percent100=42.15;grad_percent300=24.43;grad_percent1s=13.4;
    %define constants for entry into q equation
a20=zeros(1,16);a100=zeros(1,16);a300=zeros(1,16);a1s=zeros(1,16);
for i=1:15
    a20(i+1)=a20(i)+(grad_percent20)/15; b20=a20/100;
    a100(i+1)=a100(i)+(grad_percent100)/15; b100=a100/100;
    a300(i+1)=a300(i)+(grad_percent300)/15; b300=a300/100;
    a1s(i+1)=a1s(i)+(grad_percent1s)/15; b1s=a1s/100;
end
c20=zeros(16,1);c100=zeros(16,1);c300=zeros(16,1);c1s=zeros(16,1);
for i=1:16
    c20(i)=b20(i)*b20(i);c100(i)=b100(i)*b100(i);c300(i)=b300(i)*b300(i);c1s(i)=b1s(i)*b1s(i);
end
%smalldelta and bigdelta in s
sd=1.8E-3;
%max gradient (G/cm)
G=47;
%Big Delta = 20ms, data set: cfclean072800/2/1
bd20=20E-3;
const20=7.143E8*sd*sd*(bd20+(2/3)*sd)*G*G;
x20=c20.*const20; xb20=x20(2:12); xf20=x20(4:12);
% reads the binary data from all N files in the array ser
ser20=zeros(td2,N);
for i=1:N;
    fname20=['c:/dan/matlab/cf_diff_20m/1r_',num2str(i)];
    fid20=fopen(fname20,'r','b');
    ser_ind20=fread(fid20,[td2,1],'int32');
    status=fclose(fid20);
    ser20(:,i)=ser_ind20;
end
peak20=zeros(1,N);
for i=1:N;
    ymax20=max(ser20(:,i));
    peak20(1,i)=ymax20;
end

```

```

peak20=log(peak20(1,:)/573186067);
peak20=peak20'; y20=peak20;

figure(1)
[pb20,sb20] = polyfit(x20,y20,1);
[fb20,db20] = polyval(pb20,x20,sb20);
plot(x20,y20,'b+',x20,fb20,'-')
hold on

%=====
%Big Delta = 100ms, data set: cfclean071900/32/1
ser100=zeros(td2,N);
for i=1:N;
    fname100=['c:/dan/matlab/cf_diff_100m/1r_',num2str(i)];
    fid100=fopen(fname100,'r','b');
    ser_ind100=fread(fid100,[td2,1],'int32');
    status=fclose(fid100);
    ser100(:,i)=ser_ind100;
end
peak100=zeros(1,N);
for i=1:N;
    ymax100=max(ser100(:,i));
    peak100(1,i)=ymax100;
end
peak100=log(peak100(1,:)/573186067);
peak100=peak100';
y100=peak100;
bd100=100E-3;
const100=7.143E8*sd*sd*(bd100+(2/3)*sd)*G*G;
x100=c100.*const100;
figure(1)
[pb100,sb100] = polyfit(x100,y100,1);
[fb100,db100] = polyval(pb100,x100,sb100);
plot(x100,y100,'rx',x100,fb100,'r-')
hold on

%=====
%Big Delta = 300ms, data set: cfclean071900/33/1
ser300=zeros(td2,N);
for i=1:N;
    fname300=['c:/dan/matlab/cf_diff_300m/1r_',num2str(i)];
    fid300=fopen(fname300,'r','b');
    ser_ind300=fread(fid300,[td2,1],'int32');
    status=fclose(fid300);
    ser300(:,i)=ser_ind300;
end

```

```

peak300=zeros(1,N);
for i=1:N;
    ymax300=max(ser300(:,i));
    peak300(1,i)=ymax300;
end
peak300=log(peak300(1,:)/573186067);
peak300=peak300';
y300=peak300;
bd300=300E-3;
const300=7.143E8*sd*sd*(bd300+(2/3)*sd)*G*G;
x300=c300.*const300;
figure(1)
[pb300,sb300] = polyfit(x300,y300,1);
[fb300,db300] = polyval(pb300,x300,sb300);
plot(x300,y300,'gd',x300,fb300,'g-')
hold on

%=====
%Big Delta = 1s, data set: cfclean062800/5/1
ser1s=zeros(td2,N);
for i=1:N;
    fname1s=['c:/dan/matlab/cf_diff_1s/1r_',num2str(i)];
    fid1s=fopen(fname1s,'r','b');
    ser_ind1s=fread(fid1s,[td2,1],'int32');
    status=fclose(fid1s);
    ser1s(:,i)=ser_ind1s;
end
peak1s=zeros(1,N);
for i=1:N;
    ymax1s=max(ser1s(:,i));
    peak1s(1,i)=ymax1s;
end
peak1s=log(peak1s(1,:)/573186067);
peak1s=peak1s';
y1s=peak1s;% (1:13);
bd1s=1000E-3;
const1s=7.143E8*sd*sd*(bd1s+(2/3)*sd)*G*G;
x1s=c1s.*const1s;
figure(1)
[pb1s,sb1s] = polyfit(x1s,y1s,1);
[fb1s,db1s] = polyval(pb1s,x1s,sb1s);
plot(x1s,y1s,'ms',x1s,fb1s,'m-')
hold on
%=====Plot the Data=====
figure(1)
legend('\Delta = 20ms',' ','\Delta = 100ms',' ','\Delta = 300ms',' ','\Delta = 1000ms',' ')

```

```

title('CF Resin-PGSTe Diffusion-MAS 5kHz (\tau_e=3.2ms)')
xlabel('\gamma^2 g^2 \delta^2 (\Delta + 2/3 \delta) (s/cm^2)')
ylabel('ln(I/I_0)')

plot(x20,y20,'b+')
hold on
plot(x100,y100,'rx')
hold on
plot(x300,y300,'gd')
hold on
plot(x1s,y1s,'ms')
hold on

Db20=['D(20m)=',num2str(-pb20(1),2),'cm^2/s'];
Db100=['D(100m)=',num2str(-pb100(1),2),'cm^2/s'];
Db300=['D(300m)=',num2str(-pb300(1),2),'cm^2/s'];
Db1s=['D(1s)=',num2str(-pb1s(1),2),'cm^2/s'];
gtext(Db20); gtext(Db100); gtext(Db300); gtext(Db1s)

pause

%plots the data as a stack
[ymax20,n]=max(ser20(:,1));
x20n=td./(2*dw*td2)-n/(2*dw*td2);
hold on
figure(2)
hold on
for i=1:N;
    x20new=x20n(31500:34000);
    y20new=x20new;
    y20new(:)=x20(i);
    z=ser20(31500:34000,i);
    plot3(x20new,y20new,z)
end
view(148,60)
xlabel('Frequency (Hz)')
ylabel('Time (ms)')
title('CF Clean - PGSTE Diffusion,MAS 5KHz, cfclean071900/31, \Delta=20ms, \tau_e=3.2ms')
pause

[ymax100,n]=max(ser100(:,1));
x100n=td./(2*dw*td2)-n/(2*dw*td2);
hold on
figure(3)
hold on
for i=1:N;

```

```

x100new=x100n(31500:34000); y100new=x100new; y100new(:)=x100(i);
z=ser100(31500:34000,i);
plot3(x100new,y100new,z)
end
view(148,60)
xlabel('Frequency (Hz)')
ylabel('Time (ms)')
title('CF Clean - PGSTE Diffusion,MAS 5KHz, cfclean071900/32, \Delta=100ms,
\tau_e=3.2ms')
pause

```

```

[ymax300,n]=max(ser300(:,1));
x300n=td./(2*dw*td2)-n/(2*dw*td2);
hold on
figure(4)
hold on
for i=1:N;
x300new=x300n(31500:34000); y300new=x300new; y300new(:)=x300(i);
z=ser300(31500:34000,i);
plot3(x300new,y300new,z)
end
view(148,60)
xlabel('Frequency (Hz)')
ylabel('Time (ms)')
title('CF Clean - PGSTE Diffusion,MAS 5KHz, cfclean071900/33, \Delta=300ms,
\tau_e=3.2ms')
pause

```

```

[ymax1s,n]=max(ser1s(:,1));
x1sn=td./(2*dw*td2)-n/(2*dw*td2);
hold on
figure(5)
hold on
for i=1:N;
x1snew=x1sn(31500:34000); y1snew=x1snew; y1snew(:)=x1s(i);
z=ser1s(31500:34000,i);
plot3(x1snew,y1snew,z)
end
view(148,60)
xlabel('Frequency (Hz)')
ylabel('Time (ms)')
title('CF Clean - PGSTE Diffusion,MAS 5KHz, cfclean071900/34, \Delta=1s, \tau_e=3.2ms')

```



```
pb=polyfit(x(2:6),peak1(2:6),1);
fb = polyval(pb,x(2:6));
plot(x(2:6),peak1(2:6),'rd',x(2:6),fb,'b-')
hold on
```

```
p0=polyfit(x(7:16),peak1(7:16),1);
f0 = polyval(p0,x(7:16));
plot(x(7:16),peak1(7:16),'ro',x(7:16),f0,'r-')
hold on
```

```
Db=['D(s) = ',num2str(-pb(1),2),'cm^2/s'];
Df=['D(b) = ',num2str(-p0(1),2),'cm^2/s'];
hold on
```

```
title('CF Resin-CPMG(\tau_e=200us,T=550ms)+ PGSTE Diffusion (5kHz,peak plot)-
\tau_e=3.2ms, \Delta=20ms')
xlabel('\gamma^2 g^2 \delta^2 (\Delta + 2/3 \delta) (s/cm2)')
ylabel('ln(I/Io)')
legend('Free Water (small q)', 'Free Water (big q)', ' ')
gtext(Db)
gtext(Df)
```

```
pause
```

```
    %plots the data as a stack
```

```
[ymax20,n]=max(size(x20n));
x20n=td./(2*dw*td2)-n/(2*dw*td2);
hold on
figure(2)
hold on
for i=1:N;
    x20new=x20n(31500:34000);
    y20new=x20new;
    y20new(:)=x(i);
    z=ser(31500:34000,i);
    plot3(x20new,y20new,z)
end
view(148,60)
xlabel('Frequency (Hz)')
ylabel('\gamma^2 g^2 \delta^2 (\Delta + 2/3 \delta) (s/cm2)')
title('CF Clean - CPMG(>550ms)+PGSTE Diffusion,MAS 5KHz, cfclean071900/35,
\Delta=20ms, \tau_e=3.2ms')
```


[THIS PAGE INTENTIONALLY LEFT BLANK]

APPENDIX 4.0:

NMR SPECTROSCOPY DATA

A.4.1. Data Set 1: Spectral Deconvolution of MAS Experiments

A.4.1.1. 3T spectral plot and deconvolution of clean CF resin

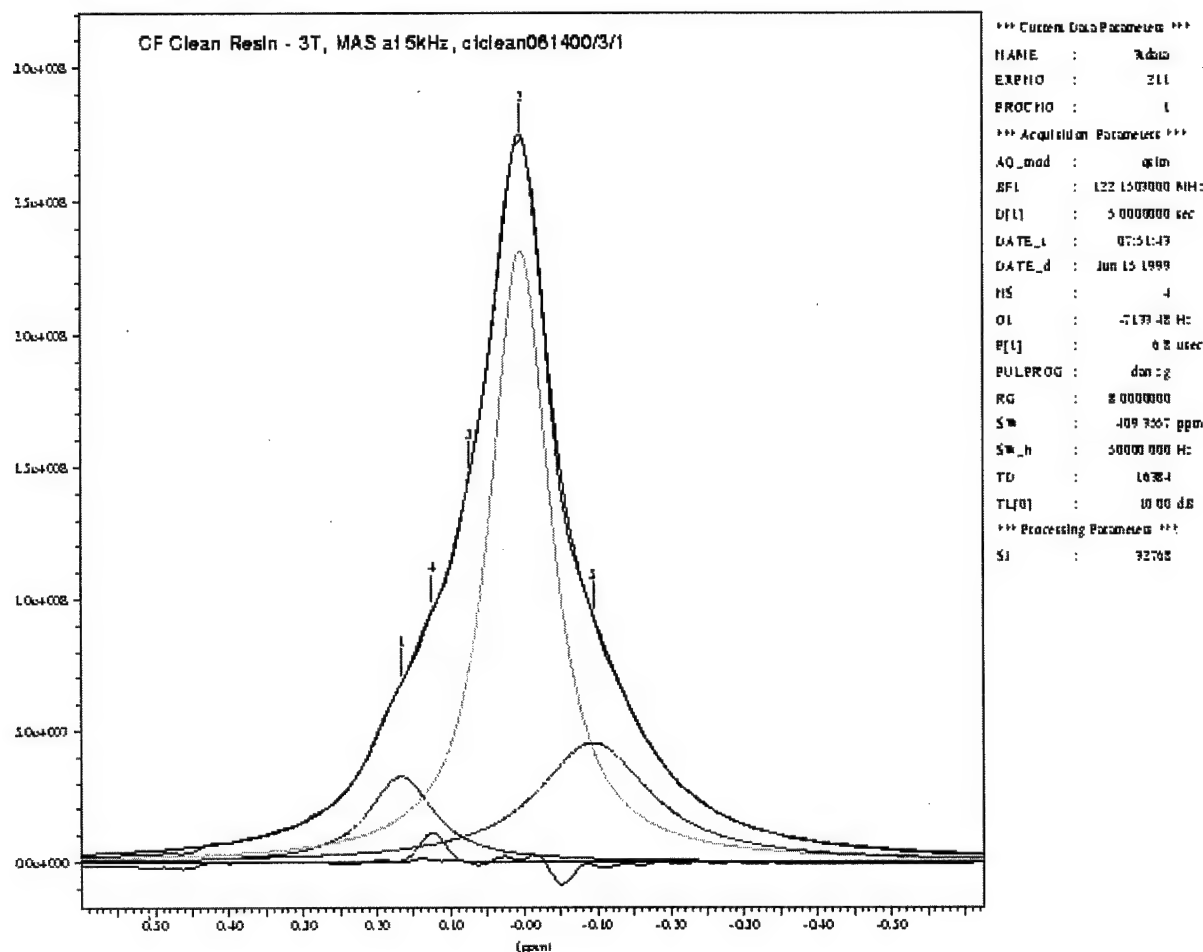


Figure A.4.1: Spectral plot and deconvolution of clean CF resin. The spectrum was collected using magic-angle spinning (MAS) at 5 kHz on the 3T magnet. The spectrum is fit with four peaks where the center peak belongs to the interstitial or plasticizer water, the right peak represents the bound water, and the left peaks are from the free water. The lower line represents the residual from the fit. The x-axis is in parts-per-million (ppm) and the y-axis is signal intensity. The table to the right contains the acquisition and processing parameters.

Table A.4.1: Data for CF Resin spectral deconvolution from the 3T

Peak No.	Position [ppm/Hz]	Intensity [absolute]	Width [Hz]	T ₂ Time [ms]	Gauss/Lorenz. ratio	Integral [absolute]	Population %
1	0.1671/20.4	3.26E+07	13.1	24.3	0.0	4.40E+08	8.8%
2	0.0042/0.5	2.32E+08	12.0	26.6	0.1	2.80E+09	55.4%
3	0.0739/9.0	5.36E+07	12.7	25.2	0.0	6.98E+08	14.0%
4	0.1247/15.2	1.12E+07	4.9	65.2	1.0	4.47E+07	0.9%
5	-0.0947/-11.6	4.54E+07	22.5	14.1	0.0	1.05E+09	20.9%

A.4.1.2. 12T spectral plot and deconvolution of clean CF resin

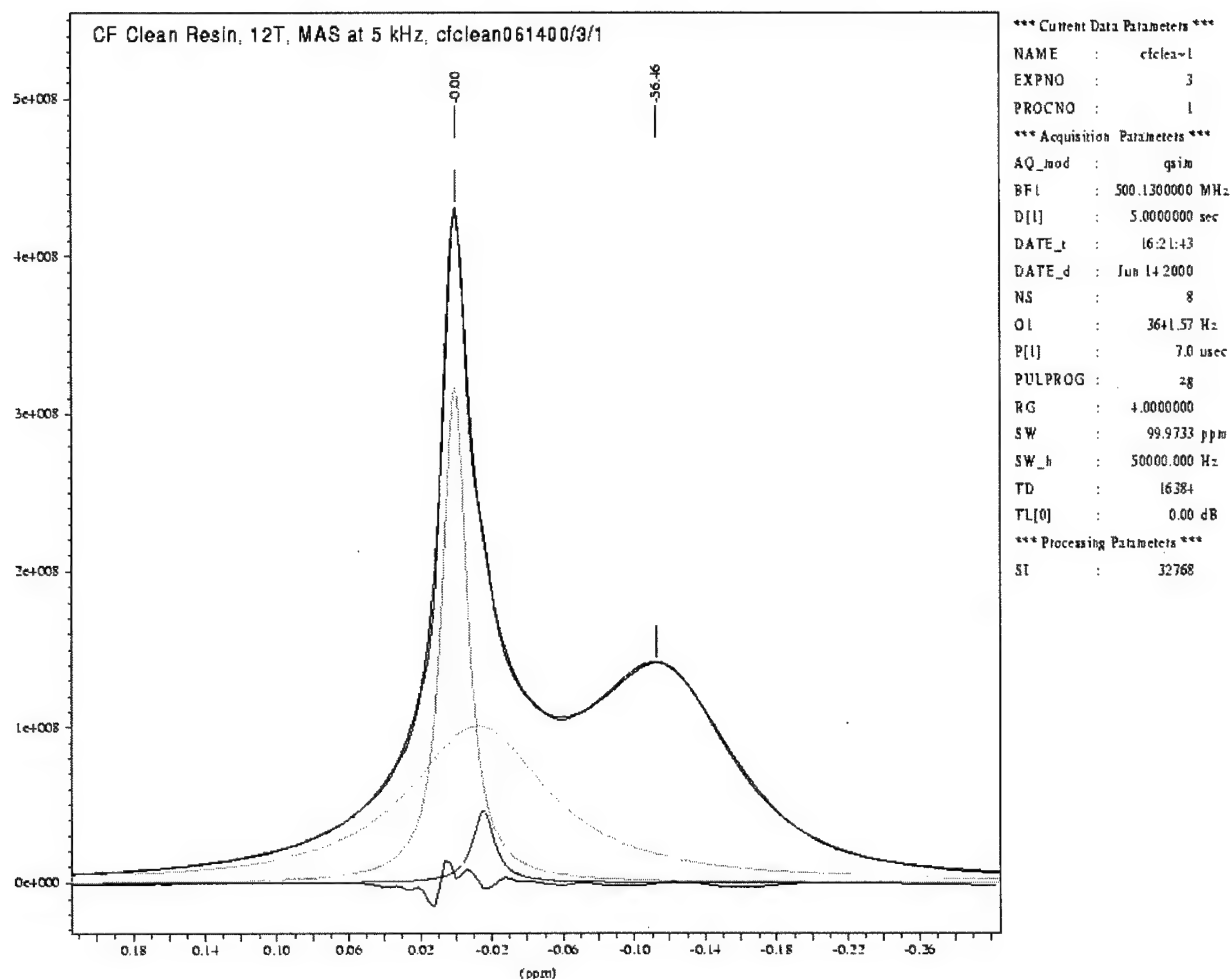


Figure A.4.2: Spectral plot and deconvolution of clean CF resin. The spectrum was collected using magic-angle spinning (MAS) at 5 kHz on the 12T magnet. The spectrum is fit with four peaks where the center peak belongs to the interstitial/plasticizer water, the right peak represents the bound water, and the left peaks are from the free water. The lower line represents the residual from the fit. The x-axis is in parts-per-million (ppm) and the y-axis is signal intensity. The table to the right contains the acquisition and processing parameters.

Table A.4.2: Data for CF Resin spectral deconvolution from the 12T

Peak No.	Position [ppm/Hz]	Intensity [absolute]	Width [Hz]	T ₂ Time [ms]	Gauss/Lorenz. ratio	Integral [absolute]	Population %
1	-0.0156/-7.8	4.60E+07	7.1	44.6	0.0	3.38E+08	2.5%
2	0.0004/0.2	3.17E+08	8.3	38.4	0.1	2.64E+09	19.8%
3	-0.1152/-57.6	1.22E+08	47.2	6.7	0.4	5.45E+09	40.9%
4	-0.0125/-6.3	1.01E+08	47.1	6.7	0.0	4.89E+09	36.7%

A.4.1.3. 3T spectral plot and deconvolution of clean RF resin

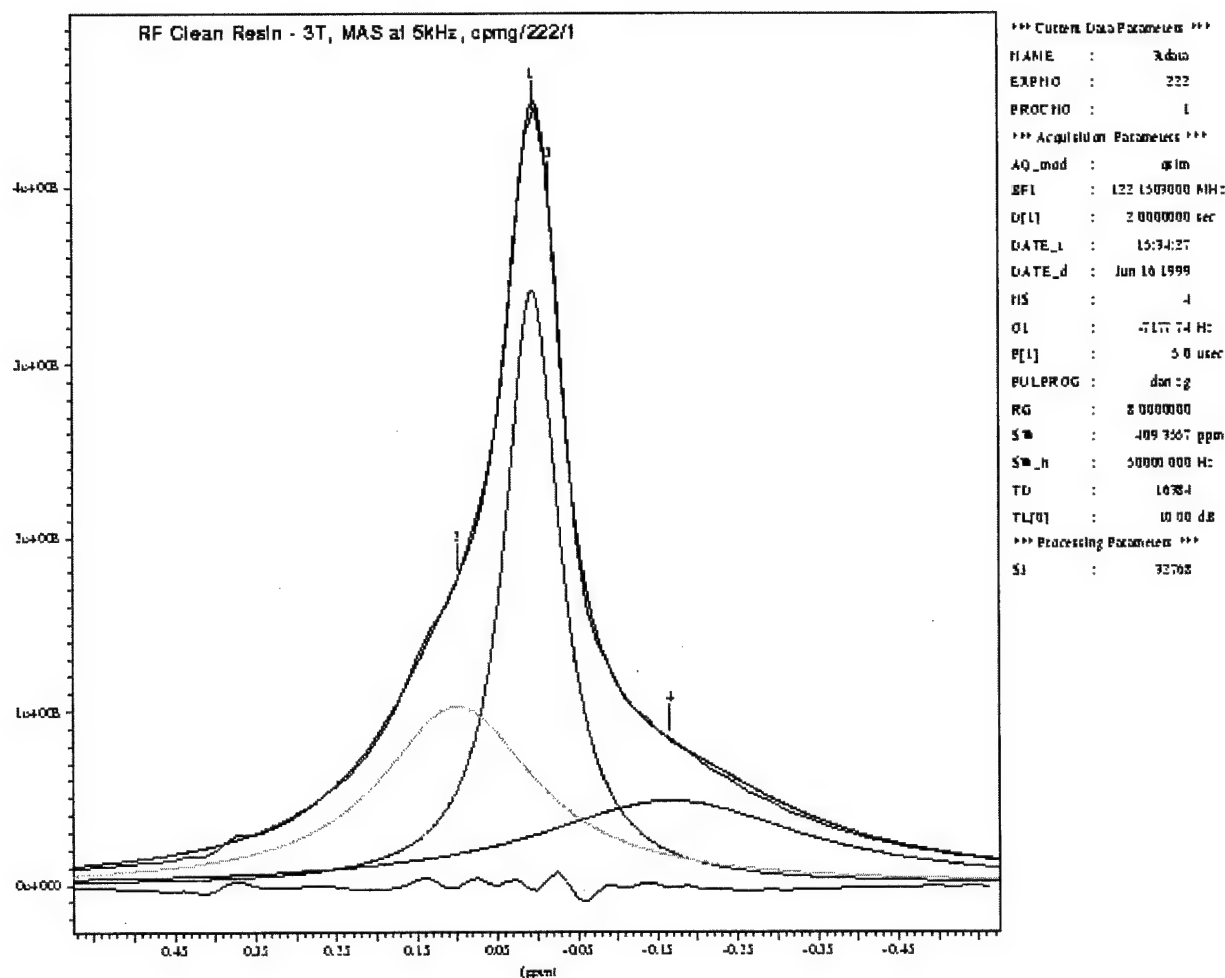


Figure A.4.3: Spectral plot and deconvolution of clean RF resin. The spectrum was collected using magic-angle spinning (MAS) at 5 kHz on the 3T magnet. The spectrum is fit with three main peaks where the center peak belongs to the interstitial/plasticizer water, the right peak represents the bound water, and the left peak is from the free water. The lower line represents the residual from the fit, and the small center peak most likely belongs to the plasticizer pool. The x-axis is in parts-per-million (ppm) and the y-axis is signal intensity. The table to the right contains the acquisition and processing parameters used in the data collection.

Table A-4.3: Data for RF Resin spectral deconvolution from the 3T

Peak No.	Position [ppm/Hz]	Intensity [absolute]	Width [Hz]	T ₂ Time [ms]	Gauss/Lorenz. ratio	Integral [absolute]	Population %
1	0.0047/0.6	3.41E+08	10.1	31.5	0.0	3.56E+09	38.6%
2	0.0988/12.1	1.03E+08	28.5	11.2	0.0	3.02E+09	32.8%
3	-0.016/-1.95	3.46E+07	4.9	65.2	1.0	1.39E+08	1.5%
4	-0.1667/-20.4	4.84E+07	50.2	6.4	0.0	2.50E+09	27.1%

A.4.1.4. 12T spectral plot and deconvolution of clean RF resin

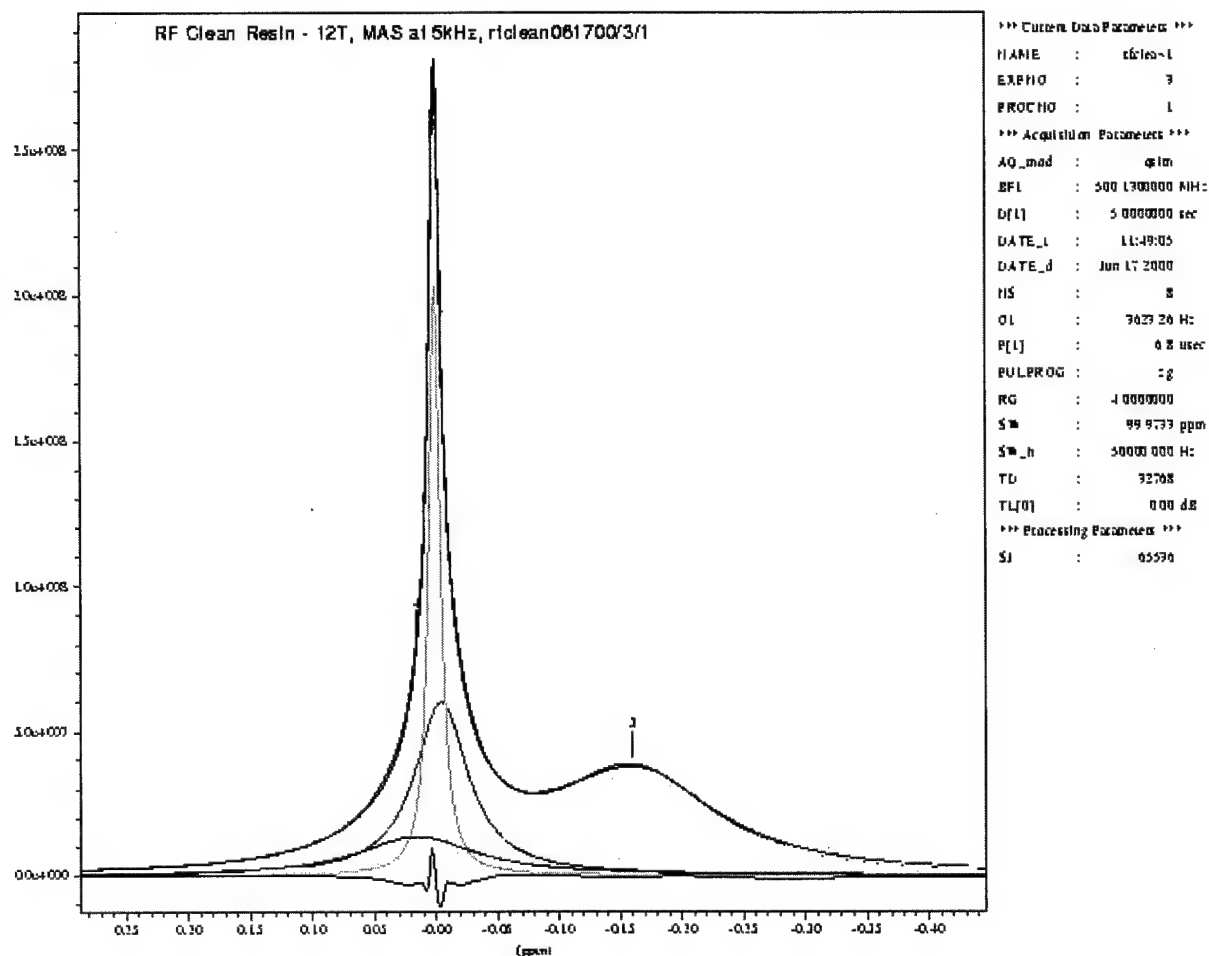


Figure A.4.4: Spectral plot and deconvolution of clean RF resin. The spectrum was collected using magic-angle spinning (MAS) at 5 kHz on the 12T magnet. The spectrum is fit with four peaks where the center peak belongs to the interstitial/ plasticizer water, the right peak represents the bound water, and the left peak is from the free water. The lower line represents the residual from the fit, and the small center peak most likely belongs to the free pool. The x-axis is in parts-per-million (ppm) and the y-axis is signal intensity. The table to the right contains the acquisition and processing parameters used in the data collection.

Table A-4.4: Data for RF Resin spectral deconvolution from the 12T

Peak No.	Position [ppm/Hz]	Intensity [absolute]	Width [Hz]	T ₂ Time [ms]	Gauss/Lorenz. ratio	Integral [absolute]	Population %
1	-0.0046/-2.3	6.03E+07	26.2	12.1	0.0	3.25E+09	25.3%
2	0.0004/0.2	2.04E+08	5.5	57.7	0.0	2.32E+09	18.1%
3	-0.1607/-80.4	3.55E+07	79.1	4.0	0.1	5.67E+09	44.1%
4	0.0153/7.7	1.36E+07	57.1	5.6	0.0	1.60E+09	12.5%

A.4.2. Data Set 2: Inversion Recovery T_1 Data from Static and MAS Experiments

A.4.2.1. Plot of static, 3T, clean CF resin inversion-recovery data

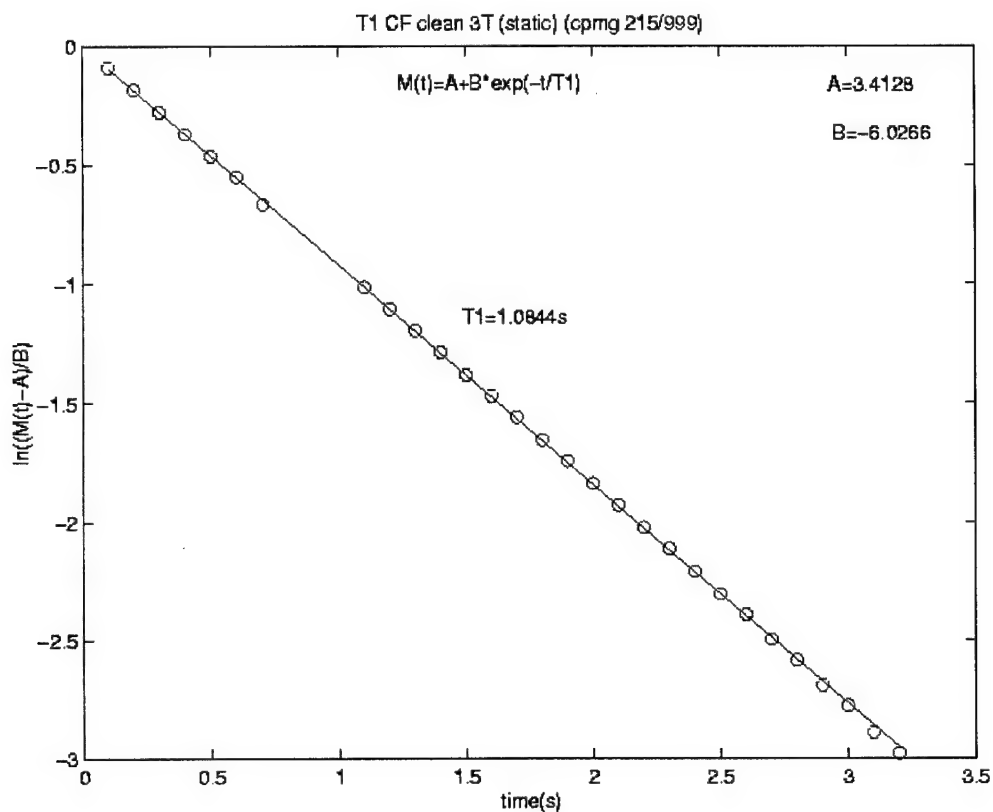


Figure A.4.5: Plot of static, 3T, clean CF resin inversion-recovery data to determine the T_1 relaxation time of water-saturated resin. The data, $M(t)$, is determined from the peak heights of the interstitial/free water, and it is plotted versus the inversion or storage time (D2). The data is fit with a three parameter single exponential fit as suggested by Levy and others.^[1] The T_1 for the interstitial water in the CF resin is measured to be 1.08 s. The data was collected using the 3T magnet with a D1 delay time of 15 seconds.

¹ G.C. Levy, J. Kowalewski, L.F. Johnson, and L. Palmer, J. Magn. Resonance, 26, 533-536, 1977.

A.4.2.2. Plot of static, 12T, clean CF resin inversion-recovery data

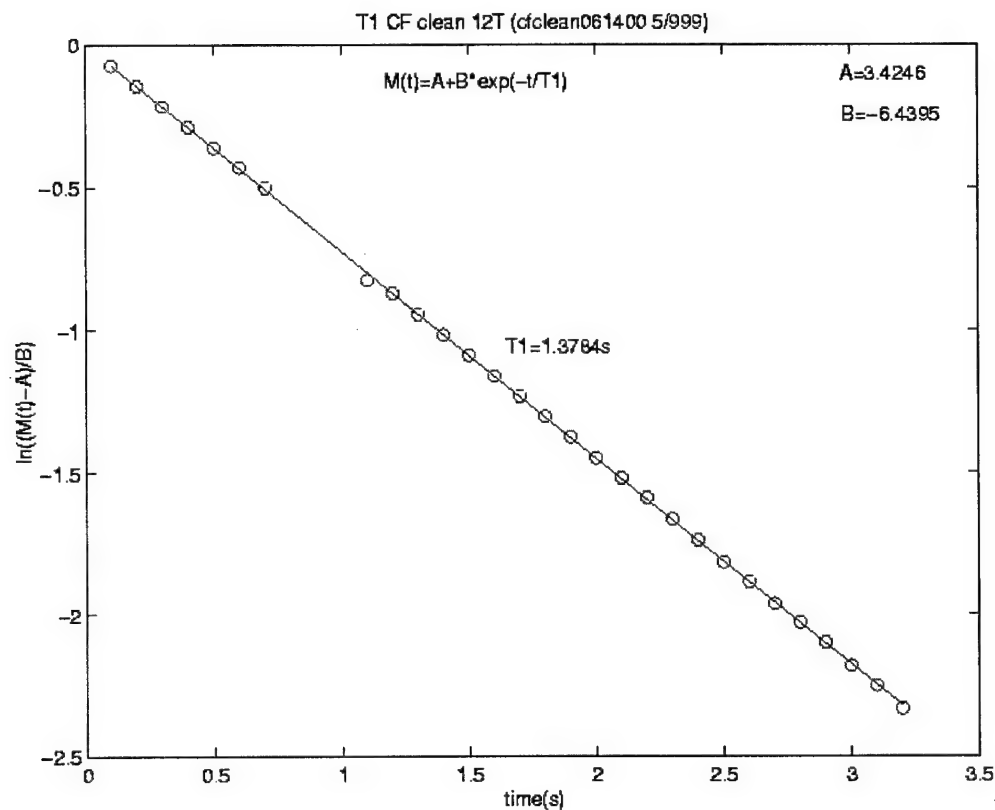


Figure A.4.6: Plot of static 12T clean CF resin inversion-recovery data to determine the T_1 relaxation time of water-saturated resin. The data, $M(t)$, is determined from the peak heights of the interstitial/free water, and it is plotted versus the inversion or storage time (D2). The data is fit with a three parameter single exponential fit as suggested by Levy and others.^[2] The T_1 for the interstitial water in the CF resin is measured to be 1.38 s. The data was collected using the 12T magnet with a D1 delay time of 15 seconds.

² G.C. Levy, J. Kowalewski, L.F. Johnson, and L. Palmer, J. Magn. Resonance, 26, 533-536, 1977.

A.4.2.3. Stacked plot of MAS, 12T, clean CF resin inversion-recovery data

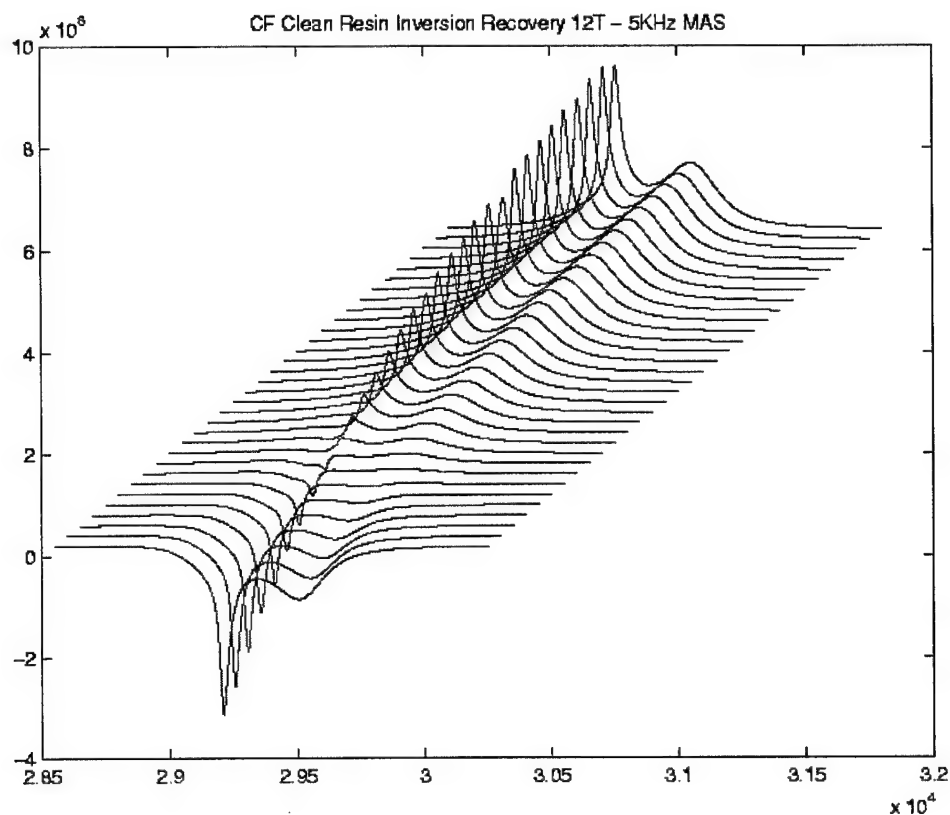


Figure A.4.7: CF clean resin inversion recovery stack plot from the 12T with MAS at 5 kHz. The plot shows the chemical shift of the free/plasticizer and bound water components and the similar rate of T_1 decay for both spin pools. The peak heights are plotted in the following figures.

A.4.2.4. Plot of MAS, 12T, clean CF resin inversion-recovery data for interstitial water

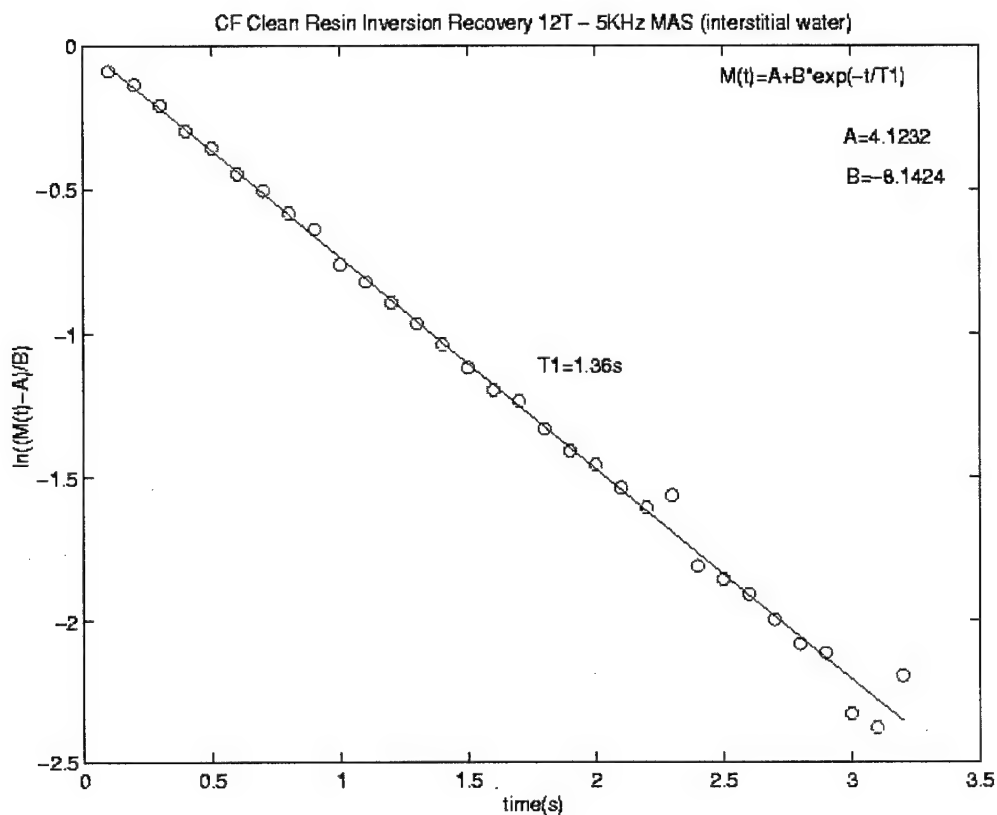


Figure A.4.8: Plot of MAS 12T clean CF resin inversion-recovery data to determine the T_1 relaxation time of the water associated with the main center spectral peak. The data ($M(t)$) comes from the peak heights of the interstitial/free water and it is plotted versus the inversion or storage time (D_2). The data is fit with a three parameter single exponential fit as suggested by Levy and others.^[3] The T_1 for the interstitial water in the CF resin is measured to be 1.36 s. The data was collected using the 12T magnet with MAS at 5 kHz, and a D_1 relaxation delay of 15 seconds.

³ G.C. Levy, J. Kowalewski, L.F. Johnson, and L. Palmer, J. Magn. Resonance, 26, 533-536, 1977.

A.4.2.5. Plot of static, 12T, clean CF resin inversion-recovery data for bound water

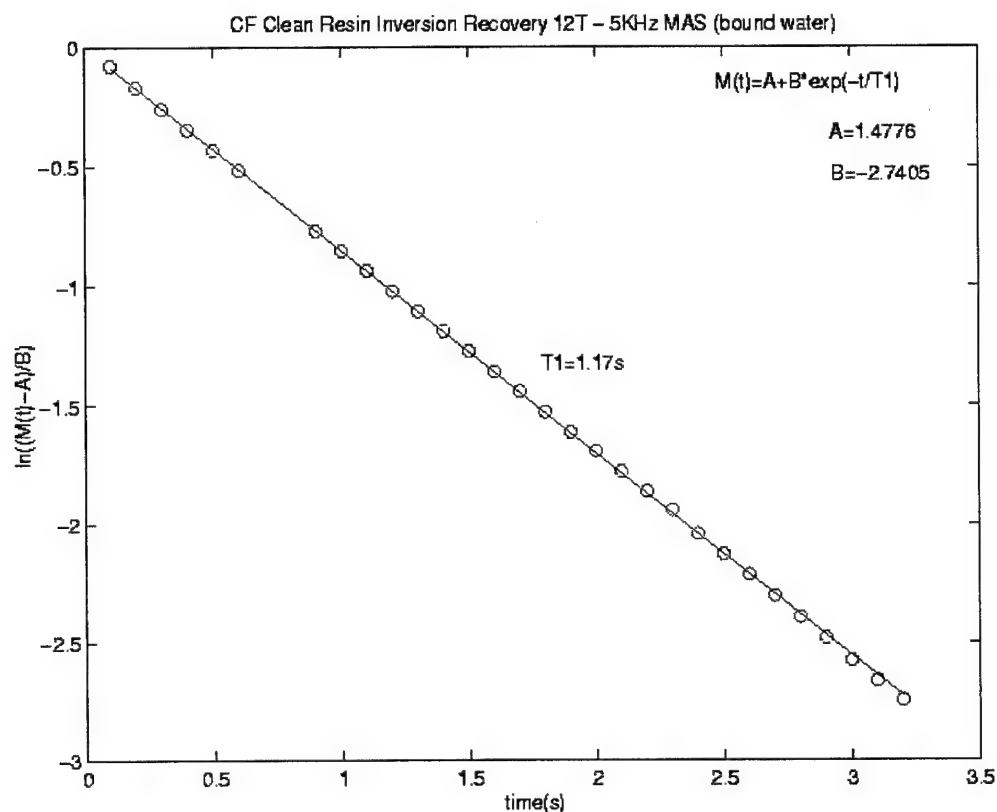


Figure A.4.9: Plot of MAS 12T clean CF resin inversion-recovery data to determine the T_1 relaxation time of the bound water. The data ($M(t)$) comes from the peak heights of the bound water and it is plotted versus the inversion or storage time (D2). The data is fit with a three parameter single exponential fit as suggested by Levy and others.^[4] The T_1 for the bound water in the CF resin is measured to be 1.17 s. The data was collected using the 12T magnet with MAS at 5 kHz, and a D1 relaxation delay of 15 seconds.

⁴ G.C. Levy, J. Kowalewski, L.F. Johnson, and L. Palmer, J. Magn. Resonance, 26, 533-536, 1977.

A.4.2.6. Plot of static, 3T, clean RF resin inversion-recovery data

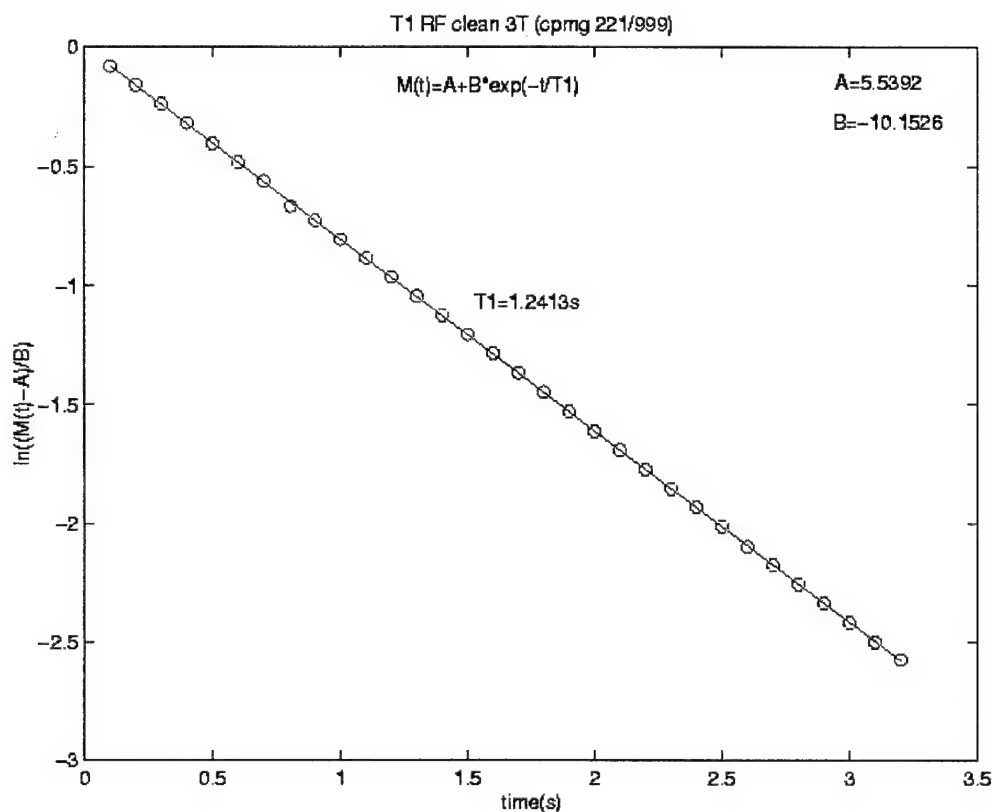


Figure A.4.10: Plot of static 3T clean RF resin inversion-recovery data to determine the T_1 relaxation time of water-saturated resin. The data, $M(t)$, is determined from the peak heights of the interstitial/free water, and it is plotted versus the inversion or storage time (D2). The data is fit with a three parameter single exponential fit as suggested by Levy and others.^[5] The T_1 for the interstitial water in the CF resin is measured to be 1.24 s. The data was collected using the 3T magnet with a D1 delay time of 15 seconds.

⁵ G.C. Levy, J. Kowalewski, L.F. Johnson, and L. Palmer, J. Magn. Resonance, 26, 533-536, 1977.

A.4.2.7. Plot of static, 12T, clean RF resin inversion-recovery data

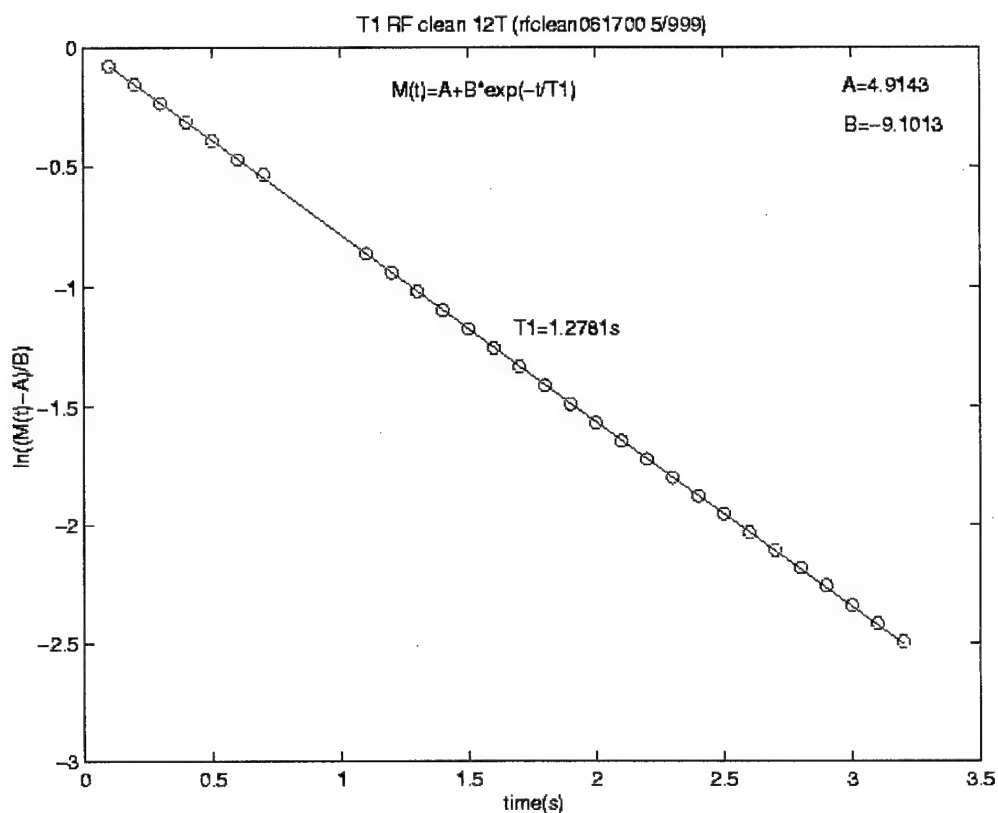


Figure A.4.11: Plot of static 12T clean RF resin inversion-recovery data to determine the T_1 relaxation time of water-saturated resin. The data, $M(t)$, is determined from the peak heights of the interstitial/free water, and it is plotted versus the inversion or storage time (D2). The data is fit with a three parameter single exponential fit as suggested by Levy and others.^[6] The T_1 for the interstitial water in the CF resin is measured to be 1.28 s. The data was collected using the 12T magnet with a D1 delay time of 15 seconds.

⁶ G.C. Levy, J. Kowalewski, L.F. Johnson, and L. Palmer, J. Magn. Resonance, 26, 533-536, 1977.

A.4.3. Data Set 3: CPMG T_2 Data from Static and MAS Experiments

A.4.3.1. Static 3T CPMG plot for clean CF resin

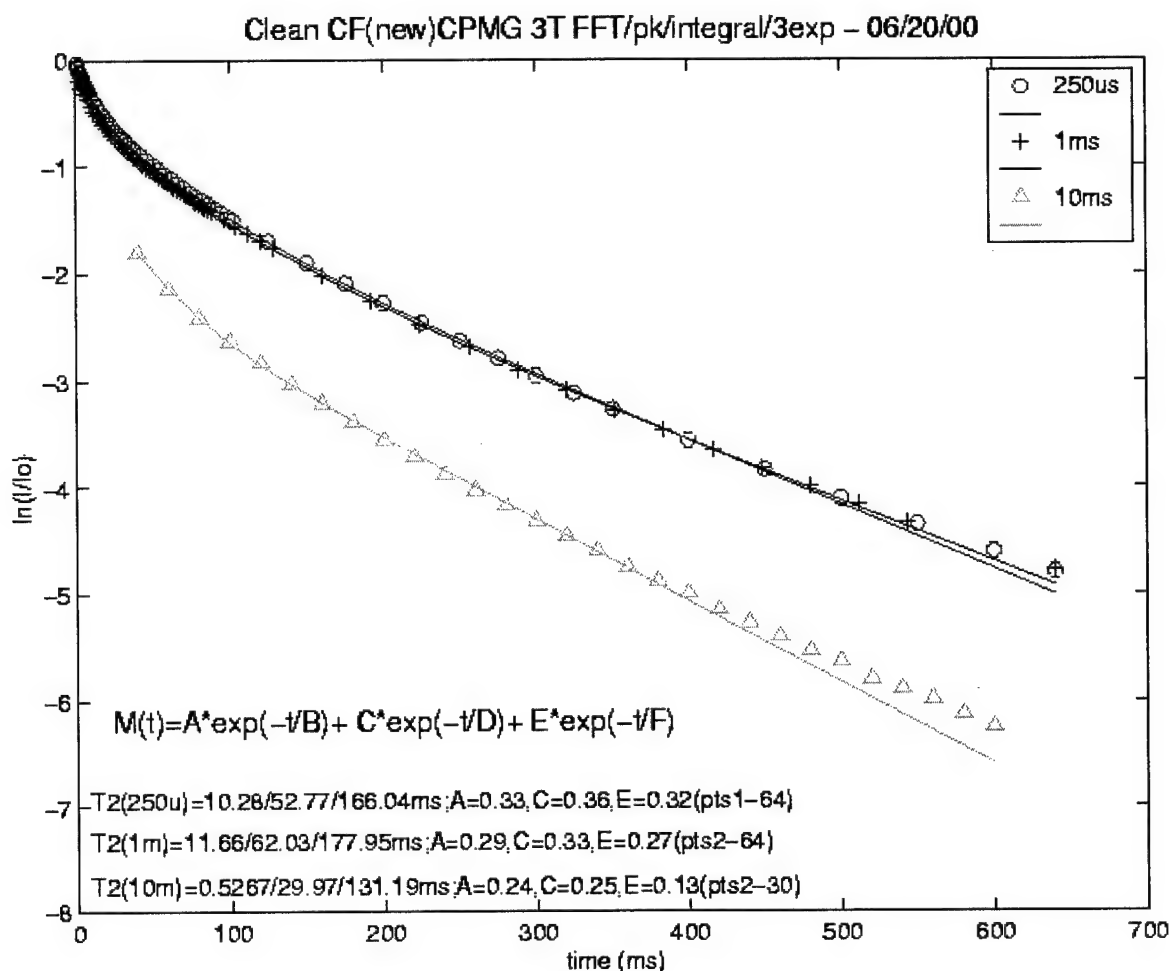


Figure A.4.12: Static 3T CPMG plot for clean CF resin. The integrated area of each static spectrum is plotted versus the total echo time, and three echo times of 250us, 1ms, and 10ms were used. A 3-exponential least squares fit was made to integral data. The relative population and T_2 time corresponding to exponential fits is provided, which is related to the three spin pools. The bound water T_2 is less than 10.3 ms, the plasticizer or interstitial water T_2 is about 50-60 ms and the T_2 is greater than 130 ms for the free water. The data was collected and processed on the 3T magnet.

A.4.3.2. Static 12T CPMG plot for clean CF resin

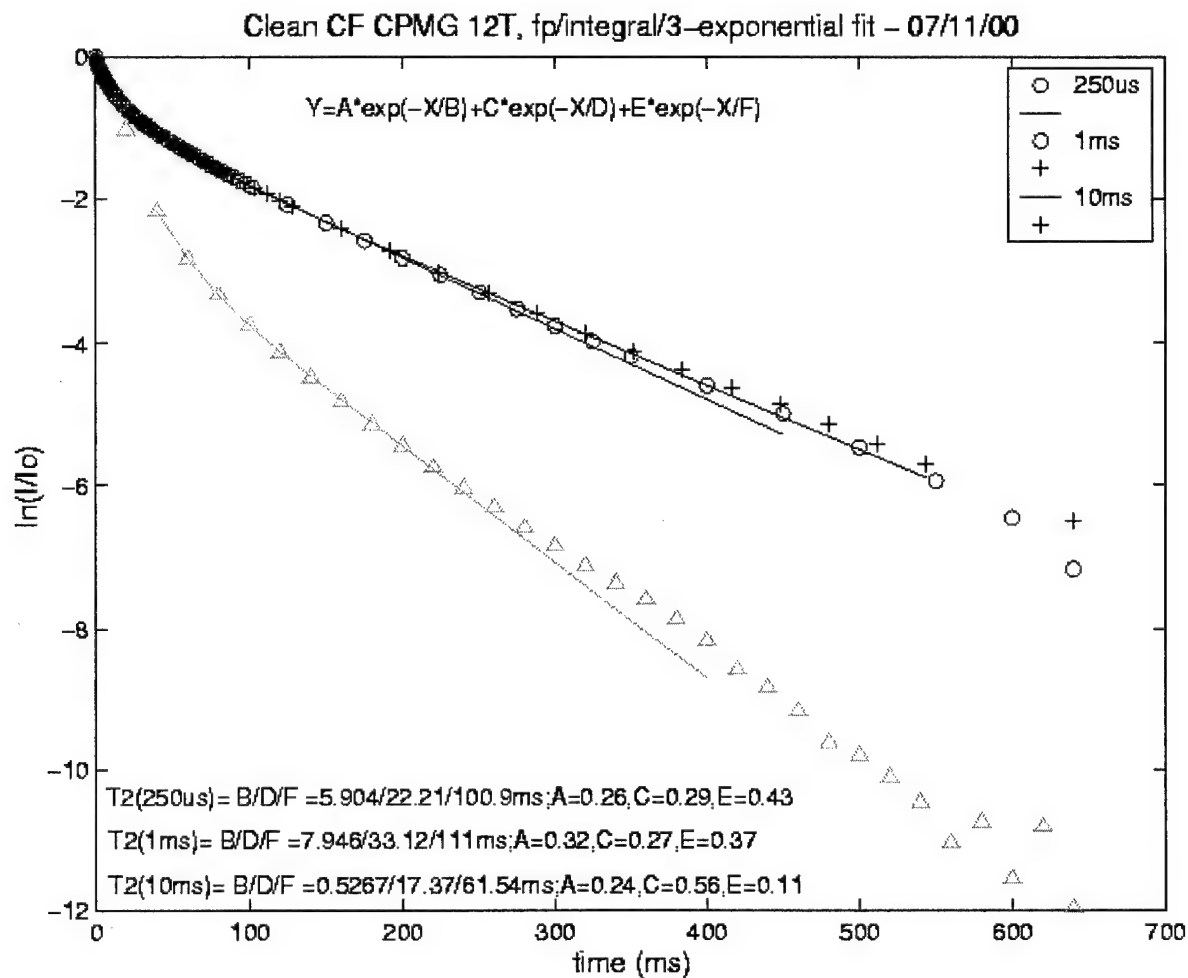


Figure A.4.13: Static 12T CPMG plot for clean CF resin. The integrated area of each static spectrum is plotted versus the total echo time, and three echo times of 250us, 1ms, and 10ms were used. A 3-exponential least squares fit was made to integral data. The relative population and T_2 time corresponding to exponential fits is provided, which is related to the three spin pools. The bound water T_2 is less than 6 ms, the plasticizer or interstitial water T_2 is about 20-30 ms, and the T_2 is greater than 110 ms for the free water. The data was collected and processed on the 12T magnet.

A.4.3.3. MAS (fast 5kHz) 12T CPMG stacked plot for clean CF resin (even spacing)

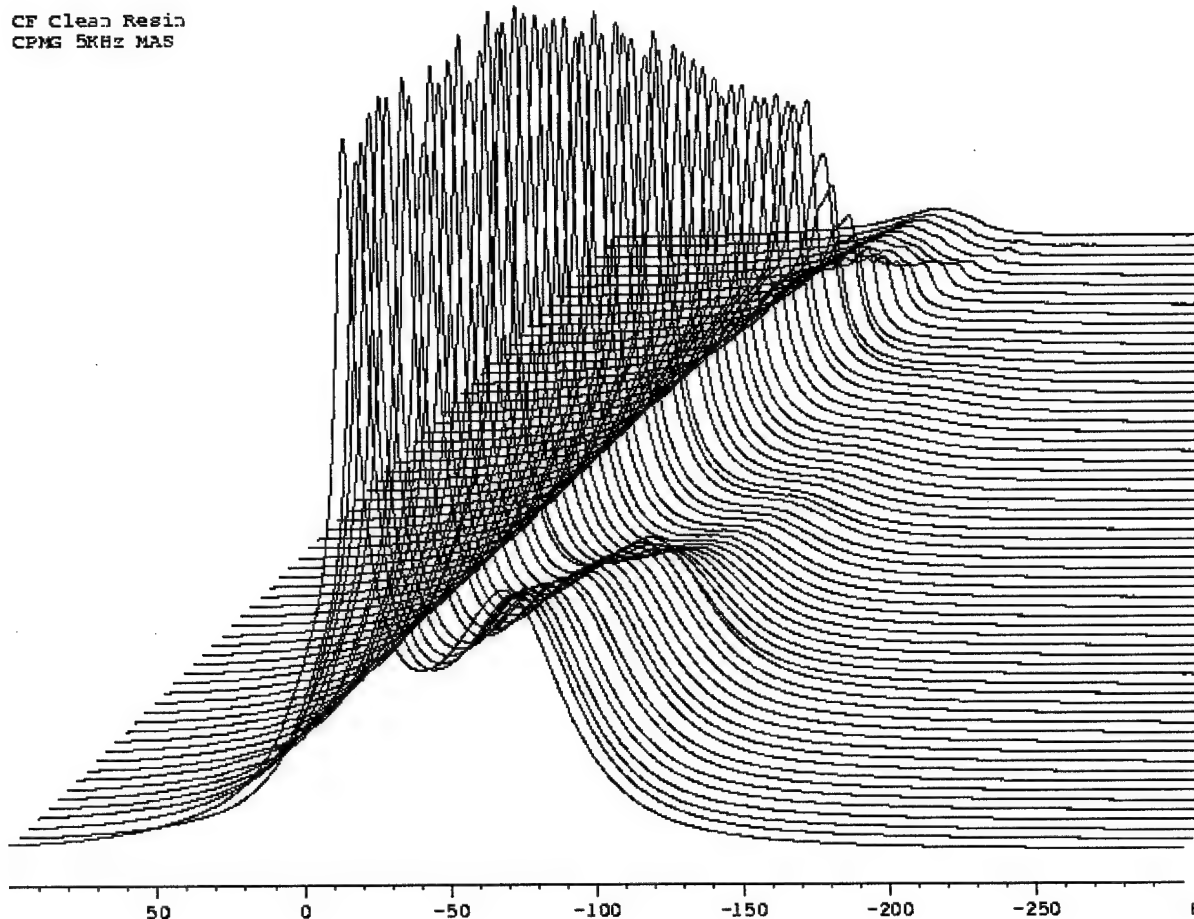


Figure A.4.14: Stacked plot of clean CF resin from a 12T CPMG sequence with MAS of 5kHz (fast MAS). This stacked plot shows is a display of all spectral information without regard to the temporal component. The x-axis is in hertz and each spectrum represents increasing echo time from 400us to 640ms. The plot clearly shows the bound and free spin pools with the free water shown by the main peak and the bound by the broad peak to the right. A third peak associated with the plasticizer spin pool can be seen to the left of the main peak at long times.

A.4.3.4. MAS (5kHz) 12T CPMG stacked plot for clean CF resin (temporal spacing)

CF Clean – CPMG 5KHz, ciclean070300/3, $\tau_e=200\mu s$

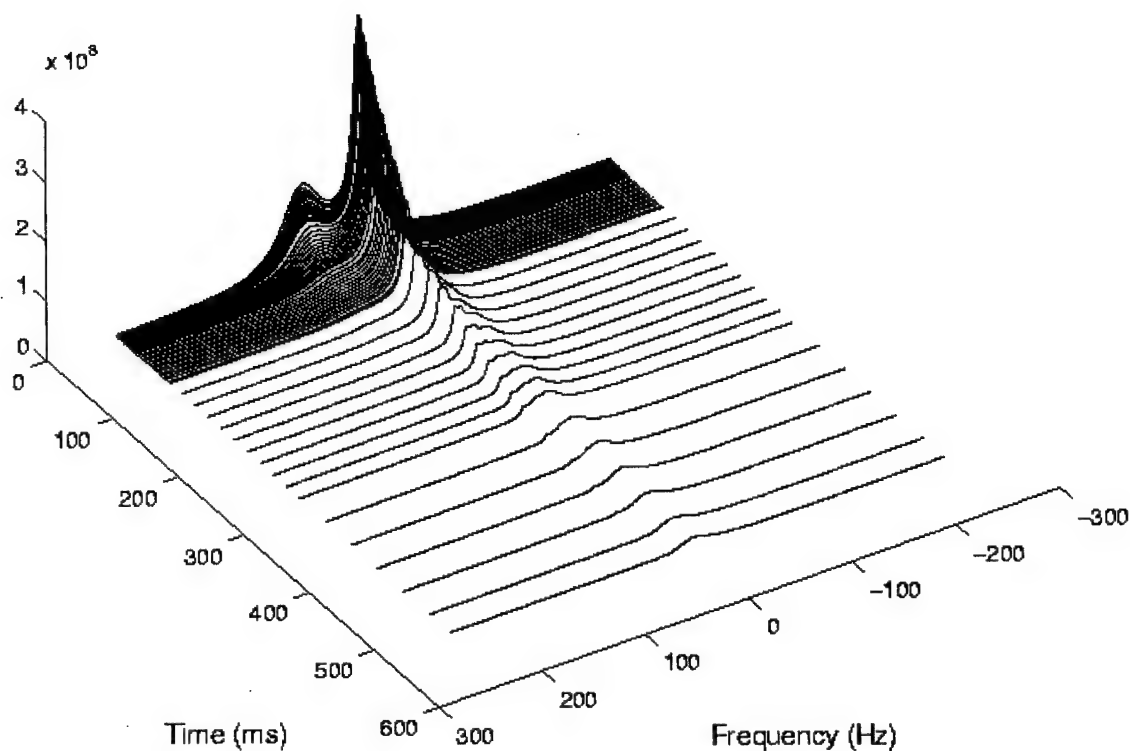


Figure A.4.15: CF clean resin stacked plot of CPMG MAS data from the 12T with a short echo time of 200 μs and fast spinning (5 kHz). This stacked plot displays the spectra in terms of the decay time and frequency. The plot shows the separation of the bound and interstitial components as well as the free component with the long, broad T_2 decay time. The peak heights of the two main components are plotted in the following figure.

A.4.3.5. MAS 12T CPMG plot for clean CF resin

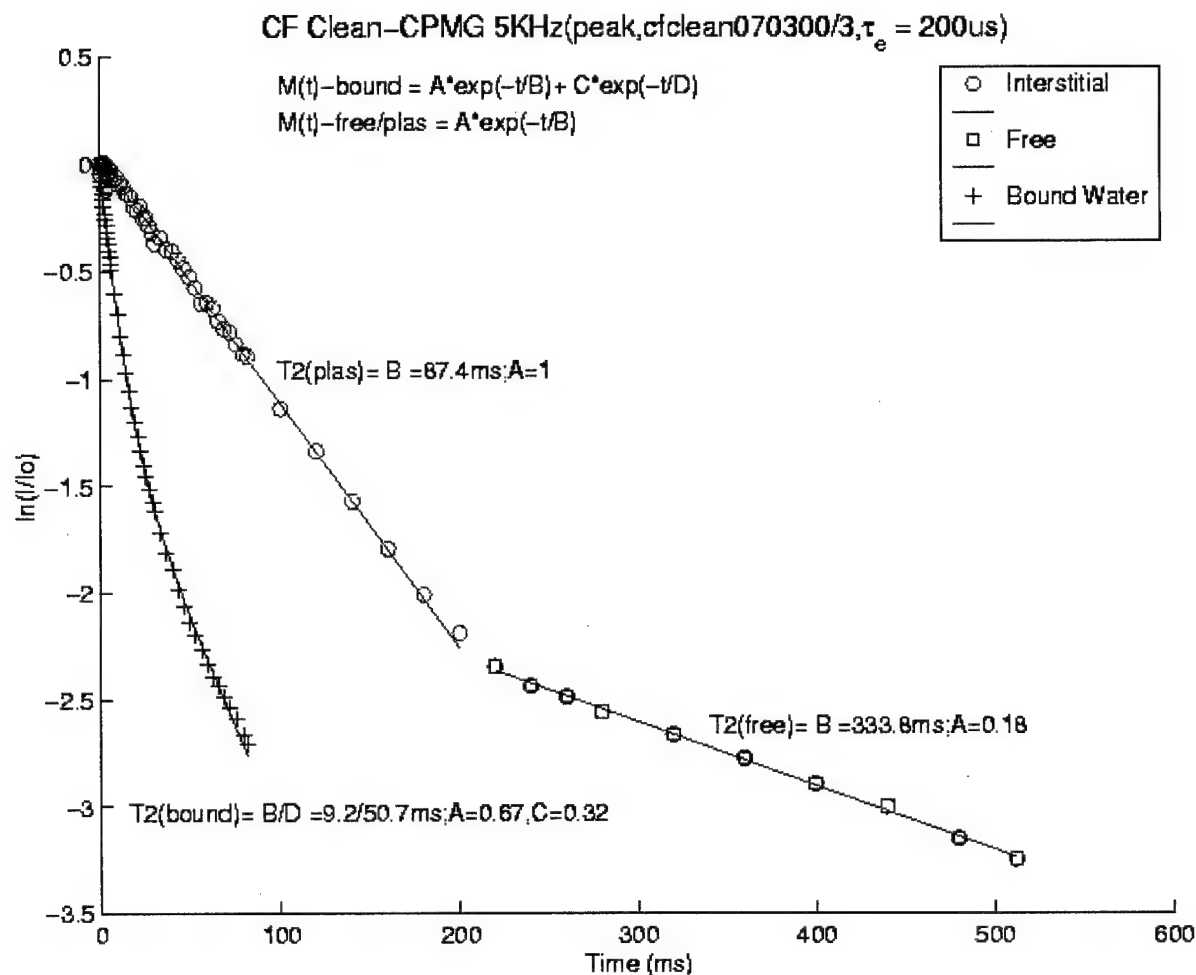


Figure A.4.16: 12T CPMG plot for clean CF resin with MAS of 5 kHz (fast spinning) and echo time of 200 μs . The peak intensities of the three spin pools seen in the previous stacked spectra are plotted versus the echo time. The T_2 corresponding to the three spin pools is provided as 9.2 ms for the bound water, 87.4 ms for the interstitial or plasticizer water, and 333.8 ms for the free water.

A.4.3.6. Static 3T CPMG plot for clean RF resin

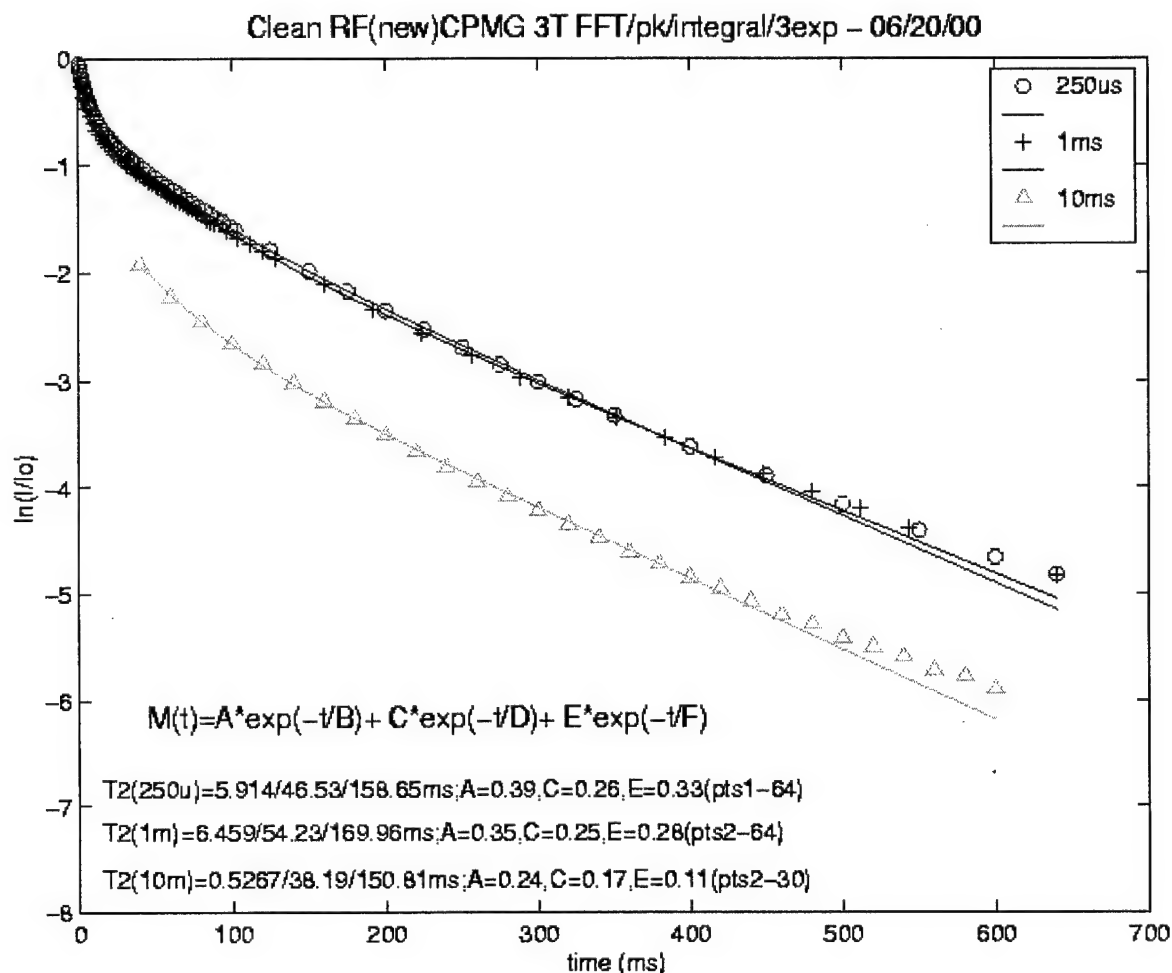


Figure A.4.17: Static 3T CPMG plot for clean RF resin. The integrated area of each static spectrum is plotted versus the total echo time, and three echo times of 250us, 1ms, and 10ms were used. A 3-exponential least squares fit was made to integral data. The relative population and T₂ time corresponding to exponential fits is provided, which is related to the three spin pools. The bound water T₂ is less than 6.5 ms, the plasticizer water T₂ is about 40-50 ms and the T₂ is greater than 150 ms for the free water. The data was collected and processed on the 3T magnet.

A.4.3.7. Static 12T CPMG plot for clean RF resin

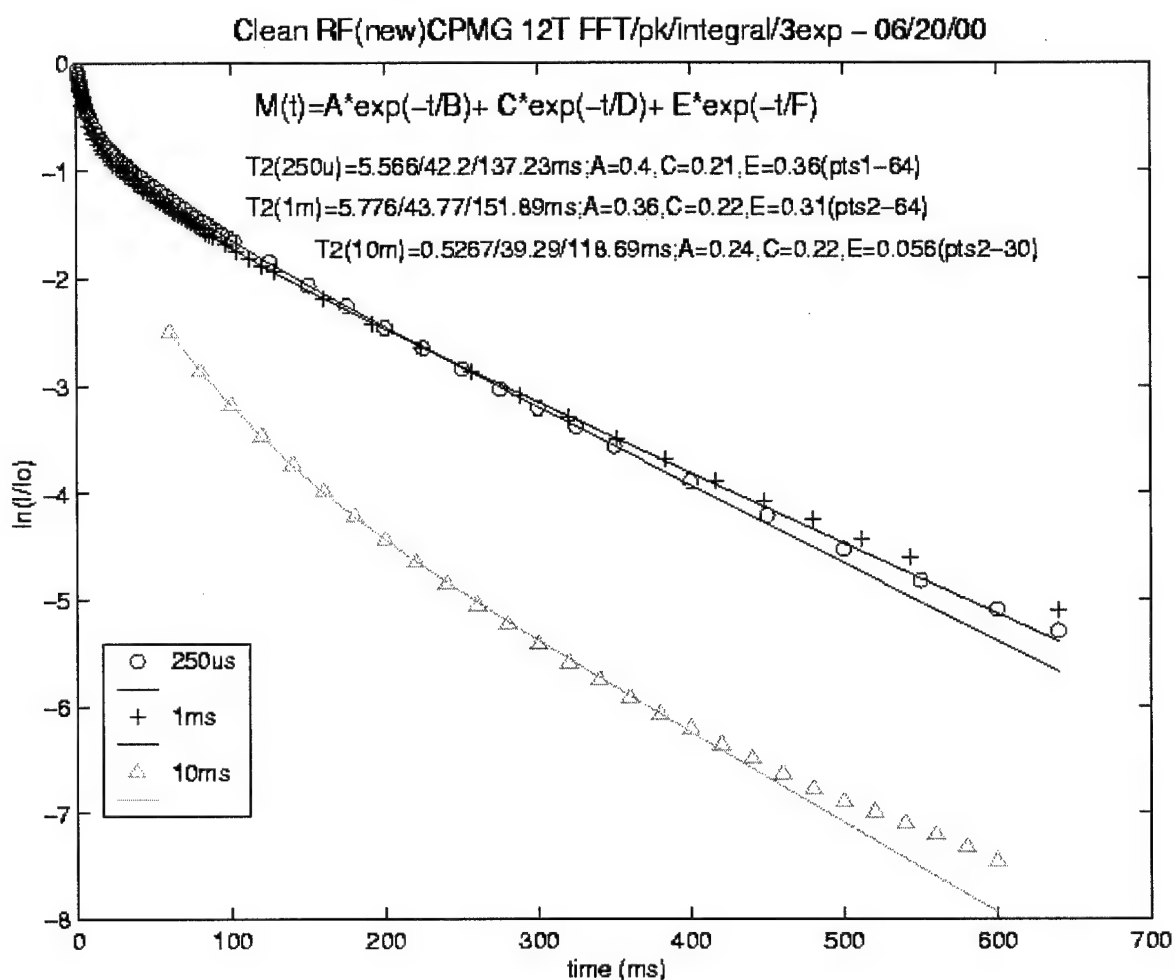


Figure A.4.18: Static 12T CPMG plot for clean RF resin. The integrated area of each static spectrum is plotted versus the total echo time, and three echo times of 250us, 1ms, and 10ms were used. A 3-exponential least squares fit was made to integral data. The relative population and T_2 time corresponding to exponential fits is provided, which is related to the three spin pools. The bound water T_2 is less than 6 ms, the plasticizer water T_2 is about 40 ms, and the T_2 is greater than 120 ms for the free water. The data was collected and processed on the 12T magnet.

A.4.3.8. MAS (fast 5kHz) 12T CPMG stacked plot for clean RF resin (even spacing)

RF Clean Resin
CPMG 5kHz MAS

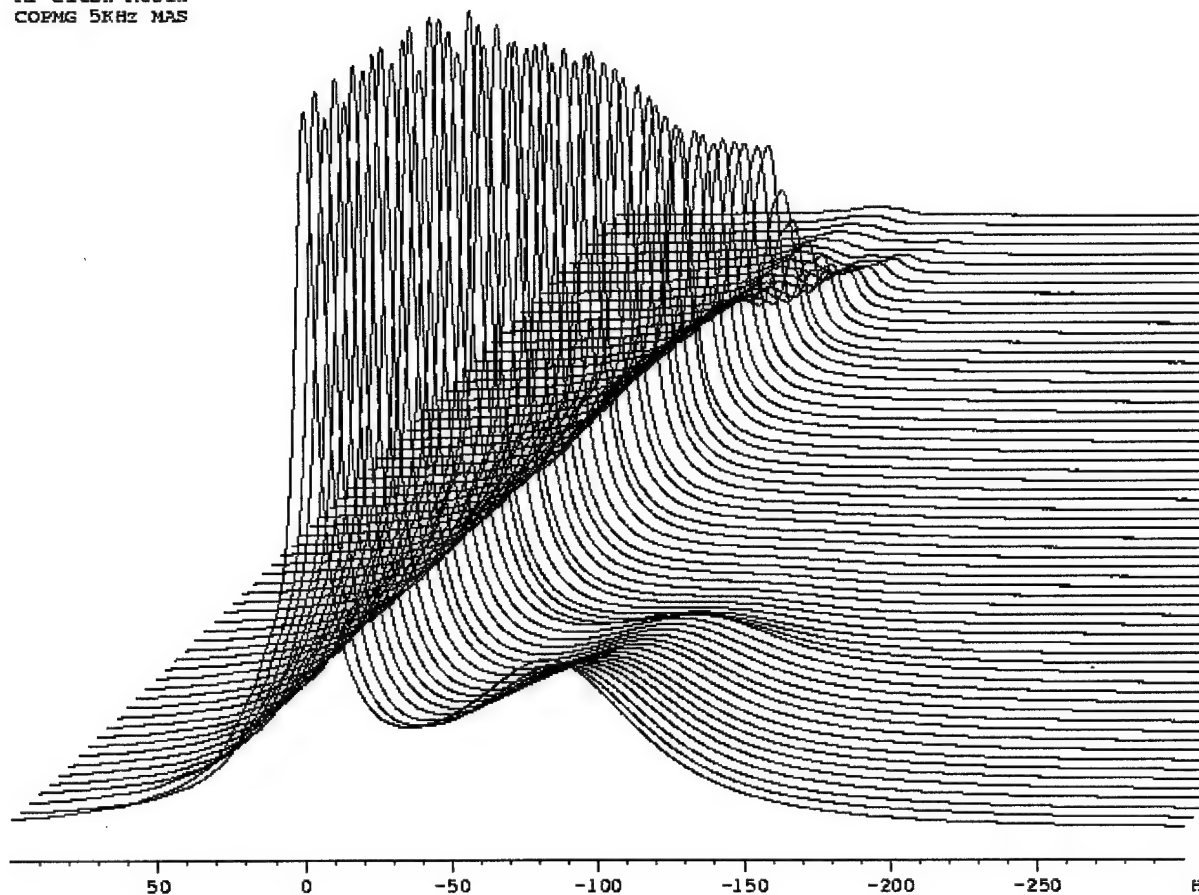


Figure A.4.19: Stacked plot of clean RF resin from a 12T CPMG sequence with MAS of 5kHz (fast MAS). The x-axis is in hertz and each spectrum represents increasing echo time from 400us to 640ms. The plot clearly shows the bound and free/plasticizer spin pools, with the free/plasticizer water shown by the main peak and the bound by the broad peak to the right. A third peak associated with the free spin pool can be seen to the left of the main peak at long times.

A.4.3.9. MAS (5kHz) 12T CPMG plot for clean RF resin

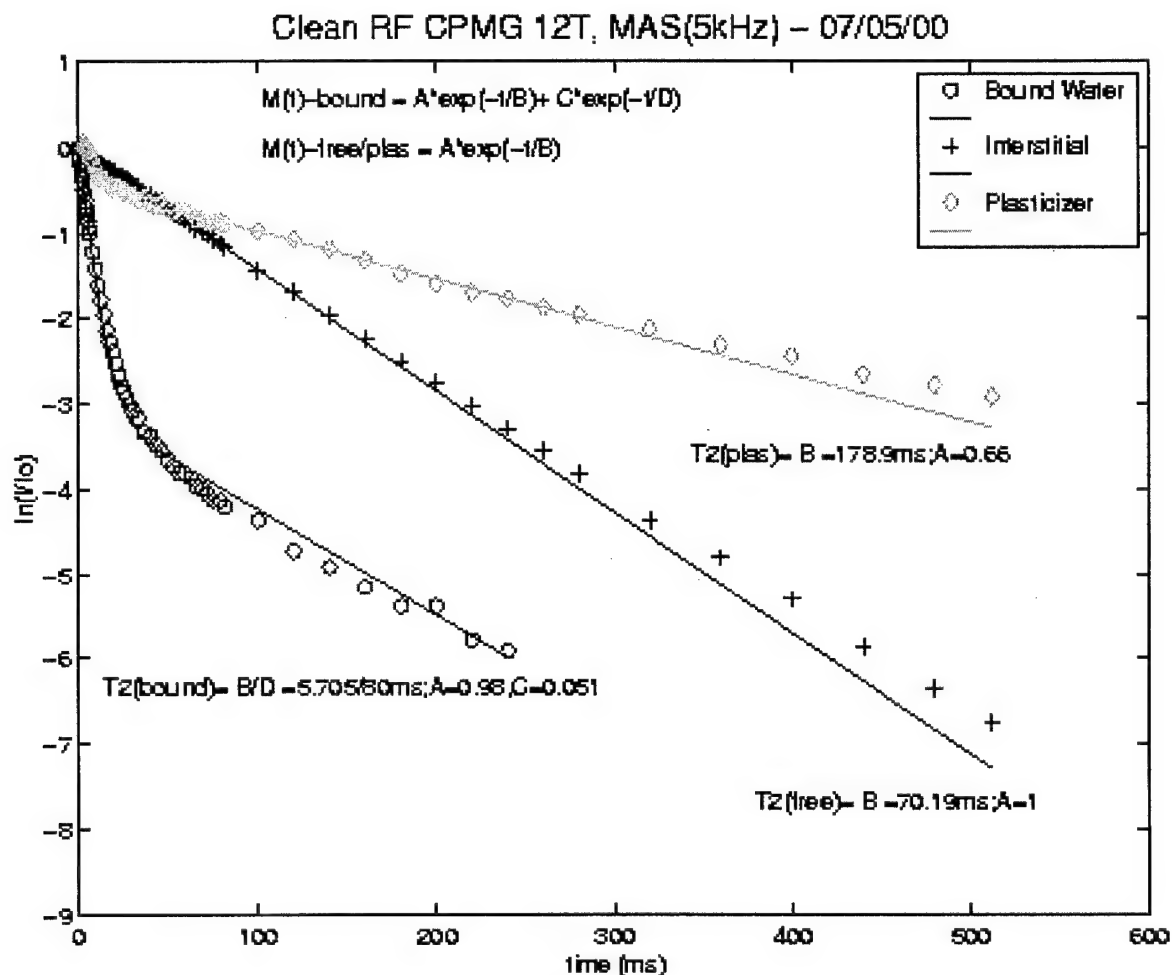


Figure A.4.20: 12T CPMG plot for clean RF resin with MAS of 5 kHz (fast spinning). The peak intensities of the three spin pools seen in the previous stacked spectra were plotted versus the echo time. The T_2 corresponding to the three spin pools is provided as 5.7 ms for the bound water, 70.2 ms for the plasticizer or interstitial water, and 178.9 ms for the free water.

A.4.4. Data Set 4: Pulsed Gradient Stimulated Echo (PGSTE) Diffusion Experiments

A.4.4.1. MAS 12T PGSTE experiment of clean CF resin (0.5ms echo time)

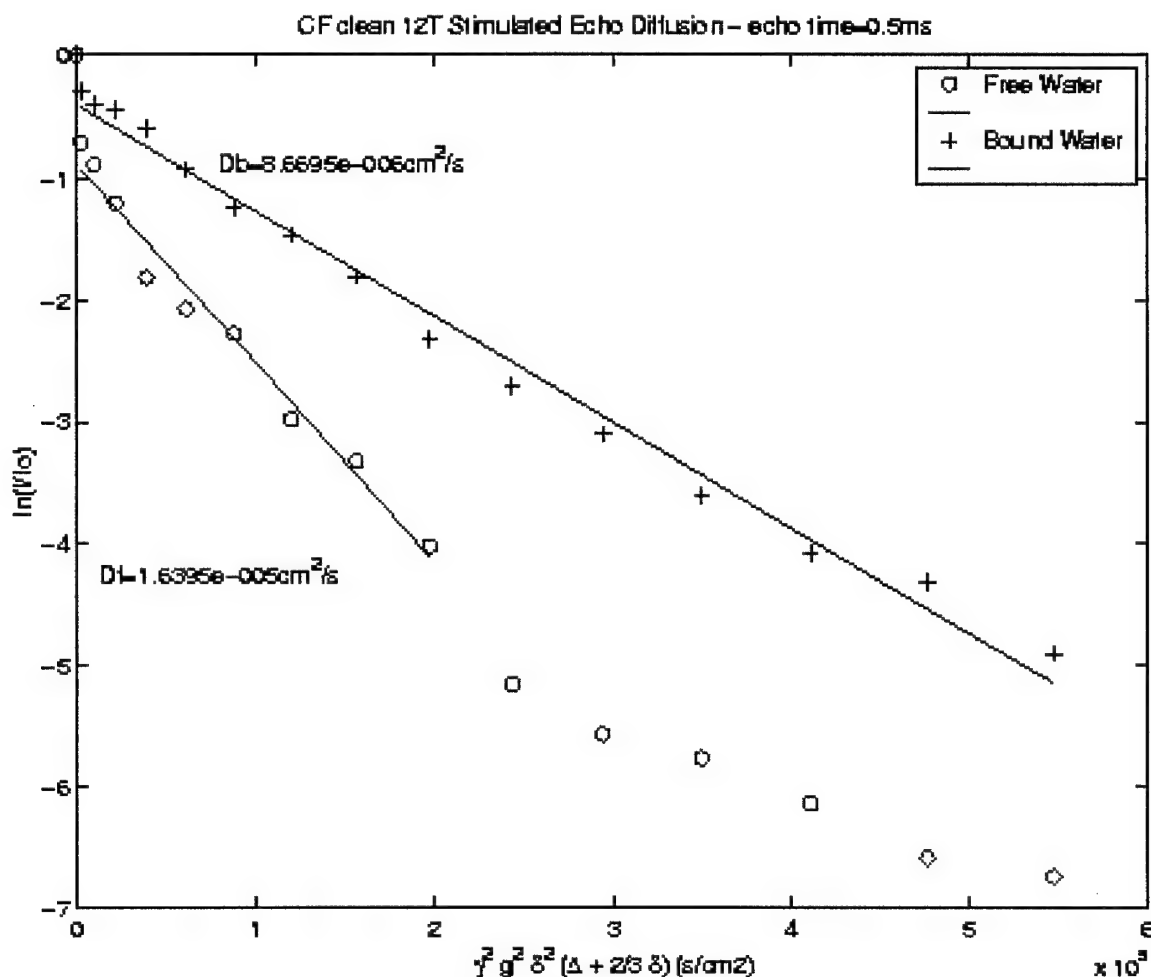


Figure A.4.21: 12T MAS PGSTE experiment of clean CF resin showing of the diffusion of free/interstitial and bound water at various gradient strengths (g) at short echo time (500us). The data shows that at restricted diffusion in the later case. The experiment was done on the 12T magnet with MAS of 5 kHz, an echo time of 0.5 ms, and a storage time of 152ms.

A.4.4.2. MAS 12T PGSTE stacked plot of clean CF resin (20ms storage time)

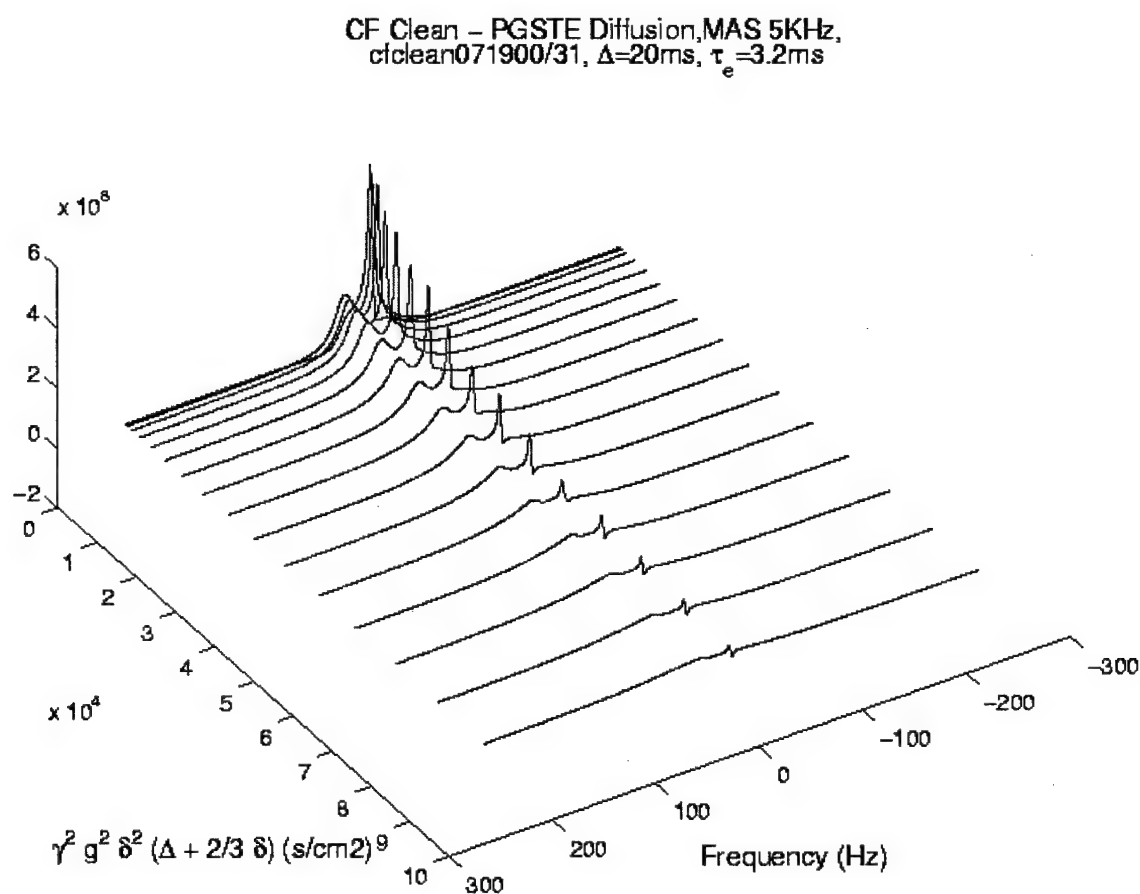


Figure A.4.22: CF clean resin stacked plot of Pulsed Gradient Stimulated Echo (PGSTE) diffusion data with MAS at 5 kHz, a storage time (Δ) of 20 ms, and an echo time (τ_e) of 3.2 ms. The spectra are plotted versus the relative gradient strength squared and frequency. This 20 ms data results in a diffusion coefficient of $2.9\text{E-}5 \text{ cm}^2/\text{s}$.

A.4.4.3. MAS 12T PGSTE stacked plot of clean CF resin (100ms storage time)

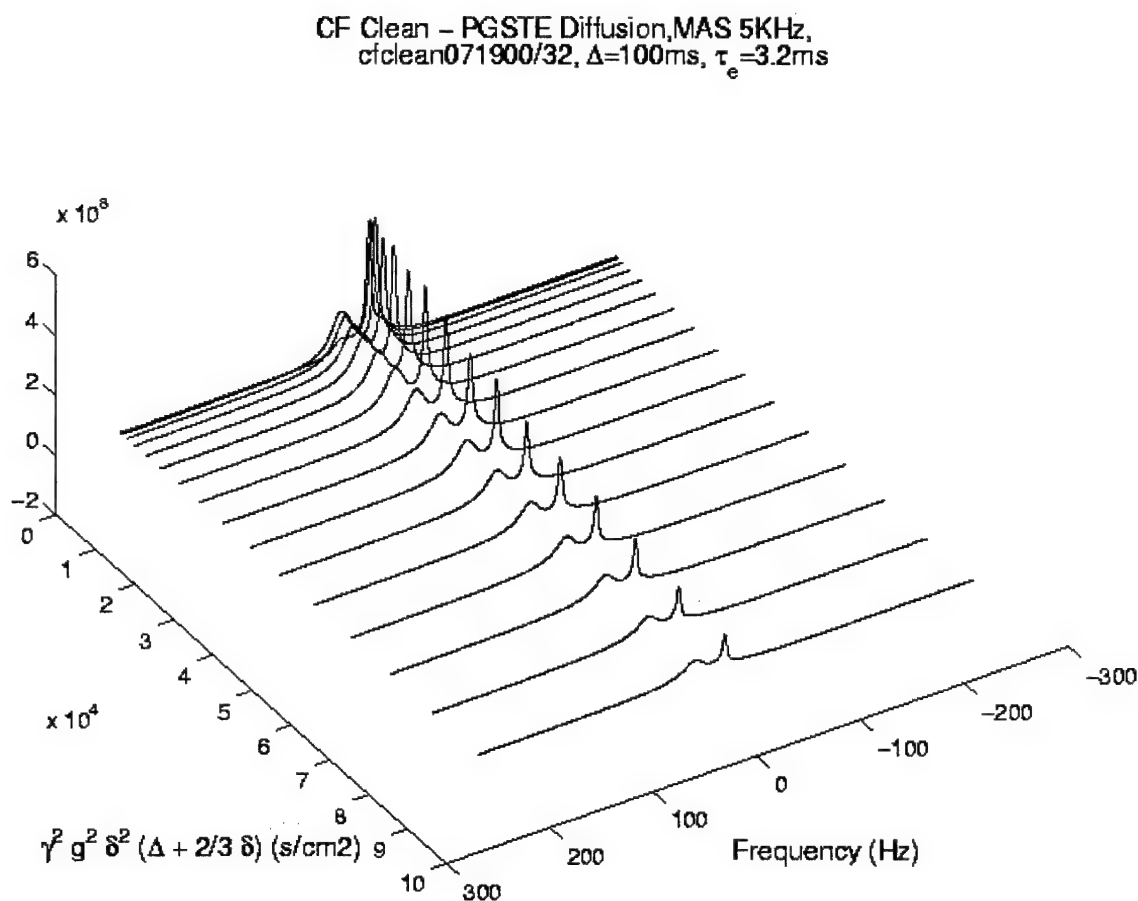


Figure A.4.23: CF clean resin stacked plot of Pulsed Gradient Stimulated Echo (PGSTE) diffusion data with MAS at 5 kHz, a storage time (Δ) of 100 ms, and an echo time (τ_e) of 3.2 ms. The spectra are plotted versus the relative gradient strength squared and frequency. This 100 ms data results in a diffusion coefficient of $1.5\text{E-}5 \text{ cm}^2/\text{s}$.

A.4.4.4. MAS 12T PGSTE stacked plot of clean CF resin (300ms storage time)

CF Clean – PGSTE Diffusion, MAS 5KHz,
cfclean071900/33, $\Delta=300\text{ms}$, $\tau_e=3.2\text{ms}$

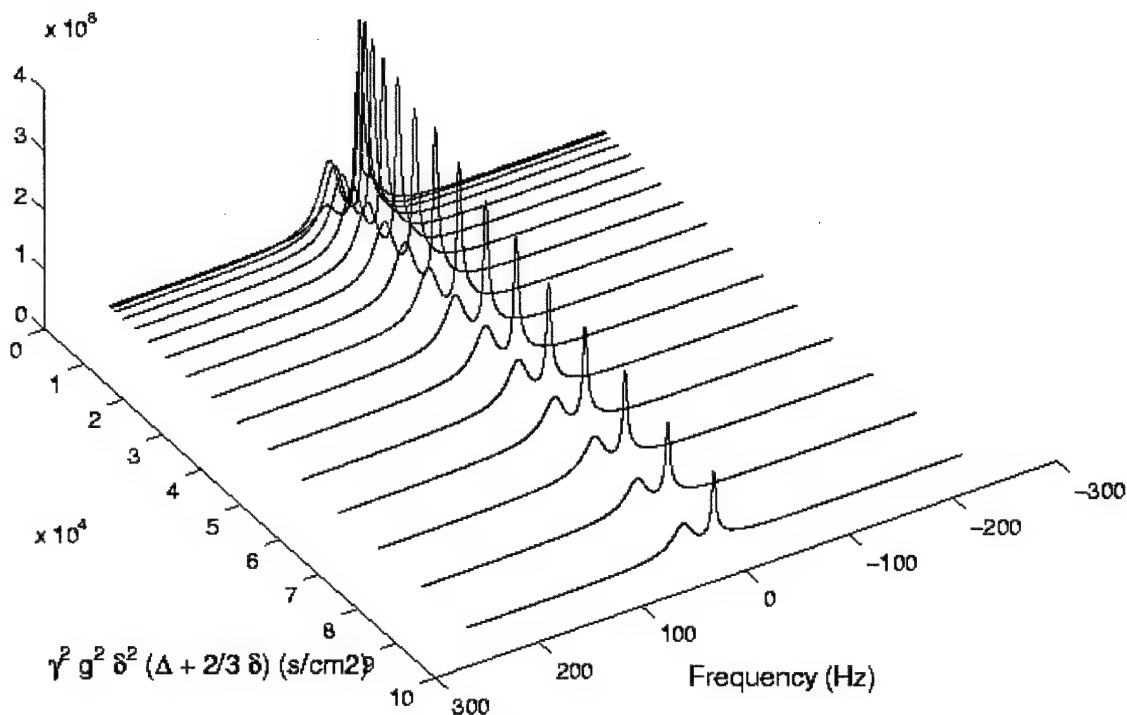


Figure A.4.24: CF clean resin stacked plot of Pulsed Gradient Stimulated Echo (PGSTE) diffusion data with MAS at 5 kHz, a storage time (Δ) of 300 ms, and an echo time (τ_e) of 3.2 ms. The spectra are plotted versus the relative gradient strength squared and frequency. This 300 ms data results in a diffusion coefficient of $1.1\text{E-}5\text{ cm}^2/\text{s}$.

A.4.4.5. MAS 12T PGSTE stacked plot of clean CF resin (1s storage time)

CF Clean – PGSTE Diffusion, MAS 5KHz,
cfclean071900/34, $\Delta=1$ s, $\tau_e=3.2$ ms

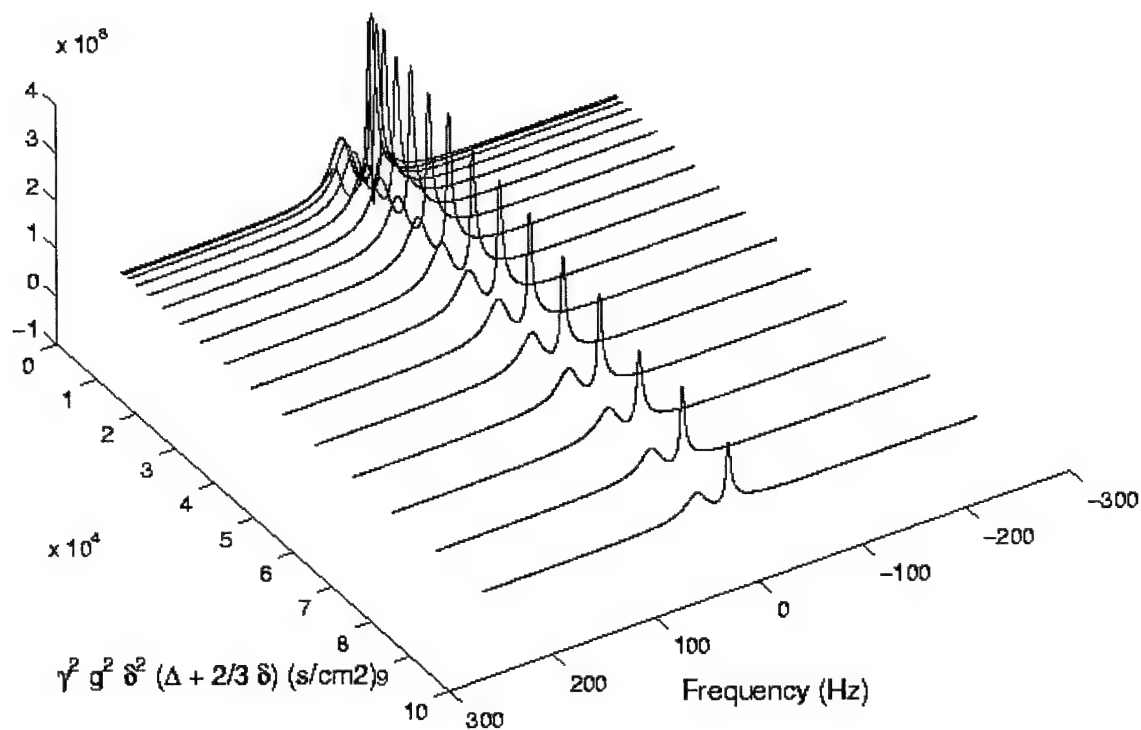


Figure A.4.25: CF clean resin stacked plot of Pulsed Gradient Stimulated Echo (PGSTE) diffusion data with MAS at 5 kHz, a storage time (Δ) of 1 s, and an echo time (τ_e) of 3.2 ms. The spectra are plotted versus the relative gradient strength squared and frequency. This 1 s data results in a diffusion coefficient of $1.1\text{E-}5 \text{ cm}^2/\text{s}$.

A.4.4.6. MAS 12T PGSTE plot of clean CF resin (3.2ms echo time)

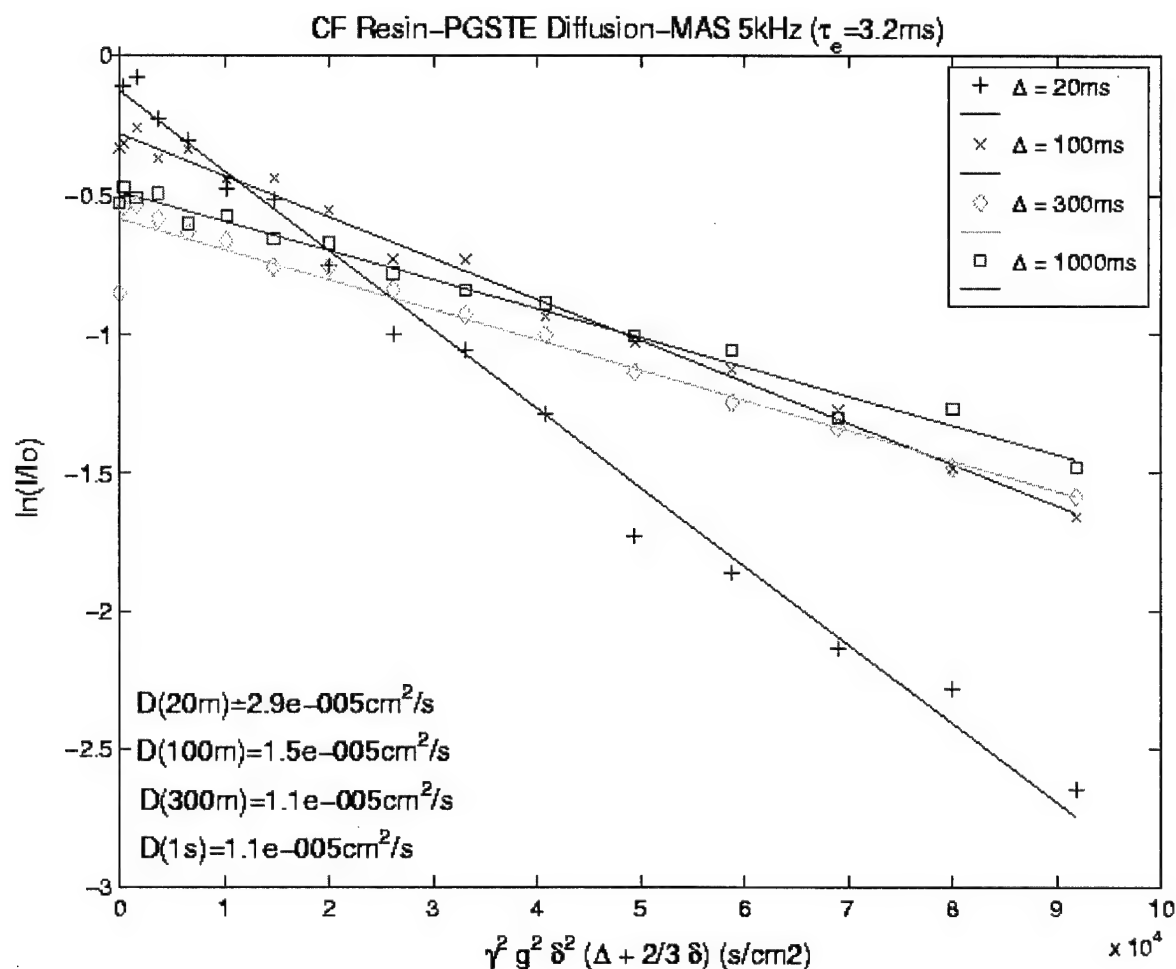


Figure A.4.26: 12T MAS PGST experiment of clean CF resin showing of the diffusion of free/interstitial water at various long storage times (Δ). The data shows that as the storage time decreases, the diffusion constant (D) approaches that of free water, and D decrease as the storage time increases due to exchange of the plasticizer water with the bound component. The experiment was done on the 12T magnet with MAS of 5 kHz and an echo time of 3.2 ms.

A.4.4.7. MAS 12T PGSTE plot of clean CF resin (center peak-free/interstitial water)

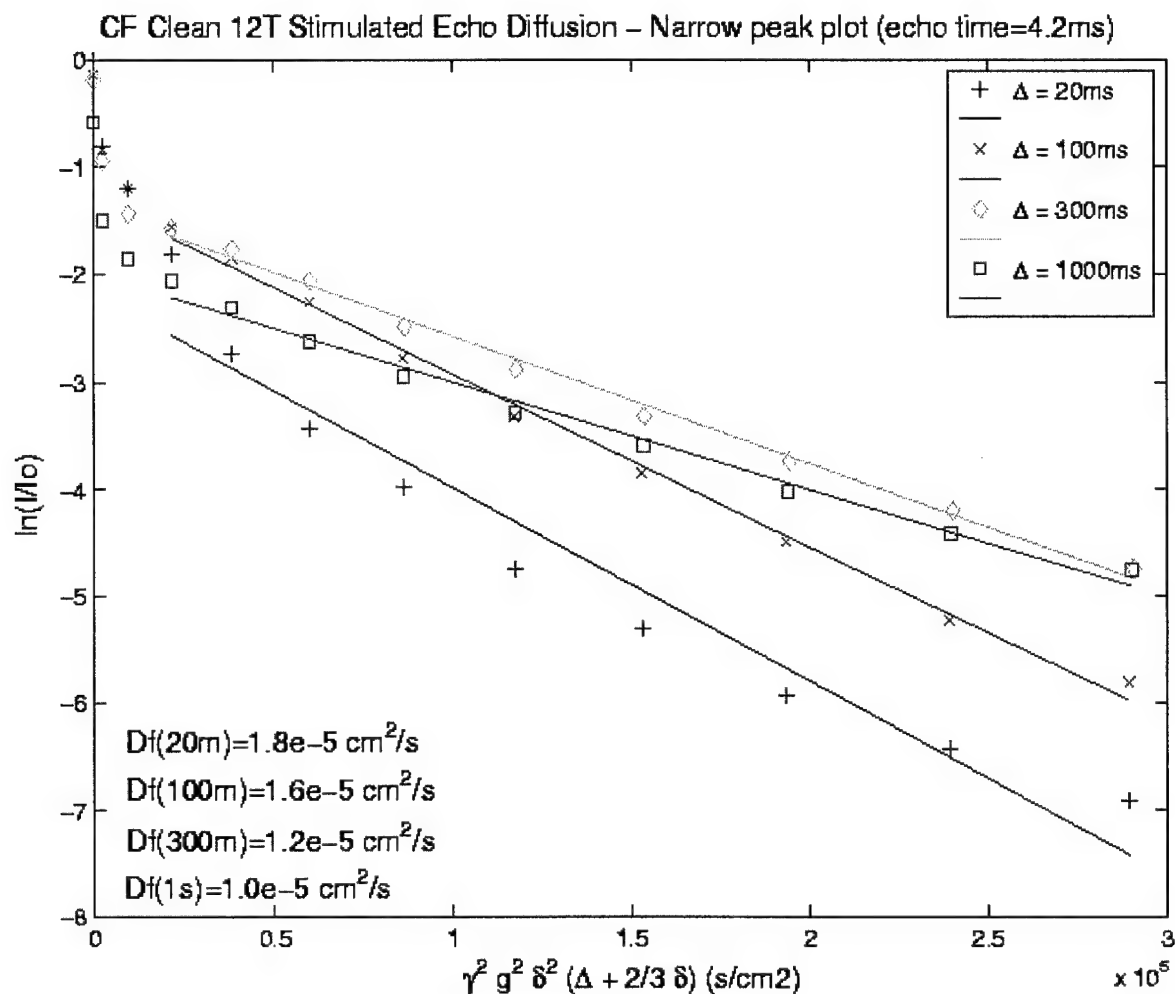


Figure A.4.27: 12T MAS PGSTE experiment of clean CF resin showing of the diffusion of free/interstitial water at various long storage times (Δ). The data shows that as the storage time decreases, the diffusion constant (D) approaches that of free water, and D decrease as the storage time increases due to exchange of the plasticizer water with the bound component. The experiment was done on the 12T magnet with MAS of 5 kHz and an echo time of 4.2 ms.

A.4.4.8. MAS 12T PGSTE plot of clean CF resin (side peak-bound water)

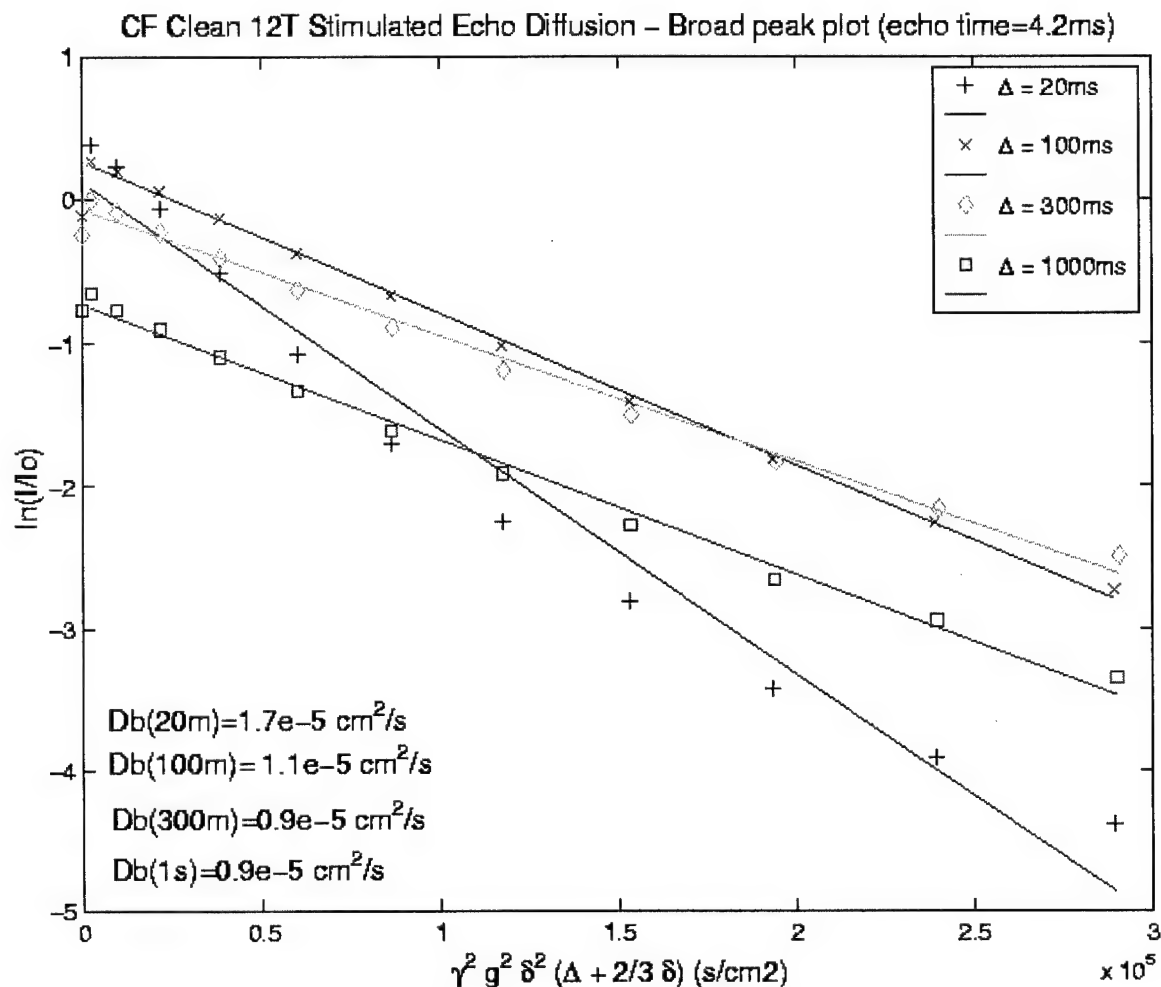


Figure A.4.28: 12T MAS PGSTE experiment of clean CF resin showing of the diffusion of bound water at various long storage times (Δ). The data shows that as the storage time decreases, the diffusion constant (D) approaches free water, and D decrease as the storage time increases due to bounded diffusion. The experiment was done on the 12T magnet with MAS of 5 kHz and an echo time of 4.2 ms.

A.4.4.9. MAS 12T CPMG(550ms)+PGSTE stacked plot of clean CF resin

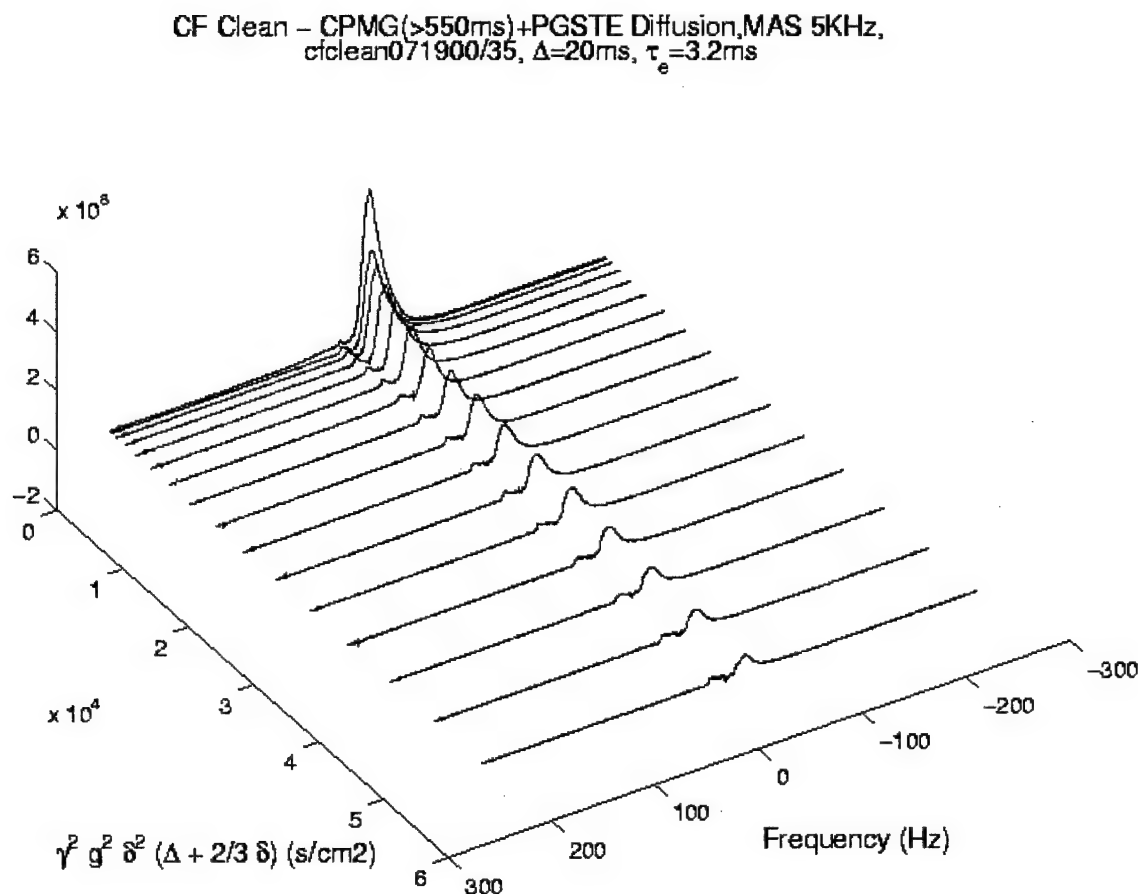


Figure A.4.29: CF clean resin stacked plot of CPMG +PGSTE diffusion data with MAS at 5 kHz, a storage time (Δ) of 20 ms, and an echo time (τ_e) of 3.2 ms. This experiment was used to measure the diffusion rate of the long T_2 component (free water). The CPMG sequence was run for 550ms to allow the plasticizer peak to decay, and then the PGSTE was run. The spectra are plotted versus the relative gradient strength squared and frequency. This diffusion coefficient for the free water was measured to be $2.2\text{E-}5 \text{ cm}^2/\text{s}$ as seen in the following plot.

A.4.4.10. MAS 12T CPMG(550ms)+PGSTE plot of clean CF resin

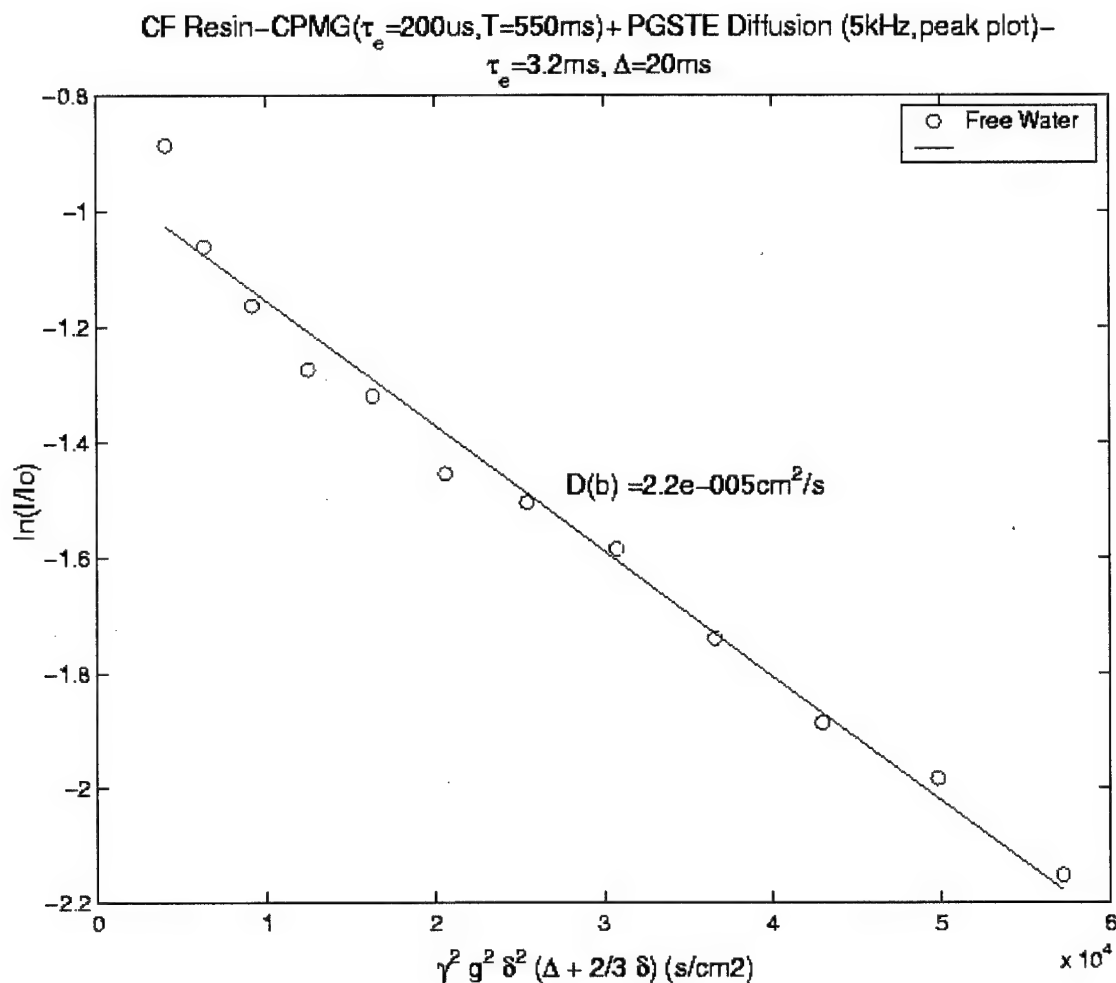


Figure A.4.30: 12T MAS PGSTE experiment of clean CF resin showing of the diffusion of the long-lived free water at a storage time (Δ) of 20 ms, echo time (τ_e) of 3.2 ms, and MAS at 5 kHz. The data shows the apparent diffusion constant (D) is $2.2E-5 \text{ cm}^2/\text{s}$, which is very close to the diffusion constant for free water (as expected).

A.4.4.11. MAS 12T PGSTE plot of clean RF resin (0.5ms echo time)

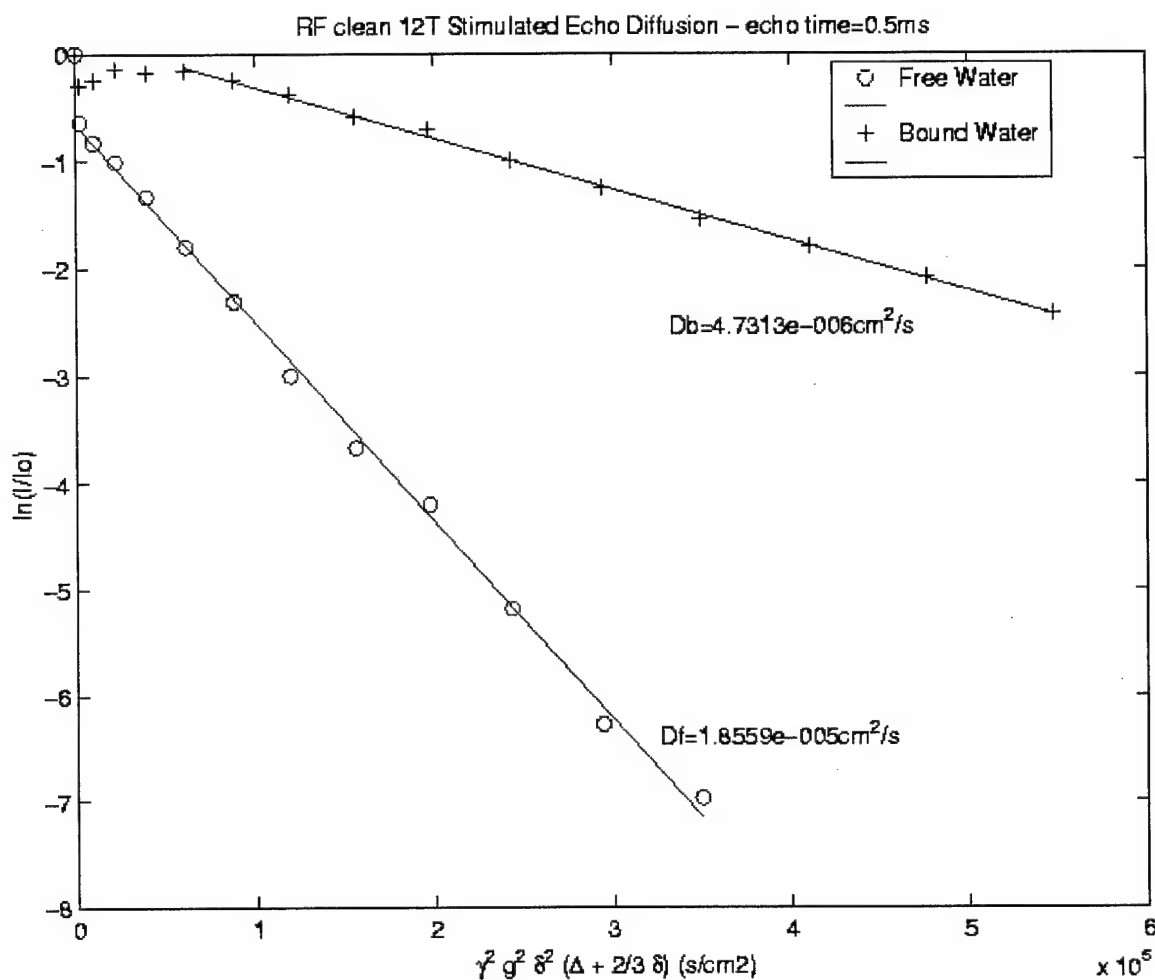


Figure A.4.31: 12T MAS PGSTE experiment of clean RF resin showing of the diffusion of free/interstitial and bound water at various gradient strengths (g) at short echo time (500 μ s). The data shows that at diffusion constant (D) of free/interstitial water is greater than that of bound water due to the bounded diffusion. The D of the interstitial water approaches that of free, unbounded water. The experiment was done on the 12T magnet with MAS of 5 kHz, an echo time of 0.5 ms, and a storage time of 152 ms.

A.4.4.12. MAS 12T PGSTE plot of clean RF resin (15ms echo time)

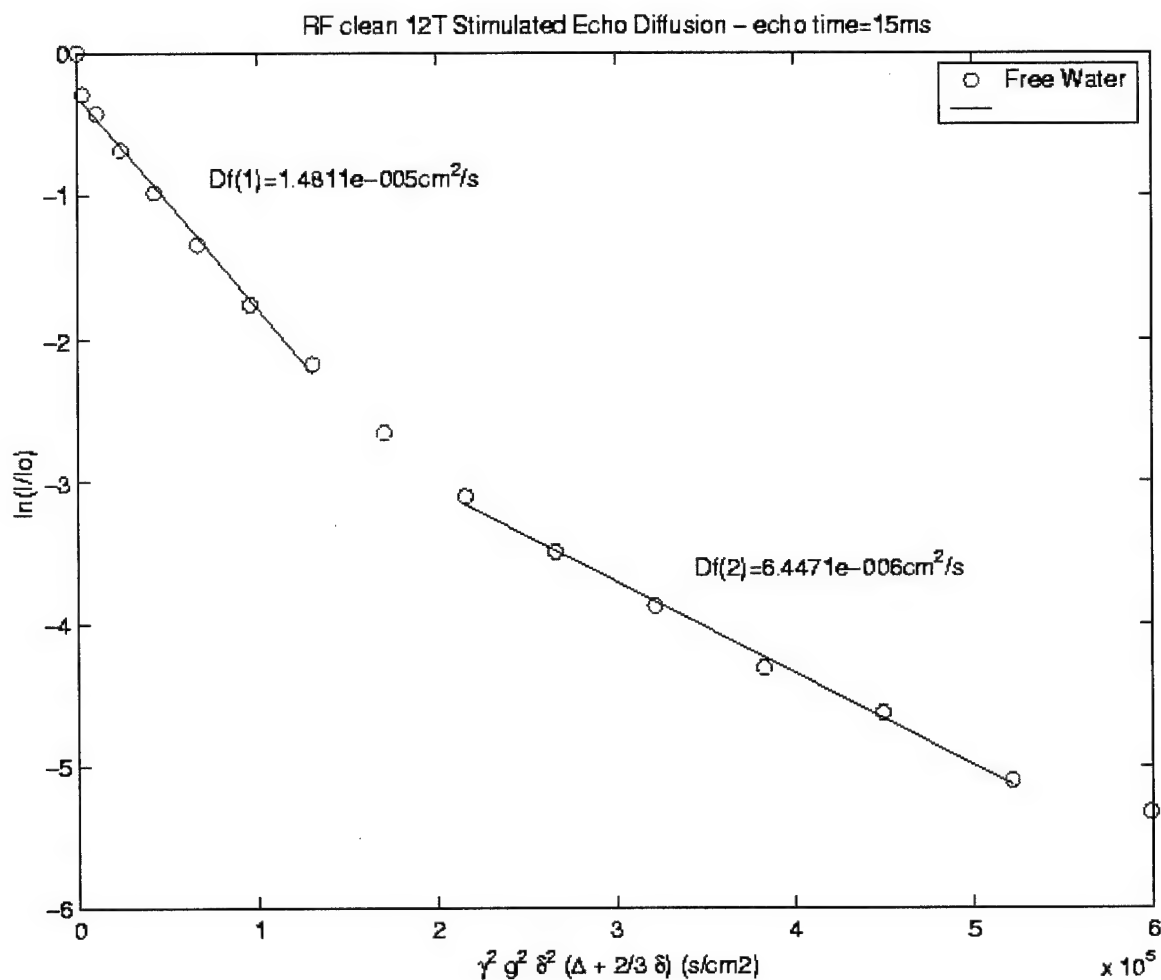


Figure A.4.32: 12t MAS PGSTE experiment of clean RF resin showing of the diffusion of free/interstitial water at various gradient strengths (g) and long echo time (15ms). The data shows that at small g values the diffusion constant, (D), approaches that of free water, and D decreases as the gradient strength increases. The bound component had already decayed providing no useable data. The experiment was done on the 12T magnet with MAS of 5 kHz, an echo time of 15 ms, and a storage time of 165 ms.

A.4.5. Data Set 5: Goldman-Shen Exchange Rate Experiments

A.4.5.1. MAS 12T Goldman-Shen plot of clean CF resin

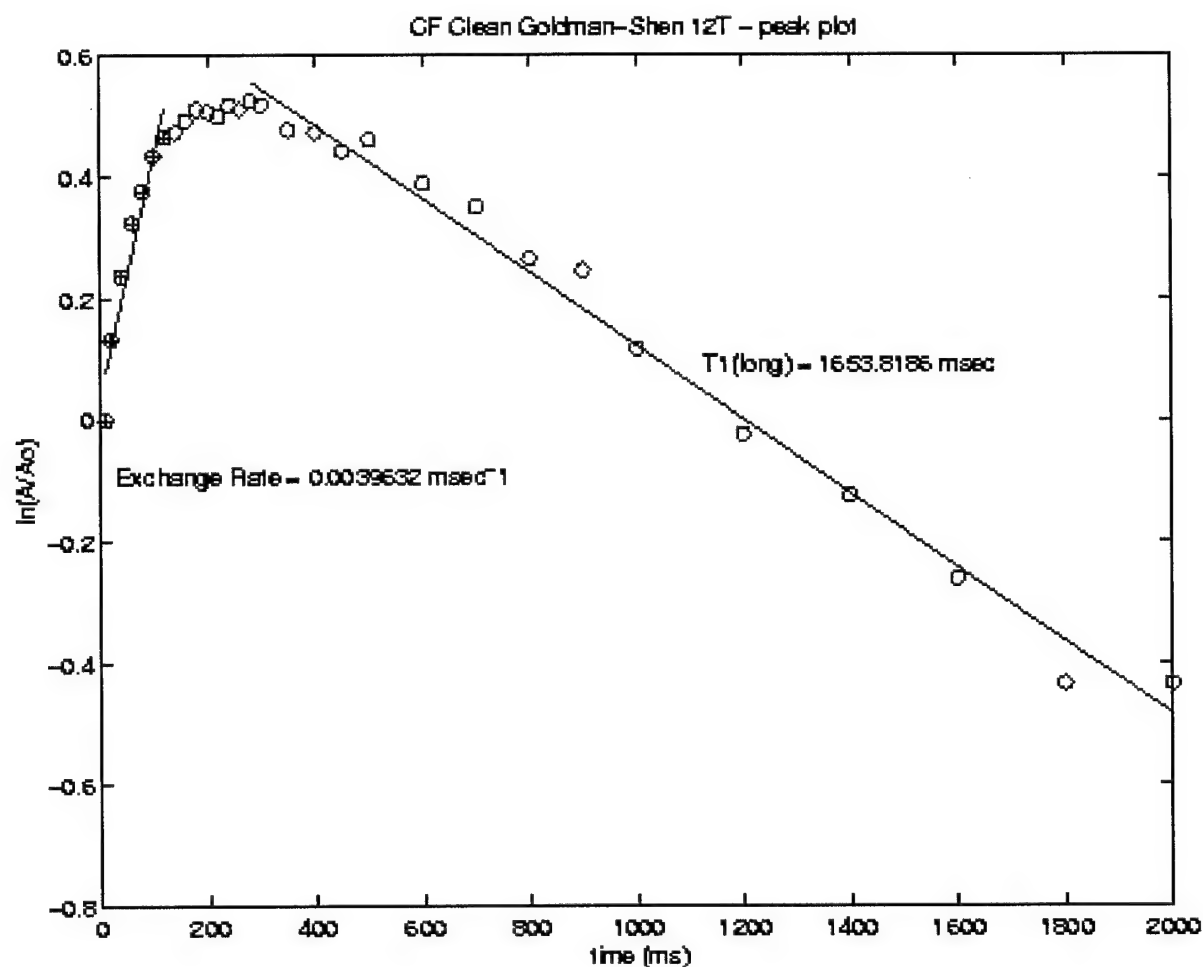


Figure A.4.33: Plot showing the results of 12T Goldman-Shen experiment [7] on clean CF resin. The plot shows the peak height bound water component versus the storage time. The early time shows the exchange of plasticizer water into the bound water pool, and the rate of exchange is given as the slope in this regime. The long time data provides pure T_1 decay. The data shows an exchange rate of $3.96\text{E-}3 \text{ ms}^{-1}$ or a time constant of 252.5 ms. This experiment was performed on the 12T magnet at MAS of 5 kHz and an short delay time of 20 ms.

⁷ M. Goldman and L. Shen, Phys. Rev., 144, 321, 1966.

A.4.5.2. MAS 12T Goldman-Shen plot of clean RF resin

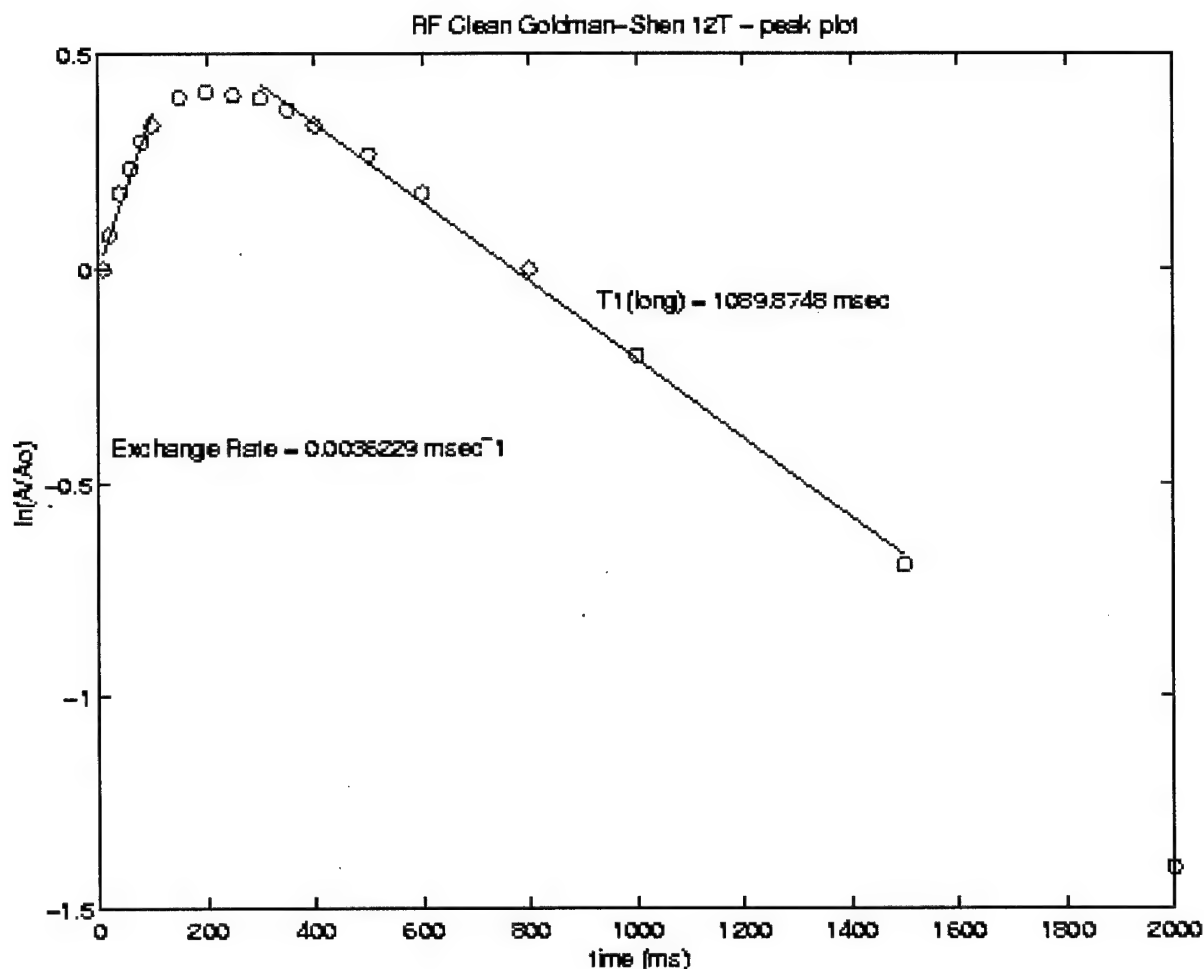


Figure A.4.34: Plot showing the results of the 12T Goldman-Shen experiment [⁸] on clean RF resin. The plot shows the peak height bound water component versus the storage time. The early time shows the exchange of plasticizer water into the bound water pool, and the rate of exchange is given as the slope in this regime. The long time data provides pure T₁ decay. The data shows an exchange rate of 3.62E-3 ms⁻¹ or a time constant of 276.2 ms. This experiment was performed on the 12T magnet at MAS of 5 kHz and an short delay time of 15 ms.

⁸ M. Goldman and L. Shen, Phys. Rev., 144, 321, 1966.

APPENDIX 5.0

NMR IMAGING DATA

2-D NMR Experiment of Flow Structure

1 mM Gd solution into 1cm RF resin showing plugging behavior

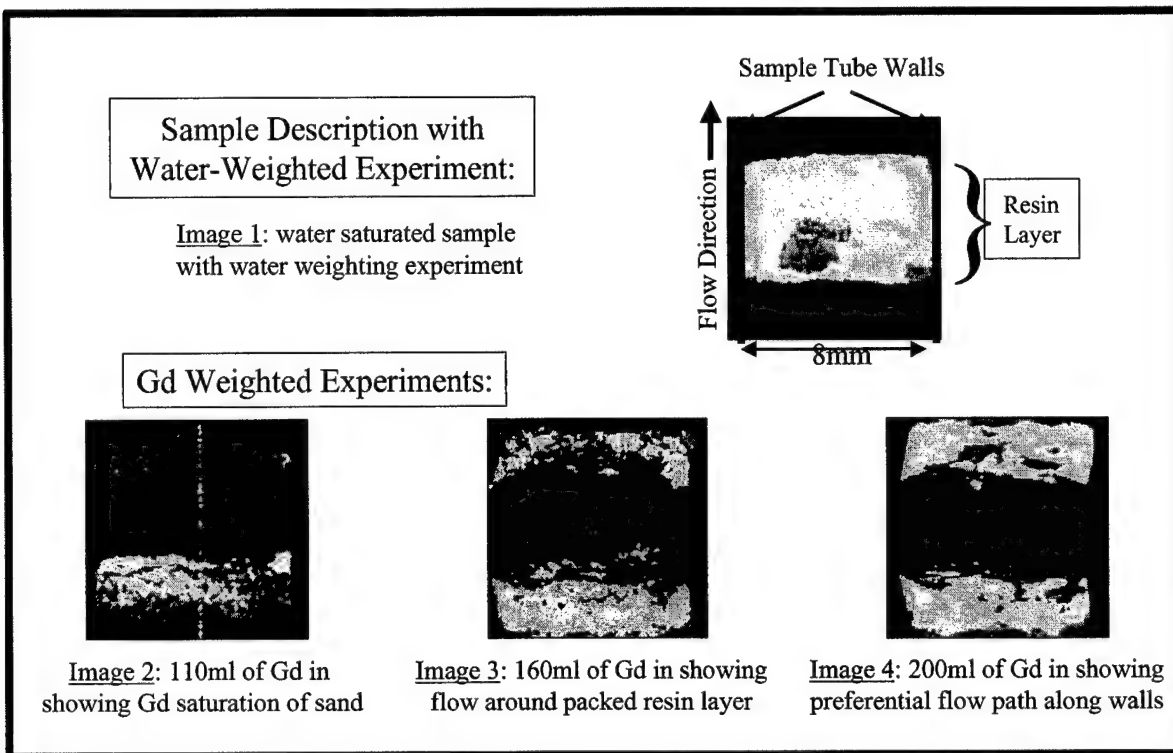


Figure A-5.1: 2-D image sequence showing preferential flow along the tube walls. Packing structure of the resin is also clearly seen in the last image.

NMR Imaging Studies of 2-D Flow

1.0 mM Gd into homogenized CF resin

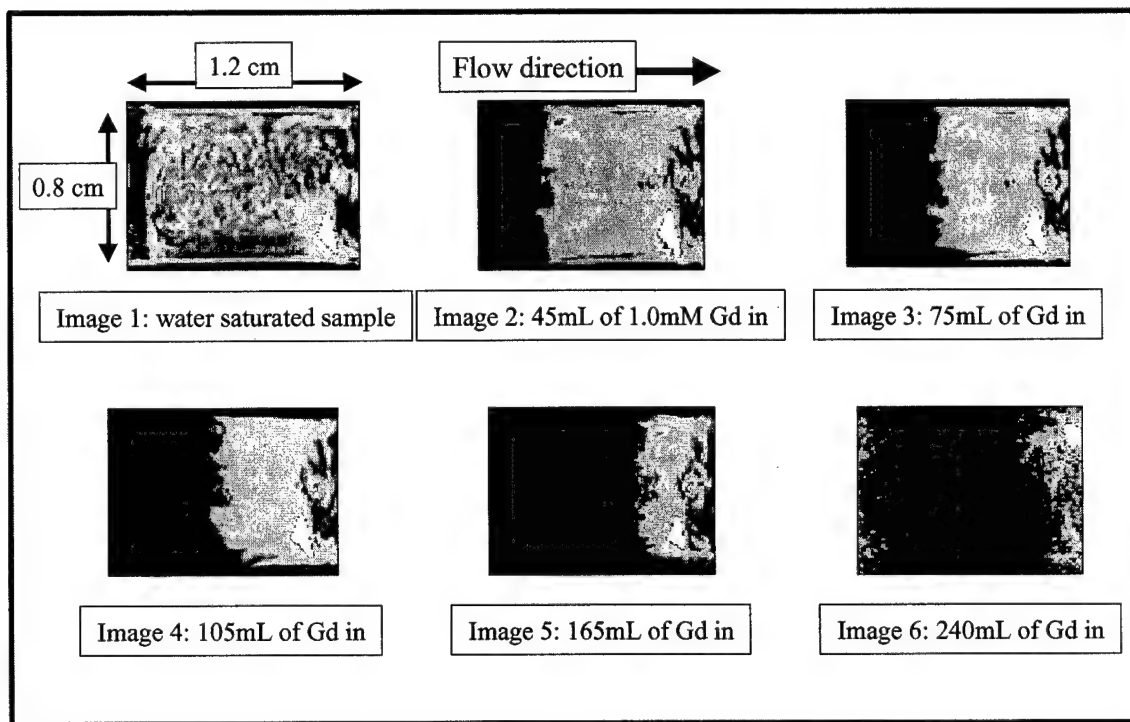


Figure A-5.2: 2-D image sequence of CF resin loading with 1.0 mM Gd solution. The flow appears to be plug-type flow indicating turbulent flow conditions. The degree of fingering appears low and the loading appears uniform.

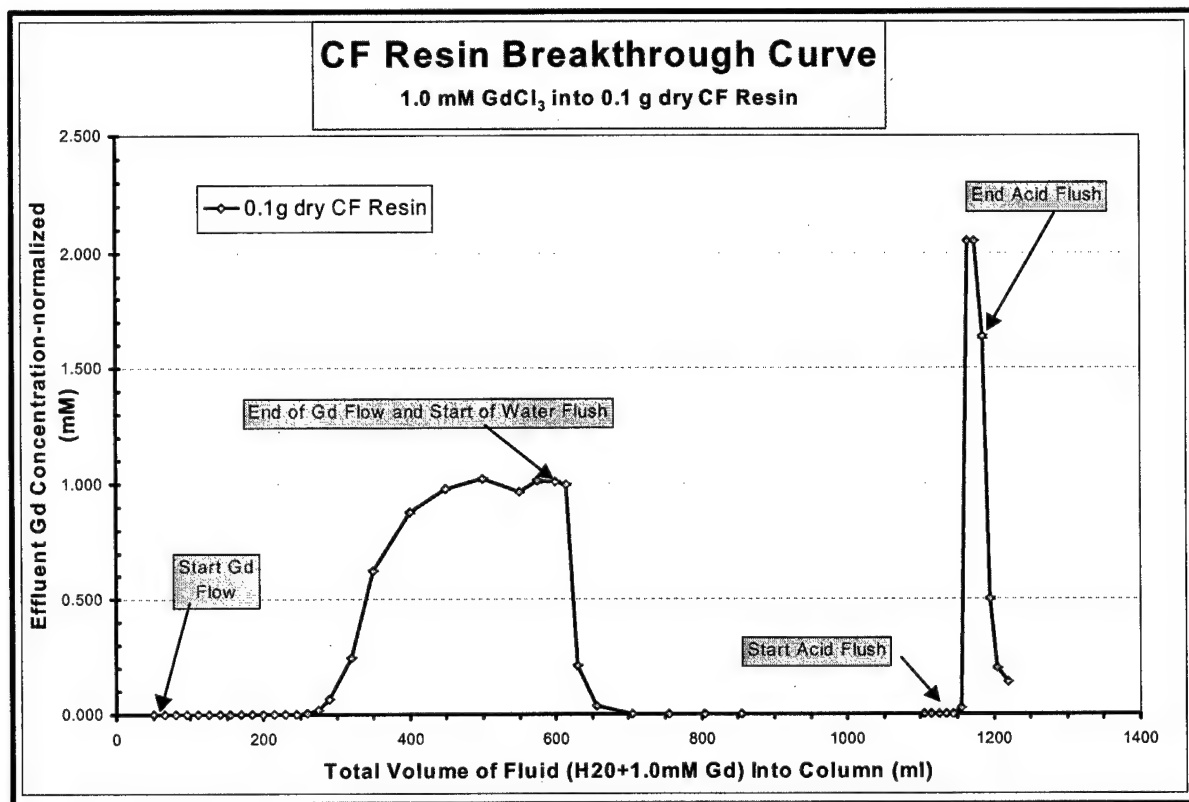


Figure A-5.3: CF Resin breakthrough curve from the image sequence in Figure A-5.2. The breakthrough curve shows a steep rise and drop indicating little channeling or fingering behavior. The high degree of Gd removal after an acid flush is also plotted.

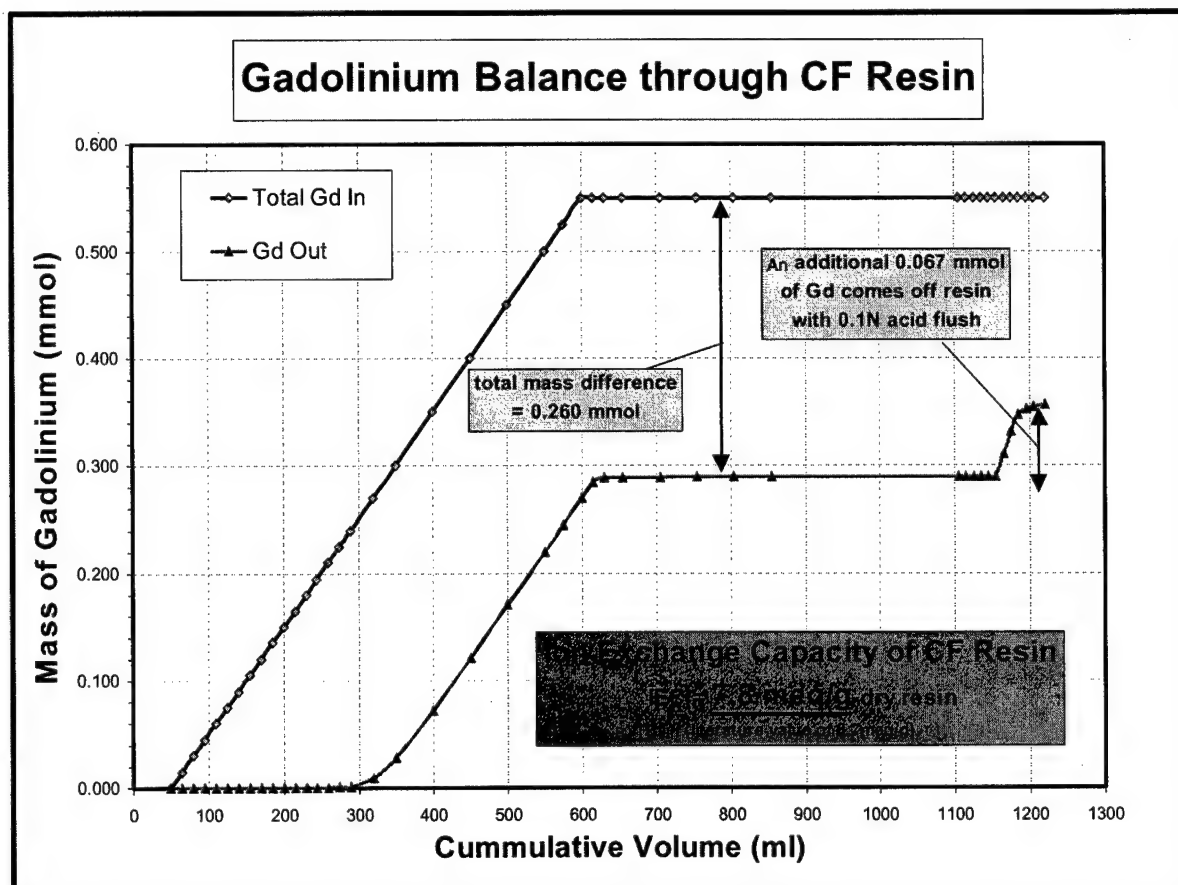


Figure A-5.4: Gd balance plot from the CF flow studies. The plot shows the amount of Gd put into the column and the amount collected in the effluent. The measured proton (ion) exchange capacity is 7.8 meq/g.

NMR Imaging Studies of 2-D Flow

Quantifying Flow and Sorption Using Contour Plots

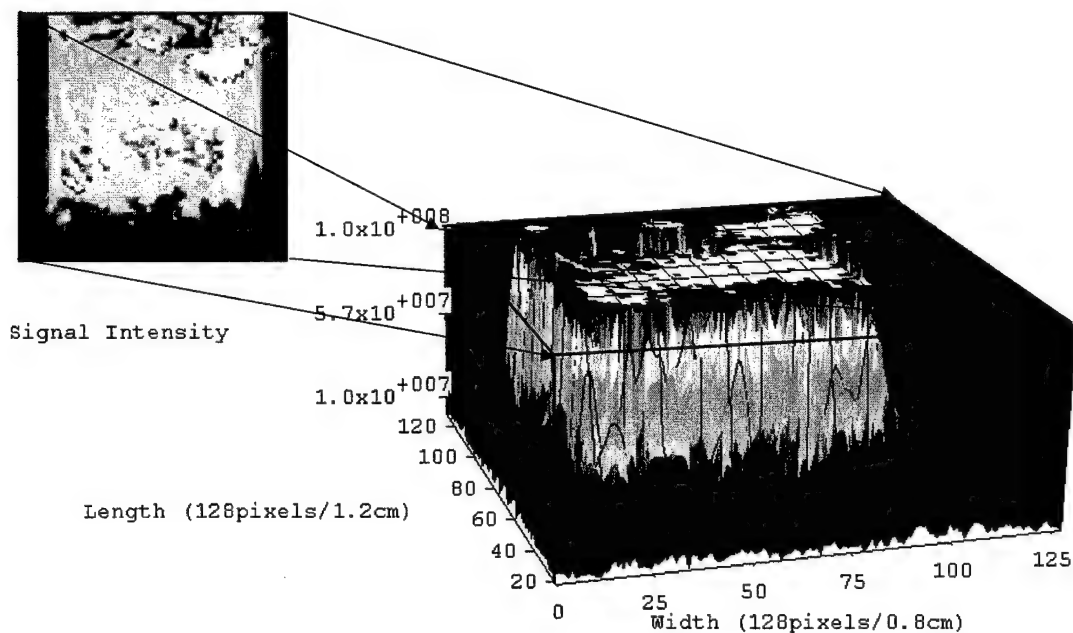


Figure A-5.5: A contour plot from a 2-D image is shown above. This type of display clearly shows the channeling through the resin. Using this type of plot, the degree of resin accessed by the Gd can easily be measured.

Work In Progress: NMR Images of Nevada Test Site Welded Tuft

■ imaging used to evaluate porosity, flow path, connectivity, and sorption sites

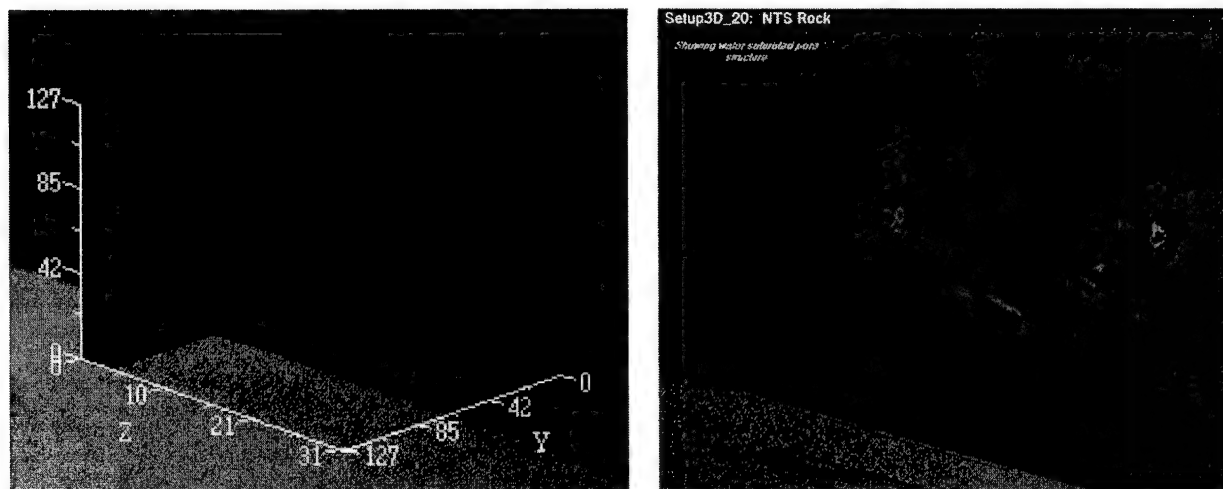


Figure A-5.6: 3-D images of Nevada Test Site welded tuft showing saturated with water. The bright spots are the water pores. More detailed analysis of these type of images could lead to a better understanding of flow structure and connectivity in environmental samples.

[THIS PAGE INTENTIONALLY LEFT BLANK]

APPENDIX 6.0

ICP-AES DATA

Table A-6.1: RF Resin Column Experiment Data

Sample Number	Description	Volume (ml)	Gd Vol In (ml)	Total Vol In (ml)	Gd Count Rate (cps)	Gd Conc. (mM)	Gd Concentration Normalized (mM)	Std Dev. (cps)	Std Dev (mM)
1	DI Water post-flush	50		50	734	0.000	0.0004	107.5	0.0001
2	10+5+5ml 1.0 mM Gd in	20	20	70	927	0.001	0.0005	158.5	0.0001
3	5+5ml 1.0 mM Gd in	10	30	80	837	0.000	0.0005	157.5	0.0001
4	5+25ml 1.0 mM Gd in	25	55	105	5761	0.003	0.0034	182.6	0.0001
5	5+5+15ml 1.0 mM Gd in	25	80	130	2043	0.001	0.0012	294.4	0.0002
6	10+10ml 1.0 mM Gd in	20	100	150	33394	0.018	0.0196	951	0.0006
7	10+10ml 1.0 mM Gd in	20	120	170	64668	0.036	0.0379	128.5	0.0001
8	10+10ml 1.0 mM Gd in	20	140	190	162720	0.090	0.0953	3520	0.0021
9	10+10ml 1.0 mM Gd in	20	160	210	185291	0.103	0.1085	1318	0.0008
10	10+10ml 1.0 mM Gd in	20	180	230	372468	0.206	0.2181	2464	0.0014
11	10+10ml 1.0 mM Gd in	20	200	250	540178	0.299	0.3163	7356	0.0043
12	50ml 1.0mM Gd in	50	250	300	734247	0.407	0.4300	6166	0.0036
14	50ml 1.0mM Gd in	50	300	350	1072400	0.594	0.6280	11269	0.0066
15	50ml 1.0mM Gd in	50	350	400	1287000	0.713	0.7536	9946	0.0058
16	50ml 1.0mM Gd in	50	400	450	1401400	0.776	0.8206	27680	0.0162
17	50ml 1.0mM Gd in	50	450	500	1519200	0.841	0.8896	8617	0.0050
18	50ml 1.0mM Gd in	50	500	550	1540800	0.853	0.9023	16500	0.0097
19	50ml 1.0mM Gd in	50	550	600	1580500	0.875	0.9255	15655	0.0092
20	50ml 1.0mM Gd in	50	600	650	1516700	0.840	0.8882	8269	0.0048
21	25ml 1.0mM Gd in	25	625	675	1553600	0.860	0.9098	13583	0.0080
22	25ml 1.0mM Gd in	25	650	700	1557400	0.862	0.9120	7369	0.0043
23	25ml 1.0mM Gd in	25	675	725		0.860	0.9096		0.0000
24	25ml 1.0mM Gd in	25	700	750	1549100	0.858	0.9071	3633	0.0021
25	25ml 1.0mM Gd in	25	725	775		0.865	0.9148		0.0000
26	25ml 1.0mM Gd in	25	750	800	1575400	0.872	0.9225	25674	0.0150
27	25ml 1.0mM Gd in	25	775	825		0.888	0.9391		0.0000
28	25ml 1.0mM Gd in	25	800	850	1632100	0.904	0.9557	8729	0.0051
29	50ml 1.0mM Gd in	50	850	900		0.916	0.9687		0.0000
30	50ml 1.0mM Gd in	50	900	950	1676400	0.928	0.9817	9794	0.0057
31	50ml 1.0mM Gd in	50	950	1000	1665000	0.922	0.9750	5929	0.0035
32	5+5+15ml Flush Water in	25		1025	1238200	0.686	0.7251	6083	0.0036
33	25ml Flush Water in	25		1050	39513	0.022	0.0231	145.7	0.0001
34	50 ml Flush Water in	50		1100	7452	0.004	0.0044	574	0.0003
35	50 ml Flush Water in	50		1150		0.000	0.0000		0.0000
36	50+500 ml Flush Water in	550		1700		0.000	0.0000		0.0000
37	50 ml Flush Water in	50		1750	2805	0.002	0.0016	612	0.0004
38	Pure DI Water from reservoir	50			778	0.000	0.0005	160.1	0.0001
39	1.0 mM Gd From Reservoir	50			1707700	0.946	1.0000	4387	0.0026

Table A-6.2: CF Resin Column Experiment Data

Sample Number	Description	Sample Vol(mL)	Gd Vol In (mL)	Total Vol In (mL)	Gd Count Rate (cps)	Gd Conc. (mM)	[Gd] mM Normalized	StdDev (cps)	StdDev mM
1	DI Water post-flush	50		50	14001	0.000	0.000	107.5	0.000
2	15mL 1.0 mM Gd in	15	15	65	14943	0.001	0.001	158.5	0.000
3	15mL 1.0 mM Gd in	15	30	80	15397	0.001	0.001	69.5	0.000
4	15mL 1.0 mM Gd in	15	45	95	15487	0.001	0.001	84.4	0.000
5	15mL 1.0 mM Gd in	15	60	110	15743	0.001	0.001	91.8	0.000
6	15mL 1.0 mM Gd in	15	75	125	15604	0.001	0.001	95.1	0.000
7	15mL 1.0 mM Gd in	15	90	140	15558	0.001	0.001	106.5	0.000
8	15mL 1.0 mM Gd in	15	105	155	15696	0.001	0.001	15.2	0.000
9	15mL 1.0 mM Gd in	15	120	170	15485	0.001	0.001	15.32	0.000
10	15mL 1.0 mM Gd in	15	135	185	15798	0.001	0.001	41.29	0.000
11	15mL 1.0 mM Gd in	15	150	200	16443	0.001	0.002	36.74	0.000
12	15mL 1.0 mM Gd in	15	165	215	15623	0.001	0.001	32.86	0.000
13	15mL 1.0 mM Gd in	15	180	230	16050	0.001	0.001	36.74	0.000
14	15mL 1.0 mM Gd in	15	195	245	16280	0.001	0.002	32.86	0.000
15	15mL 1.0 mM Gd in	15	210	260	21754	0.004	0.005	58.6	0.000
16	15mL 1.0 mM Gd in	15	225	275	40328	0.015	0.018	375.4	0.000
17	15mL 1.0 mM Gd in	15	240	290	106350	0.052	0.065	557	0.000
18	30mL 1.0mM Gd in	30	270	320	366220	0.196	0.246	2613	0.001
19	30mL 1.0mM Gd in	30	300	350	909904	0.500	0.626	2829	0.002
20	50mL 1.0mM Gd in	50	350	400	1269600	0.700	0.877	8626	0.005
21	50mL 1.0mM Gd in	50	400	450	1410700	0.779	0.976	4445	0.002
22	50mL 1.0mM Gd in	50	450	500	1472100	0.813	1.019	13487	0.008
23	50mL 1.0mM Gd in	50	500	550	1390900	0.768	0.962	5082	0.003
24	25mL 1.0mM Gd in	25	525	575	1461500	0.807	1.011	12093	0.007
25	25mL 1.0mM Gd in	25	550	600	1458100	0.805	1.009	2720	0.002
26	15mL H2O Flush	15	550	615	1437100	0.794	0.994	5057	0.003
27	15mL H2O Flush	15	550	630	316572	0.169	0.211	1980	0.001
28	50mL H2O Flush	25	550	655	63975	0.028	0.035	459.2	0.000
29	50mL H2O Flush	50	550	705	16764	0.002	0.002	34.19	0.000
30	50mL H2O Flush	50	550	755	16666	0.001	0.002	140.3	0.000
31	50mL H2O Flush	50	550	805	16477	0.001	0.002	79.6	0.000
32	50mL H2O Flush	50	550	855	16236	0.001	0.002	93.8	0.000
33	250mL H2O Flush	250	550	1105	15198	0.001	0.001	52.05	0.000
34	10mL H2O Flush	10	550	1115	16217	0.001	0.002	104.4	0.000
35	10mL H2O Flush	10	550	1125	15196	0.001	0.001	71.3	0.000
36	10mL H2O Flush	10	550	1135	15198	0.001	0.001	109.1	0.000
37	10 mL 0.1M HNO3	10	550	1145	15688	0.001	0.001	35.61	0.000
38	10 mL 0.1M HNO3	10	550	1155	51302	0.021	0.026	910	0.001
39	10 mL 0.1M HNO3	10	550	1165	2948400	1.637	2.050	3136	0.002
40	10 mL 0.1M HNO3	10	550	1175	2948200	1.637	2.050	3134	0.002
41	10 mL 0.1M HNO3	10	550	1185	2352500	1.304	1.634	10021	0.006
42	10mL H2O Flush	10	550	1195	731108	0.400	0.501	7890	0.004
43	10mL H2O Flush	10	550	1205	298310	0.159	0.199	631	0.000
44	15mL H2O Flush	15	550	1220	215064	0.112	0.140	1411	0.001
45	DI Water from reservoir	50	550	1205	14554	0.000	0.000	87.8	0.000
46	1.0 mM Gd from reservoir	50	550	1205	1445100	0.798	1.000	87.8	0.000

Table A-6.3: PF Resin Column Experiment Data

Sample #	Description	Sample Vol(mL)	Gd Vol In (mL)	Total Vol In (mL)	Gd Count Rate (cps)	[Gd] (mM)	[Gd] mM Normalized	StdDev (cps)	StdDev mM
b-1	10mL 0.1mM Gd	10	10	10	30855	0.000	0.000	168	0.000
o-1	25mL 0.1 mM Gd in	25	35	35	32482	0.000	0.000	233.8	0.000
o-2	25mL 0.1 mM Gd in	25	60	60	33023	0.000	0.000	69.6	0.000
o-3	50mL 0.1 mM Gd in	50	110	110	32657	0.000	0.000	122.3	0.000
o-4	50mL 0.1 mM Gd in	50	160	160	32749	0.000	0.000	83.3	0.000
o-5	50mL 0.1 mM Gd in	50	210	210	32878	0.000	0.000	81.3	0.000
o-6	25mL 0.1 mM Gd in	25	235	235	31816	0.000	0.000	235.1	0.000
o-7	25mL 0.1 mM Gd in	25	260	260	31331	0.000	0.000	237.2	0.000
o-8	25mL 0.1 mM Gd in	25	285	285	32389	0.000	0.000	213.6	0.000
o-9	35mL 0.1 mM Gd in	35	320	320	31481	0.000	0.000	81.3	0.000
o-10	40mL 0.1 mM Gd in	40	360	360	31274	0.000	0.000	2.835	0.000
o-11	25mL 0.1 mM Gd in	25	385	385	31230	0.000	0.000	282.5	0.000
o-12	25mL 0.1 mM Gd in	25	410	410	31341	0.000	0.000	97	0.000
o-13	25mL 0.1 mM Gd in	25	435	435	78682	0.003	0.003	309.6	0.000
o-14	25mL 0.1 mM Gd in	25	460	460	32571	0.000	0.000	320.9	0.000
o-15	25mL 0.1 mM Gd in	25	485	485	32262	0.000	0.000	110.4	0.000
o-16	25mL 0.1 mM Gd in	25	510	510	31778	0.000	0.000	155.9	0.000
o-17	25mL 0.1 mM Gd in	25	535	535	32223	0.000	0.000	83.7	0.000
o-18	25mL 0.1 mM Gd in	25	560	560	31022	0.000	0.000	153.6	0.000
o-19	25mL 0.1 mM Gd in	25	585	585	31314	0.000	0.000	109	0.000
o-20	25mL 0.1 mM Gd in	25	610	610	31787	0.000	0.000	309.8	0.000
o-21	25mL 0.1 mM Gd in	25	635	635	31424	0.000	0.000	208.4	0.000
o-22	25mL 0.1 mM Gd in	25	660	660	31277	0.000	0.000	74.5	0.000
o-23	25mL 0.1 mM Gd in	25	685	685	34245	0.000	0.000	89.1	0.000
o-24	25mL 0.1 mM Gd in	25	710	710	68257	0.002	0.002	750	0.000
o-25	50mL 0.1 mM Gd in	50	760	760	390893	0.024	0.024	3931	0.000
w-26	40mL 0.1 mM Gd in	100	860	860	911783	0.059	0.058	4685	0.000
w-27	100mL 0.1 mM Gd in	40	900	900	1295100	0.084	0.084	2767	0.000
b-2	10mL H2O Flush	10	900	910	129736	0.007	0.007	620	0.000
b-3	10mL H2O Flush	10	900	920	44045	0.001	0.001	26.63	0.000
w-28	100mL H2O Flush	100	900	1020	31838	0.000	0.000	109.4	0.000
b-4	10 mL 0.1M HNO3 Acid flush	10	900	1030	38771	0.001	0.001	169.3	0.000
b-5	10 mL 0.1M HNO3 Acid flush	10	900	1040	40186	0.001	0.001	320	0.000
b-6	10 mL 0.1M HNO3 Acid flush	10	900	1050	2942000	0.195	0.193	214	0.000
b-7	10 mL 0.1M HNO3 Acid flush	10	900	1060	2939700	0.194	0.193	221.9	0.000
b-8	15 mL 0.1M HNO3 Acid flush	15	900	1075	1599600	0.105	0.104	10104	0.001
b-9	15 mL 0.1M HNO3 Acid flush	15	900	1090	287061	0.017	0.017	2460	0.000
b-10	15 mL 0.1M HNO3 Acid flush	15	900	1105	195326	0.011	0.011	900	0.000
b-11	15mL H2O Flush	15	900	1120	116227	0.006	0.006	427.7	0.000
w-29	35mL H2O Flush	35	900	1155	105190	0.005	0.005	488.2	0.000
w-30	50 mL H2O Flush	50	900	1205	34444	0.000	0.000	115.1	0.000
b-12	10 mL 1.0M HNO3 Acid flush	10	900	1215	28711	0.000	0.000	272	0.000
b-13	10 mL 1.0M HNO3 Acid flush	10	900	1225	28661	0.000	0.000	187.1	0.000
b-14	15 mL 1.0M HNO3 Acid flush	15	900	1240	125940	0.006	0.006	1256	0.000
b-15	10 mL 1.0M HNO3 Acid flush	10	900	1250	57778	0.002	0.002	128.9	0.000
b-16	15 mL 1.0M HNO3 Acid flush	15	900	1265	41239	0.001	0.001	185.6	0.000
b-17	15 mL 1.0M HNO3 Acid flush	15	900	1280	34629	0.000	0.000	47.73	0.000
b-18	12 mL 1.0M HNO3 Acid flush	12	900	1292	34871	0.000	0.000	106.4	0.000
b-19	10mL H2O Flush	10	900	1302	41987	0.001	0.001	186.6	0.000
b-20	10mL H2O Flush	10	900	1312	99189	0.005	0.005	782	0.000
b-21	10mL H2O Flush	10	900	1322	258893	0.015	0.015	2156	0.000
w-31	100mL H2O Flush	100	900	1422	78287	0.003	0.003	217.4	0.000
b-22	10 mL 6.0M HNO3 Acid flush	10	900	1432	43696	0.001	0.001	158.7	0.000
b-23	10 mL 6.0M HNO3 Acid flush	10	900	1442	51537	0.001	0.001	185.1	0.000
b-24	10 mL 6.0M HNO3 Acid flush	10	900	1452	44109	0.001	0.001	114.6	0.000
b-25	10 mL 6.0M HNO3 Acid flush	10	900	1462	34079	0.000	0.000	155.7	0.000
w-32	100mL H2O Flush	100	900	1562	41790	0.001	0.001	158.4	0.000

w-33	100mL H2O Flush	100	900	1662	31862	0.000	0.000	37.57	0.000
w-34	100mL H2O Flush	100	900	1762	32890	0.000	0.000	248	0.000
b-26	15 mL 1.0mM EDTA flush	15	900	1777	30714	0.000	0.000	172.2	0.000
b-27	15 mL 1.0mM EDTA flush	15	900	1792	31011	0.000	0.000	233.8	0.000
b-28	13 mL 1.0mM EDTA flush	13	900	1805	31192	0.000	0.000	297.9	0.000
b-29	15mL H2O Flush	15	900	1820	29792	0.000	0.000	137	0.000
b-30	15mL H2O Flush	15	900	1835	29734	0.000	0.000	30.37	0.000
w-35	100mL H2O Flush	100	900	1935	31025	0.000	0.000	115	0.000
	0.1mM Gd from Reservoir	1000	900		1540800	0.101	0.100	2789	0.000

[THIS PAGE INTENTIONALLY LEFT BLANK]

APPENDIX 7.0

NITROGEN BET SURFACE AREA ANALYSIS OF PHENOLIC RESINS

The data presented in this appendix was prepared by Marc Vial using a Quantachrome 1000 surface area analyzer using a single-point nitrogen BET method.

Table A-7.1: Summary table of specific surface area (SSA in m^2/g) for phenolic resins in the H^+ and Na^+ forms

resin	<SSA>	stdev
RF-H	0.5098	0.2615
CF-H	1.1146	0.3364
CF-Na	0.3011	0.0892
PF-Na	0.6113	0.1920

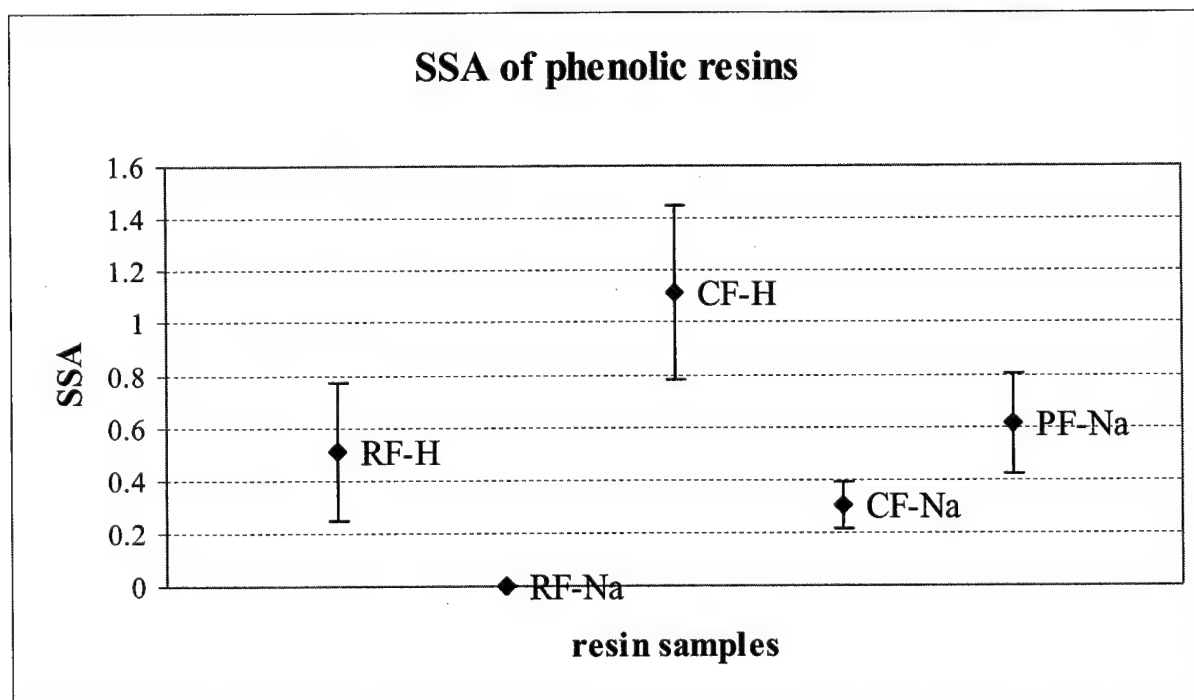


Figure A-7.1: Plot of specific surface area (SSA in m^2/g) for CF, RF and PF resins in the hydrogen (H^+) form and the sodium (Na^+) forms. The data has a very large standard deviation and is much lower than would be anticipated from a polymeric species. This is most likely due to the bound water which does not readily dissociate.

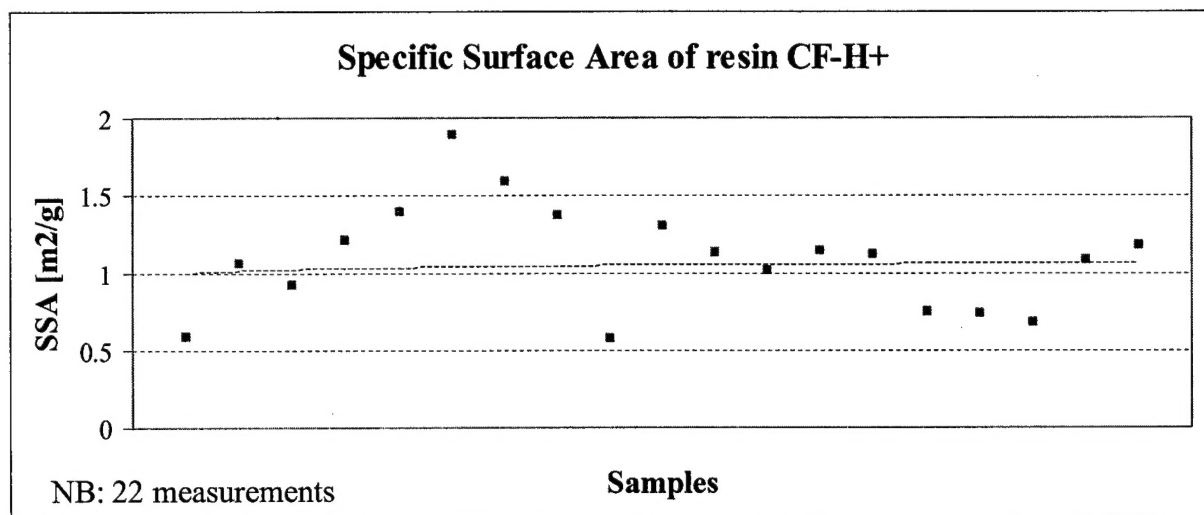


Figure A-7. 2: Plot of the CF H⁺-form resins showing the wide spread of specific surface areas (SSA) with an average SSA of approximately 1.1 m²/g.

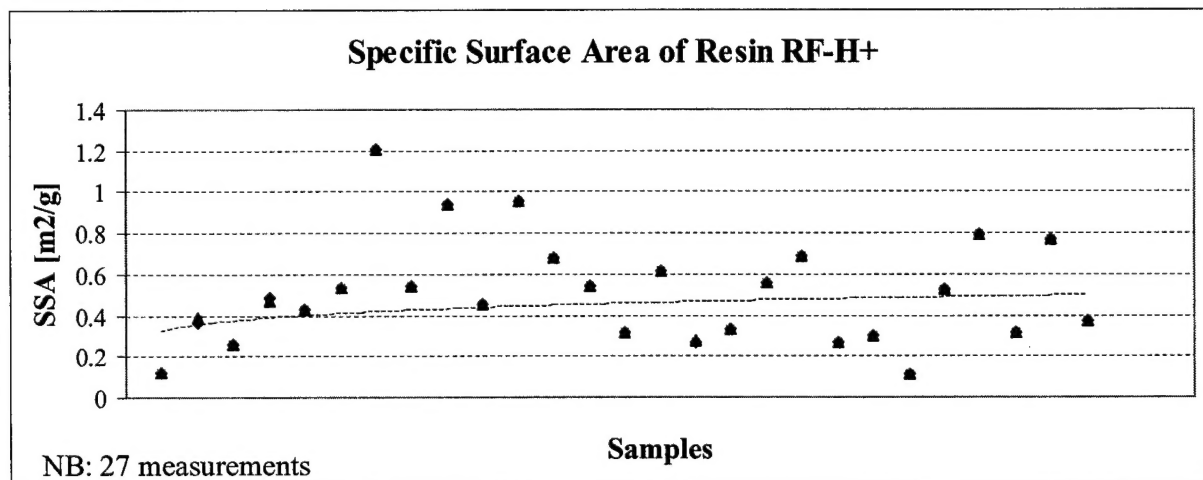


Figure A-7.3: Plot of the RF H⁺-form resins showing the wide spread of specific surface areas (SSA) with an average SSA of approximately 0.5 m²/g.

Table A-7.2: Surface area analysis data for the CF H⁺-form resin

sample 2 CF-H+

sample 2	SSA [m ² /g]	SA [m ²]	m [g] (tube&powder)	m(g) powder	degas time [hr]	degas temp [C]	mass variation
initially	-	-	8.3371	8.3371	0	-	-
after degas 1	-	-	8.3235	8.3235	1.5	95	-0.16%
after degas 2	-	-	8.3234	8.3234	3	95	0.00%
after degas 3	-	-	8.3232	8.3232	5	95	0.00%
1st	0.5251	0.1045	-	-	5	95	
2nd	0.4296	0.0393	8.3234	8.3234	5	95	
3rd	0.5874	0.0539	8.3240	8.3240	5	95	0.01%
after degas 4	-	-	8.3224	8.3224	6/11	110	-0.02%
4th	1.0685	0.0969	8.3231	8.3231	6/11	110	0.01%
5th	0.929	0.0849	8.3234	8.3234	6/11	110	0.00%
6th	1.2114	0.1111	8.3232	8.3232	6/11	110	0.00%
7th	1.4031	0.1284	8.3229	8.3229	6/11	110	0.00%
8th	1.8916	0.1725	8.3233	8.3233	6/11	110	0.00%
9th	1.5968	0.1463	8.3232	8.3232	6/11	110	0.00%
10th	1.3797	0.1262	8.3234	8.3234	6/11	110	0.00%
11th	0.5792	0.0531	8.3235	8.3235	6/11	110	0.00%
after 1 week off	-	-	8.3235	8.3235	-	-	0.00%
12th	1.3097	0.1202	8.3236	8.3236	116	110	0.00%
13th	1.1319	0.104	8.3234	8.3234	116	110	0.00%
14th	1.0177	0.0933	8.324	8.3240	116	110	0.01%
15th	1.1403	0.1053	8.3241	8.3241	116	110	0.00%
16th	1.126	0.104	8.3241	8.3241	116	110	0.00%
17th	0.7568	0.0699	8.3245	8.3245	116	110	0.00%
after degas 1bis	-	-	8.3216	8.3216	116	110	-0.03%
18th	0.7354	0.0661	8.3238	8.3238	116	110	0.03%
19th	0.678	0.0624	8.3219	8.3219	116	110	-0.02%
degas	-	-	8.3219	8.3219	66	110	0.00%
20th	1.0901	0.0983	8.3226	8.3226	66	110	0.01%
21th	1.1832	0.1075	8.3227	8.3227	66	110	0.00%
22th	0.89	0.081	8.3226	8.3226	66	110	0.00%
average	1.05443	0.0956	8.3237	8.3237			-0.01%
stdev	0.32006	0.0277939	0.004014623	0.004			0.03%

m(tube) 8.4328 g

Table A-7.3: Surface area analysis data for the RF H⁺-form resin

sample 1 **RF-H+**

sample 1	SSA [m ² /g]	SA [m ²]	m [g] (tube&powder)	m(g) powder	degas time [hr]	degas temp [C]	mass variation
initially	-	-	8.6505	8.6505	0	-	-
after degas 1	-	-	8.6315	8.6315	1.5	95	-0.22%
1st	0.0124	0.0025	8.6398	8.6398	1.5	95	0.10%
2nd	0.2428	0.0503	8.6324	8.6324	1.5	95	-0.09%
after degas 2	-	-	8.6305	8.6305	17.5	95	-0.02%
3rd	0.1251	0.0247	8.6300	8.6300	17.5	95	-0.01%
4th	0.3919	0.0714	8.6303	8.6303	17.5	95	0.00%
5th	0.2606	0.0515	8.6299	8.6299	17.5	95	0.00%
after 2day stored	-	-	8.6303	8.6303	0.5	110	0.00%
after degas 1bis	-	-	8.6326	8.6326	0.5	110	0.03%
6th	0.4678	0.0975	8.6303	8.6303	0.5	110	-0.03%
7th	0.4319	0.0853	8.6302	8.6302	0.5	110	0.00%
8th	0.534	0.1054	8.6303	8.6303	0.5	110	0.00%
after degas 2bis	-	-	8.6287	8.6287	8.5	110	-0.02%
9th	1.2088	0.2368	8.6297	8.6297	8.5	110	0.01%
10th	0.5445	0.1072	8.6325	8.6325	8.5	110	0.03%
11th	0.941	0.1879	8.6299	8.6299	8.5	110	-0.03%
12th	0.4544	0.0896	8.6296	8.6296	8.5	110	0.00%
13th	0.951	0.1872	8.6299	8.6299	8.5	110	0.00%
14th	0.6813	0.1343	8.6298	8.6298	8.5	110	0.00%
15th	0.5451	0.1074	8.63	8.6300	8.5	110	0.00%
16th	0.3181	0.0627	8.6298	8.6298	8.5	110	0.00%
17th	0.6181	0.1218	8.6301	8.6301	8.5	110	0.00%
after degas 3bis	-	-	8.6287	8.6287	22.5	110	-0.02%
18th	0.2711	0.0531	8.6293	8.6293	22.5	110	0.01%
19th	0.3307	0.065	8.6294	8.6294	22.5	110	0.00%
20th	0.558	0.1097	8.6288	8.6288	22.5	110	-0.01%
21st	0.688	0.135	8.629	8.6290	22.5	110	0.00%
22nd	0.264	0.0518	8.629	8.6290	22.5	110	0.00%
23rd	0.2955	0.058	8.6293	8.6293	22.5	110	0.00%
24th	0.1164	0.0229	8.6296	8.6296	22.5	110	0.00%
25th	0.524	0.1031	8.6297	8.6297	22.5	110	0.00%
26th	0.7956	0.1567	8.6295	8.6295	22.5	110	0.00%
27th	0.3129	0.0616	8.6295	8.6295	22.5	110	0.00%
28th	0.7658	0.1506	8.6296	8.6296	22.5	110	0.00%
29th	0.3718	0.0732	8.6297	8.6297	22.5	110	0.00%
average	0.4741	0.0935	8.6308	8.6308			-0.01%
stdev	0.2256	0.0446	0.0039	0.0039			0.04%

m(tube) 8.4328 g

[THIS PAGE INTENTIONALLY LEFT BLANK]